The clustering and evolution of massive galaxies

Ross, Nicholas Patrick

THE CLUSTERING AND EVOLUTION OF MASSIVE GALAXIES

NICHOLAS PATRICK ROSS

A thesis submitted to the University of Durham

in accordance with the regulations for admission to the

Degree of Doctor of Philosophy.

UNIVERSITY OF DURHAM

2007

THE CLUSTERING AND EVOLUTION OF MASSIVE GALAXIES

NICHOLAS PATRICK ROSS

ABSTRACT

In this thesis we investigate the clustering and evolutionary properties of massive galaxies. We present new measurements of galaxy clustering over a range of redshifts using data from the 2SLAQ Survey and the AAOmega LRG Pilot Survey. The clustering properties of Luminous Red Galaxies (LRGs) are measured using nearly 9 000 2SLAQ LRGs at a mean redshift of $z = 0.55$. We find that the real-space 2-point correlation function is well described by a single power-law of the form $\xi(r) = (r/r_0)^{-\gamma}$, where $\gamma = 1.72 \pm 0.06$ and the correlation length $r_0 = 7.45 \pm 0.35 \;\; h^{-1}$ Mpc. Then we study the redshift-space distortions that are present in the clustering signal. From these dynamical and geometric distortions, we derive a value of $\Omega_{\rm m} = 0.30 \pm 0.15$ and $\beta(z = 0.55) = 0.45 \pm 0.05$, where $\Omega_{\rm m}$ is the present day matter density parameter and $\beta = \Omega_{\rm m}/b$ where b is the linear bias parameter. We find for 2SLAQ LRGs, $b(z = 0.55) = 1.66 \pm 0.35$. If one then assumes a "high-peaks" bias model, this value of b is consistent with the measured clustering strengths for low-redshift, massive early-type galaxies, under the assumption that gravitational growth leaves the comoving space density of early-types independent of redshift. We then use the new AAOmega instrument to perform a study of redshift $z \sim 0.7$ LRGs selected using *riz*-band photometry. We find a redshift-space correlation length of $s_0 = 9.9 \pm 0.5 \;\; h^{-1}$ Mpc and show that using LRGs as tracers would be a very competitive strategy for baryon acoustic oscillation studies in future galaxy redshift surveys. We also confirm that this population again has a clustering strength consistent with the above "high-peaks" bias model. Finally, we use data from the *Spitzer* and *Hubble* Space Telescopes taken in the COSMOS field and find tentative evidence for dust emission possibly coming from obscured star formation. We also show that $z \sim 0.7$ LRGs are predominantly early-type galaxies.

Contents

List of Figures

List of Tables

DECLARATION

The work described in this thesis was undertaken between October 2003 and April 2007 whilst the author was a research student under the supervision of Prof. Tom Shanks in the Department of Physics at the University of Durham. This work has not been submitted for any other degree at this, or any other, university.

The major collaborators involved in this thesis are Prof. Tom Shanks, Dr. José da Ângela and Dr. Phil Outram. Minor collaborators include Dr. David Wake and Dr. Alastair Edge, with Prof. John Peacock contributing Section 6.2.2.

Results from this thesis have appeared in the following papers:

- Ross, N.P. *et al.*, submitted to MNRAS, astro-ph/0612400 (Chapters 3 and 4)
- Ross, N.P. *et al.*, submitted to MNRAS, astro-ph/0704.3739 (Chapters 5 and 6) and
- Cannon, R.D., *et al.*, 2006, MNRAS, 372, 425, (astro-ph/0607631), which provides the source for a significant part of Chapter 2. However, since the thesis author was an integral member of the 2SLAQ Survey team (spending 12 nights observing at the Anglo-Australian Telescope), a co-author on this paper and the relevant details are vital to this thesis, we reproduced parts of this paper herein. All graphs are either originally produced or reproduced by the author, except where explicitly stated.

Results from this thesis have also appeared in the following conference proceedings:

- Ross N.P. & Shanks, T. 2006, ASP Conf. Proc., Vol. 379

CHAPTER 1 | INTRODUCTION

His name was Gaal Dornick and he was just a country boy who had never seen Trantor before. That is, not in real life. He had seen it many times on the hyper-video, and occasionally in tremendous three-dimensional newscasts covering an Imperial Coronation or the opening of a Galactic Council. Even though he had lived all his life on the world of Synnax, which circled a star at the edges of the Blue Drift, he was not cut off from civilization, you see. At that time, no place in the Galaxy was.

- **Isaac Asimov, *Foundation*.**

1.1 MODERN COSMOLOGY

The current Big Bang Theory is based on three pillars of observation:

1. The expansion of the Universe.
2. The Cosmic Microwave Background.
3. Nucleosynthesis of light elements.

The first of these comes from observing distant galaxies and noting that the Doppler shift of the spectral lines implies these galaxies are receding in all directions. We shall return to the expansion of the Universe in due course.

Observations of the Cosmic Microwave Background (CMB), have come to maturity in the last 15 or so years. The power spectrum of the temperature anisotropies that are measured in the CMB tell us a wealth of information about the content of the Universe. The latest results are presented below (Section 1.1.3).

The third of these pillars does not directly concern us here and the reader is directed to reviews such as Boesgaard & Steigman (1985) and Burles et al. (1999) for further details and discussion.

1.1.1 The Hubble Expansion

Although scientists prior to Edwin Hubble had suggested it, e.g. Curtis (1920) and references therein, it was Hubble who first presented evidence for the velocity-distance relationship of galaxies (Hubble, 1929),

$$v = H_0 d \tag{1.1}$$

where v is recessional velocity in units of kilometres per second (kms^{-1}), d is distance from observer in units of megaparsecs (Mpc) and H_0 is the present-day value of a constant of proportionality, now called *Hubble's Constant* where we define $h = H_0/100$ km s^{-1} Mpc^{-1} to parameterise our ignorance of the exact value of H_0. The estimate of the velocity at which an object is receding, is made from the spectrum of the emitted light,

$$\frac{\lambda_{\mathrm{obs}}}{\lambda_{\mathrm{lab}}} = 1 + z \tag{1.2}$$

where λ_{obs} is the observed wavelength of a photon, λ_{lab} is the wavelength of the photon measured in a laboratory and z is the redshift.

1.1.2 GRAVITY, MATTER AND GEOMETRY

The timing of Hubble's observations were critical. Ever since Albert Einstein had formulated his General theory of Relativity in 1916 (GR; Einstein, 1916), various attempts had been made to solve the GR Field equations and build a cosmological model.

Alexander Friedman (or Friedmann) in 1922, Georges Lemaître in 1927 and Howard Robertson and Arthur Walker in 1933 all investigated the most general homogeneous, isotropic and non-stationary solutions for the field equations of GR. As such, we can write down the Friedmann-Lemaître-Robertson-Walker (FLRW) metric which is an exact solution of the Einstein field equations of GR. This describes a homogeneous, isotropic expanding or contracting universe,

$$ds^2 = dt^2 + a(t)^2 \left(\frac{dr^2}{1 - kr^2} + r^2(d\theta^2 + \sin^2\theta d\phi^2) \right) \tag{1.3}$$

where t is the time coordinate and the spatial coordinates are represented in polar form. The constant k represents the spatial curvature, of the Universe. $a(t)$ is the *scale factor*, which represents the time dependence of cosmological distance due to the expansion of the Universe and is related to the redshift by $a_0/a = 1 + z$ where the index 0 indicates the present time and $a(t_0) = a_0 = 1$.

This metric gives rise to the Friedmann Equation, which relates the evolution of the scale factor to the overall energy density of the Universe, ρ,

$$H(t)^2 = \left(\frac{\dot{a}}{a}\right)^2 = \frac{8\pi G}{3}\rho - \frac{kc^2}{a^2} \tag{1.4}$$

where G is the gravitational constant and $H(t)$ gives the rate of expansion of the Universe and is called the Hubble Parameter, with $H(t = t_0) = H_0$. The energy-density and pressure of the fluids of the Universe are related via the Fluid Equation,

$$\dot{\rho} + 3H(\rho + p) = 0 \tag{1.5}$$

and combining Equations 1.4 and 1.5 gives rise to the Second Friedmann equation which describes the Universe's acceleration,

$$\frac{\ddot{a}}{a} = -\frac{4\pi G}{3}\left(\rho + \frac{3p}{c^2}\right). \tag{1.6}$$

Here we can decompose the general energy-density term, ρ into three parts,

$$\rho = \rho_{\mathrm{M}} + \rho_{\gamma} + \rho_{\Lambda}, \tag{1.7}$$

where M stands for the matter content of the Universe, γ for the radiation content of the Universe and Λ for the contribution of the vacuum energy-density. We can also write down an Equation of State which relates the density and the pressure of the fluids we are considering,

$$p = w\rho c^2 \tag{1.8}$$

where w is the equation of state parameter and c is the speed of light, which will be omitted from here on. Since $p = w\rho$, then $w = p/\rho$ and it follows from equations 1.4 and 1.5 (or equation 1.6) that $\rho \propto a^{-3(1+w)}$. For non-relativistic matter, $p_{\mathrm{M}} = 0$ implying $w = 0$ and $\rho \propto a^{-3}$. For radiation, $p_{\gamma} = \rho/3$ implying $w = 1/3$ and $\rho \propto a^{-4}$. At early times, when a was small, radiation played the dominant role in the expansion. However, today, the radiation content of the Universe seems to have a negligible contribution to the energy budget (Mather et al., 1990). For our purposes, we can therefore assume $\rho_{\gamma} = 0$ from here on. For the vacuum: $p_{\Lambda} = -\rho_{\Lambda}$ so $w = -1$ and $\rho \propto a^0$. This value of $w = -1$ is what is required for a "Cosmological Constant". This was a term first introduced by Einstein into the GR field equations when he was trying to reconcile a theoretically dynamic system with the contemporary observational evidence of a static Universe. Note that any equation of of state with $w < -1/3$ implies that the rate of the Hubble expansion is increasing.

Using Equation 1.4, we can define a critical density,

$$\rho_c = \frac{3H^2}{8\pi G} \tag{1.9}$$

with $k \equiv 0$ and

$$\Omega = \frac{\rho_t}{\rho_c}, \qquad \Omega_{\rm M} = \frac{\rho_{\rm M}}{\rho_c}, \qquad \Omega_\Lambda = \frac{\rho_\Lambda}{\rho_c}. \tag{1.10}$$

If $\Omega = 1$, the Universe is said to be "flat" and the energy-density is equal to the critical density. Recent measurements from e.g. distant Type Ia Supernovae (SNe I; Riess et al., 1998, 2004, 2006; Perlmutter et al., 1999), large-scale structure (LSS; Eisenstein et al., 2005; Cole et al., 2005; Tegmark et al., 2006; Percival et al., 2006a) and the CMB (Spergel et al., 2003, 2006), suggest that this is indeed the case and the Universe is (or is *very* near to) flat. These recent measurements also suggest that $\Omega_{\rm M} < 1$ and thus for a flat Universe where $\Omega_{\rm M} + \Omega_\Lambda = 1$, $\Omega_\Lambda \neq 0$. The best current values for these Ω's are given below in Section 1.5.2.

1.1.3 The Cosmic Microwave Background

The FLRW Universe and the idea of an early very hot and very dense universe was fully confirmed by the detection of the CMB in 1965 by Penzias and Wilson (Penzias & Wilson, 1965) along with the theoretical interpretation by Dicke, Peebles, Roll and Wilkinson (Dicke et al., 1965).

The original detection of the CMB by Penzias and Wilson has been followed by many other experiments and missions, all of them too numerous to mention here. However, three of the most critical missions have been on board the *COBE* satellite, the *BOOMERanG* balloon and the *WMAP* satellite. *COBE* (COsmic Background Explorer; Smoot et al., 1992) showed that the CMB was extremely well represented by black body emission with a temperature of 2.73 K, while there were also tiny, 1 part in 10^5, temperature anisotropies.

The *BOOMERanG* (Balloon Observations Of Millimetric Extragalactic Radiation and Geophysics; de Bernardis et al., 2000; Netterfield et al., 2002) was the first experiment to make a significantly large area, high signal-to-noise observation of the CMB temperature anisotropies, such that when combined with a contemporary value of H_0, gave strong indications that the Universe had a flat geometry, at least under certain assumptions of the matter components.

The Wilkinson Microwave Anisotropy Probe (*WMAP*; Bennett et al., 2003) satellite had the main aim to measure the temperature anisotropies in the CMB. With the publication of the 3 year *WMAP* data (Jarosik et al., 2006) the angular power spectrum of temperature anisotropies is known to exquisite accuracy (Hinshaw et al., 2006) and the polarisation power spectrum has also been measured (Page et al., 2006). WMAP has provided an exquisite measurement of the acoustic peaks in the temperature anisotropy power spectrum, placing strong constraints on certain cosmological parameters.

The almost completely homogeneous nature of the CMB on large scales, combined with the axiom that we do not live in a special region of the Universe, leads to the Cosmological Principle:

There is no preferred location or direction in the Universe; the Universe is homogeneous and isotropic

And yet, the observation of the night sky shows many inhomogeneities.

1.2 STRUCTURE FORMATION

1.2.1 DENSITY FLUCTUATIONS

On the largest scales the Universe is believed to be homogeneous and isotropic. However, the primordial density fluctuations first detected in the CMB radiation by *COBE*, correspond to fluctuations in the matter density and it is the subsequent growth of these matter density fluctuations that give rise to the stars, galaxies and superclusters we see today. These tiny matter fluctuations of size δ are described by

$$\delta(\mathbf{x}) = \frac{\rho(\mathbf{x}) - \bar{\rho}}{\bar{\rho}} = \frac{\delta\rho}{\rho_0} \tag{1.11}$$

where $\rho(\mathbf{x})$ is the local density and $\bar{\rho} = \rho_0$ is the mean density of the Universe. We can then define the auto-correlation function as

$$\xi(\mathbf{r}) = \langle \delta(\mathbf{x})\delta(\mathbf{x}+\mathbf{r}) \rangle \tag{1.12}$$

where $r = |\mathbf{r}|$ is a measurement of the separation between two local overdensities. $\delta(\mathbf{x})$ can also be written as a sum of its Fourier modes,

$$\delta(\mathbf{x}) = \sum_{\mathbf{k}} \delta_k \exp(i\mathbf{k}\cdot\mathbf{x}) = \sum_{\mathbf{k}} \delta_k^* \exp(-i\mathbf{k}\cdot\mathbf{x}). \tag{1.13}$$

with the power spectrum, $P(k)$, being defined as

$$P(k) \equiv \langle |\delta_k|^2 \rangle \tag{1.14}$$

where k is the wavenumber, and the scale (or wavelength) λ of a fluctuation is related to the wavenumber k by $k = 2\pi/\lambda$. If the primordial density fluctuations are drawn from a Gaussian distribution, the power spectrum gives a complete statistical description of the fluctuations. One could assume, in its simplest form, the power spectrum could be a power law,

$$P(k) \propto k^n \tag{1.15}$$

where the index, n, governs the balance between large and small scale power. A power spectrum with $n = 1$ will have no preferential scale and is called a Harrison-Zeldovich spectrum. The Harrison-Zeldovich spectrum is often the choice for a primordial Power Spectrum, $P_{\rm pri}(k)$, where the primordial Power Spectrum at very high redshift is related to the Power Spectrum observed at recombination by

$$P_{\rm rec}(k) = T(k)^2 \, P_{\rm pri}(k). \tag{1.16}$$

Here, $T(k)$ is the *transfer function* and conveys all the information about the pre-recombination evolution and the nature of the matter content. Indeed, the transfer function will give a prescription for the weak oscillatory features that are expected, given the Universe has a non-zero baryon content. These are called the *baryon acoustic oscillations* (BAOs). Also, as the density contrast grows and $\delta\rho/\rho$ becomes > 1, non-linear evolution will contribute signatures in the density field.

The relationship between the power spectrum, $P(k)$, and the correlation function, $\xi(r)$, is given by

$$\xi(\mathbf{r}) = \frac{V}{(2\pi)^3} \int |\delta_{\mathbf{k}}|^2 e^{-i\mathbf{k}\cdot\mathbf{r}} \, d^3k. \tag{1.17}$$

In an isotropic universe, the density perturbation cannot contain a preferred direction, and so we must have an isotropic power spectrum: $\langle |\delta_{\mathbf{k}}|^2(\mathbf{k}) \rangle = |\delta_k|^2(k)$. Also, if μ is the cosine of the angle between $\mathbf{k}$ and $\mathbf{r}$, then noting that ξ is real, the integral over all directions of $\mathbf{r}$ gives

$$\int_\Omega e^{-ikr\mu} \, d\Omega = \int_0^{2\pi} d\phi \int_{-1}^{+1} e^{-ikr\mu} \, d\mu = 4\pi \frac{\sin \, kr}{kr} \tag{1.18}$$

and therefore,

$$\xi(r) = \frac{V}{(2\pi)^3} \int P(k) \frac{\sin kr}{kr} 4\pi k^2 \, dk. \tag{1.19}$$

The correlation function is the Fourier transform of the power spectrum. Over a range of scales

from ~ 0.1 to $\sim 20\ h^{-1}$ Mpc, the correlation function, ξ, is well described by a power-law such that

$$\xi(r) = \left(\frac{r}{r_0}\right)^{-\gamma} \tag{1.20}$$

where r_0 is the *correlation length* and γ is the *power-law slope* with $r_0 \simeq 5\ h^{-1}$ Mpc and $\gamma \simeq 1.8$ in the range $0.1\ h^{-1}$ Mpc $\leq r \leq 10\ h^{-1}$ Mpc (e.g. Shanks et al., 1989).

1.2.2 Evolution of Structure

If one probes large-enough scales such that non-linear effects are not relevant, then the growth of density perturbations is given by (e.g. Peacock, 1999)

$$\ddot{\delta} + 2\frac{\dot{a}}{a}\dot{\delta} - \delta\left(4\pi G\rho_0 - \left(\frac{c_s k}{a}\right)^2\right) = 0 \tag{1.21}$$

where $c_s = \sqrt{\partial p/\partial\rho}$ is the sound speed. To simplify matters, we can ignore the second term in the brackets (originating from the consideration of pressure gradients) and also assume $\Omega_{\rm M} = 1$ and $4\pi G\rho_0 = 3H^2/2 = 2/3t^2$. Then we have two solutions,

$$\delta(t) \propto t^{2/3} \quad \text{or} \quad t^{-1}. \tag{1.22}$$

Let us consider the first solution, the "growing mode", where $\delta\rho/\rho \propto t^{2/3}$. As a marker, $\delta\rho/\rho \sim 1/1+z$ in a baryonic, $\Omega_{\rm M} = 1$ Universe. As first seen by *COBE*, δT/T $\sim 2\times10^{-5}$ on 1° scales and thus $\delta\rho/\rho \sim 6\times10^{-5}$ at a redshift of $z \sim 1100$. Today at redshift $z = 0$, we predict $\delta\rho/\rho \sim 6\times10^{-2}$. Essentially, this is not a large enough density contrast to explain the large-scale structure we observe at the present epoch in the universe. Very small fluctuations in the CMB, growing only by gravity, form the inhomogeneous structures of galaxies, groups and clusters we observe today. It is therefore one of the key tasks of modern cosmology to understand the other components of the Universe such that the large observed density contrasts can be explained.

One of these additional components is *cold dark matter* (CDM) which is suspected to be a massive yet collisionless form of matter and which does not emit electromagnetic radiation, hence the description 'dark'. The 'cold' refers to the non-relativistic motions of the theorised dark matter particles.

By combining equation 1.21 with equation 1.4 we can probe the evolution of the density perturbations in different cosmological scenarios. We can then measure the clustering of structure and compare with that from linear theory and N-body predictions, in order to determine the density parameters that describe the energy content of the Universe.

1.2.3 Further Ingredients for Large-Scale Structure

Before we can give a final recipe for large-scale structure we must introduce one more assumption.

This assumption is that the luminous matter in the Universe traces the overall underlying matter distribution. With good evidence that galaxies more massive than the smallest dwarfs are unable to prevent luminous star formation e.g. Taylor & Webster (2005) (however see also Minchin et al., 2005), it seems reasonable that the luminous matter distribution will in some way trace the underlying matter distribution. However, it is also reasonable to assume that the luminous matter might be a *biased* tracer of the overall matter distribution. As an initial guide, we can define the *linear bias parameter*, b, as

$$\delta_{\mathrm{g}} = b\,\delta_{\mathrm{M}} \tag{1.23}$$

where δ_{g} is the galaxy density contrast and δ_{M} the mass density contrast. Further care has to be taken when discussing bias since we know (e.g. Saunders et al., 1992; Norberg et al., 2002a) that different populations have different measured biases values and indeed bias may be

scale-dependent (Smith et al., 2007, and references therein). The investigation of bias will be one of the main themes in the remainder of this thesis.

Now we can give the ingredients for large-scale structure; a primordial $n = 1$ Harrison-Zeldovich Power Spectrum; $T(k)$ the transfer function (including the weak oscillatory features that are expected if the Universe has a non-zero baryon content); non-linear clustering; cold dark matter and a bias prescription will together all lead to suggestions of what one might see in a galaxy clustering observation.

One of the best ways to study the clustering and evolution of large-scale structure is by performing surveys of the cosmic web. By statistically analysing the clustering of galaxies from redshift surveys, we can probe how structure has grown and study the evolutionary properties of the Universe as it expands.

1.3 GALAXY REDSHIFT SURVEYS

Over recent years the results from two redshift surveys have dramatically increased our understanding of large-scale structure and the extra-galactic population locally. The 2 degree Field Galaxy Redshift Survey (2dFGRS; Colless et al., 2001, 2003) used the 3.9m Anglo-Australian Telescope (AAT) and the 2dF instrument with its multi-fibre optics to observe and measure redshifts for ~220,000 galaxies over 1 700 square degrees of the Southern Hemisphere. The 2dFGRS probed galaxies with luminosities ranging from $0.1L^* \lesssim L \lesssim 2L^*$ and redshifts of $0 < z < 0.3$*. The primary science aims that the 2dFGRS achieved included measuring the power spectrum and detection of baryon acoustic oscillations (Percival et al., 2001; Cole et al., 2005), both optical (Norberg et al., 2002b) and near-infrared luminosity functions (Cole et al., 2001), measurement of the cosmological mass density via clustering (Peacock et al., 2001; Hawkins et al., 2003) and the investigation of various galaxy properties by galaxy type (e.g. Madgwick et al., 2003). An incomplete list of further discoveries included obtaining an upper limit on the total neutrino mass (Elgarøy et al., 2002), studying the biasing properties of galaxies (Verde et al., 2002; Wild et al., 2005) and examining galaxy groups (e.g Eke et al., 2004). Observations were completed in 2002 and the full 2dFGRS catalogue can be found at `http://www.mso.anu.edu.au/2dFGRS/`.

The Sloan Digital Sky Survey (SDSS; York et al., 2000) combines a five-band imaging survey of the northern Galactic Cap, with a multi-fibre spectroscopic follow-up programme. The observations for the primary SDSS have been completed, and the final data release, DR5 was made in July 2006. The DR5 Imaging footprint is 8 000 square degrees, and the number of unique objects in the Imaging Catalogue is 215 million, while the Spectroscopic footprint was 5 740 square degrees, and the number of spectra in the Spectroscopic Catalogue is 1 048 960.

*Though in most of the subsequent analyses, redshift cuts were made at around $z = 0.2$.

The SDSS collaboration plan to have three further data releases (DR6 through DR8) as part of the "SDSS-II" project.

The SDSS spectroscopic survey consists of two parts. The dominant portion, with about 88% of the fibre allocation, was a flux-limited sample that reached a magnitude of $r = 17.77$ (Strauss et al., 2002). This is commonly referred to as the MAIN sample.

The other 12% of the galaxy spectroscopic sample was devoted to galaxies fainter than the MAIN galaxy flux cut but which were expected, based on observed colours, to be intrinsically red and at higher redshift. This is the more specialised redshift survey, called the SDSS Luminous Red Galaxy (LRG) Survey. At the outset, the goal of the SDSS Luminous Red Galaxy sample was to produce a volume-limited sample of intrinsically luminous ($\gtrsim 3L^*$) red galaxies out to $z = 0.5$ (Eisenstein et al., 2001). The mean redshift of the SDSS LRG Survey is $z \simeq 0.35$ (e.g. Tegmark et al., 2006).

1.3.1 Luminous Red Galaxies

The primary science driver for the SDSS LRG spectroscopic survey was to probe a volume of $\sim 1h^{-3}$ Gpc^3 with sufficient galaxy number density to yield a definitive detection of the BAO signature in the clustering signal. Luminous Red Galaxies are the ideal candidate galaxies to use for this task for several reasons. They are intrinsically luminous and therefore visible to large distances. They also have distinctive colours leading to a clean and efficient selection. However, the primary reason for choosing LRGs was that they have the ideal number density for probing the Power Spectrum around the BAO scale of $k \sim 0.05\,h\,\mathrm{Mpc}^{-1}$. The amount of cosmological information gleaned from a galaxy redshift survey depends on the "effective volume" that is surveyed, where effective volume is given by (e.g. Tegmark, 1997; Seo & Eisenstein, 2003;

Eisenstein et al., 2005; Tegmark et al., 2006)

$$V_{\rm eff} = \int \left[\frac{n(\mathbf{r})\, P(k)}{1 + n(\mathbf{r})\, P(k)} \right]^2 d^3 r \tag{1.24}$$

where $n(\mathbf{r})$ is the comoving number density of the sample, in units of h^3 Mpc^{-3}, and $P(k)$ is the value of the Power Spectrum at wavenumber k. $V_{\rm eff}$ has units of volume, h^{-3} Mpc^3. A commonly used expression for the error on the Power Spectrum measurement is from Feldman et al. (1994),

$$\frac{\sigma_P}{P} = \sqrt{\frac{2}{n_{\rm modes}}} \left(1 + \frac{1}{nP} \right) \tag{1.25}$$

where $n_{\rm modes}$ is the number of Fourier modes present in spherical shell, width δk, which depends upon the survey volume, V: $n_{\rm modes} = 4\pi^2 \delta k / (2\pi)^3$. The first term on the right hand side of this equation can be thought of as the sample variance, while the second term on the RHS can be thought of as the Poisson shot noise term. Using values quoted in Eisenstein et al. (2005), LRGs having $n \sim 10^{-4}\ h^3$ Mpc^{-3} and $P(k \approx 0.05) = 4 \times 10^4 h^{-3}$ Mpc^3 thus leads to a value of $nP \sim$ a few, which reduces the shot noise term.

The final reason for choosing LRGs is that they are the most massive galaxies and are believed to reside in over-dense peaks of the underlying matter distribution and are thus potentially excellent tracers of large scale-structure. Put another way, they are highly biased objects. The linear bias parameter, b, relates the power spectrum, or correlation function, of the luminous tracers (i.e. galaxies) to that of the underlying matter distribution via

$$P_g(k) = b^2\, P_m(k) \tag{1.26}$$

or equivalently

$$\xi_g(r) = b^2\, \xi_m(r). \tag{1.27}$$

This relates to equation 1.25, and essentially means that fewer galaxies are required to make the same accuracy of measurement if they have larger biases. As a guide, an $\sim L^*$ galaxy from the 2dFGRS has a $b \approx 1$ (Norberg et al., 2002a), while a $\sim 3L^*$ SDSS LRG has $b \approx 2$ (Padmanabhan et al., 2006).

The SDSS LRG Survey has achieved its main aim in regarding the detection of BAOs e.g. Eisenstein et al. (2003, 2005); Tegmark et al. (2006); Percival et al. (2006a,b). This detection is strong experimental evidence that we now have a detection and measurement of the Doppler Peaks in the local, $z \ll 1$, Universe, connecting them to the those at the last scattering surface at $z \sim 1100$. However, BAOs are not the only dynamical and geometric information contained in the clustering signal.

1.4 REDSHIFT-SPACE DISTORTIONS

Measuring the clustering of distant objects in redshift surveys does not provide a direct determination of their true spatial distribution, or the *real*-space clustering of the underlying dark matter. The "real-space" distances are distorted by dynamical distortions due to peculiar velocities and also by geometric distortions if the wrong cosmology is assumed when converting the observed redshifts into physical distances. Thus, the distances estimated from an objects' redshift, will not correspond to a true distance and are therefore said to have been measured in *redshift*-space (z-space).

1.4.1 DYNAMIC DISTORTIONS

When a redshift is measured, the assumption is made that there are two terms contributing to the galaxy's motion. The first (and usually dominant term) is from the Hubble Expansion, v_H, while the second term is due to the contribution from the objects' own peculiar motion, $v_{\rm pec}$. This peculiar velocity term itself contains two contributions, due to two mechanisms involved in the redshift-space dynamical distortions.

The first part of the peculiar velocity from the *random motion* a galaxy has due to the influence of its local potential well. If the distribution of distant galaxies has, on average, a spherically symmetric clustering pattern in real space, then a large velocity dispersion - caused by random motions - will cause the clustering signal at small scales to be smeared along the line-of-sight. These features are often referred to as "Fingers-of-God" and can be seen in radial wedge plots of distant galaxy surveys.

The second part of the peculiar velocity is due to *coherent infall*. As structures in the Universe grow through gravity, the flow and infall of objects from low density to higher-density

regions contributes to the measured redshifts. At larger-scales this leads to a "flattening" of the clustering signal along the line-of-sight. The infall can be parameterised by comparing the large-scale clustering in real- and redshift-space. In terms of the power-spectrum, Kaiser (1987) showed

$$P_{\rm gal}(k_s) = P_{\rm gal}(k_r)(1+\beta\mu^2)^2 \tag{1.28}$$

where the subscripts r and s refer to the real- and redshift-space measurements respectively. μ is the cosine of the angle between the wavevector k and the line-of-sight. β relates the observed large-scale infall to the clustering of the underlying matter and is defined below. For completeness, we can also note at this point that $P_{\rm gal}(k_s)$ can be decomposed (Cole et al., 1994),

$$\begin{aligned} P_{\rm gal}(k_s) &= P_{\rm gal}(k_r)(1+\beta\mu^2)^2 \\ &= \left[\left(1+\frac{2}{3}\beta+\frac{1}{5}\beta^2\right)\mathcal{P}_0(\mu)\right. \\ &+ \left(\frac{4}{3}\beta+\frac{4}{7}\beta^2\right)\mathcal{P}_2(\mu) \\ &+ \left.\left(\frac{8}{35}\beta^2\right)\mathcal{P}_4(\mu)\right] P_{\rm gal}(k_r) \end{aligned} \tag{1.29}$$

where the $\mathcal{P}_l(\mu)$ are the Legendre polynomials with $\mathcal{P}_0 = 1, \mathcal{P}_2 = (3\mu^2-1)/2$ and $\mathcal{P}_4 = (35\mu^4 - 30\mu^2 - 3)/8$. Equation 1.28 above can be written in terms of the correlation function as well (Hamilton, 1992),

$$\xi_{\rm gal}(s) = \xi_{\rm gal}(r)\left(1+\frac{2}{3}\beta+\frac{1}{5}\beta^2\right). \tag{1.30}$$

β is related to cosmology and the matter distribution by

$$\beta \simeq \frac{f(\Omega_{\rm m}^0, \Omega_\Lambda^0, z)}{b} \tag{1.31}$$

where the 0 superscripts imply present day values of $\Omega_{\rm m}$ and Ω_Λ, and b is the linear bias (mentioned above in equations 1.23, 1.26 and 1.27), which relates the luminous matter clustering

to that of the underlying matter. $f(\Omega_{\rm m}^0, \Omega_\Lambda^0, z)$ quantifies the growth of structure as a function of the cosmological parameters (Peebles, 1980),

$$f(\Omega_{\rm m}^0,\, \Omega_\Lambda^0,\, z) = \frac{d\ln\delta}{d\ln a} \tag{1.32}$$

which in the case of a flat Universe can be approximated to (Lahav et al., 1991),

$$f(z) \approx \Omega_{\rm m}(z)^{0.6} + \frac{1}{70}\left(1 - \frac{1}{2}\Omega_{\rm m}(z)(1 + \Omega_{\rm m}(z))\right) \tag{1.33}$$

where the second term is usually neglected. Hence,

$$\beta(z) = \frac{\Omega_{\rm m}(z)^{0.6}}{b}. \tag{1.34}$$

Landy & Szalay (2002) point out there are currently four different frameworks regarding the estimation of β that have been developed; 1) by measuring the ratio of the z and real-space correlation function/power spectrum (e.g. Loveday et al., 1996; Hawkins et al., 2003); 2) by measuring the ratio of the quadrupole to monopole moments of the z-space correlation function/power spectrum (e.g. Hamilton, 1993; Cole et al., 1994; Peacock et al., 2001); 3) by setting the amplitude of the modes of the redshift-space galaxy density field, β and the power spectrum as model parameters (Heavens & Taylor, 1995; Ballinger et al., 1995) and 4) the method given in Landy & Szalay (2002) itself, estimating β by Fourier inverting the z-space distortions seen in the density field.

1.4.2 Geometric Distortions

The second type of distortions that can affect clustering measurements and lead to anisotropies in the clustering signal are due to geometric distortions.

The conversion between redshift, z, and distance, r, in a flat ($\Omega_{\rm m} + \Omega_\Lambda = 1$) Universe, with a cosmological constant is (e.g. Peebles, 1993);

$$r = \frac{c}{H_0} \int_0^z \frac{dz'}{\sqrt{\Omega_{\rm m}^0 (1+z')^3 + \Omega_\Lambda^0}} \tag{1.35}$$

Here, r is the line-of-sight comoving distance. However, as shown by Alcock & Paczynski (1979), if one assumes a cosmology that is different from the true, underlying cosmology of the Universe to convert redshifts to distances, the effect on separations *along* the line-of-sight, differs from the effect *across* the line-of-sight. As a consequence, the clustering signal might appear elongated (or squashed) in the redshift direction. As shown by those authors, these *geometric* distortions can be a powerful cosmological test, namely to determine Ω_Λ. If Δz is the redshift difference between two galaxies, and $\Delta\theta$ their angular separation then,

$$\frac{\Delta z}{z \Delta\theta} = \frac{D_A(z)(1+z)}{cz/H(z)} \tag{1.36}$$

where $H(z)$ is the Hubble Parameter at redshift z and

$$D_A = \frac{c}{H_0(1+z)} \int_0^z \frac{dz'}{\sqrt{\Omega_{\rm m}^0 (1+z')^3 + \Omega_\Lambda^0}} \tag{1.37}$$

is the angular diameter distance (assuming a spatially flat universe with matter and cosmological constant). This ratio is close to unity for small z, but at high redshift, it deviates from unity, by an amount that depends on the cosmological parameters.

As discussed in Ballinger et al. (1996), it is however non-trivial to disentangle the effects of geometric distortions from those caused by peculiar velocities. As we shall see later, while there is a degeneracy in the effects seen by both dynamical and geometric distortions, if you can correctly take into account the dynamical signature in a galaxy clustering measurement, one then has a road into making a measurement of the value of Ω_Λ.

1.5 THE CURRENT PARADIGM

1.5.1 THE BARYON ACOUSTIC OSCILLATIONS

The initial prediction of the acoustic phenomenon in the early universe was made by Peebles & Yu (1970) and Sunyaev & Zeldovich (1970).

The early universe at $\approx 400,000$ years after the Big Bang, consisted of a plasma of mainly electrons, protons, and CMB photons which is usually referred to as the photon-baryon plasma. The fluid is self-gravitating, leading to the growth of over- (and under-) densities as the plasma collapses in localised regions. However, radiation pressure acts as a repulsive, restoring force and thus oscillations akin to sound waves are set up. The resulting acoustic peaks are seen in the CMB angular power spectrum (de Bernardis et al., 2000; Netterfield et al., 2002; Spergel et al., 2003, 2006).

At redshift of $z \simeq 1100$ when the Universe cools sufficiently to allow hydrogen atoms to form, the epoch of Recombination, the photon-baryon plasma decouples and the sound waves are frozen into the matter distribution. A preferential scale, s, is then set such that

$$s = \int_0^{t_{\rm Rec}} dt\, c_s(t)\,(1 + z_{\rm Rec}) \tag{1.38}$$

which gives a zeroth-order estimate for the physical value of the preferential scale. If, $t_{\rm Rec} =$ 379 000 yrs, $c_s = c/\sqrt{3}$ and $z_{\rm Rec} = 1089$ then $s \simeq 70\ \ h^{-1}$ Mpc ≈ 100 Mpc.

In the local redshift $z \approx 0$ Universe, this preferential scale can be detected in the underlying matter distribution traced out by the luminous matter, i.e. by galaxies.

The power of the BAO signature comes by realising that BAOs can be used as a standard ruler at different cosmological epochs. Thus by measuring the scale of acoustic oscillations at $z = 1100$ seen in the CMB power spectrum, and the scale of acoustic oscillation at $z = 0$ seen in

the galaxy power spectrum (or correlation function) one can use this standard measuring rod to see if the geometry of the Universe has changed due to the effects of an accelerated cosmological expansion.

We have already noted the need for redshift surveys of the cosmic web as a prime investigatory tool into the clustering properties of galaxies and the evolution of large scale structure. We now note, the need for redshift surveys that sample *large* volumes of the Universe in order to detect the faint BAO signature at $\sim$ 100 Mpc scales.

1.5.2 THE FASHIONABLE COSMOLOGY

The current values of certain cosmological parameters derived from large-scale structure and CMB measurements are presented in Table 1.5.2. These values are from the "Vanilla" model quoted in Tegmark et al. (2006, Table III, 3rd column;) and from the "b6" parameter model in Sánchez et al. (2006, Table 3, 3rd column). Care should be made when comparing these values of cosmological parameters in Table 1.5.2 since different assumptions and prior information are used for both. However, for the values quoted above, the joint-constraint estimates are used and we can see that all the values quoted are consistent. Note that in both cases the value of $\Omega_{\rm total}$ is set to 1 and w, the equation of state parameter for vacuum energy, is fixed at -1. From these values we see that baryonic matter is only $\approx$ 4% of the energy-density content and contributes $\sim$ 18% of the total matter content. The other 82% or so of the matter content is classed as *dark matter* i.e. $\Omega_{\rm dark\ matter} \approx 0.196\,\Omega_{\rm total}$. Meanwhile, it seems that more than $\frac{3}{4}$ of the Universe's energy-density is in the form of Ω_Λ - popularly called *dark energy.*

Thus, since we have no direct confirmation of a dark matter sub-atomic particle, and if the values in Table 1.5.2 are correct, we are left in a slightly embarrassing - but extremely exciting

Parameter	Tegmark et al. (2006)	Sánchez et al. (2006)
h	$0.730^{+0.022}_{-0.018}$	$0.735^{+0.022}_{-0.018}$
Ω_{total}	1	1
Ω_{Λ}	$0.761^{+0.017}_{-0.018}$	$0.763^{+0.020}_{-0.020}$
Ω_{matter}	$0.239^{+0.018}_{-0.017}$	$0.237^{+0.020}_{-0.020}$
Ω_{baryon}	$0.042^{+0.002}_{-0.002}$	$0.042^{+0.002}_{-0.002}$
w_{Λ}	-1	-1

Table 1.1: The current best estimations of certain Cosmological Parameters from Tegmark et al. (2006) and Sánchez et al. (2006). A flat cosmology is assumed in both cases and hence Ω_{total}=1. Note also that in both cases, the value of w, the equation of state parameter is fixed to -1 and the mass of neutrinos is also set to $M_{\nu} = 0$.

- position of not knowing what 95% of the Universe is made of. The nature of the "Dark Sector" is arguably the most challenging problem not only in astrophysics but in the whole of the physical sciences at the beginning of the 21st Century. As such we need as many different routes and examples of independent proof to actually verify the claim that dark energy and dark matter actually exist.

1.6 MOTIVATION AND LAYOUT OF THESIS

1.6.1 MOTIVATION OF THESIS

With the claim that roughly 95% of the Universe's composition is currently unexplained, it is scientifically prudent not to rely on a single observational route for confirmation. This has begun to be achieved with the synergy of different datasets (e.g. CMB, LSS, SNIa and cluster abundances). However, further, independent cross-checks must be encouraged and this provides the initial motivation for this thesis. Additional motivation comes from acknowledging that if there *is* a dominant dark energy component present in the Universe, then it is highly desirable to explore its properties and to see if there is a potentially evolving equation of state parameter, $w(z)$.

This thesis is concerned with measuring the clustering and evolution properties of Luminous Red Galaxies in order to understand the properties of the Large-Scale Structure of the Universe. We shall measure the clustering properties via the correlation function using LRGs from two new surveys, the 2dF-SDSS LRG And QSO (2SLAQ) Survey and the AAOmega LRG Pilot Survey.

Using both dynamical and geometric redshift-space distortions in the redshift $z = 0.55$ 2SLAQ LRG clustering pattern, we shall break the degeneracy between Ω_M and β and thus give an independent measurement of the matter density parameter. We shall then also use a simple model of bias to predict the evolution of the clustering of LRGs.

Next, using data obtained from the AAOmega LRG Pilot Survey we shall show that the AAOmega facility at the AAT would be ideal for an LRG BAO project, that LRG clustering remains high at redshifts of $z \simeq 0.7$ and we derive a typical $z \simeq 0.7$ LRG halo mass.

Finally, we investigate the near-infrared colour and the optical morphologies of redshift $z \simeq 0.7$ LRGs using data from space telescopes.

1.6.2 LAYOUT OF THESIS

This thesis is divided into 8 chapters.

- In Chapter 2, we re-cap some of the technical details and relevant results from the SDSS LRG Survey. We also introduce the 2dF-SDSS LRG And QSO (2SLAQ) Survey.
- In Chapter 3, we establish the statistical techniques we use in order to measure the galaxy correlation function and we present the 2SLAQ LRG 2-Point Correlation function, reporting on the clustering properties of the Luminous Red Galaxies in the 2SLAQ Survey.
- In Chapter 4 we present constraints on cosmological parameters using and analysing geometric and dynamical information present in the 2SLAQ LRG clustering pattern.
- In Chapter 5 we discuss the galaxy selection techniques needed for a large, redshift $z \sim 0.7$ survey and give details of the AAOmega LRG Pilot Run.
- In Chapter 6 we present the clustering results from the AAOmega LRG Redshift Pilot Run, estimate LRG halo masses, and compare LRG and emission line galaxy (ELG) surveys.
- In Chapter 7, we use data from *Spitzer* Space satellite and the *Hubble Space Telescope* to study the evolution and morphological properties of LRGs.
- We draw our main conclusions in Chapter 8 and look towards future work and prospects.

CHAPTER 2

GALAXY REDSHIFT SURVEYS

"How long this time? More taxpayer's money 2 look thru an oversized toilet roll for a few nites to draw a graph of a small section of infinity we've not seen yet"

- Text message from **Michael J. Sunderland** in response to the news that I was going back to the AAT in Australia.

In this chapter, we discuss in greater detail the Sloan Digital Sky Survey (SDSS), concentrating on the Luminous Red Galaxy (LRG) Spectroscopic Survey. We then introduce the 2dF-SDSS LRG And QSO (2SLAQ) Survey, and focus on the equipment needed to perform and analyse data from this recently completed and analysed redshift survey.

2.1 THE SDSS LRG SURVEY

The Sloan Digital Sky Survey (SDSS) is currently the "state of the art" astronomical survey. Using a dedicated, 2.5-metre telescope at the Apache Point Observatory, New Mexico, U.S.A., (Latitude 32°46′49″ N, Longitude 105°49′13″ W, altitude 2788 metres), the SDSS plans to image over a quarter of the sky ($\sim$ 10 000 deg^2) by the time of its completion. The SDSS has

had six major data releases (the Early Data Release and Data Releases 1 through 5) with DR5 containing 215 million objects. The first phase of the SDSS, SDSS-I, was completed in June 2005. The SDSS is now in its second phase, SDSS-II, which shall continue until mid-2008. A full list of publications from the SDSS can be found at `http://www.sdss.org/publications/`, though the most relevant references for this section are Fukugita et al. (1996), Gunn et al. (1998), Uomoto et al. (1999), York et al. (2000), Eisenstein et al. (2001), Strauss et al. (2002), Blanton et al. (2003) and Gunn et al. (2006), which give extensive technical and target selection details.

The SDSS is a combined imaging and spectroscopic survey. For the imaging survey, the telescope operates in a drift-scanning mode. For a given observation, the telescope moves along great circles on the sky, while the camera reads the CCDs as the data is being collected, such that images of objects move along the columns of the CCDs at the same rate the CCDs are being read. This results in the camera producing five images of a given object, one image for each of the 5 bands. The SDSS has a 3° field-of-view and the five imaging bands, u, g, r, i and z are centred at approximately 3551Å, 4686Å, 6165Å, 7481Å and 8931Å respectively. The throughput of the survey's photometric system is shown in Figure 2.1 and the zero-points for these bands were intended to satisfy the AB convention (Fukugita et al., 1996).

For the Spectroscopic Survey, spectra are observed 640 at a time, for a total integration time of 45 to 60 minutes, depending on observing conditions, using a pair of optical fibre-fed spectrographs (York et al., 2000). The wavelength resolution, $\lambda/\Delta\lambda$ is 1800 (Uomoto et al., 1999). The fibres are located at the focal plane via plug plates constructed for each area of sky. The fibre diameter is 0.2mm, equivalent to 3″ on the sky. Adjacent fibres cannot be located more closely than 55″ (c.f. $\approx 30''$ for the 2dF instrument, see below). Therefore, both members

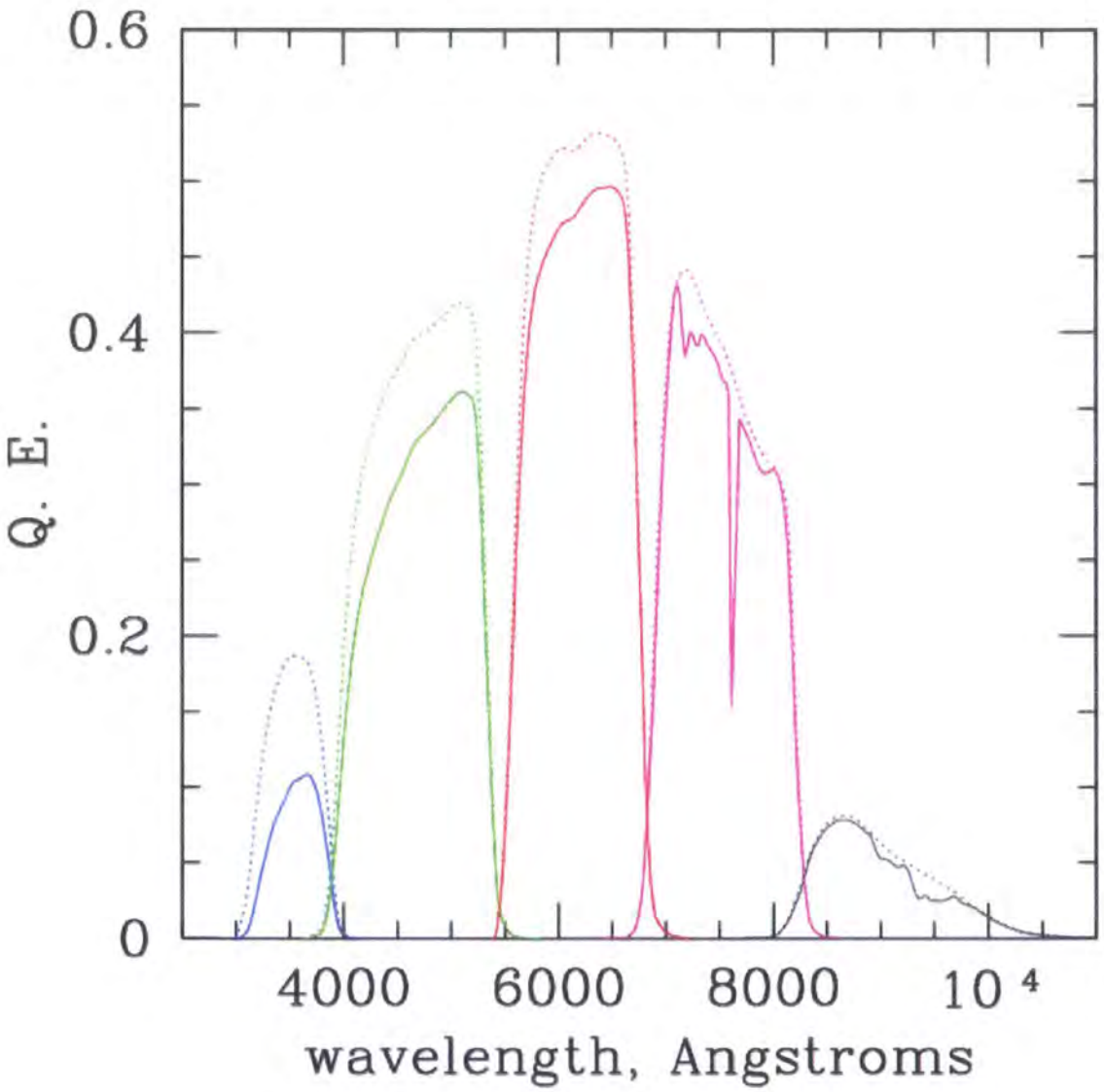

Figure 2.1: The SDSS *ugriz*-bands. The solid response curves show the throughput defining the survey's photometric system, which includes the filter transmission, CCD response, flux loss due to the optics and extinction through an airmass of 1.3 at Apache Point Observatory. For reference, the dashed curves do not include any atmospheric extinction. Q. E. stands for quantum efficiency.

of a pair of objects closer than this separation can only be observed spectroscopically if they are located in the overlapping regions of adjacent tiles. A "tile" is essentially the area covered by one pointing of the 3° diameter plate.

As mentioned in Chapter 1, the SDSS Spectroscopic Survey is split into the MAIN and the LRG surveys, and for the remainder of this section, we shall concentrate on the SDSS LRG survey.

2.1.1 SDSS LRG Photometric Selection

The SDSS LRG Survey was designed to select intrinsically luminous, passively evolving galaxies in such a way as to make a volume-limited sample out to redshifts of $z \sim 0.5$. Complete selection details are given in Eisenstein et al. (2001) which also gives the basis for the rest of this section.

For an early-type galaxy, the 4000Å break due to the Calcium II H and K absorption lines, provide a sharp feature in the galaxy's spectral energy distribution (SED) from which one can infer redshifts. For galaxies with redshifts $z < 0.38$, this feature lies within the SDSS g-band.

Thus, if all galaxies had the same SED, then the $(g - r)$ colour would be an excellent redshift indicator. However, since galaxies show a range of break strengths, $(g - r)$ actually only measures a degenerate combination of the position of the break (i.e. the redshift of the galaxy) and the strength of the break. One could break this degeneracy with the $(u - g)$ colour but since $r \sim 19$ for the galaxies of interest means that $u \sim 22$ and this is close to the SDSS u-band detection limit. Hence the $(u - g)$ colour is very noisy (Eisenstein et al., 2001). One can then turn to the $(r - i)$ colour. However, there is a potential problem here too as galaxies with early-type SEDs at low redshift, occupy the same place in the $g - r - i$ colour-colour space as late-type galaxies with high redshifts.

This problem is alleviated at $z > 0.38$, since the SDSS is sensitive enough in the g-band to measure a $(g - r)$ colour that separates early and late type galaxies. Thus, to select LRGs, two selection cuts need to be invoked, one for redshifts $z < 0.38$ and one for higher redshifts, $z > 0.38$.

For the SDSS LRG "Cut I" (selection for LRGs with redshift $z < 0.38$), to break the *gri* degeneracy mentioned above, a sliding flux/apparent magnitude cut is employed such that a luminosity threshold is set as a function of redshift and the luminosities and colours of a passively evolving galaxy population are selected. This selection effectively works on the fact that most super-L^* galaxies in the Universe have old stellar populations, and although intrinsically very luminous and blue galaxies at high redshift would pass the cut, these types of galaxy are extremely rare.

The "Cut II" selection (for LRGs with redshift $z > 0.38$), is a much simpler flux-limited cut, with $r \approx 19.5$, (the magnitude and hence redshift range is limited by realising a ~ 45 minute exposure time on the 2.5m telescope) which takes advantage of the unique *gri*-colours that a luminous, early-type galaxy has at $z > 0.4$. The problem for objects in Cut II becomes contamination due to faint, red, late-type stars. However, there are effective star-galaxy separation echniques that can be employed to combat this.

Eisenstein et al. (2001) gives considerably fuller details about the LRG selection than are presented here. They also prove that Cut I and Cut II are extremely efficient at selecting massive, luminous early-type galaxies up to redshifts of $z \sim 0.5$.

2.1.2 Clustering Results from the SDSS LRG Survey

As continued motivation for the study of LRG clustering, we briefly report here the major clustering studies published so far with data from the SDSS LRG Survey.

Masjedi et al. (2006) present the very small-scale, $0.01 < r < 8 \ h^{-1}$ Mpc, projected correlation function, $w_p(\sigma)$, (defined below in Section 3.3.5) and real-space correlation function, $\xi(r)$, of 24 520 LRGs across the redshift range $0.16 < z < 0.36$. They note that "fibre collision" incompleteness of the SDSS spectroscopic sample at scales smaller than $55''$ prevents measurements of the correlation function for LRGs on scales smaller than $\sim 0.3 \ h^{-1}$ Mpc by the usual methods. Therefore, a cross-correlation between the spectroscopic sample with the imaging sample, with a weighting scheme to account for the collisions, is employed and tested against mock catalogues. Their main findings are the correlation function $\xi(r)$ slope is surprisingly close to a r^{-2} power-law over almost 4 orders of magnitude in separation and as a result, is too steep at small scales to be explained in simple halo occupation distribution models. clustering. A major claim of this work is the inference of an LRG-LRG merger rate of $\lesssim 0.6 \times 10^4$ Gyr^{-1} Gpc^{-3} for this sample and the suggestion that LRG-LRG mergers are *not* the main mode of mass growth for LRGs at redshifts $z < 0.36$.

Zehavi et al. (2005a) report on the intermediate-scale, $0.3 - 40 \ h^{-1}$ Mpc, clustering of 35 000 LRGs at redshifts $z = 0.16 - 0.44$. They measure the redshift-space two-point correlation function, $\xi(s)$, the projected correlation function, $w_p(\sigma)$, and the ("de-projected") real-space correlation function $\xi(r)$, for approximately volume-limited samples. They show that LRGs are highly clustered objects, with correlation lengths (defined in Equation 1.20) varying from 9.8 ± 0.2 to $11.2 \pm 0.2 \ h^{-1}$ Mpc, depending on the specific luminosity range. For their $-23.2 < M_g < -21.2$ LRG sample, the inferred bias, b, is calculated to be 1.84 ± 0.11 for scales $1 < \sigma \lesssim$

10 h^{-1} Mpc. These authors claim there is a detection of luminosity-dependent bias within the full LRG sample but see no evidence for redshift evolution in the clustering between $z = 0.2$ and $z = 0.4$. There are strong reports for deviations from the power-law form of ξ in the real-space correlation function, with a dip at ~ 2 h^{-1} Mpc scales and an upturn on smaller scales.

Although not explicitly stated in Zehavi et al. (2005a), these deviations in the power-law form of ξ can be explained by the Halo Occupation Distribution (HOD) framework. A halo can be thought of as a unit structure made up of dark matter, plus one, many or even no luminous galaxies. The HOD model can then theoretically describe the bias between galaxies and mass in terms of the probability distribution $P(N|M)$ that a dark matter galaxy halo of virial mass M contains N galaxies of a given type, together with prescriptions for the relative bias of galaxies and dark matter within virialised haloes (Zehavi et al., 2005b). Further discussion of the HOD model is outside the remit of this chapter but more detail can be found in the recent papers by Zehavi et al. (2005b) and Phleps et al. (2006) as well as the references therein.

For cosmological work, the main LRG studies are Eisenstein et al. (2005), Tegmark et al. (2006), Percival et al. (2006a), Hütsi (2006a,b), Padmanabhan et al. (2006) and Blake et al. (2007). All these studies use the detection of the baryon acoustic oscillations in the clustering signal to constrain estimates of cosmological parameters including $\Omega_{\rm M}$ and Ω_Λ. In Eisenstein et al. (2005) this is done via studying the correlation function, while in Tegmark et al. (2006), Percival et al. (2006a), Hütsi (2006a,b), Padmanabhan et al. (2006) and Blake et al. (2007), the power spectrum is used.

Padmanabhan et al. (2006) and Blake et al. (2007) use *photometric* redshifts. Here, instead of studying the spectra of an object (and its distinct spectral features, e.g. the 4000Å break), an estimate of the redshift is made from the photometric properties of the object. Often prior

information is needed to refine the photometric redshift estimation such as the photometric properties of classes of galaxies with well measured (spectroscopic) redshifts.

The primary advantage of photometric redshifts is that more redshifts can be obtained per unit telescope time than for spectroscopic redshifts. The primary disadvantage is that they are far less accurate.

The higher redshift Cut II of the SDSS LRG Survey was used to select LRGs with redshifts out to $z \sim 0.5$. However, in order to further study the properties of luminous red galaxies, an extension to the SDSS LRG project was suggested to extend the LRG colour selection and redshift range such that a large spectroscopic sample of LRGs could be obtained with a mean redshift of $z \sim 0.5$ and out to redshifts of $z \sim 0.8$.

2.2 THE 2DF-SDSS LRG AND QSO SURVEY

The 2dF-SDSS LRG And QSO (2SLAQ) Survey is a completed redshift survey which has produced a sample of over 13 000 spectroscopically confirmed galaxies, of which nearly 11 500 are in the redshift range $0.4 < z < 0.8$ (Cannon et al., 2006). A similar number of faint, $g < 21.85$ Quasi-Stellar Objects (QSOs) have also been observed (Croom et al. 2007, in prep.)

The two key features of the survey are the use of Sloan Digital Sky Survey (SDSS) photometric data to select the relatively rare target galaxies, and of the 2-degree Field (2dF) multi-fibre system (Lewis et al., 2002) on the Anglo-Australian Telescope (AAT) to obtain their spectra. The multicolour SDSS photometry provides the essential selection criteria for intrinsically bright but distant LRGs, as the 4000Å break characteristic of early-type galaxies marches through the g, r and i-bands, while the larger aperture 3.9m AAT, combined with longer exposure times, allows spectra to be obtained for objects down to a magnitude limit of $i = 19.8$ (c.f. $r \sim 19.5$ in Eisenstein et al., 2001). The deeper, $i = 19.8$ magnitude limit was designed so as to pick out luminous red galaxies at redshift $z \sim 0.5$ with comparable absolute magnitudes and luminosities to those in the SDSS LRG Sample at $z \approx 0.35$, but the SDSS and 2SLAQ samples have very different space densities of LRGs.

The resulting data complements the original 2dFGRS survey of the 'local' universe (220,000 galaxies with $0 < z < 0.3$; Colless et al., 2001, 2003) and the SDSS LRG spectroscopic survey (Eisenstein et al., 2001) which finds intermediate redshift LRGs out to $z \sim 0.4$. A brief comparison of the three surveys is given in Table 2.1.

The primary aims of the 2SLAQ LRG survey were to investigate large-scale 3-dimensional structure at z $\sim$ 0.55 (when the universe was a little over half its present age) and to look at the effects of evolution on the most luminous galaxies.

Survey	median redshift	D_L	D_A	No. of Objects	Area/deg^2
2dFGRS[1]	0.11	356.8	289.6	221 414	≈ 1800
SDSS LRG[2]	$\simeq 0.35$	1299.8	713.2	58 360	4259
2SLAQ LRG[3]	0.55	2224.0	925.7	14 978	180

Table 2.1: A comparison between the 2dFGRS, SDSS LRG and 2SLAQ LRG Surveys. D_L is the luminosity distance and D_A is the angular diameter distance (equation 1.37) in h^{-1} Mpc at the mean redshifts assuming a $(\Omega_{\rm M}, \Omega_\Lambda) = (0.3, 0.7)$ cosmology. Based on [1]Colless et al. (2001, 2003), [2]Tegmark et al. (2006), [3]Cannon et al. (2006) and Wake et al. (2006).

Results from the 2SLAQ Survey are presented by Wake et al. (2006) who calculate the LRG luminosity function; Roseboom et al. (2006) report on the variation of LRG star formation activity with redshift, while Sadler et al. (2006) study the radio properties 2SLAQ LRGs to redshifts of $z \sim 0.7$. Meanwhile, both Padmanabhan et al. (2005) and Collister et al. (2007) use the 2SLAQ LRGs as training sets for photometric redshift estimation for the cosmological parameter papers mentioned in the previous section (Padmanabhan et al., 2006; Blake et al., 2007, respectively). From the QSO part of the 2SLAQ Survey, Richards et al. (2005) measure the QSO luminosity function and the clustering and fuelling efficiencies of AGN are calculated by da Ângela et al. (2006).

In this thesis we utilise the 2SLAQ LRG Survey data in order to investigate the clustering properties of massive galaxies over the redshift range $0.4 < z < 0.8$, which we report on in Chapters 3 and 4.

2.2.1 PHOTOMETRIC TARGET SELECTION CRITERIA

By extending the total exposure time with the AAT and 2dF to 4 hours, it was possible to work two magnitudes fainter than the 2dFGRS (which had an original target magnitude limit at $b_J = 19.45$). However, simply working to a fainter magnitude limit is not an efficient strategy for finding higher-z galaxies, since many of the targets will be intrinsically fainter galaxies at low redshift, with very few high-z objects.

The selection of distant ($z > 0.4$) LRGs is done on the basis of the SDSS *gri* photometric data, primarily using the two-colour plot of $(g - r)$ against $(r - i)$ and the i-band magnitude. A galaxy with a dominant passively evolving early-type population becomes rapidly redder in $(r - i)$ with approximately constant $(g - r)$ as z increases from 0.4 to 0.7 and the 4000Å break moves through the r-band. Beyond $z = 0.7$ the break enters the i-band and the $(r - i)$ colour becomes bluer, while $(g - r)$ may become bluer or redder, depending on the past rate of star formation - see Figure 2.2.

The SDSS imaging has a number of different magnitude definitions (see Stoughton et al., 2002)*. Unless explicitly noted, all magnitudes and colours quoted here are the *modelMag*. The *modelMag* is based on the better-fitting of two profiles; a de Vaucouleurs profile with $I \propto r^{-1/4}$, and an exponential profile with $I \propto \exp(-r)$, where I is surface brightness, r is radius and the measurements are performed in the r-band. The main exception to this will be the magnitude limit quoted for the 2SLAQ Survey, $i_{\rm deV}$, where $i_{\rm deV}$ is the total magnitude based on the fit to a de Vaucouleurs profile.

Figure 2.2 illustrates the colour selection boundaries, with some representative evolutionary tracks based on Bruzual and Charlot models (Bruzual & Charlot, 2003), superimposed on

*and `http://www.sdss.org/dr5/algorithms/photometry.html`

model line	model type	$z_{\rm form}$	IMF	τ/Gyr	$Z/Z_{\odot}$
solid green	single burst	10	Salpeter	-	1
dashed yellow	exponential SF	10	Salpeter	1	1

Table 2.2: Values for the Bruzual and Charlot stellar population synthesis models (Bruzual & Charlot, 2003) that are used in Figures 2.2 and 2.3.

the SDSS photometric data. The evolutionary tracks shown (courtesy of U. Sawangwit) in Figures 2.2 and 2.3 are from the models presented in Bruzual & Charlot (2003), the details of which are given in Table 2.2. Each solid square represents an increment of 0.1 in redshift with the redshift $z = 0$ points at the bottom left-hand corner and the final squares are at a redshift of $z = 1$.

Most galaxies of all types lie along a common locus in the lower left hand corner of Fig. 2.2, becoming redder in $(g - r)$ with increasing redshift until the 4000Å break moves into the r-band at $z \simeq 0.4$. Thereafter, the $(r - i)$ colour becomes rapidly redder until the break moves into the i-band at $z \simeq 0.7$. Thus the most massive and luminous intermediate redshift galaxies, i.e. LRGs with a dominant passively-evolving population, are expected to lie along a vertical track with $g - r \sim 1.7$, as is suggested in Fig. 2.2.

As such, we employ cuts above lines of constant $d_{\perp}$ where

$$d_{\perp} = (r - i) - \frac{(g - r)}{8.0} \tag{2.1}$$

(c.f. Eisenstein et al., 2001) to select early-type galaxies at increasingly high redshift, which works up to redshift $z \simeq 0.7$, beyond which the model tracks turn round. A second cut above $c_{\parallel}$ where

$$c_{\parallel} = 0.7(g - r) + 1.2(r - i - 0.18) \tag{2.2}$$

serves to eliminate lower luminosity, later-type galaxies and is identical to equation (3) in Eisenstein et al. (2001). Lines of $d_\perp = 0.65$ and $c_{||} = 1.6$ are shown in Fig. 2.2. $d_\perp$ and $c_{||}$ get their names from the definitions in Eisenstein et al. (2001) since originally $c_\perp$, and now $d_\perp$, was a measure of the perpendicular distance away from the common galaxy locus at lower $z \simeq 0.4$ redshift, while $c_{||}$ was orthogonal to this and would move parallel to the common galaxy locus. (The shallower slope of $d_\perp$ here as compared to $c_\perp$ in Eisenstein et al. (2001) loses some of the "orthogonality".) Further cuts on $0.5 \leq (g-r) < 3.0^\dagger$ and $(r-i) < 2$ eliminate objects too far from the main LRG locus (possibly composite objects or photometric errors).

Star/galaxy separation based on the SDSS images eliminates most stellar contamination from the sample. Two criteria were used, $i_{\rm psf} - i_{\rm model} > 0.2 + 0.2 \times (20.0 - i_{\rm deV})$ and $R_{i_{\rm deV}} > 0.2$, where $i_{\rm psf}$ is the i-band magnitude described by a Point Spread Function and $R_{i_{\rm deV}}$ is the i-band de Vaucouleurs radius in arcseconds. However, some red M-type stars inevitably remain in the lists of targets (see upper left panel in Figure 2.3).

Initially, the faint magnitude limit for the 2SLAQ LRG Survey was taken at $i_{\rm deV} = 19.5$. However, early tests showed that a reasonable redshift success rate could be maintained down to $i_{\rm deV} = 20$. Thus, for the 2SLAQ LRG Survey, the magnitude limits were set at $17.5 \leq i_{\rm deV} < 19.8$.

Objects too diffuse to yield useful spectra using the 2 arcsec diameter 2dF fibres are eliminated by requiring $i_{\rm fiber} < 21.4$, where $i_{\rm fiber}$ is the flux contained within the aperture of a SDSS spectroscopic fiber ($3''$ in diameter) calculated in the i-band.

In order to match the number of targets to the number of fibres and end with a reasonably complete and uniform set of redshifts, it was decided best to define a primary top priority

†For the March and April 2003 runs only, the lower limit was $1.0 \leq (g-r)$.

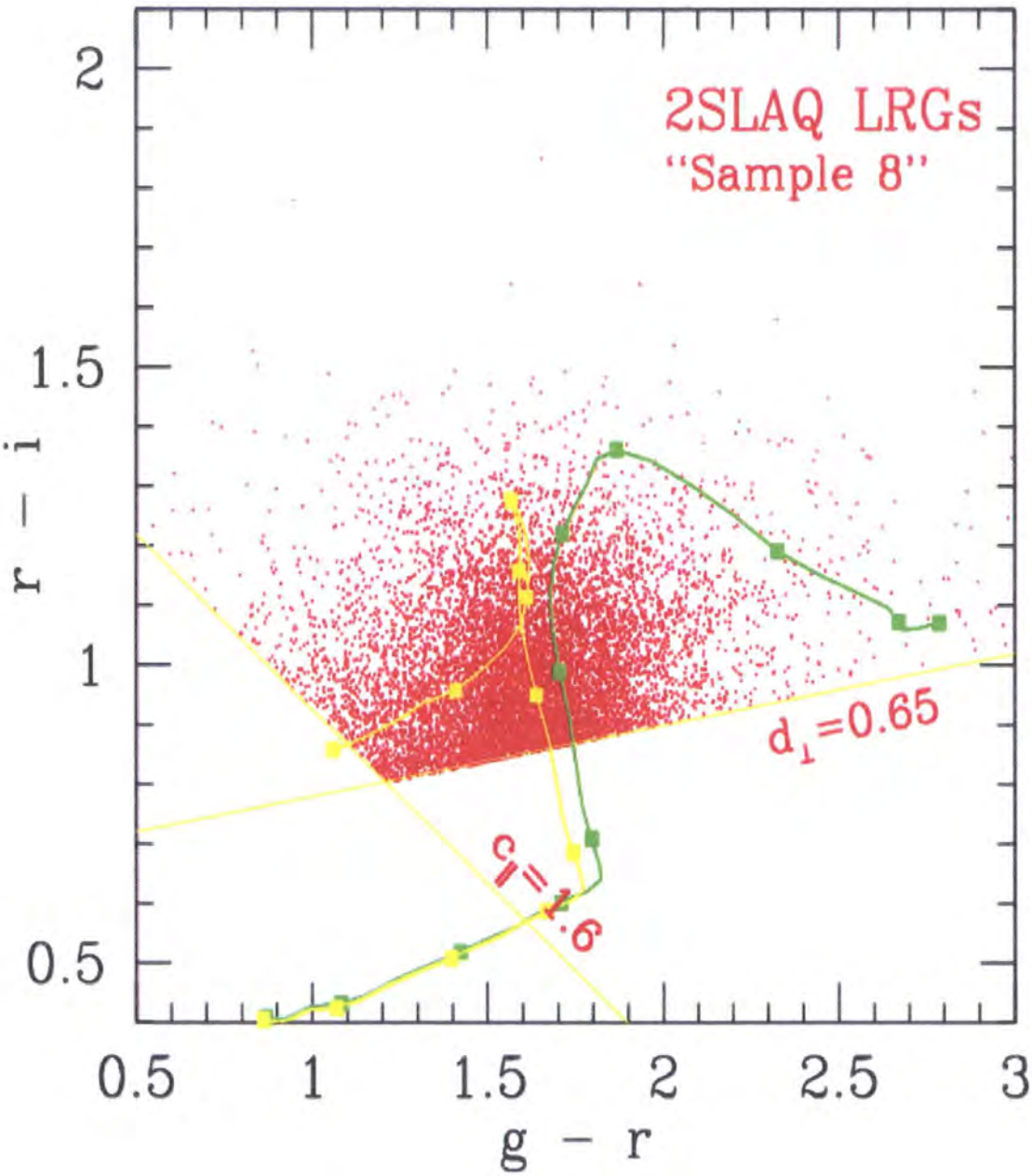

Figure 2.2: 2SLAQ LRG selection boundaries in the gri two-colour plane. The primary "Sample 8" LRGs are shown, lying above the lines of $c_{\parallel} = 1.6$ and $d_{\perp}$=0.65. The tracks are from the Bruzual and Charlot models, details of which are given in the text and Table 2.2.

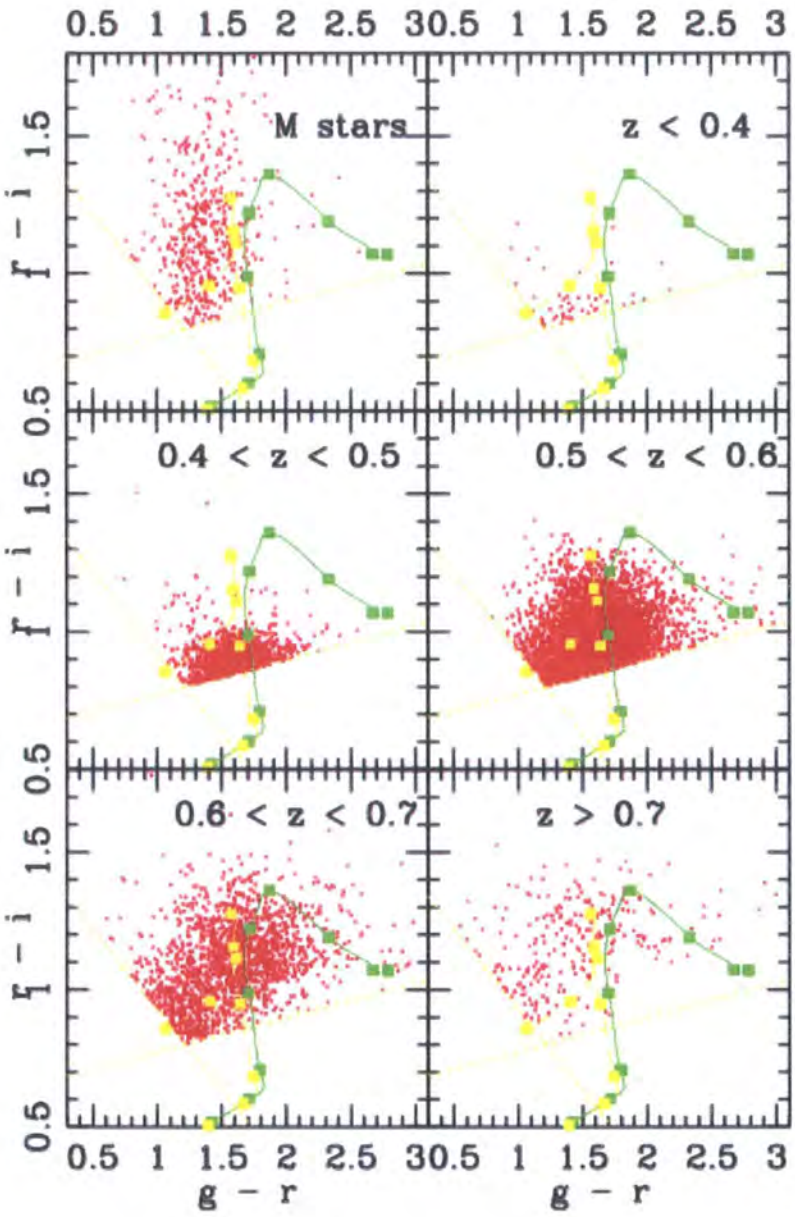

Figure 2.3: The redshift distribution in the $(g-r)$-$(r-i)$ colour-colour plane for confirmed 2SLAQ objects, split into 5 redshift slices. Objects with confirmed stellar spectra are shown in the top-left panel. The Bruzual and Charlot model tracks are shown as before, with details in Table 2.2.

sample of targets with a density of about 65 objects per square degree. This was done by making the primary LRG cut at $d_\perp \geq 0.65$, with a second lower priority sample having $0.55 \leq d_\perp < 0.65$. By an historical quirk of fate, the primary cut sample has come to be known as "Sample 8", with the second, lower priority sample being termed "Sample 9".

For the early observations (Semester 2003A) somewhat different cuts and priorities were used. However, the colour cuts for the 2SLAQ LRG survey were finalised in Semester 2003B (July 2003) as

$$i_{\rm fibre} < 21.4 \tag{2.3}$$

$$17.5 < i_{\rm deV} < 20.0 \tag{2.4}$$

$$i_{\rm psf} - i_{\rm model} > 0.2 + 0.2 \times (20.0 - i_{\rm deV}) \tag{2.5}$$

$$\mathrm{radius}_{\rm deV}(i) > 0.2'' \tag{2.6}$$

$$d_\perp = (r - i) - (g - r)/8.0 \tag{2.7}$$

$$c_\parallel = 0.7 \times (r - i) + 1.2 \times (r - i - 0.18) \geq 1.6 \tag{2.8}$$

As will be demonstrated later on, these criteria ultimately lead to a very high selection rate of LRGs.

2.2.2 OBSERVATIONS

There are some important observational points that should be stated and acknowledgement is made of the 12 nights that the author spent at the Anglo-Australian Telescope (AAT) at the Siding Spring Observatory (SSO) in New South Wales, Australia. The AAT (latitude = 31°16′37.37″ South, longitude =149°03′58″ West, altitude 1164 metres) has a 3.9m main mirror and is orientated on an equatorial mount. The (pre-summer 2006) 2 degree Field instrument

(Lewis et al., 2002) had two spectrographs mounted at the top end of the telescope, with 200 optical fibres running from the configured focal plane to each spectrograph. The beauty of 2dF was its ability to configure (i.e. position fibres) on one field, while observing another. At the end of one set of observations, the plates would tumble, allowing near continuous multi-object observing of several fields over one night.

Due to the design of the 2SLAQ survey and the two available spectrographs at the AAT, observations were optimised by using one spectrograph for the LRGs and the other for the QSOs. Almost all LRG spectra cover the rest wavelength range of 5050Å to 7250Å.

As with the earlier 2dFGRS survey, the LRG survey was combined with a parallel faint quasar survey, mainly because the density of LRG targets is too low to fully utilise all 400 2dF fibres. One extra benefit in this case is that there is overlap in redshift range between the LRGs and QSOs, enabling direct comparison between the clustering properties of the two classes.

A significant difference between the 2SLAQ surveys and the earlier 2dFGRS/2QZ combination arises because different spectrograph configurations are optimal for the LRGs and the faint QSOs. The new QSO survey uses the same set-up as the 2QZ, with a low resolution 300B lines/mm grating. However, the LRGs with mean $z \sim 0.5$ yield little information below 5000Å and are badly contaminated by terrestrial atmospheric emission and absorption beyond 7200Å. They are therefore best observed at higher dispersion with a 600V lines/mm grating, centred at 6150Å. Since 2dF has two spectrographs with 200 fibres going to each one, the simple solution is to observe all the LRGs with one spectrograph and the QSOs with the other, although this loses some flexibility in target allocation.

Each 2 degree diameter field was given a total exposure of 4 hours to obtain the survey magnitude limits. This was broken into two sets of 4 $\times$ 1800 second exposures over two consecutive

nights.

The survey covers two narrow stripes along the celestial equator ($|\delta| < 1.5°$). The Northern Stripe runs from 08h 12m to 15h 18m in Right Ascension and is broken into 5 sub-stripes to utilise the best photometric data. The Southern Stripe runs from 20h 36m to 4h 00m. Figure 2.4 shows the layout of the target stripes and the 2dF fields observed. The total area of the survey, including the overlap regions, was approximately 180 degrees^2. Complete details of the Survey fields are given by Cannon et al. (2006).

2.2.3 OTHER 2DF ISSUES

It is important to be aware of the tiling strategy of the 2SLAQ survey when estimating the clustering of the LRGs. A simpler tiling scheme was used for 2SLAQ than for the preceding 2dFGRS/2QZ survey. For instance, for 2SLAQ, the 2dF tiles were offset by 1.2 deg in the RA direction as opposed to a variable spacing strategy employed by the 2dFGRS and 2QZ. Again, contrary to the 2dFGRS/2QZ, the galaxies in 2SLAQ were given higher fibre assignment priority, with the LRGs always having priority over the QSOs. This makes sure the LRG selection was not biased by the QSOs. The details of the survey mask and selection function will be described in detail in Section 3.3.2.

Due to the nature of the 2dF instrument, there are 400 optic fibres which are robotically positioned so light from a given astronomical target (in our case an LRG or QSO) can be collected. For the 2SLAQ survey, 200 fibres are allocated to LRG targets and 200 to QSO targets. Also, the fibres themselves have a finite physical size which means that no two fibres can be placed less than 1.6mm apart which is the equivalent of approximately 30 arcseconds. Thus, target objects which are this separation or smaller apart could potentially be missed. This

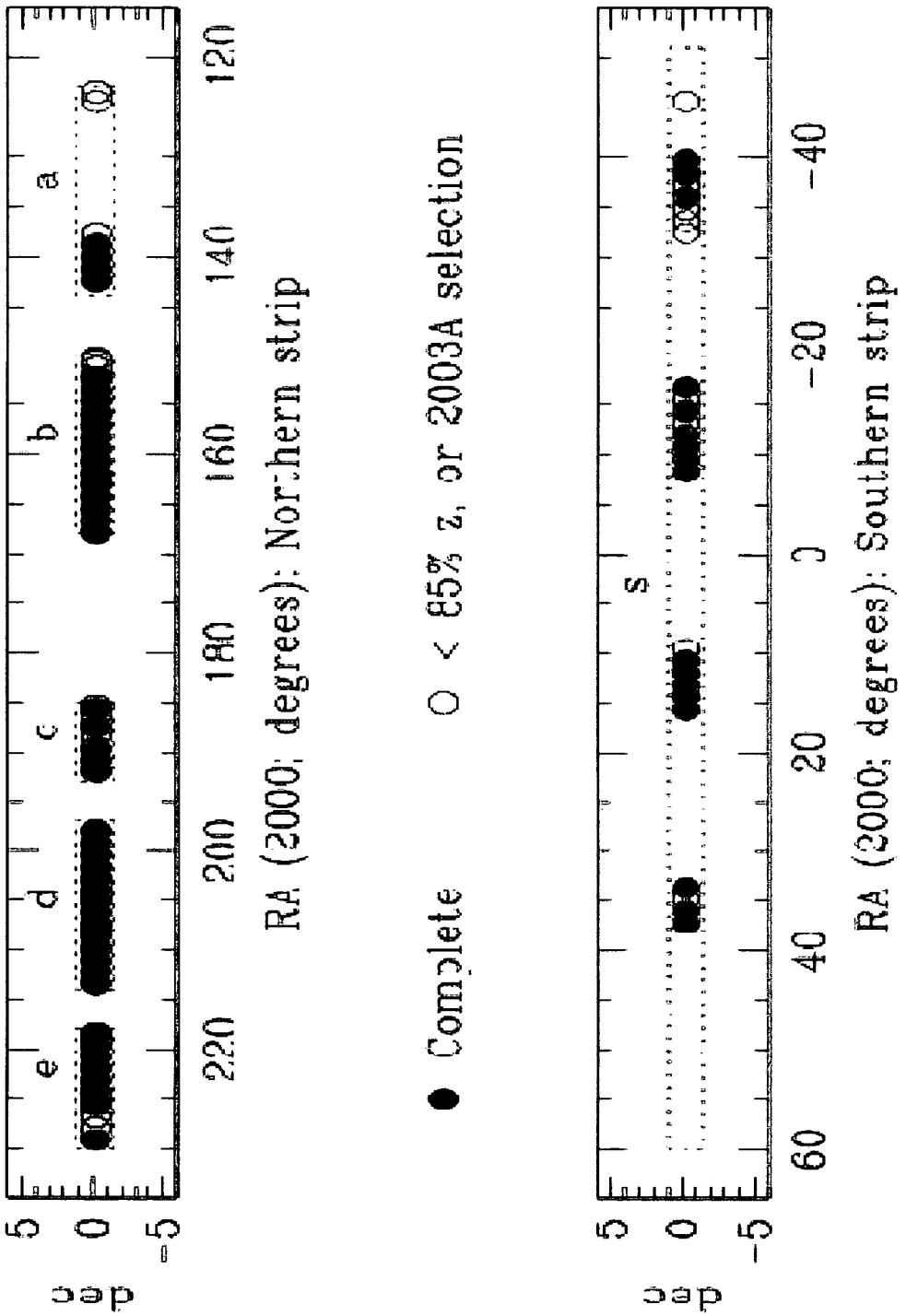

Figure 2.4: The location of the 2SLAQ Input Catalogue (dotted rectangles) and observed fields (circles). Solid circles indicate fully observed fields with high completeness, open circles have less than 85% spectroscopic completeness or fields with earlier selection criteria including i_{deV} <19.5.

effect can be alleviated with the overlapping fields and tiling strategy. However, one must be careful in choosing the tiling strategy since a compromise between maximising the observations of close pairs with very close field separations and considerable areas of overlap, and maximising the overal area of the survey by observing fields which only minimally overlap has to be made. After much discussion within the 2SLAQ collaboration, the centres of overlapping fields were placed at a separation of 1.2°, which has been shown to be the best compromise separation where clustering is picked up but also the overall survey coverage area is still large.

A closely related effect can be produced if the configuration of the placement of the fibres is not done with great care, especially when the number density of objects approaches 65 objects per square degree and you have more target objects than available fibres. Due to the design of the 2dF instrument, the optical fibres are moored at the edge of the circular focal plane plate. Once a fibre is moved from the edge of the plate to its allocated position on the field, no other fibre can be placed along its radial path due to the physical obstruction of the fibre-feed itself. Although not a severe problem on individual configurations, a definite effect becomes apparent if order $\sim$1000 configurations are modelled (the centre of the field gets undersampled while a saw-effect appears around the edge due to alternate bundles of 10 fibres going to one or the other of the spectrographs). To compensate for this, simulations were carried out to test potential field configurations before they were observed to make sure configuration and fibre allocation was not a problem. The LRGs were assigned priority classes to ensure that all top priority objects had a sufficiently low number density to guarantee observation and the formation of a fair sample.

2.2.4 Data Reduction

Colless et al. (2001) and Bailey et al. (2005) have extensive details regarding the data reduction techniques and software used with the 2dF instrument. In brief, the 2SLAQ data were reduced using the 2dF data reduction pipeline software, `2dfdr`. For each field the location of the fibres on the CCD was determined using a quartz lamp exposure which was also used as a flat field to remove pixel-to-pixel sensitivity variations. Two arc exposures provide wavelength calibration. All spectra were scaled according to the relative throughput of the fibres, as determined from the strongest night sky lines, and a median sky spectrum was subtracted from each object spectrum. The different frames from each field were combined using mean flux weighting, which takes account of the variable signal levels arising from changes in the "seeing", transparency or exposure time. Cosmic ray events were removed during this final step.

The `2dfdr` software was developed for the analysis of the 2dFGRS and 2QZ (Croom et al., 2004). For those surveys, the data for each field consisted of several similar frames with precisely the same 200 targets, all taken on the same night. Thus the `2dfdr` software was modified during the course of the 2SLAQ Survey to cope with data taken on different nights, sometimes with significant changes to the central wavelength and often with altered allocations of fibres to targets.

2.2.5 Redshifting

The definition of "quality flag" comes from the process of redshift calculation. The software used to find the redshifts of objects, ZCode, (developed by W. Sutherland and others for the 2dFGRS) can be run in either manual or automatic mode. ZCode uses 8 or 9 (version depending) model spectrum templates and then runs a cross-correlation algorithm to find the

best-fit between a model spectrum and the given data. Depending on the confidence of this fit (which itself depends on the strength of the absorption and possible emission features of the spectrum, the value of the cross-correlation coefficient given by ZCODE, the returned redshift and how the redshift changes using an alternative template spectra) a quality flag value was returned. This value is an integer between 1 and 5 inclusive and is called "$Q_{\rm op}$". As a guide, a $Q_{\rm op}$ value of 1 or 2 implies the quality of the spectra is not sufficient to record the returned redshift. A value of 3 is returned when the data is of sufficient quality to record the calculated redshift and a value of 4 or 5 means the redshift is very secure due to the data having excellent signal to noise or very obvious spectral features.

The main point to note about the redshifting procedure is the automated and manual runs of ZCODE return very similar completion rates and quality flag values. Ultimately though, all 2SLAQ LRG spectra were visually inspected by two or more independent observers and the manually checked redshifts are used.

As the survey progressed, it became apparent that redshifts of (usually the brighter) LRGs could be securely measured after just 2 hours of observations. Thus, seeing as the typical observation of one field was 4 hours, split over 2 nights, it was possible to *re-assign* fibres between nights. Since these re-assigned targets had lower observational and configurational priority than the regular LRGs, the yield of spectroscopically confirmed LRGs was increased, at no extra risk to jeopardising the completeness or tiling pattern of the 2SLAQ Survey.

There have also been several other consistency checks made during the observations e.g. spectral quality as a function of fibre position; signal-to-noise as a function of magnitude; colour-colour and plots of observed objects. Cannon et al. (2006) gives extensive details.

Having now described the motivation for galaxy redshift surveys in general and the 2SLAQ LRG Survey in particular, as well as discussing the survey design, we continue on and report the clustering measurements made from this survey.

CHAPTER 3

THE 2SLAQ LRG 2-POINT CORRELATION FUNCTION

from the North to the South, Ebudæ into Khartoum,

from the deep Sea of Clouds, to the Island of the Moon,

carry me on the waves to the lands I've never been,

carry me on the waves to the lands I've never seen.

we can sail, we can sail, with the Orinoco flow,

we can sail, we can sail, sail away, sail away, sail away

- **Enya, *Orinoco Flow*.**

In this chapter, we review the statistical techniques used to measure the galaxy correlation function and then report on the clustering properties of redshift $z = 0.55$ Luminous Red Galaxies observed as part of the 2SLAQ Survey.

3.1 MOTIVATION

Recent measurements of the galaxy correlation function, ξ, have produced a series of impressive results. Whether it be the detection of baryonic acoustic oscillations (Eisenstein et al., 2005),

clustering properties of different spectral types of galaxy (Madgwick et al., 2003), or the evolution of AGN black hole mass as an interpretation of the 2QZ clustering measurement(Croom et al., 2005), the two-point correlation function continues to be a key statistic when studying galaxy clustering and evolution. There have also been a series of recent studies (e.g., Zehavi et al., 2005a; Le Fèvre et al., 2005; Coil et al., 2004; Phleps et al., 2006) investigating the clustering properties and evolution with redshift of galaxies from $0.3 < z < 1.5$. Amongst these, Zehavi et al. (2005a) use the Sloan Digital Sky Survey (SDSS; York et al., 2000) to examine the clustering properties of Luminous Red Galaxies (LRGs) at a redshift of $z \simeq 0.35$. They find that correlation length depends on LRG luminosity and that there is a deviation from a power-law in the real-space correlation function, with a dip at $\sim$ 2 Mpc scales as well as an upturn on smaller scales.

Although the form of the 2-point correlation function is in itself a worthwhile cosmological datum, more information can be gained by studying the dynamical distortions at both small and large scales in the clustering pattern (Kaiser, 1987). Measured galaxy redshifts consist of a component from the Hubble expansion plus the motion induced by the galaxy's local potential. This leads to one type of distortion in *redshift*-space from the *real*-space clustering pattern. There are two basic forms of dynamical distortion (a) small scale virialised velocities causing elongations in the redshift direction - 'Fingers of god', but at larger scales there will also be flattening of the clustering in the redshift direction due to dynamical infall. Another type of geometric distortion can be introduced if we assume the wrong cosmology to convert redshifts to comoving distances (Alcock & Paczynski, 1979). Under the assumption that galaxy clustering is isotropic in real-space, a test can be performed in redshift-space by determining which cosmological parameters return an isotropic clustering pattern.

In the linear regime, dynamical effects are broadly determined by the parameter β, where $\beta = \Omega_{\rm m}^{0.6}/b$, $\Omega_{\rm m}$ is the matter density parameter and b is the linear bias parameter. If we assume, as is common, a zero spatial curvature model, then the main parameter determining geometric distortion is $\Omega_{\rm m}$. We can therefore use these redshift-space distortions to our advantage and derive from them estimates of $\Omega_{\rm m}$ and β, (e.g., Kaiser, 1987; Loveday et al., 1996; Matsubara & Suto, 1996; Matsubara & Szalay, 2001; Ballinger et al., 1996; Peacock et al., 2001; Hoyle et al., 2002; da Ângela et al., 2005). Unfortunately, there is often a degeneracy between these parameters, but this can be broken by the inclusion of other information. This additional information is introduced via orthogonal constraints obtained from linear evolution theory of cosmological density perturbations (da Ângela et al., 2005, and references therein).

In this chapter, we extend the redshift coverage of the SDSS LRG survey by using the data from the recently completed 2dF-SDSS LRG And QSO (2SLAQ) Survey (Cannon et al. (2006); Croom et al. (2007), in prep.). We concentrate on the clustering of the 2SLAQ LRG sample, extending the work of the SDSS LRG Survey (Eisenstein et al., 2001; Zehavi et al., 2005a) to higher redshift. We calculate the 2-point galaxy correlation function in both redshift-space and real-space for LRGs over the redshift range $0.4 < z < 0.8$. Then using information gained from geometric distortions in the redshift-space clustering pattern, values of the cosmological parameters $\Omega_{\rm m}$ and β can be found (e.g. Alcock & Paczynski, 1979; Ballinger et al., 1996; Hoyle et al., 2002; da Ângela et al., 2005).

3.2 2SLAQ LRG DATA

The total 2SLAQ LRG dataset consists of a total of 18 487 spectra for 14 978 discrete objects; 13 784 of these (92%) have reliable, "Qop" ≥ 3 redshifts. From these "Qop"≥ 3 objects, 663 are identified as being stars, leaving a total of 13 121 galaxies. The distribution of 2SLAQ LRGs, along with recent local galaxy and LRG surveys, for the North Galactic Pole (NGP) and South Galactic Pole (SGP) are shown in radial wedge plots in Fig. 3.1 and Fig. 3.2 respectively.

For our clustering analysis, we cut this sample down further by using only those confirmed LRGs which were part of the top priority "Sample 8" selection as described in the previous chapter. The sample we use does include observations taken in the 2003A semester, where a brighter ($i_{deV} < 19.5$) magnitude limit was used, as long as the observed LRG would have made the "Sample 8" selection. We do not include observations taken from fields a01, a02 and s01 (see Cannon et al. (2006)) as they have low completeness and should not be used in statistical analyses.

Once the final selection criteria had been decided, there were 25 795 "Sample 8" LRG targets at a sky density of around 70 per square degree. Approximately 40% (10 072) of these objects were observed, with 9 307 obtaining "Qop"≥ 3. After imposing the cuts above, this leaves a total of 8 656 LRGs, 5 995 in the Northern Galactic Stripe and 2 661 in the Southern Galactic Stripe. For all further analysis, this is the sample utilised which we call the "Gold Sample" and has a $\bar{z}_{Gold} = 0.55$.

With the data now in hand, we shall review the specific techniques we shall use in order to analyse and measure the clustering properties of the 2SLAQ LRGs in the next section.

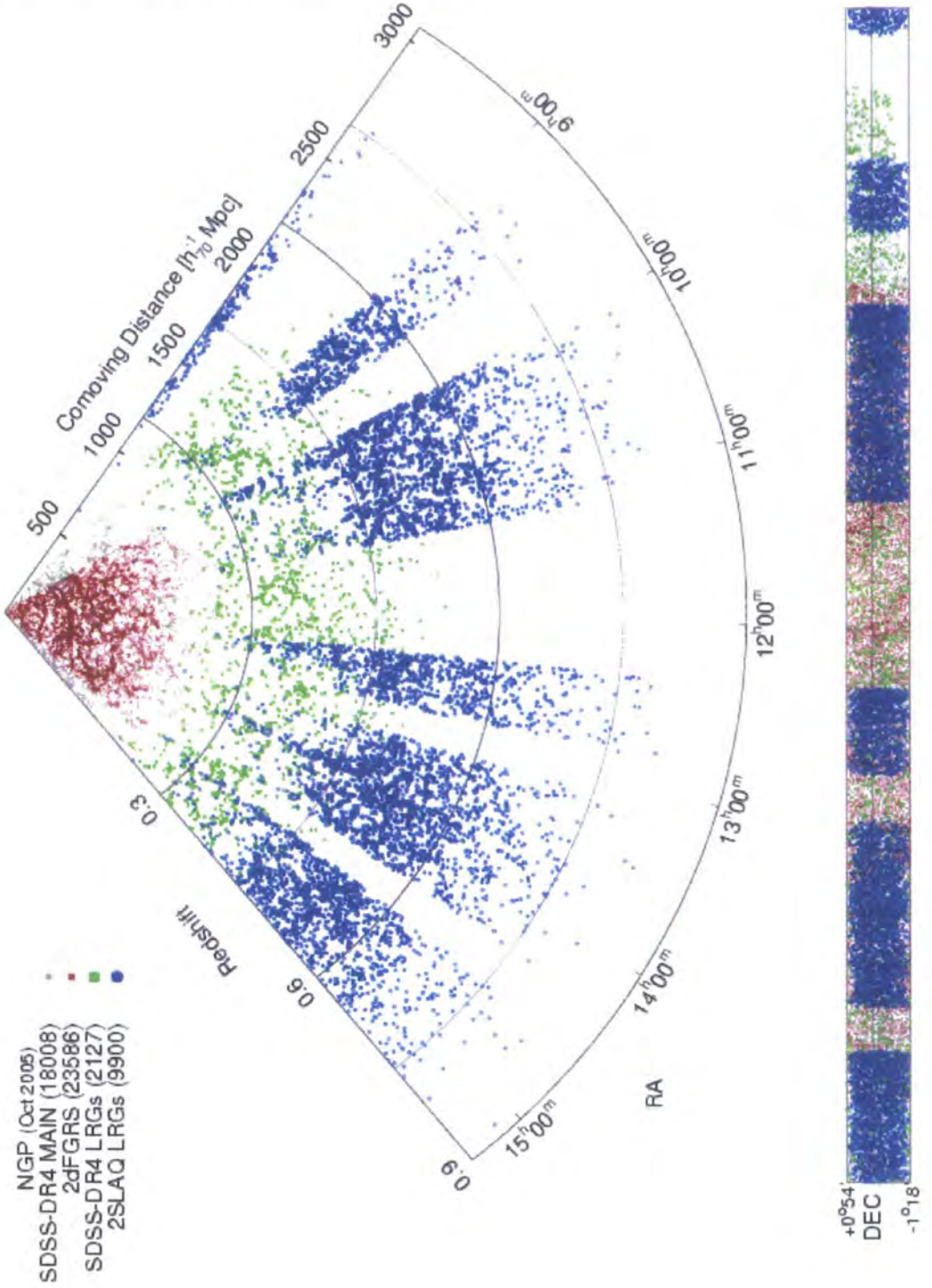

Figure 3.1: The 2SLAQ LRG NGP Wedge Plot (courtesy of P. Weilbacher). The comoving distances are calculated assuming an $\Omega_{\rm M} = 0.3, \Omega_\Lambda, h = 0.7$ cosmology.

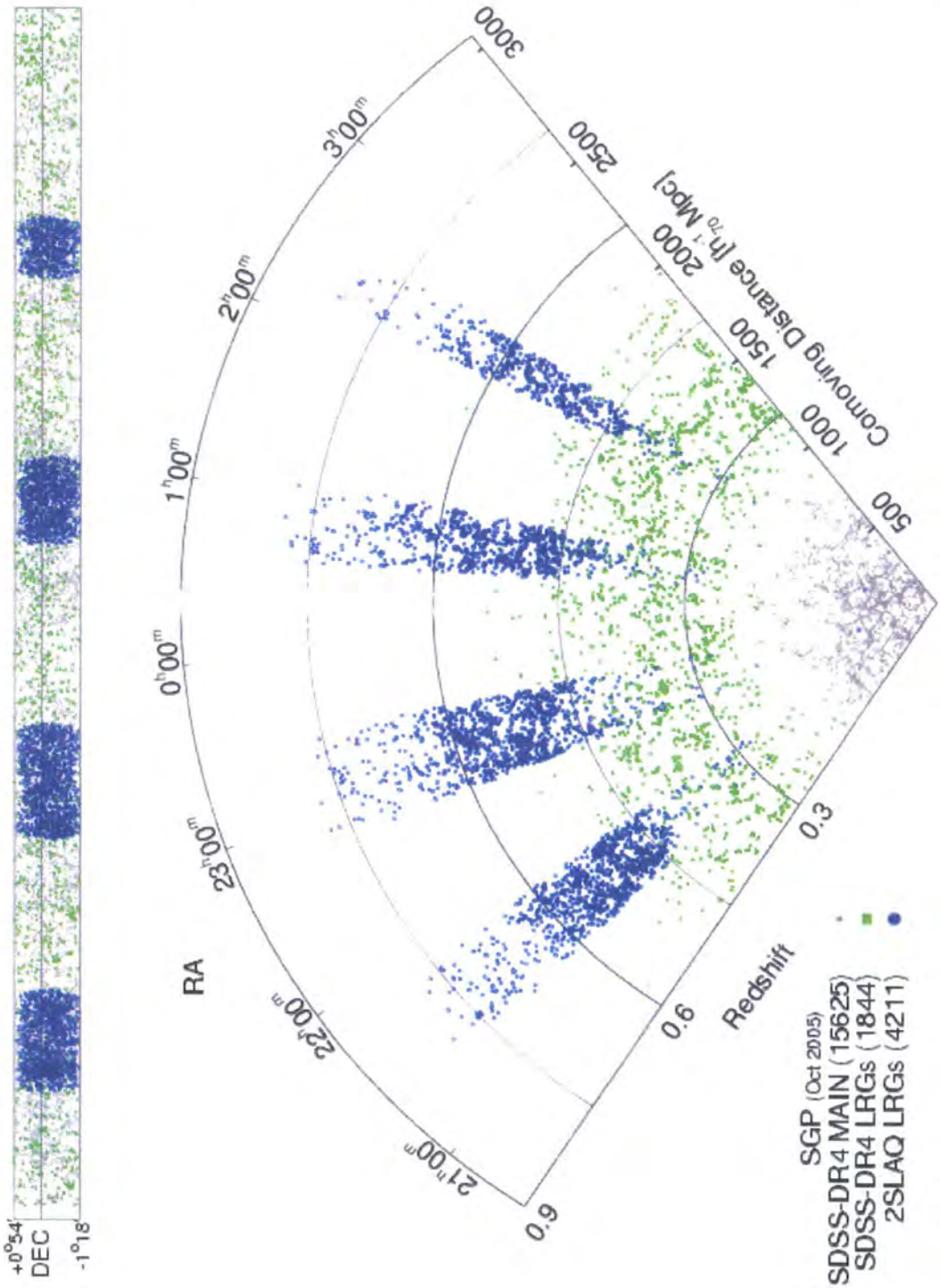

Figure 3.2: The 2SLAQ LRG SGP Wedge Plot (courtesy of P. Weilbacher). The comoving distances are calculated assuming an $\Omega_{\rm M} = 0.3, \Omega_\Lambda, h = 0.7$ cosmology.

Sample Description	Number in sample	North	South
Unique Objects	14 978	10 369	4 609
"Qop" ≥ 3	13 784	9 726	4 058
M Stars	663		
LRGs	13 121	9 280	3 841
LRG Sample 8	8 756	6 076	2 680
excl. a01, a02, s01	**8 656**	**5 995**	**2 661**

Table 3.1: The 2SLAQ LRG Survey; Numbers of galaxies in different samples. Over 18 000 spectra were obtained, resulting in 13 121 spectroscopically confirmed Luminous Red Galaxies. We use the LRGs with the "Sample 8" Input Priority settings for our analysis but do not include the data taken in the a01, a02 and s01 fields which have low redshift completeness and should be excluded from statistical analysis (Cannon et al., 2006). Thus we are left with 8 656 in our "Gold Sample".

3.3 CLUSTERING ANALYSIS

3.3.1 THE TWO-POINT CORRELATION FUNCTION

Here we give a brief description of the 2-point correlation function (2PCF); for a more formal treatment the reader is referred to Peebles (1980) which presents the basis for the rest of the section. To denote the *redshift*-space (or z-space) correlation function, we will use the notation $\xi(s)$ and to denote the *real*-space correlation function, $\xi(r)$ will be used, where s is the redshift-space separation of two galaxies and r is the real-space separation.

The 2-point correlation function, $\xi(x)$, is defined by the joint probability that two galaxies are found in the two volume elements dV_1 and dV_2 placed at separation x,

$$dP_{12} = n^2[1 + \xi(x)]\, dV_1 dV_2. \tag{3.1}$$

To calculate $\xi(x)$, N points are given inside a window W of observation, which is a three-dimensional body of volume $V(W)$. An estimation of $\xi(x)$ is based on an average of the counts of neighbours of galaxies at a given scale, or more precisely, within a narrow interval of scales. An extensively used estimator is that of Davis & Peebles (1983) and is usually called the standard estimator,

$$\xi_{Std}(s) = \left(\frac{N_{rd}}{N}\frac{DD(s)}{DR(s)}\right) - 1 \tag{3.2}$$

where $DD(s)$ is the number of pairs in a given catalogue (within the window W) and $DR(s)$ is the number of pairs between the data and the random sample with separation in the same interval. N_{rd} is the total number of random points and N is the total number of data points. A value of $\xi = 1$ implies there are twice as many pairs of galaxies than expected for a random distribution and the scale at which this is the case is called the correlation length.

3.3.2 Constructing a random catalogue and survey Completeness

The two point correlation function, ξ, is measured by comparing the actual galaxy distribution to a catalogue of randomly distributed galaxies. Following the method of Hawkins et al. (2003) and Ratcliffe et al. (1998), these randomly distributed galaxies are subject to the same redshift, magnitude and mask constraints as the real data and we modulate the surface density of points in the random catalogue to follow the completeness variations. We now look at the various factors this involves.

Following Croom et al. (2004), we discuss issues regarding the 2SLAQ Survey completeness. As with the rest of this chapter, we are only concentrating on the properties of the luminous red galaxies. One might think the parallel 2SLAQ QSO survey would have a bearing on subsequent discussion but due to the higher priority given to the fibres assigned to observe the LRGs,the QSO Survey has no impact on LRG clustering considerations, as already noted. For more description of the clustering of the QSOs the reader is referred to da Angela et al. (2006).

Three main, separate types of completeness are going to be considered; i) Coverage completeness, f_c, which we define as the fraction of the input 2SLAQ catalogue sources that have spectroscopic observations. Identically to Croom et al. (2004), we calculate f_c, as being the ratio of observed to total sources in each of the sectors defined by overlapping 2SLAQ fields, which are pixelized on 1 (one) arcminute scales; ii) Spectroscopic completeness, f_s which can be said to be the fraction of observed objects which have a certain spectroscopic quality; iii) Incompleteness due to fibre collisions which is dealt with separately from coverage completeness.

For coverage completeness and spectroscopic completeness we assume that both are functions of angular position only, i.e. $f_c(\theta)$ and $f_s(\theta)$ respectively. The spectroscopic (i.e. redshift) completeness does depend on magnitude but this is not relevant for any of the purposes of this

chapter.

3.3.2.1 Angular + Spectroscopic Completeness and Fibre Collisions

There are various technical details associated with the 2dF instrument which can have an impact on the clustering analysis. Variations in target density, the small number of broken or otherwise unuseable fibres and constraints owing to the minimum fibre separation placing (see below) could introduce false signal into the clustering pattern. For our analysis, the 2SLAQ survey consists of 80 field pointings. Many of these pointings overlap, alleviating some of these technical issues.

The design of the 2dF instrument means that fibres cannot be placed closer than approximately 30 arcsec (Lewis et al., 2002) so both members of a close pair of galaxies cannot be targeted in a single fibre configuration. The simple, fixed-spacing tiling strategy of the 2SLAQ Survey means that not all such close pairs are lost. Neighbouring tiles have significant areas of overlap and much of the survey sky area is targeted more than once. This allows us to target both galaxies in some close pairs. Nevertheless, the survey misses a noticeable fraction of close pairs. It is important to assess the impact of this omission on the measurement of galaxy clustering and to investigate schemes that can compensate for the loss of close pairs.

To quantify the effect of these so-called 'fibre collisions' we have followed previous 2dF studies (e.g. Hawkins et al., 2003; Croom et al., 2004) and calculated the angular correlation function for galaxies in the 2SLAQ parent catalogue, $w_p(\theta)$, and for galaxies with redshifts used in our ξ analysis, $w_z(\theta)$. We used the same mask to determine the angular selection for each sample.

As shown in Figure 3.3, on scales $\theta \gtrsim 2'$, the angular correlations of the Parent and Redshift

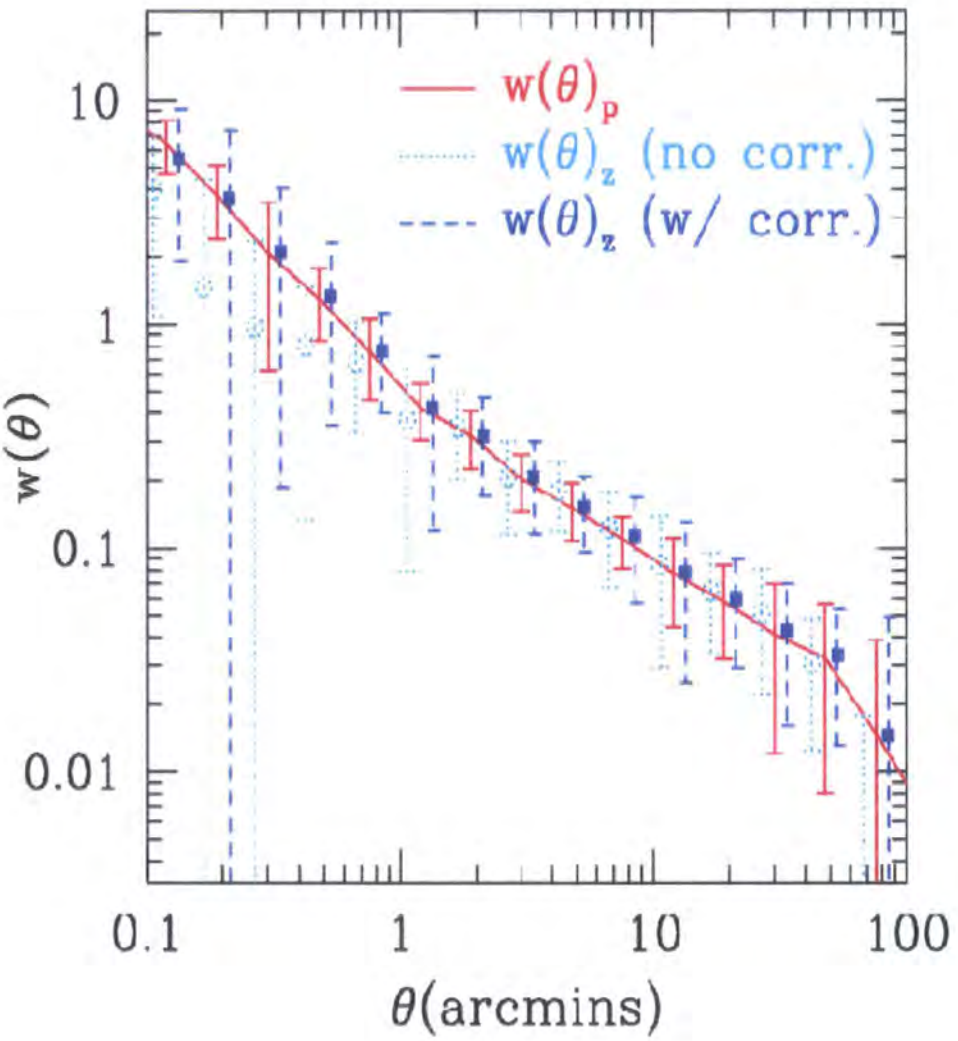

Figure 3.3: The angular correlation function, $w(\theta)$, for the 2SLAQ redshift catalogue (light blue) dotted, open circles compared to the parent catalogue, solid (red) line. The errors quoted are "field-to-field" errors, using 9 sub-areas, with the sub-areas used given by Table 3.2. The filled blue squares, with dashed error bars, show the $w(\theta)$ from the redshift catalogue after the correction for fibre collisions has been applied. The values for the uncorrected (corrected) $w(\theta)$ from the redshift catalogue have been moved by $\Delta \log = -(+)0.05$ in the abscissa for clarity. Note also that the solid line is equal to the filled squares given in Figure 3.6.

catalogue are very nearly consistent. At scales $\theta \lesssim 1'$, we begin to lose close pairs. To correct for this effect, we use a similar method to Hawkins et al. (2003) and Li et al. (2006). The quantity $w_{\rm cor}(\theta) = (1 + w_p)/(1 + w_z)$ is used to weight our 3-D DD pairs. For each DD pair, the angular separation on the sky is calculated and the galaxy-galaxy pair is weighted by the $w_{\rm cor}(\theta)$ ratio given by the relevant angular separation. The result of weighting by this factor, is shown by the filled (dark blue) squares in Fig. 3.3.

The last stage in determining the angular "mask" is to evaluate the spectroscopic completeness of the survey, $f_s(\theta)$ which for our purposes, we again assume depends on sky position only. This function essentially describes the success rate in obtaining a spectrum and reliable redshift for a given fibred object. Here the advantage of LRGs becomes apparent. With their well-defined early-type spectra and often very strong Ca H+K break around 4000Å, a high success rate was achieved when calculating a redshift for the 2SLAQ LRG objects. Also, it became apparent that our 4 hour per field exposure time was on occasion generous and relatively high S/N spectra were recorded. The coverage completeness has been estimated at 94.5 per cent for the primary "Sample 8" and the redshift (spectroscopic) completeness at 96.7 per cent, giving an overall completeness of 91.4 per cent (Cannon et al. 2006, Section 5.5, Figure 5).

3.3.2.2 Radial Selection Function and Estimates of the LRG $N(z)$

The observed distribution of galaxy redshifts is given in Figure 3.4. Plotted are the $N(z)$ distributions, binned into redshift slices of Δz=0.02, for the "Gold Sample". Also shown is a polynomial fit (7th order) to the $N(z)$ distribution, which is used to generate the random distributions. Checking the $N(z)$ fits using higher order polynomials or a convolved double Gaussian does not give tighter reproduction of the observed LRG redshift distribution.

Combining the radial selection function and the completeness map, we generate a random catalogue of points which we now use to calculate the LRG correlation function.

3.3.3 Calculating the 2-point Correlation Function

As the LRG correlation function, $\xi(s)$, probes high redshifts and large scales, the measured values are highly dependent on the assumed cosmology. In determining the comoving separation of pairs of LRGs we choose to calculate $\xi(s)$ for two representative cosmological models. The first uses the cosmological parameters derived from WMAP, 2dFGRS and other data (Spergel et al., 2003, 2006; Percival et al., 2002; Cole et al., 2005; Sánchez et al., 2006) with $(\Omega_{\rm m},\Omega_\Lambda) = (0.3, 0.7)$, which we will call the Λ cosmology. The second model assumed is an Einstein-de Sitter cosmology with $(\Omega_{\rm m},\Omega_\Lambda) = (1.0, 0.0)$ which we denote as the EdS cosmology. We quote distances in terms of h^{-1} Mpc, where h is the dimensionless Hubble constant such that $H_0 = 100h$ km s^{-1} Mpc^{-1}.

We have used the minimum variance estimator suggested by Landy & Szalay (1993) to calculate $\xi(s)$. Using notation from Martínez & Saar (2002), this estimator is

$$\xi_{\rm LS}(s) = 1 + \left(\frac{N_{rd}}{N}\right)^2 \frac{DD(s)}{RR(s)} - 2\left(\frac{N_{rd}}{N}\right)\frac{DR(s)}{RR(s)} \quad (3.3)$$

$$\equiv \frac{\langle DD\rangle - \langle 2DR\rangle + \langle RR\rangle}{\langle RR\rangle}, \quad (3.4)$$

where the angle brackets denote the suitably normalised LRG-LRG, LRG-random and random-random pairs counted at separation s. We use bin widths of $\delta \log(s/\ h^{-1}\ {\rm Mpc}) = 0.1$. The density of random points used was 20 times the density of LRGs. The Hamilton estimator is also utilised (Hamilton, 1993) where

$$\xi_{\rm Ham}(s) = \frac{DD(s)\cdot RR(s)}{DR(s)^2} - 1 \quad (3.5)$$

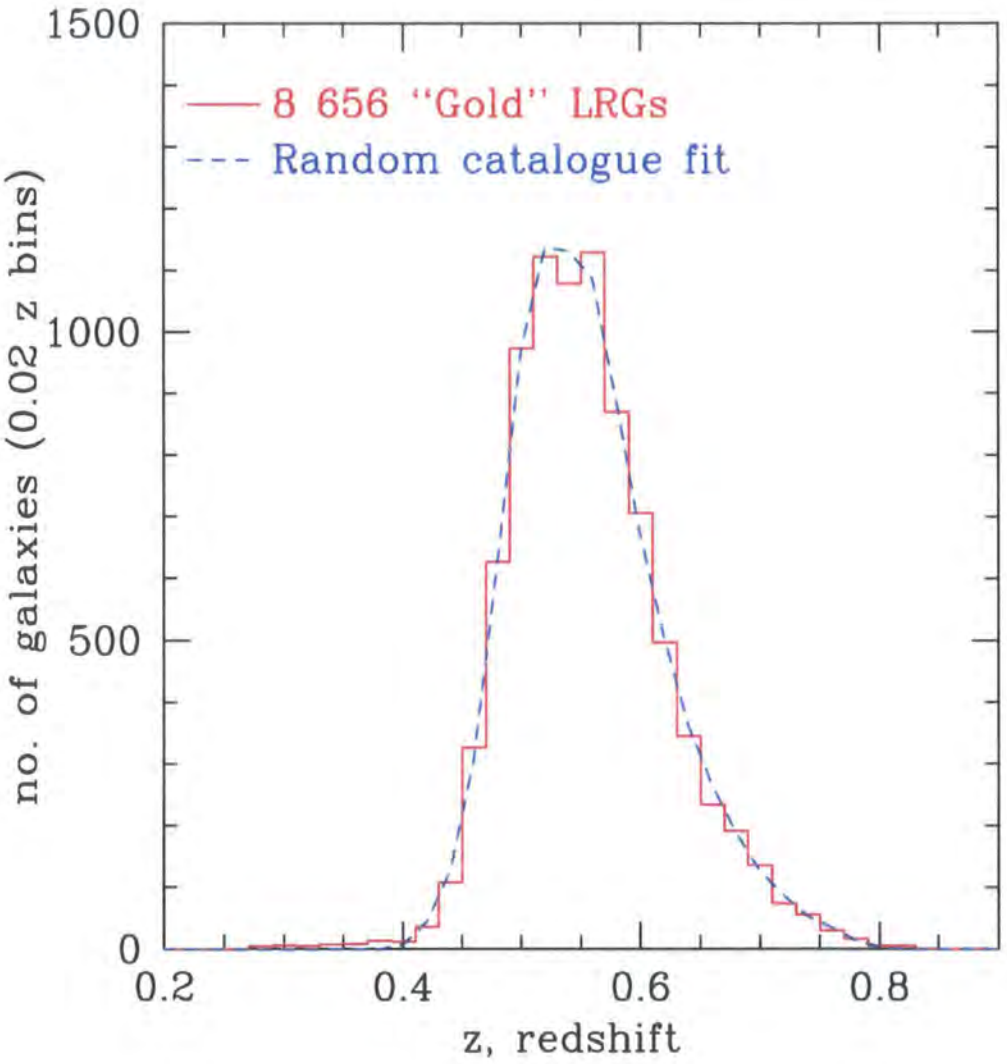

Figure 3.4: The redshift distribution for the 2SLAQ LRG "Gold" Sample we use. The solid red histogram is for the "Gold" Sample. The dashed blue line is from the normalised random catalogue.

and no normalisation is required. Since we find the differences of the Hamilton estimator compared to the Landy-Szalay method are negligible, the Landy-Szalay method is quoted in all $\xi(s)$ figures unless explicitly stated otherwise.

Three methods are employed to estimate the likely errors on our measurements. The first is a calculation of the error on $\xi(s)$ using the modified Poisson estimate of

$$\sigma_{\rm Poi}(s) = \frac{1+\xi(s)}{\sqrt{DD(s)}}. \tag{3.6}$$

The second error estimate method is what we shall call the *field-to-field* errors, calculated by

$$\sigma^2_{\rm FtF}(s) = \frac{1}{N-1}\sum_{i=1}^{N}\frac{DR_i(s)}{DR(s)}[\xi_i(s)-\xi(s)]^2 \tag{3.7}$$

where N is the total number of subsamples i.e. "the fields" and $\xi_i(s)$ is from one field. $\xi(s)$ is the value for ξ from the entire sample and is not the mean of the subsamples. Essentially, these field-to-field errors are 1σ standard deviations in the value of the correlation function between fields, inverse variance-weighted to account for the different numbers of sources in each field. Thus the $DR_i(s)/DR(s)$ factor weights each field so that fields with more objects are lent more significance in the error calculation (see e.g. Myers et al., 2003). For our studies the natural unit of the "Field-to-field" (FtF) subsample is given by the area geometry covered by the survey. Thus we take $N = 9$, and split the NGP area into five regions, *a,b,c,d,e* and the SGP in to four regions, named *s06, s25, s48, s67* around 330, 350, 10 and 30 degrees RA, respectively. Details of the FtF subsamples are given in Table 3.2.

The third method is usually referred to as the *jackknife* estimate, and has been used in other correlation studies (e.g. Scranton et al., 2002; Zehavi et al., 2002, 2005a). Here we estimate σ as

$$\sigma^2_{\rm Jack}(s) = \sum_{i'=1}^{N} \frac{DR_{i'}(s)}{DR(s)} [\xi_{i'}(s) - \xi(s)]^2 \tag{3.8}$$

where i' is used to signify the fact that each time we calculate a value of $\xi(s)$, all subsamples are used bar one. For the jackknife errors, we divide the survey into 32 approximately equal sized areas, leaving out ~4.5 square degrees from the entire survey area at one time. Thus a jackknife subsample will contain ~8,350 LRGs. We can then work out the covariance matrix in the traditional way,

$$\mathrm{Cov}(\xi_i, \xi_j) = \frac{N-1}{N} \sum_{l=1}^{N} (\xi_i^l - \bar{\xi}_i^l)(\xi_j^l - \bar{\xi}_j^l) \tag{3.9}$$

where $\bar{\xi}$ is the mean value of ξ measured from all the jackknife subsamples and $N = 32$ in our case (c.f. Zehavi et al. (2002)). The variances are obtained from the leading diagonal elements of the covariance matrix,

$$\sigma_i^2 = \mathrm{Cov}(\xi_i, \xi_i) \tag{3.10}$$

When examining the covariance matrix, we find the measurements to be slightly noisy as well as an indicating anti-correlation of adjacent bins (contrary to theoretical expectations). However, we note that in the other recent clustering studies, noisy covariances and anti-correlations were also noted (e.g. Scranton et al., 2002; Zehavi et al., 2002, 2005a).

The ratio of Poisson to jackknife errors, Poisson to 'field-to-field' errors, and the 'field-to-field' to jackknife errors are given in Figure 3.5. As can be seen, all error estimators are comparable on scales $\lesssim 10\ \ h^{-1}$ Mpc, while on larger scales than this the jackknife and 'field-to-field' errors are considerably larger than the simple Poisson estimates. The magnitude of the 'field-to-field' and jackknife errors are very similar from the smallest scales considered here, up to $\approx 40\ \ h^{-1}$ Mpc. This behaviour has been noted in other correlation function work, e.g. da

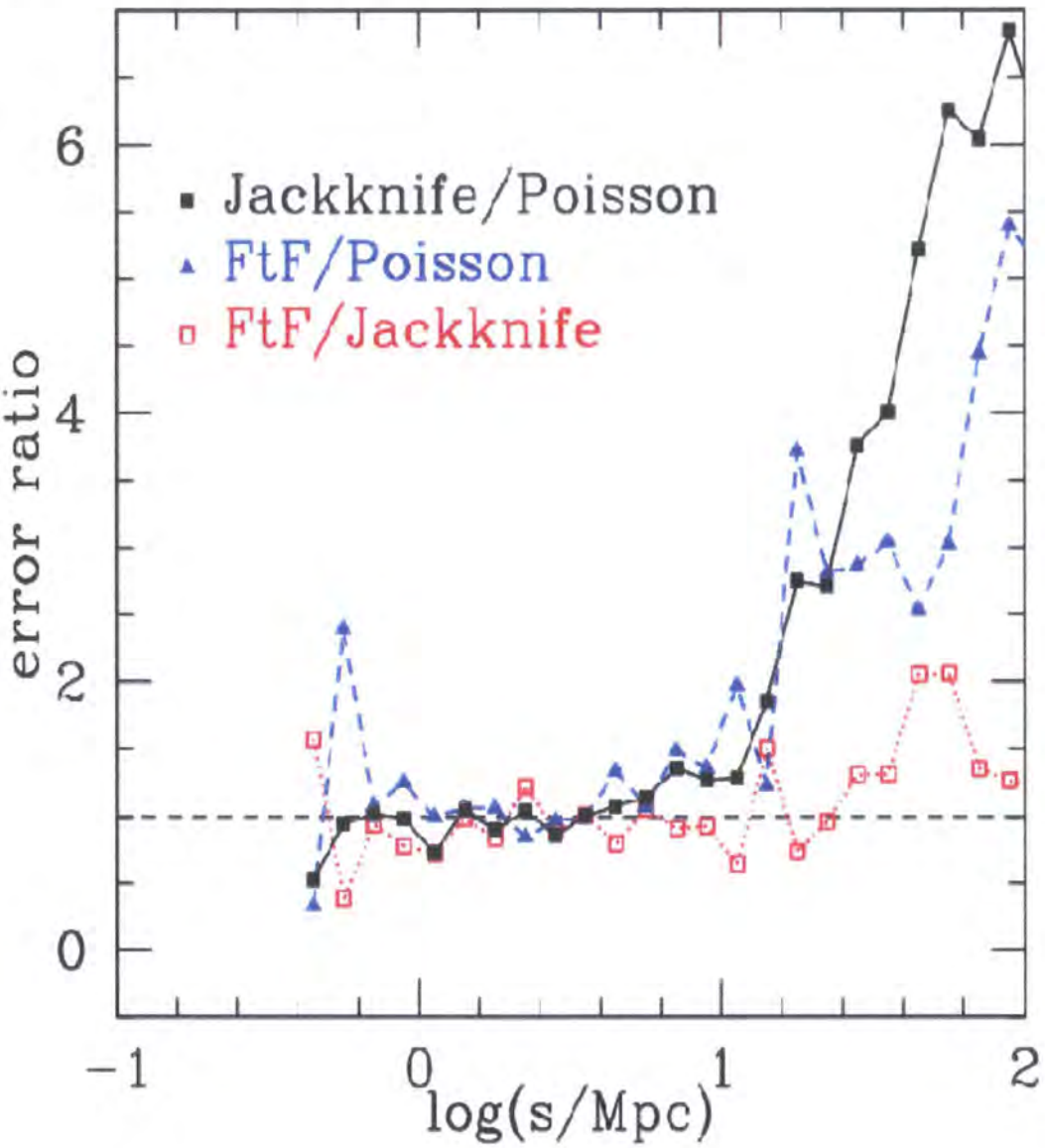

Figure 3.5: The ratio of jackknife to Poisson errors (solid black line and squares), 'field-to-field' to Poisson errors, (dashed blue line and triangles) and 'field-to-field' to jackknife errors (dotted red line and open squares). As can be seen, all error estimators are comparable on scales $\lesssim 10\ h^{-1}$ Mpc, while on larger scales than this the jackknife and 'field-to-field' errors are considerably larger than the simple Poisson estimates. The magnitude of the 'field-to-field' and jackknife errors are very similar from the smallest scales considered here up to $\approx 40\ h^{-1}$ Mpc.

Area Name	RA(J2000) range/°	LRGs	Randoms	ρ_{rd}/ρ_{LRG}
a	120.0 - 145.0	617	10 745	17.41
b	145.0 - 175.0	1 837	35 449	19.30
c	175.0 - 195.0	572	14 484	25.32
d	195.0 - 215.0	1 723	34 373	19.95
e	215.0 - 240.0	1 246	24 849	19.94
s06	300.0 - 330.0	745	12 457	16.72
s25	330.0 - 360.0	876	18 499	21.12
s48	0.0 - 30.0	658	13 516	20.54
s67	30.0 - 60.0	382	8 749	22.90
Entire Survey		8 656	173 120	20.00

Table 3.2: The 2SLAQ LRG Survey; Names and Right Ascension ranges for the $N = 9$ sections used when calculating the field-to-field errors. The final column gives the ratio of the number density of random to data points in each area.

Ângela et al. (2005). We also note that field-to-field and jackknife errors are more comparable in size, regardless of scale. Hence, the errors that are quoted on all correlation functions from here on are the square roots of the variances from the jackknife method, *except* for the case of the angular correlation function, $w(\theta)$, where we quote the "field-to-field" error.

3.3.4 MEASURING $\xi(\sigma, \pi)$

Having described how we calculate galaxy-galaxy separations in redshift-space in order to measure $\xi(s)$, we can now study the clustering perpendicular, σ, and parallel, π, to the line of sight.

We work out the difference in co-moving distances bewteen two objects, and define this as the π value. Thus, already knowing the redshift-space separation, s, we can use

$$s^2 = \sigma^2 + \pi^2 \tag{3.11}$$

to find σ. At this point it should be noted that σ is sometimes designated by r_p, where $r_p \equiv \sigma$. Here, we shall continue to use σ for the perpendicular separation. Closely following Hoyle et al. (2002), $\xi(\sigma, \pi)$ can be estimated in a similar way to $\xi(s)$. A catalogue of points, that have the same radial selection function and angular mask as the data but which are *unclustered*, is used to estimate the effective volume of each bin. As stated above, the unclustered, random catalogue also contains 20 times more points than the data. The $DD(\sigma, \pi)$, $DR(\sigma, \pi)$ and the $RR(\sigma, \pi)$, where again D stands for data LRG and R stands for random, counts in each σ and π bins are found and the Landy-Szalay estimator

$$\xi_{LS}(\sigma, \pi) = \frac{\langle DD(\sigma, \pi) \rangle - \langle 2DR(\sigma, \pi) \rangle + \langle RR(\sigma, \pi) \rangle}{\langle RR(\sigma, \pi) \rangle}, \tag{3.12}$$

is used to find $\xi(\sigma, \pi)$, with bins of $\delta \log(\sigma / \ h^{-1} \text{ Mpc}) = \delta \log(\pi / \ h^{-1} \text{ Mpc}) = 0.2$. Again, we compute three types of errors to use as a guide; Poisson, "Field-to-field" and Jackknife errors are calculated for $\xi(\sigma, \pi)$ as in equations 3.6 to 3.8. Again, after comparing the different $\xi(\sigma, \pi)$ error estimators we find that on the scales we are considering, the jackknife error is sufficient for our purposes.

3.3.5 The Projected Correlation Function, $w_p(\sigma)$

Although we are now in a position to calculate the redshift-space correlation function, the real-space correlation function, $\xi(r)$, which measures the physical clustering of galaxies and is independent of redshift-space distortions, remains unknown. However, due to the fact that

redshift distortion effects only appear in the radial component, by integrating along the π direction, we can calculate the projected correlation function,

$$w_p(\sigma) = 2\int_0^\infty \xi(\sigma,\pi)d\pi. \tag{3.13}$$

In practice we set the upper limit on the integral to be $\pi_{\rm max} = 70$ Mpc as at this large-scale, the effect of clustering is negligible, while linear theory should also apply. The effect of z-space distortions due to small-scale peculiar velocities or redshift errors is also minimal on this scale. Changing the value of $\pi_{\rm max}$ from 25 Mpc to 100 Mpc makes negligible difference to the result.

Due to $w_p(\sigma)$ now describing the real-space clustering, the integral in Equation 6.3 can be re-written in terms of $\xi(r)$, (Davis & Peebles, 1983)

$$w_p(\sigma) = 2\int_\sigma^{\pi_{\rm max}} \frac{r\,\xi(r)}{\sqrt{(r^2-\sigma^2)}}dr. \tag{3.14}$$

If we then assume that $\xi(r)$ is a power-law of the form, $\xi(r) = (r/r_0)^{-\gamma}$, equation 3.14 can be integrated analytically such that

$$\frac{w_p(\sigma)}{\sigma} = \left(\frac{r_0}{\sigma}\right)^\gamma \left[\frac{\Gamma(\frac{1}{2})\,\Gamma(\frac{\gamma-1}{2})}{\Gamma(\frac{\gamma}{2})}\right] = \left(\frac{r_0}{\sigma}\right)^\gamma A(\gamma) \tag{3.15}$$

where $A(\gamma)$ represents the quantity inside the square brackets and $\Gamma(x)$ is the Gamma function calculated at x. We now have a method for fitting the real-space correlation length and power-law slope, denoted r_0 and γ respectively.

3.3.6 The Real-space Correlation Function, $\xi(r)$

Using the projected correlation function, $w_p(\sigma)$, it is now possible to find the r_0 and γ for the real-space correlation function. However, if one does not assume a power-law $\xi(r)$, it is still possible to estimate $\xi(r)$ by directly inverting $w_p(\sigma)$. Following Saunders et al. (1992) we can

write

$$\xi(r) = -\frac{1}{\pi}\int_r^\infty \frac{(dw(\sigma)/d\sigma)}{(\sigma^2 - r^2)^{\frac{1}{2}}} d\sigma. \tag{3.16}$$

Assuming a step function for $w_p(\sigma) = w_i$ in bins centred on σ_i, and interpolating between values,

$$\xi(\sigma_i) = -\frac{1}{\pi}\sum_{j\geq i} \frac{w_{j+1} - w_j}{\sigma_{j+1} - \sigma_j} \ln\left(\frac{\sigma_{j+1} + \sqrt{\sigma_{j+1}^2 - \sigma_i^2}}{\sigma_j + \sqrt{\sigma_j^2 - \sigma_i^2}}\right) \tag{3.17}$$

for $r = \sigma_i$. We shall be utilising this interpolation method to check whether a power-law description is valid for our 2SLAQ Survey data and, if so, what values the parameters r_0 and γ take.

3.4 2SLAQ LRG Clustering Results

3.4.1 The LRG Angular Correlation Function, $w(\theta)$

We first analyse the form of the angular correlation function, $w(\theta)$. The full input catalogue contains approximately 75 000 LRGs mainly from areas in the two equatorial stripes; about **40%** of this area was observed spectroscopically. As stated in Section 2, approximately a third of the objects in the full input catalogue pass the Sample 8 selection criteria. As well as providing estimates of fibre collision and other angular incompletenesses, the angular function is of interest in itself, particularly given the narrow redshift range from which the sample is derived. We use 25 795 "Sample 8" LRG targets to estimate the $w(\theta)$. Studying Figure 3.6, we first note that the function gives clear indication of a change of slope at $\theta = 2$ arcmin or $\approx 1\ \ h^{-1}$ Mpc in the Λ cosmology. Considering a power-law form for $w(\theta) = A\theta^{1-\gamma}$, at $\theta < 2$ arcmin the slope is -1.17 ± 0.07 and on larger scales the slope is -0.67 ± 0.03. Using Limber's formula from Phillipps et al. (1978) and assuming a double power-law form where the slope changes from -2.17 to -1.67 at $\sim 1\ \ h^{-1}$ Mpc, we found in the Λ case, a value of $r_0 = 4.64\ \ h^{-1}$ Mpc at small scales and $r_0 = 7.30\ \ h^{-1}$ Mpc at large scales (see Fig. 3.6). We shall check models of this form against the deprojected correlation function $\xi(r)$ (see Figure 3.10 below). We find that the form of this double power-law gives reasonable fits to the data in the LRG redshift survey, although the large scale slope derived from the input catalogue $w(\theta)$ appears slightly flatter than in the semi-projected and 3-D correlation functions (see below). The reason for this is not clear, although it could be that $w(\theta)$ is more sensitive to any artificial gradient in the LRG data. Thus, we checked for an angular systematic in the data by calculating the angular correlation between spectroscopic LRGs that are not at the same redshift. We find this is consistent with zero and

so such systematics do not explain the flatter slope for $w(\theta)$ at large-scales. The most likely explanation is the different fitting ranges for $w(\theta)$ and the semi-projected correlation function. This test also suggests that the upturn at $\theta < 2$ arcmins is a real feature. It will be seen that $w(\theta)$ gives the strongest evidence of all the correlation function statistics for non-power-law behaviour in $\xi(r)$. A similar feature is seen by Zehavi et al in the SDSS MAIN galaxy sample and to a lesser extent in the SDSS LRG survey. Reports of such features in galaxy correlation functions go back to Shanks et al. (1983). We simply report the existence of this feature in the LRG data and leave further interpretation as future work. Possible interpretations could include models of halo occupation distributions (HOD) in the standard model case or the possibility that it might represent a real feature in the mass distribution in the case of other models. We also show results from White et al. (2007, open, black circles, Figure 3.6) who report on the angular correlation function as a route to estimating merger rates of massive red galaxies. As can be seen, these measurements from the NOAO Deep Wide-Field Survey (NDWFS; Jannuzi & Dey, 1999) agree very well with the 2SLAQ LRG results, though as we shall discuss later, care always has to be taken when comparing measurements from galaxy surveys with different selections.

3.4.2 The LRG Redshift-Space Correlation Function, $\xi(s)$

Using the above corrections including that for fibre collisions (Section 3.3.2.1), the 2SLAQ LRG redshift-space 2PCF, $\xi(s)$, is shown in Figure 3.7. There is clear evidence for a downturn at small scales $\lesssim 2.5\ h^{-1}$ Mpc which is not described well by a single power-law. This turn-over is consistent with the redshift-space distortion effects one would expect in a $\xi(s)$ correlation function - namely the "Finger of God" effect at small scales due to intrinsic velocity dispersions

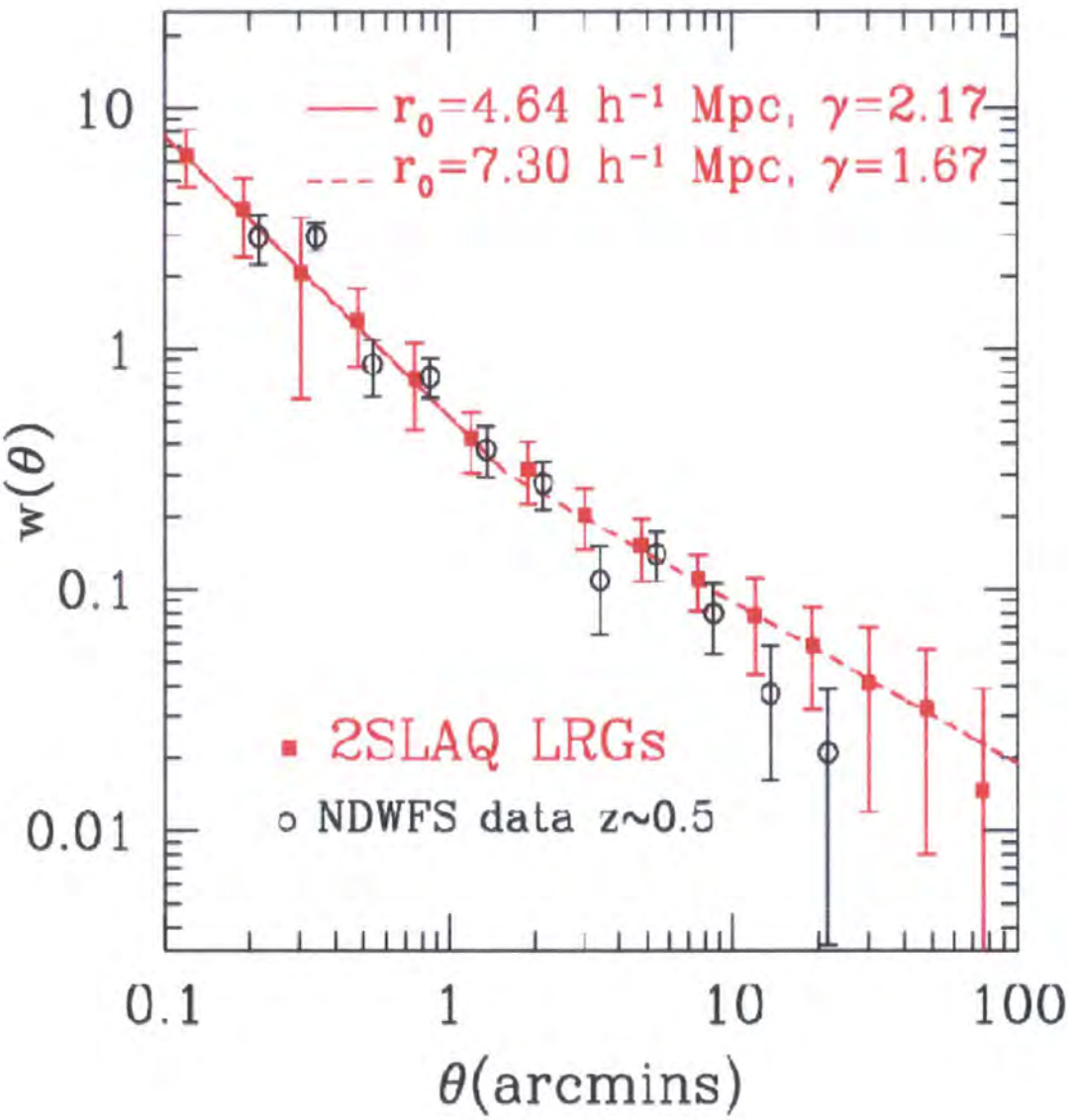

Figure 3.6: The angular correlation function, $w(\theta)$ from the 2SLAQ LRG Survey from the input catalogue containing 25 795 LRG targets (solid, red squares). Clear evidence is seen for a change of power-law slope on $\sim$ 2arcmin scales which is equivalent to $\approx 1 \ \ h^{-1}$ Mpc. The open (black) circles show the results from the NDWFS at $z \sim 0.5$ (White et al., 2007).

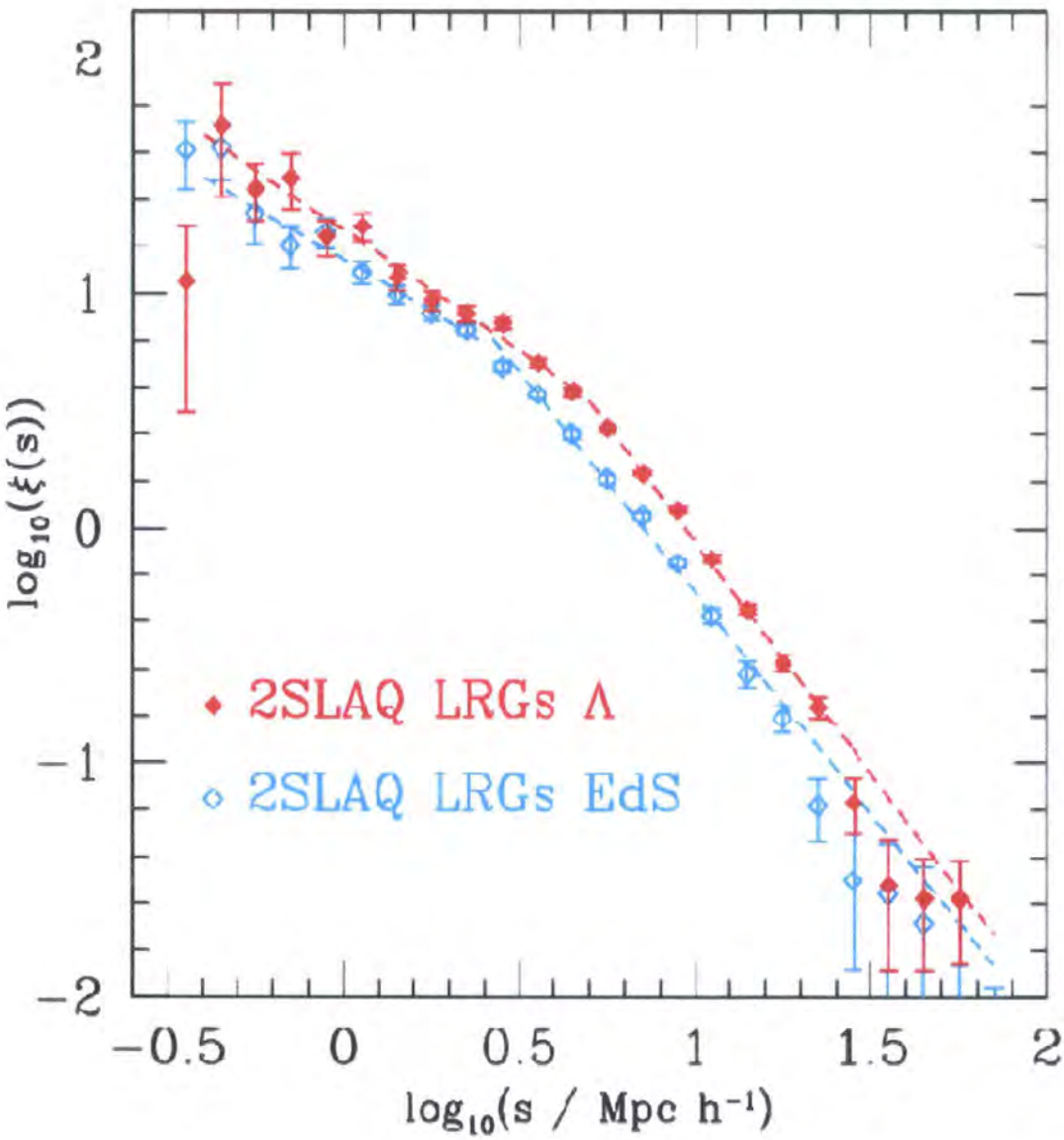

Figure 3.7: The redshift-space 2-point correlation function, $\xi(s)$ for the 2SLAQ LRG Survey in a Λ cosmology (filled, red diamonds) and an Einstein-de Sitter, $\Omega_{\rm m} = 1$, cosmology (open, cyan diamonds). The dashed lines shown are the double power-law best-fit models to data with the associated values of s_0 and γ given in Table 3.3.

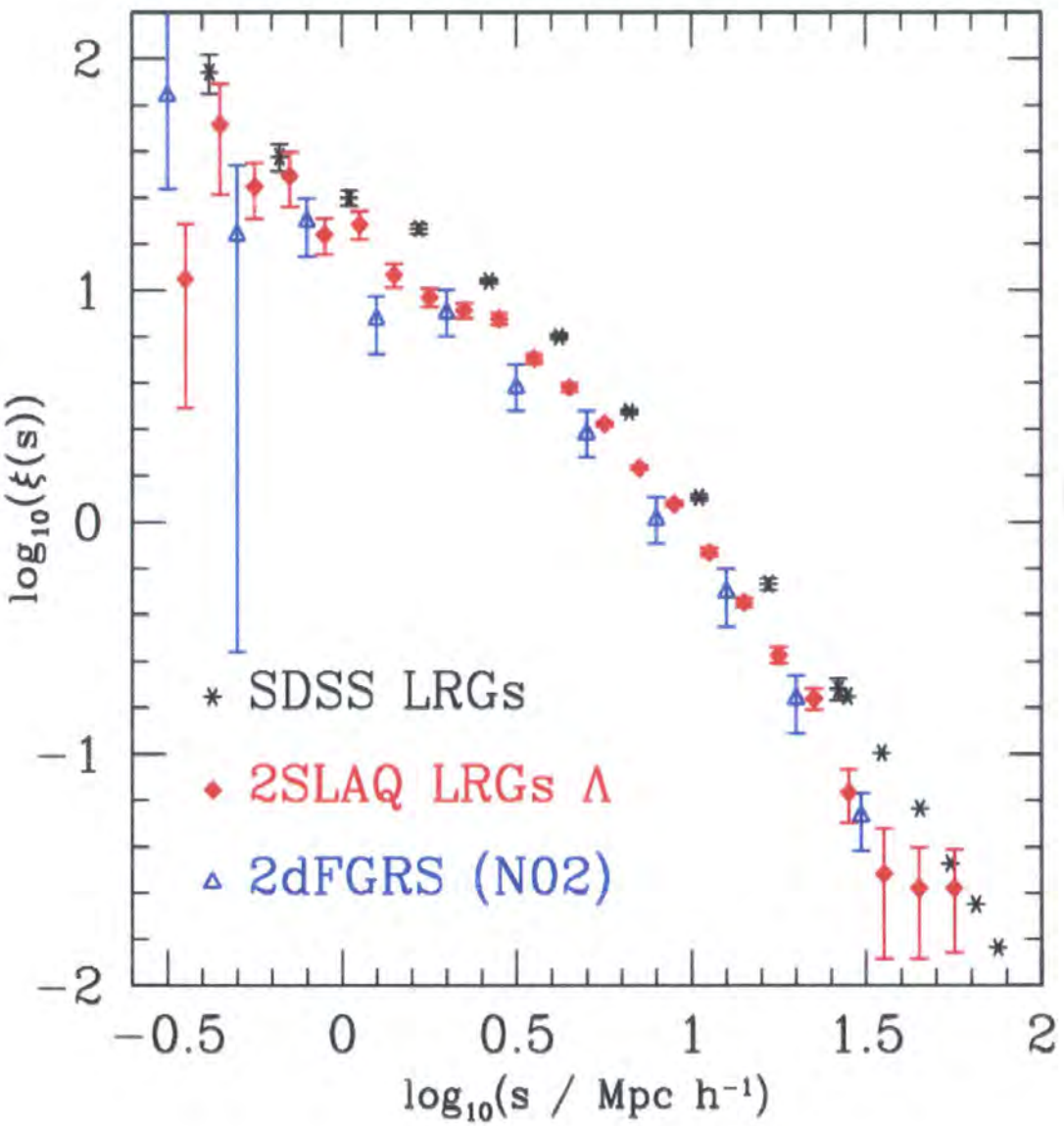

Figure 3.8: The redshift-space correlation function, $\xi(s)$ for the 2SLAQ LRG Survey (filled, red, diamonds). For comparison, data from the SDSS LRG Survey (black stars Zehavi et al., 2005a; Eisenstein et al., 2005) and the high luminosity early-type 2dFGRS, (Norberg et al., 2002a, open blue triangles) are also plotted.

(and there will also be large-scale flattening from peculiar motions due to coherent cluster in-fall). However, we note that real features in the real-space correlation function, $\xi(r)$, may also be contributing. We have also estimated the effect of the integral constraint (IC, Peebles, 1980) at larger scales. Using our global (N+S) normalisation of the correlation function, we assume a total number of 8 656 galaxies in a total volume of 4.5×10^7 h^{-1} Mpc^3 and $r_0 = 7.45$ h^{-1} Mpc. Integrating with a $\gamma = 1.8$ power-law to 20 h^{-1} Mpc gives an $IC = 3.5 \times 10^{-4}$ and to 100 h^{-1} Mpc, an $IC = 2.4 \times 10^{-3}$. Adding such contributions would make negligible contributions to any of our correlation function fits.

We now attempt to parameterise the $\xi(s)$ data. The simplest model traditionally fitted to correlation function estimates is a power law of the form

$$\xi(s) = \left(\frac{s}{s_0}\right)^{-\gamma}, \tag{3.18}$$

where s_0 is the comoving correlation length, in units of h^{-1} Mpc. However, with the redshift-space distortion effects being so evident, we find that a single-power is insufficient to describe the data and thus switch to a double power-law model

$$\xi(s) = \begin{cases} \left(\frac{s}{s_1}\right)^{\gamma_1} & s \leq s_\mathrm{b} \quad \text{and} \\ \left(\frac{s}{s_2}\right)^{\gamma_2} & s > s_\mathrm{b} \end{cases} \tag{3.19}$$

where s_b is the scale of the "break" from one power-law description to the other. This $\xi(s)$ model is used later in Section 4.1. We fit the double power-law continuously over the range $0.4 < s < 70$ h^{-1} Mpc. We fix the break-scale at 4.5 h^{-1} Mpc for the Λ cosmology and at 2.5 h^{-1} Mpc for the EdS cosmology. We perform a χ^2-fit, following the prescription given by Press et al. (1992, Chap. 15)., to find the best-fit values for s_1, γ_1, s_2, and γ_2. We plot the best fit double-power law models in Figure 3.7 and quote the values of s_1, γ_1, s_2, and γ_2, in

Λ	$s < 4.5\ h^{-1}$ Mpc	$s > 4.5\ h^{-1}$ Mpc
$s_0/\ h^{-1}$ Mpc	$17.3^{+2.5}_{-2.0}$	9.40 ± 0.19
γ	1.03 ± 0.07	2.02 ± 0.07
χ^2_{min} (reduced)	1.95	1.88
d.o.f.	9	10
EdS	$s < 2.5\ h^{-1}$ Mpc	$s > 2.5\ h^{-1}$ Mpc
$s_0/\ h^{-1}$ Mpc	$20.3^{+9.4}_{-5.0}$	7.15 ± 0.13
γ	0.88 ± 0.11	$1.88^{+0.05}_{-0.04}$
χ^2_{min} (reduced)	0.91	3.43
d.o.f.	6	12

Table 3.3: Values of the redshift-space correlation length and slope for the 2SLAQ LRG Survey from $\xi(s)$. When a Λ cosmology was assumed, s_b was set at 4.5 h^{-1} Mpc. When a EdS cosmology was assumed, s_b was set at 2.5 h^{-1} Mpc.

Table 3.3. The errors quoted in Table 3 are only indicative because no account has been taken of the non-independence of the correlation function points in deriving the $\xi(s)$ fits.

For comparison, in Figure 3.8 results from the SDSS LRG study are plotted (Zehavi et al., 2005a; Eisenstein et al., 2005) as well as selected measurements from the 2dFGRS (Norberg et al., 2002a). The 2dFGRS is a blue, b_J selected survey of generally $\sim L^*$ galaxies. However, in Norberg et al. (2002a), the sample is segregated by luminosity and spectral type, the latter governed by the η parameter (Madgwick et al., 2003). Assuming a conversion of $M_r^{0.2} - M_{b_J} \simeq -1.1$, we calculate that the faintest 2SLAQ LRGs in our sample have an $M_{b_J} \approx -20.5$. Weighting according to number, we thus use the Norberg et al. (2002a) $-21.00 > M_{b_J} - 5\log h > -22.00$

and $-20.50 > M_{b_J} - 5\log h > -21.50$ luminosity ranges from their "early-type" volume-limited sample. This is shown by the (blue) open triangles in Figure 3.8.

The 2SLAQ LRG measurement is lower than the SDSS LRG result. It should not be concluded that this is evidence of evolution because although the SDSS survey is at a lower mean redshift, it was designed in order to target generally redder, more luminous LRGs (Eisenstein et al., 2001). The 2SLAQ LRG colour selection criteria is relatively relaxed for an "LRG" survey, leading to bluer and less luminous galaxies making it into our sample. We note here that it is non-trivial comparing clustering amplitudes and bias strengths for surveys with (sometimes very) different colour/magnitude/redshift selections. As such, a more detailed analysis of the clustering evolution for SDSS and 2SLAQ LRGs is presented in Wake et al. (2007, in prep.).

The 2dFGRS $M_{b_J} < -20.5$, early-type sample is at least approximately matched in terms of luminosity to the 2SLAQ LRGs. Once we have determined the linear bias parameter b for the $z = 0.55$ 2SLAQ LRGs, we shall be able to use a simple model of bias evolution, to compare these low redshift 2dFGRS and 2SLAQ LRG results.

3.4.3 The Projected Correlation Function, $w_p(\sigma)$

Again, after applying coverage, spectroscopic and fibre collision corrections, the projected correlation function, $w_p(\sigma)$, is presented in Figure 3.9. We again fit a single power-law to the 2SLAQ data and find that for the Λ cosmology, a single power-law is an adequate description, returning a reduced $\chi^2 = 1.17$ over $0.4 < \sigma < 70 \ \ h^{-1}$ Mpc. Over the wider range of $0.1 < \sigma < 70 \ \ h^{-1}$ Mpc, the χ^2 increases to 1.71. Thus the projected correlation function appears to deviate from a single power law at small scales in the way described in Section 3.4.1. The results for r_0 and γ assuming a single power-law are given in Table 3.4. The errors are

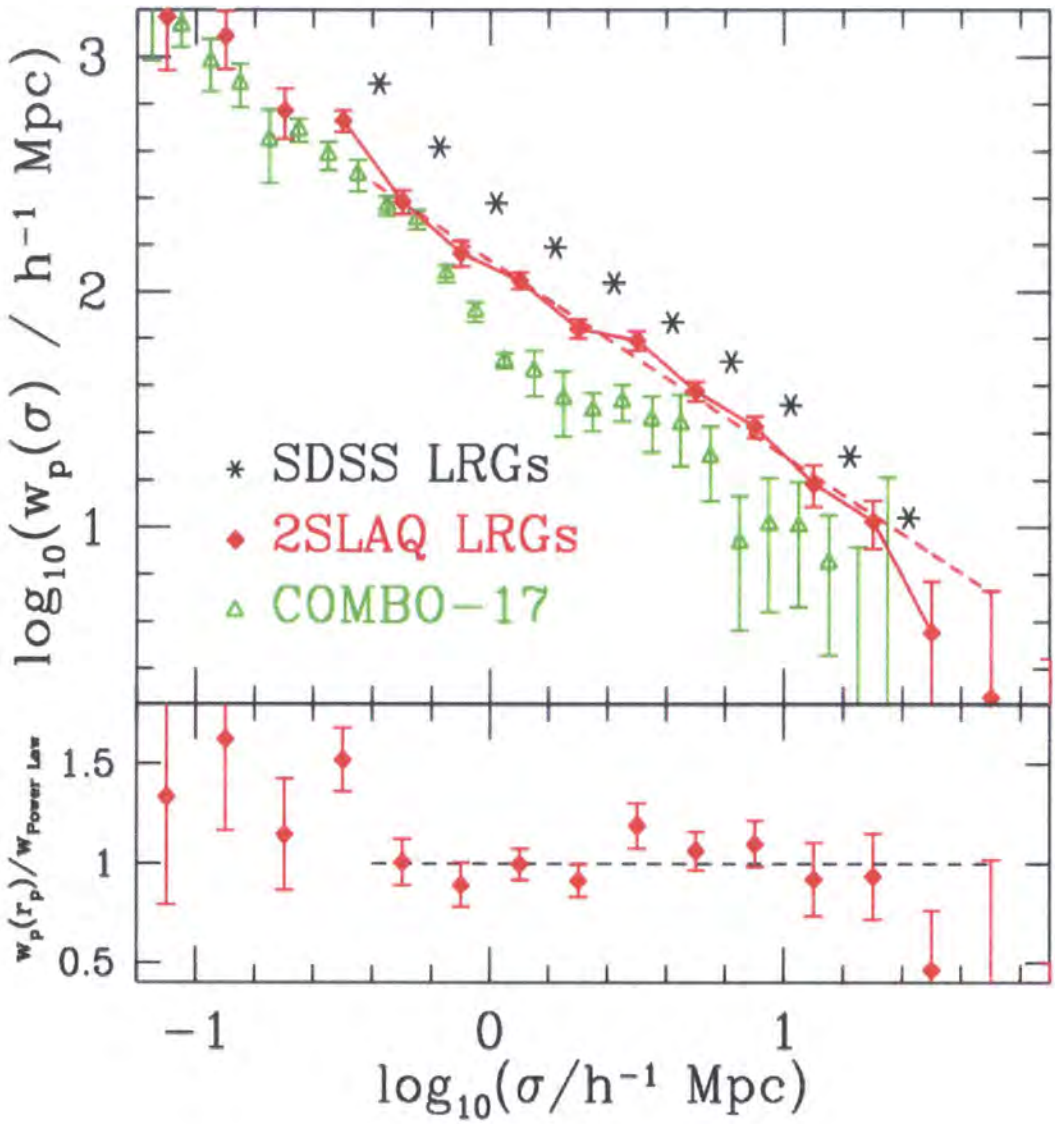

Figure 3.9: The 2SLAQ LRG projected correlation function, $w_p(\sigma)$, with errorbars from the "Jackknife" estimates (solid, red diamonds). The dashed line is the power-law that gives the best fitting line from the χ^2 analysis (see Table 3.4). The measurements from the SDSS LRGs (Zehavi et al., 2005a) are shown as a guide, with the SDSS errors being of comparable size to the plotted stars. The open (green) triangles are from COMBO-17 Red Sequence (Phleps et al., 2006). The lower panel shows the 2SLAQ LRG $w_p(\sigma)$ measurements divided by this best-fitting power law with the dashed line covering $0.4 < \sigma < 70\ \ h^{-1}$ Mpc.

	Λ	EdS
$r_0/\ h^{-1}$ Mpc	7.30 ± 0.34	5.40 ± 0.31
γ	1.83 ± 0.05	1.82 ± 0.06
χ^2_{min} (reduced)	1.17	1.39
d.o.f.	9	9

Table 3.4: Values of the projected correlation function, $w_p(\sigma)$, correlation length and slope for the 2SLAQ LRG Survey. In the Λ model, fits were performed over the range $0.4 < \sigma < 70.0\ h^{-1}$ Mpc, whereas for the EdS model, fits were performed over $0.25 < \sigma < 40.0\ h^{-1}$ Mpc. The value of r_0 was found using equation 3.15.

taken from jack-knife estimates found by dividing the survey into 32 subareas.

This deviation from the best fitting power law on small scales in the projected correlation function is in line with recent results seen in other galaxy surveys, e.g. the SDSS MAIN sample (Zehavi et al. (2004), not plotted) and the SDSS LRGs (Zehavi et al., 2005a). A "shoulder" is reported in these studies around $\sim 1\ h^{-1}$ Mpc scales. This feature is currently believed to be a consequence of the transition from the measuring of galaxies that reside within the *same* halo (the "one-halo" term) to the measuring of galaxies in *separate* haloes (the "two-halo" term). Changes in the slope of the projected correlation function are a generic prediction of HOD models. Thus for the 2SLAQ LRG Survey, we set a fiducial model, based on our best-fitting single power-law model of $w_p(\sigma)$ and find that if we divide the data out by this model, the results (bottom panel, Figure 3.9) are potentially comparable to the Zehavi et al. (2005a) results (their Figure 11). Despite the fact that our LRG sample is at higher redshifts and extends to lower luminosities, the form of the projected correlation function appears close

to that seen in the SDSS LRG sample, although at lower amplitude. We conclude that the 2SLAQ LRG correlation function is consistent with a change in slope similar to the SDSS LRG semi-projected correlation function.

Continuing with $w_p(\sigma)$, we compare the 2SLAQ LRGs with the COMBO-17 Survey. COMBO-17 (Classifying Objects by Medium-Band Observations, Wolf et al., 2001) uses a combination of 17 filters to obtain photometric redshifts accurate to $\sigma_z/(1+z) \simeq 0.01$ for the brightest ($R_{\rm Vega} < 20$ mag) objects. This is a comparable sample to our own in that it covers the same redshift range ($0.4 < z < 0.8$), but care must be taken when comparing the results; although the COMBO-17 galaxies described here are defined as Red Sequence, on the whole they will not be LRGs and will have a fainter magnitude and different colour selection. Figure 3.9 gives the projected correlation function of the 2SLAQ LRGs and red COMBO-17 galaxies from Phleps et al. (2006) (assuming a flat Λ cosmology). The change in slope is clearly seen in COMBO-17 and indeed is modelled successfully with a HOD prescription (Phleps et al., 2006). The upturn in slope in COMBO-17 versus 2SLAQ seems to occur on slightly different scales ($\simeq 1-2\ h^{-1}$ Mpc versus $\simeq 5\ h^{-1}$ Mpc) and is more dramatic than for either of the LRG samples. The errors on the COMBO-17 data are also much greater. Whether the differences are real, caused by the fainter magnitude of the COMBO-17 galaxies, or whether they are due to anomalies caused by the photometric redshifts, remains unclear.

3.4.4 The Real-Space Correlation Function, $\xi(r)$

We now use the methods quoted in Section 2 to estimate the real-space correlation function, $\xi(r)$. We show this in Figure 3.10.

Again, we attempt to fit simple power-law models to our $\xi(r)$ data in order to find values

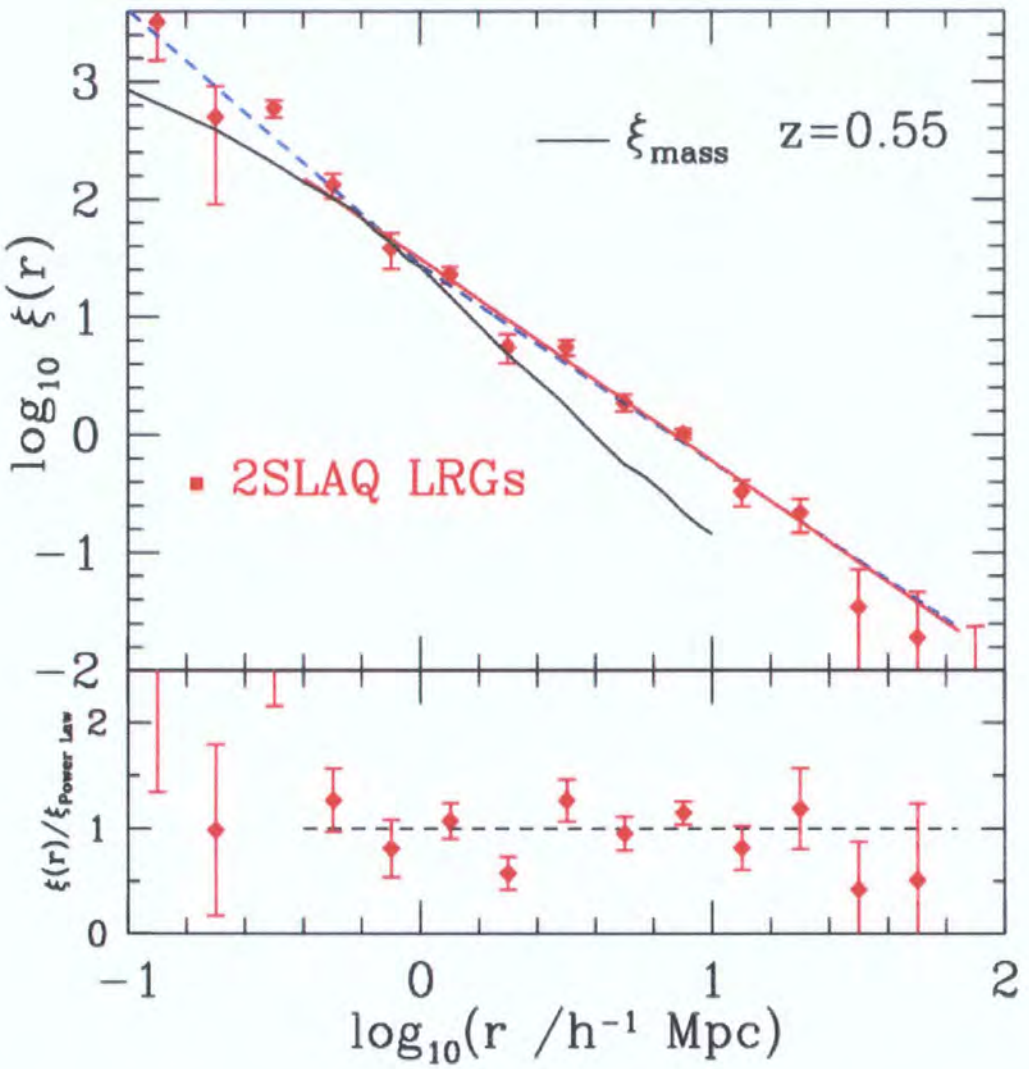

Figure 3.10: The real-space 2-point correlation function for the 2SLAQ LRG Survey (filled, red, diamonds) for the Λ cosmology. The best-fit single power-law with $r_0 = 7.45 \pm 0.35\ \ h^{-1}$ Mpc and $\gamma = 1.72 \pm 0.06$ is given by the dashed (red) line. The double power-law fit reported for the angular correlation, $w(\theta)$, in Section 3.1, is shown by the dotted (blue) line. The solid (black) line is a theoretical prediction for the $\xi_{\rm mass}(z = 0.55)$ using the simulations from Colín et al. (1999). These models have $(\Omega_{\rm m},\Omega_\Lambda) = (0.3, 0.7)$, $h = 0.7$ and a $\sigma_8 = 1.0$. We shall return to this in Section 4. The lower panel shows the 2SLAQ LRG $\xi(r)$ measurements (assuming a Λ cosmology) divided by this best-fitting power law with the dashed line covering $0.4 < \sigma < 70\ \ h^{-1}$ Mpc.

	Λ	EdS
$r_0/\ h^{-1}$ Mpc	7.45 ± 0.35	5.65 ± 0.41
γ	1.72 ± 0.06	1.67 ± 0.09
χ^2_{min} (reduced)	1.73	0.62
d.o.f.	9	9

Table 3.5: Values of the correlation length and slope for the 2SLAQ LRG Survey from the real-space correlation function, $\xi(r)$. Model fits were performed over the range $0.4 < r < 70\ \ h^{-1}$ Mpc for the Λ cosmology and over the range $0.25 < r < 40\ \ h^{-1}$ Mpc for the EdS cosmology.

for the real-space correlation length and slope, r_0 and γ, respectively. For $\xi(r)$ we attempt to take into account the information presented in the covariance matrix by estimating χ^2 fits to model $\xi(r)$ values such that

$$\chi^2 = \sum_{i,j} [\bar{\xi}(r_i) - \xi_m(r_i)]\, C^{-1}_{i,j}\, [\bar{\xi}(r_j) - \xi_m(r_j)] \tag{3.20}$$

where C^{-1}_{ij} is the inverse matrix of the covariance matrix and the subscripts i and j are indicies of separation bins. However, as has been reported in previous clustering analyses (e.g. Zehavi et al. (2002); Scranton et al. (2002)), the calculated covariance matrix is rather noisy with anti-correlations between points (contrary to theoretical expectations). Therefore, when calculating the best-fitting models, we perform a simple χ^2 fit as before, without the covariances or the covariance matrix, and take only the variances into account. As before, we fit over the scales $0.4 \leq r \leq 70.0\ \ h^{-1}$ Mpc. For the case of the real-space correlation function, we again find that a single power-law may not fit the data well with the best-fit values (and related reduced χ^2) given in Table 3.5. We find a value of γ to be 1.72 ± 0.06 and a correlation length of

$r_0 = 7.45 \pm 0.35$ (assuming a Λ cosmology). The errors on these parameters are estimated from considering the 1σ deviation from the minimised χ^2 on the 1-parameter fits. However, care has to be taken when quoting the best fit values for the joint 2-parameter fits which are shown in Figure 3.11. Here we find the values of $\delta\chi^2$ which correspond to the 1,2 and 3σ levels for a 2-parameter fit. Also shown in Fig. 3.11 are the values for the deviations in r_0 and γ, if we find the 32 best-fitting single power-law parameters from the jackknife samples. Jackknife appears to confirm the χ^2 error analysis with the assumption of Gaussian errors in Fig. 3.11. This is somewhat surprising since we have ignored the covariance between correlation function points in creating Fig. 3.11. The explanation may be that the fit at the minimum is still poor due to the deviant point at 2 h^{-1} Mpc in Fig. 3.10 and this causes the error contours in Fig. 3.11 to be larger than they would be in the absence of the deviant point. Including the full covariance matrix, the $\Delta\chi^2$ produces error contours significantly smaller than those in Fig. 3.11 and also the jackknife errors, even though the χ^2 at minimum remained the same. Overall we take the errors in Fig. 3.11 supported by the jackknife estimates as being reasonably representative of the real error.

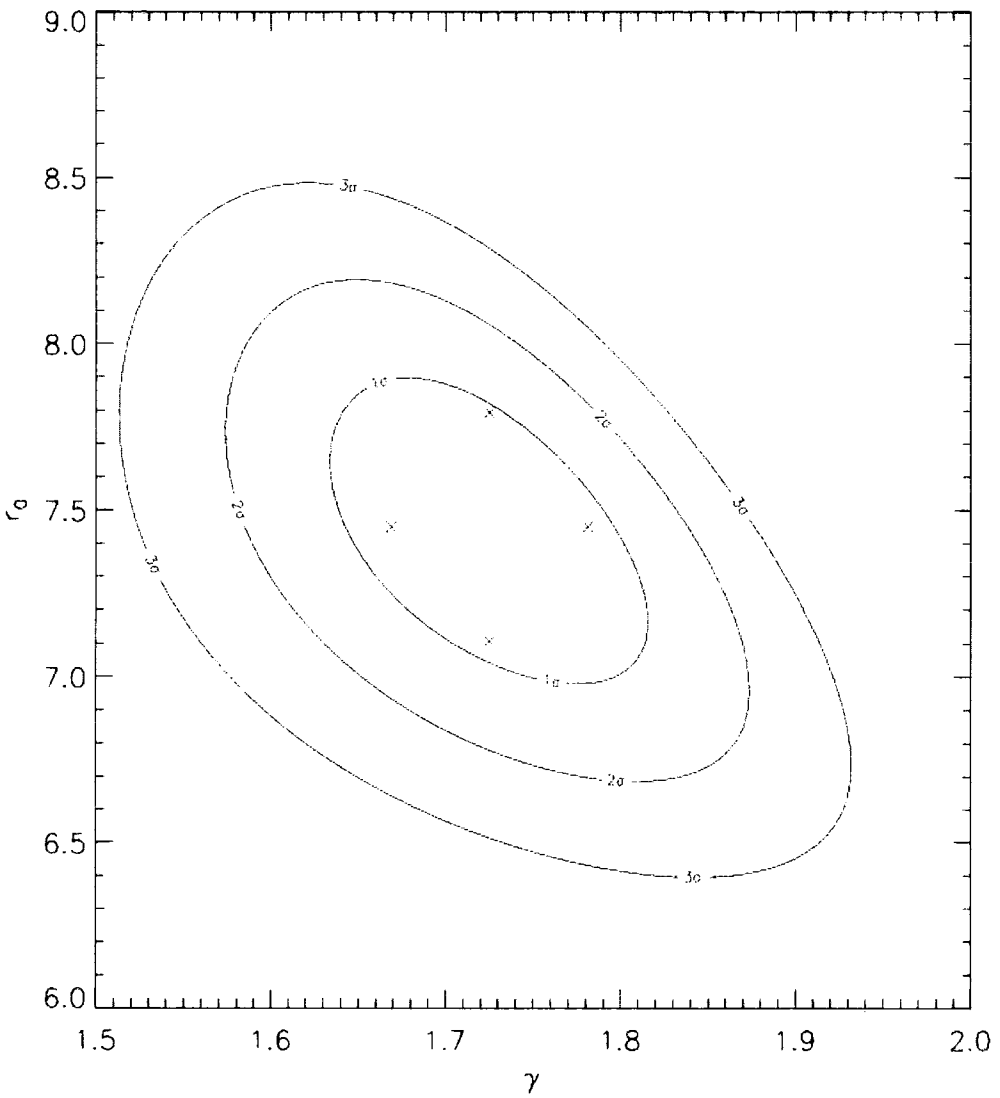

Figure 3.11: The $\delta\chi^2$ likelihoods from the joint 2 parameter fits on r_0 and γ for $\xi(r)$. The contours show the $\delta\chi^2 = (2.3, 6.17, 11.8)$ corresponding to 1, 2 and 3σ. The crosses show the deviations in r_0 and γ that we find from the 32 best-fitting single power-law using the jackknife samples.

3.5 CONCLUSIONS

We have performed a detailed analysis of the clustering of 2SLAQ LRGs in as described by the two-point correlation function. Our main conclusions for this chapter are as follows.

1. The LRG two-point correlation function, $\xi(s)$, averaged over the redshift range $0.4 < z < 0.8$, shows a slope which changes as a function of scale, being flatter on small scales and steeper on large scales, consistent with the well known redshift-space distortions.

2. The best fitting single power-law model to the real-space 2-point correlation function of the 2SLAQ LRG Survey has a clustering length of $r_0 = 7.45 \pm 0.35 \ \ h^{-1}$ Mpc and a power-law slope of $\gamma = 1.72 \pm 0.06$ (assuming a Λ cosmology) showing LRGs to be highly clustered objects.

3. Evidence for a change in the slope of the projected correlation function, which is a prediction of halo occupation distribution (HOD) models, is seen in the 2SLAQ LRG survey results, while a stronger feature is observed in the angular correlation function of the LRGs. A direct explanation for this remains unclear.

Now armed with our best-fitting single power-law model for $\xi(r)$, and we can proceed and see if modelling the redshift-space distortions introduced into the clustering pattern reveals anything about cosmological parameters.

CHAPTER 4

2SLAQ LRG REDSHIFT-SPACE DISTORTIONS

Altaira: Where have you been? I've beamed and beamed.

Robby: Sorry, miss. I was giving myself an oil-job.

Altaira: Robby, I must have a new dress, right away.

Robby: Again?

Altaira: Oh, but this one must be different! Absolutely nothing must show - below, above or through.

Robby: Radiation-proof?

Altaira: No, just eye-proof will do.

- Forbidden Planet, *1956*.

In this chapter, we study further the clustering properties of the redshift $z = 0.55$ 2SLAQ Luminous Red Galaxies, in particular the dynamical and geometric redshift-space distortions that are apparent in the clustering signal. We also test a simple "high-peaks" bias model to see if 2SLAQ LRGs have clustering properties consistent with massive early-types seen at lower, $z \approx 0.1$ redshifts.

4.1 LRG CLUSTERING AND COSMOLOGICAL IMPLICATIONS

Having calculated the z-space, projected and real-space correlation functions for the 2SLAQ Luminous Red Galaxies, we can now turn our attention to using these results to see if we can determine cosmological parameters.

4.1.1 THE $\xi(\sigma, \pi)$ LRG MEASUREMENTS

Results for the 2-D clustering of 2SLAQ LRGs are shown in the $\xi(\sigma, \pi)$ plots of Figures 4.1 and 4.2.

Galaxy peculiar velocities lead to distortions in the $\xi(\sigma, \pi)$ shape. The predominant effect on large scales in σ is the coherent infall that causes a flattening of the $\xi(\sigma, \pi)$ contours along the parallel π direction and some elongation along the perpendicular σ direction. At small σ, the random peculiar motions of the galaxies cause an elongation of the clustering signal along the π direction - the so-called "Fingers-of-God" effect. From the measurements of these effects, a determination of the coherent infall into clusters, given by the parameter β, and the pairwise velocity dispersion, $\langle w_z^2 \rangle^{1/2}$, can be made. This calculation shall be performed in Section 4.1.2. Geometric distortions also occur if the cosmology assumed to convert the observed galaxy redshifts is not the same as the true, underlying cosmology of the Universe. The reason for this is because the cosmology dependence of the separations along the redshift direction is not the same as for the separations measured in the perpendicular direction (Alcock & Paczynski, 1979). We note that modelling the geometric distortions and comparing to the presented data can yield information on cosmological parameters.

We shall closely follow the methods of Hoyle et al. (2002) and da Ângela (2005), hereafter H02 and dA05, respectively. In this section, we first discuss large-scale, linear and small-scale

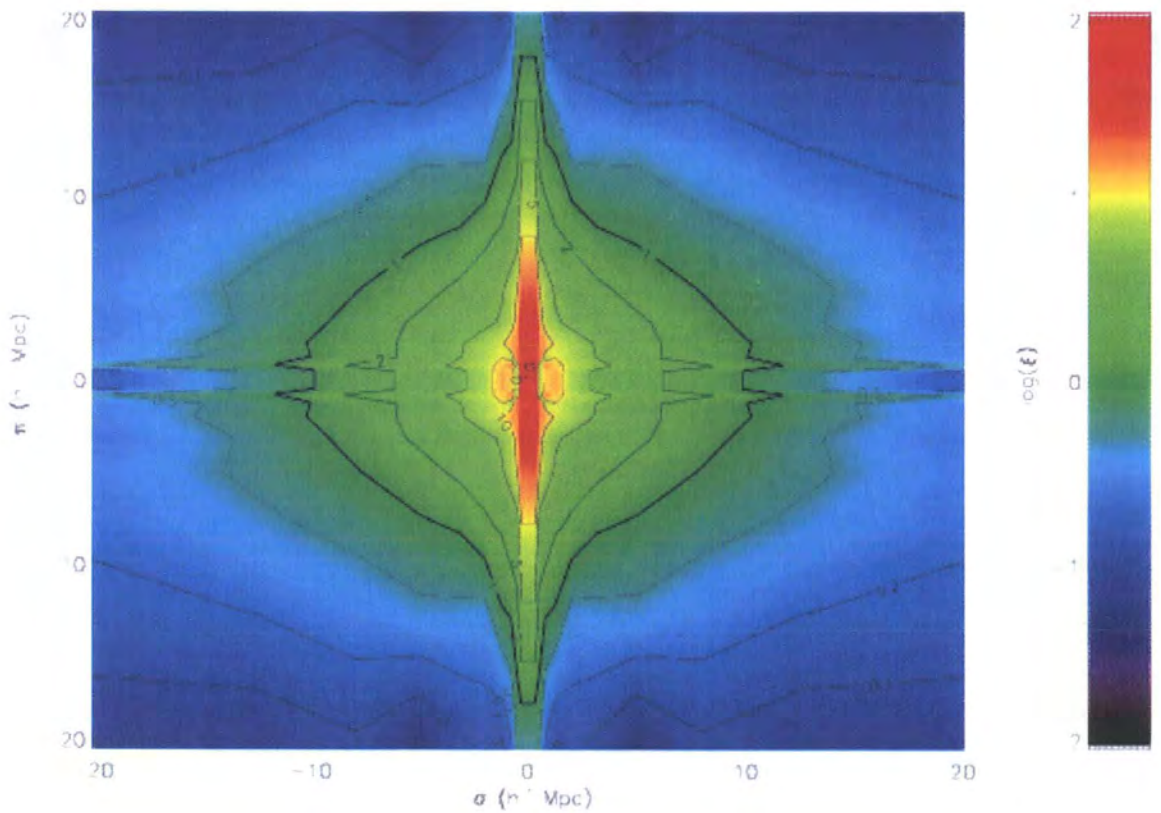

Figure 4.1: The $\xi(\sigma, \pi)$ contour plot for the 2SLAQ LRG Survey, assuming a Λ cosmology of $(\Omega_{\rm m}, \Omega_\Lambda) = (0.3, 0.7)$. The "Finger-of-God" effects, i.e. elongation of contours in the π direction at small ($\lesssim 1\ h^{-1}$ Mpc) scales, is seen. (The spikes at small π are plotting artifacts).

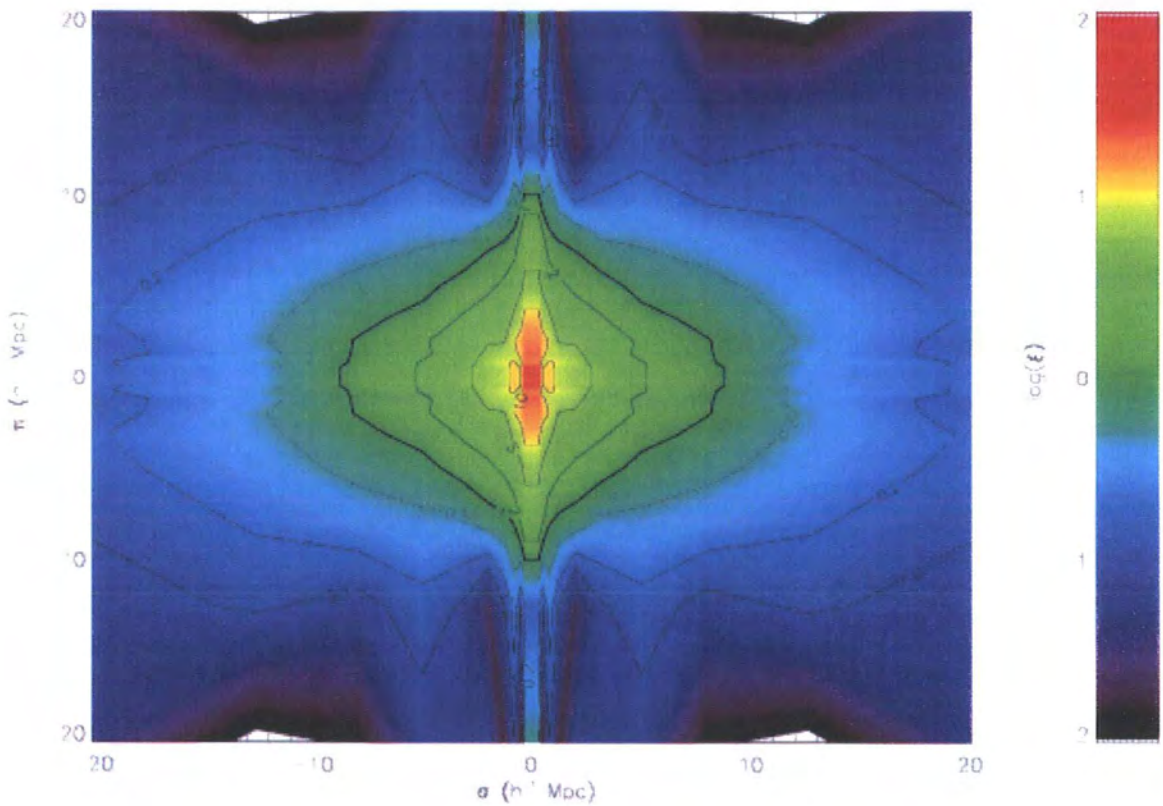

Figure 4.2: The $\xi(\sigma, \pi)$ contour plot for the 2SLAQ LRG Survey, with a $\Omega_{\rm m} = 1.0$, EdS cosmology.

non-linear z-space distortions and how they are parameterised by β and $\langle w_z^2 \rangle^{1/2}$ respectively. We then use β to find the bias of LRGs at the survey redshift. Next, we employ information gained in studying the geometric distortions to perform the "Alcock-Paczynski Test" as one route to calculating cosmological parameters. However, there is a degeneracy in the $(\beta, \Omega_{\rm m})$ plane with this approach and thus we employ further constraints from the evolution of LRG clustering to break this degeneracy.

4.1.2 REDSHIFT-SPACE DISTORTIONS, β AND PAIRWISE VELOCITIES

When measuring a galaxy redshift, one is actually measuring a sum of velocities.* The total velocity comes from the Hubble expansion plus the motion induced by the galaxy's local potential, where this second term is coined the "peculiar velocity", i.e.

$$v_{\rm Tot} = v_H + v_{\rm pec} \tag{4.1}$$

The peculiar velocity itself contains two terms,

$$v_{\rm pec} = v_{\rm rand} + v_{\rm CI} \tag{4.2}$$

The first term, $v_{\rm rand}$ is due to the small-scale random motion of galaxies within clusters. The second term, $v_{\rm CI}$ is the component due to coherent infall around clusters, where the infall is caused by the streaming of matter from underdense to overdense regions; this leads to a "flattening" in the perpendicular σ-direction away from equi-distant contours in $\xi(\sigma, \pi)$. This extension is parameterised by β, which takes into account the large-scale effects of linear z-space distortions. Kaiser (1987) showed that, assuming linear perturbation theory, and a pure power-law model for the real-space correlation function (which is fair for the 2SLAQ LRG data), one

*This section strongly follows Hawkins et al. (2003) and Croom et al. (2005).

can estimate β in the linear regime using (Hamilton, 1992),

$$\xi(s) = \xi(r)\left(1 + \frac{2}{3}\beta + \frac{1}{5}\beta^2\right). \tag{4.3}$$

and more generally

$$\xi(\sigma,\pi) = \left[1 + \frac{2(1-\gamma\mu^2)}{3-\gamma}\beta + \frac{3 - 6\gamma\mu^2 + \gamma(2+\gamma)\mu^4}{(3-\gamma)(5-\gamma)}\beta^2\right]\xi(r), \tag{4.4}$$

where μ is the cosine of the angle between r and π (the distance along the line of sight), and γ is slope of the power law (Matsubara & Suto, 1996).

Even though the "Kaiser Limit" is a widely used method for estimating β, the drawbacks in using this approach, under the assumption of Gaussianity, have been known for some time (Hatton & Cole, 1998). Scoccimarro (2004) has recently reported on the limitations of assuming a Gaussian distribution in the pairwise velocity dispersion even on very large scales. Scoccimarro's argument is that even at large scales, linear theory cannot be applied since one still has the effect of galactic motions induced on sub-halo scales i.e. galaxies that are separated by very large distances are still "humming" about inside their own dark matter haloes. Thus for the remainder of the paper, we make a note of the new formalism in Scoccimarro (2004), but continue to use the Kaiser limit, acknowledging its short-comings. We justify this by noting that we need better control on our '1st order' statistical and systematic errors before applying the '2nd order' Scoccimarro corrections. Future analysis may use the 2SLAQ LRG and QSO sample to make comparisons for small and large scale effects in the redshift distortions using both the new Scoccimarro expression as well as the Kaiser limit.

The small-scale random motions of the galaxies, $v_{\rm rand}$, leads to an extension in the parallel π-direction of $\xi(\sigma,\pi)$. We denote the magnitude of this extension by $\langle w_z^2\rangle^{1/2}$, the rms pairwise

line-of-sight velocity dispersion, which can be expressed in a Gaussian form (e.g. dA05)

$$f(w_z) = \frac{1}{\sqrt{2\pi}\langle w_z^2\rangle^{1/2}} \exp\left(-\frac{1}{2}\frac{|\mathrm{w_z}|}{\langle \mathrm{w_z^2}\rangle^{1/2}}\right). \tag{4.5}$$

Now we can combine these small-scale non-linear z-space distortions with the Kaiser formulae, and hence the full model for $\xi(\sigma, \pi)$ is given by

$$\xi(\sigma, \pi) = \int_{-\infty}^{\infty} \xi'[\sigma, \pi - w_z(1+z)/H(z)] f(w_z) dw_z \tag{4.6}$$

where $\xi'[\sigma, \pi - w_z(1+z)/H(z)]$ is given by equation 4.4 and $f(w_z)$ by equation 4.5. Using these expressions and our 2SLAQ LRG data, we can calculate β and $\langle w_z^2\rangle^{1/2}$ for the LRGs. At this juncture, it is important to note the scales we consider in our model. As can be seen from the data presented in Section 3, a power-law fits the data best on scales from 1 to 20 h^{-1} Mpc. Thus, when computing the full model for $\xi(\sigma, \pi)$ (equation 4.6), we only use data with $1 < \sigma < 20$ h^{-1} Mpc and $1 < \pi < 20$ h^{-1} Mpc (as shown in Figures 4.1 and 4.2).

Returning to Kaiser (1987), the value of β can be used to determine the bias, b, of the objects in question,

$$\beta \simeq \frac{\Omega_{\mathrm{m}}^{0.6}}{b} \tag{4.7}$$

provided you know the value of Ω_{m}, where $\Omega_{\mathrm{m}}(z)$ is given by

$$\Omega_{\mathrm{m}}(z) = \frac{\Omega_{\mathrm{m}}^0 (1+z)^3}{\Omega_{\mathrm{m}}^0 (1+z)^3 + \Omega_{\Lambda}^0}, \tag{4.8}$$

for a flat universe. The importance of the bias is that it links the visible galaxies to the underlying (dark) matter density fluctuations,

$$\delta_g = b \ \delta_m \tag{4.9}$$

where the g and the m subscripts stand for galaxies and mass respectively. From this, $\xi_g = b^2 \ \xi_m$, where we are restricting our attention to the case of linear and deterministic bias.

Equipped with these calculations we now go about determining the mentioned cosmological parameters.

4.1.3 COSMOLOGICAL PARAMETERS FROM $\xi(\sigma, \pi)$ MODELS.

The ratio of observed angular of a fixed sacle size to radial size varies with cosmology. If we have a standard ruler which is known to be isotropic, i.e. where transverse and radial intrinsic size are the same, fixing the ratio of the intrinsic radial and transverse distances yields a relation between the measured radial and transverse distances depending on cosmological parameters. This comparison is often called the "Alcock-Paczynski" test (Alcock & Paczynski 1979; Ballinger, Peacock & Heavens 1996). In order to perform this test, we assume galaxy clustering is, on average, isotropic and we compare data and model cosmologies. Following H02 and dA05, for the following sections, we define several terms.

(i) The Underlying cosmology - this is the true, underlying, unknown cosmology of the Universe.

(ii) The Assumed cosmology - the cosmology used when measuring the two-point correlation function and $\xi(\sigma, \pi)$ from the 2SLAQ LRG survey. Initially in a redshift survey, the only information available is the object's position on the sky and its redshift. In order to convert this into a physical separation, you must assume some cosmology. As was mentioned earlier, we have considered two Assumed cosmologies, the Λ ($\Omega_{\rm m}$, Ω_Λ) = (0.3,0.7) and the EdS ($\Omega_{\rm m}, \Omega_\Lambda$) = (1.0,0.0) cases.

(iii) The Test Cosmology - the cosmology used to generate the model predictions for $\xi(\sigma, \pi)$ which are then translated into the assumed cosmology.

We compare the geometric distortions in both the data and the model relative to the *same Assumed* cosmology. Thus, the key to this technique lies in the fact that when the Test cosmology matches the Underlying cosmology, the distortions introduced into the clustering pattern should be the same in model as in the data. The model should then provide a good fit to the data, *providing the redshift-space distortions have been properly accounted for.* We can then endeavour to find values of $\Omega_{\rm m}$ and β. We assume that for all further discussions, the cosmologies described are spatially flat and choose to fit the variable $\Omega_{\rm m}^0$, hence fixing $\Omega_\Lambda^0 = 1 - \Omega_{\rm m}^0$.

The relation between the separations σ and π in the Test and Assumed cosmologies (referred to by the subscripts t and a respectively) is the following (Ballinger et al. 1996, HO2, dA05):

$$\sigma_t = f_\perp \sigma_a = \frac{B_t}{B_a}\sigma_a \tag{4.10}$$

$$\pi_t = f_\parallel \pi_a = \frac{A_t}{A_a}\pi_a \tag{4.11}$$

where A and B are defined as follows (for spatially flat cosmologies):

$$A = \frac{c}{H_0}\frac{1}{\sqrt{\Omega_\Lambda^0 + \Omega_{\rm m}^0(1+z)^3}} \tag{4.12}$$

$$B = \frac{c}{H_0}\int_0^z \frac{dz'}{\sqrt{\Omega_\Lambda^0 + \Omega_{\rm m}^0(1+z')^3}}. \tag{4.13}$$

In the linear regime, the correlation function in the assumed cosmology will be the same as the correlation function in the test cosmology, given that the separations are scaled appropriately. i.e.:

$$\xi_t(\sigma_t, \pi_t) = \xi_a(\sigma_a, \pi_a). \tag{4.14}$$

Full details on the fitting procedure are given in H02 (Section 5.1) and dA05 (Section 7.7) and we summarise them here. The fitting procedure that we adopt to find which test cosmology matches the underlying cosmology is as follows:

1) Pick an assumed cosmology (here either the Λ or the EdS cosmology).

2) Calculate $\xi(\sigma, \pi)$ from the data using the assumed cosmology.

3) Pick a value for the test $\beta(\bar{z})$ at the average redshift of the survey.

4) Pick a value of the present day test $\Omega_{\rm m}^0$ for equations 4.12 and 4.13.

5) Generate the model $\xi(\sigma, \pi)$.

6) Translate the model $\xi(\sigma, \pi)$ from the test cosmology into the assumed cosmology using equations 4.10 and 4.11.

7) Calculate how well the model $\xi(\sigma, \pi)$ fits the data $\xi(\sigma, \pi)$ via the χ^2 statistic, using the Jackknife errors from the data $\xi(\sigma, \pi)$ measured in the assumed cosmology.

8) Go back to 3) using a different test cosmology, $\beta(\bar{z})$ and value for the small-scale pairwise velocity $\langle w_{\rm z}^2 \rangle^{1/2}$.

When the parameters $\beta(\bar{z})$ and $\Omega_{\rm m}^0$ match those of the underlying cosmology, the value of χ^2 should be minimised. We note that although the value of $\langle w_{\rm z}^2 \rangle^{1/2}$ is allowed to vary, we find that the minimum χ^2 is least sensitive to this parameter, and hence only present the value, with no formal error, of $\langle w_{\rm z}^2 \rangle^{1/2}$ that gives this minimum χ^2.

We fit the model $\xi(\sigma, \pi)$ to the measured 2SLAQ LRG $\xi(\sigma, \pi)$ over the range of scales $1 < \sigma, \pi < 20\ h^{-1}$ Mpc . This is to try to ensure that any non-linear effects are small and that the errors on $\xi(\sigma, \pi)$ do not dominate the actual value of $\xi(\sigma, \pi)$.

Using this AP-distortion test, we calculate values of $\Omega_{\rm m}$-β for the assumed Λ cosmology and present them in Figure 4.3. We first note that the constraint here is almost entirely on

β rather than $\Omega_{\rm m}$. Using the $\xi(r)$ fit with $r_0 = 7.45\ \ h^{-1}$ Mpc and $\gamma = 1.72$, we find that $\Omega_{\rm m} = 0.10^{+0.35}_{-0.10}$ and $\beta(z = 0.55) = 0.40 \pm 0.05$ with a velocity dispersion of $\langle w_z^2 \rangle^{1/2} = 330 {\rm kms}^{-1}$ from a χ^2 minimization. We have checked these errors by repeating the above calculations on the 32 "jackknife" sub-samples. In order to make the jackknife calculations less computationally intensive, the velocity dispersion is held fixed at 330 km s^{-1} in every case. Comparing the error contours in Fig. 4.3 with the jackknife estimates, we again find that the jackknife errors for β at ± 0.05 are comparable to, if not smaller than, those in the error contours in Fig. 4.3. The jackknife error in $\Omega_{\rm m}$ at ± 0.14 is comparable to the error contour in Fig. 4.3. As in Fig. 3.11, this agreement may be surprising given that we have ignored the covariance between the $\xi(\sigma, \pi)$ points which is almost certainly non-negligible. Again we argue that a relatively poor χ^2 fit at minimum may be responsible, leading to a somewhat fortuitous agreement of the formal and jackknife error. But on the grounds of the jackknife results we believe that the error contours shown in Fig. 4.3 are reasonably realistic and we shall quote these hereafter.

We have also fitted $\xi(\sigma, \pi)$ assuming an EdS cosmology. In principle this should give the same result as assuming the Λ model. We show these $\Omega_{\rm m} - \beta$ fits in Figure 4.4. We find that the best fit is now $\Omega_{\rm m}^0 = 0.40^{+0.6}_{-0.25}$ and $\beta(z = 0.55) = 0.45^{+0.20}_{-0.10}$ (χ^2 minimization) with a velocity dispersion of $\langle w_z^2 \rangle^{1/2} = 330 {\rm kms}^{-1}$. A model with $\gamma = 1.67$ and a (starting) correlation length of $r_0 = 5.65\ \ h^{-1}$ Mpc is used. Thus the β and the velocity dispersion values are reasonably consistent with the previous result. However, the value of $\Omega_{\rm m}$ assuming an EdS cosmology, is somewhat higher than the best-fit found assuming a Λ cosmology. We assume that the high degeneracy of $\Omega_{\rm m}$ coupled with slightly different $\xi(r)$ models in the two cases is causing this slight discrepancy. The contours in Fig. 4.4 certainly suggest that the constraint on $\Omega_{\rm m}$ is much less strict in the EdS assumed case.

r_0	γ	range / h^{-1} Mpc	Measure	Ω_m	β	$\langle w_z^2 \rangle^{1/2}$/ km s^{-1}
7.45	1.72	0.4-70	$\xi(r)$	0.10	0.40	330
7.30	1.83	0.4-70	$w_p(\sigma)$	0.02	0.40	360
7.60	1.68	0.4-20	$\xi(r)$	0.10	0.35	300
7.34	1.80	0.4-20	$w_p(\sigma)$	0.10	0.45	360

Table 4.1: Best fitting model values of Ω_m, β and pairwise velocity dispersion, $\langle w_z^2 \rangle^{1/2}$, using redshift-space distortions alone and assuming a Λ cosmology. The third column gives the range of pair separations used in the fit.

We have investigated other systematics in the $\Omega_m - \beta$ fits. Returning to an assumed Λ cosmology, there is some small dependence on the model assumed for $\xi(r)$. For example, if the slope $\gamma = 1.69$ from fitting $\xi(r)$ in the more limited range $0.4 < r < 20 h^{-1}$Mpc is assumed then we find that $\Omega_m = 0.10 \pm 0.29$ and $\beta(z = 0.55) = 0.35 \pm 0.16$ with a velocity dispersion of $\langle w_z^2 \rangle^{1/2} = 300$kms^{-1}. Further, if instead of using $\xi(r)$, $w_p(\sigma)$ is used with slope $\gamma = 1.83$ over the usual $0.4 < r < 70\ \ h^{-1}$ Mpc range, we find that the best-fit model prefers a very low value of $\Omega_m = 0.02 \pm 0.15$ and $\beta(z = 0.55) = 0.40 \pm 0.05$ with a velocity dispersion of $\langle w_z^2 \rangle^{1/2} = 360$kms^{-1}. The consistency of these different models to give values of Ω_m, β and a pairwise velocity dispersion, albeit at a cost of a very loose constraint on Ω_m, is re-assuring and summarised in Table 4.1. Since $w(\theta)$ also seems to indicate a flatter ($\gamma = -1.67 \pm 0.03$) slope in the $1 < r < 20\ \ h^{-1}$ Mpc range of interest for $\xi(\sigma, \pi)$ we take our 'best bet' estimates to be the values for $\gamma = -1.72$ given above. These values also give a good overall fit to $\xi(s)$. We next introduce a further constraint to break the $\Omega_m - \beta$ degeneracy.

4.1.4 Further Constraints on $\Omega_0^{\rm m}$ and $\beta(z)$ from LRG Clustering Evolution

Matsubara & Suto (1996) and Croom & Shanks (1996) pointed out that by combining low redshift and high redshift clustering information, further constraints on $\Omega_{\rm m}$ and Ω_Λ are possible. The basic idea described in this section is that the $\Omega_{\rm m}$:$\beta(z)$ degenerate set obtained from LRG clustering evolution is different from the $\Omega_{\rm m}$:$\beta(z)$ degenerate set obtained from analysing LRG redshift-space distortions; by using these two constraints in combination, the degeneracies may be lifted. Thus the way we proceed to break the degeneracy is to combine our current 2SLAQ LRG results with constraints derived from consideration of LRG clustering evolution.

From the value of the mass correlation function at $z = 0$, linear perturbation theory can be used, assuming a test $\Omega_{\rm m}$, to compute the value of the mass correlation function in real space at $z = 0.55$. This can then be compared to the measured LRG $\xi(r)$ at $z = 0.55$ to find the value of the bias $b(z = 0.55)$. The clustering of the mass at $z = 0$ can be determined if the galaxy correlation function is known, assuming that the bias of the galaxies used, $b(z = 0)$, is independent of scale. Fortunately, recent galaxy redshift surveys have obtained precise measurements of the clustering of galaxies at $z \approx 0$. In practice we shall start from $\xi(s)$ at $z = 0$ and $z = 0.55$ and use equation 4.3 to derive $\xi(r)$ in each case.

We therefore follow da Ângela et al. (2005) and start by introducing the volume averaged two-point correlation function $\bar{\xi}$ where

$$\bar{\xi}^s = \frac{\int_0^s 4\pi s'^2 \xi(s') ds}{\int_0^s 4\pi s'^2 ds}. \tag{4.15}$$

We do this so that non-linear effects in the sample should be insignificant due to the s^2 weighting, setting the upper limit of the integral $s = 20\ h^{-1}$ Mpc. To calculate equation 4.15 at $z = 0$, we use the double-power law form that is found by the 2dFGRS to describe $\xi(s)$ (Hawkins et al.,

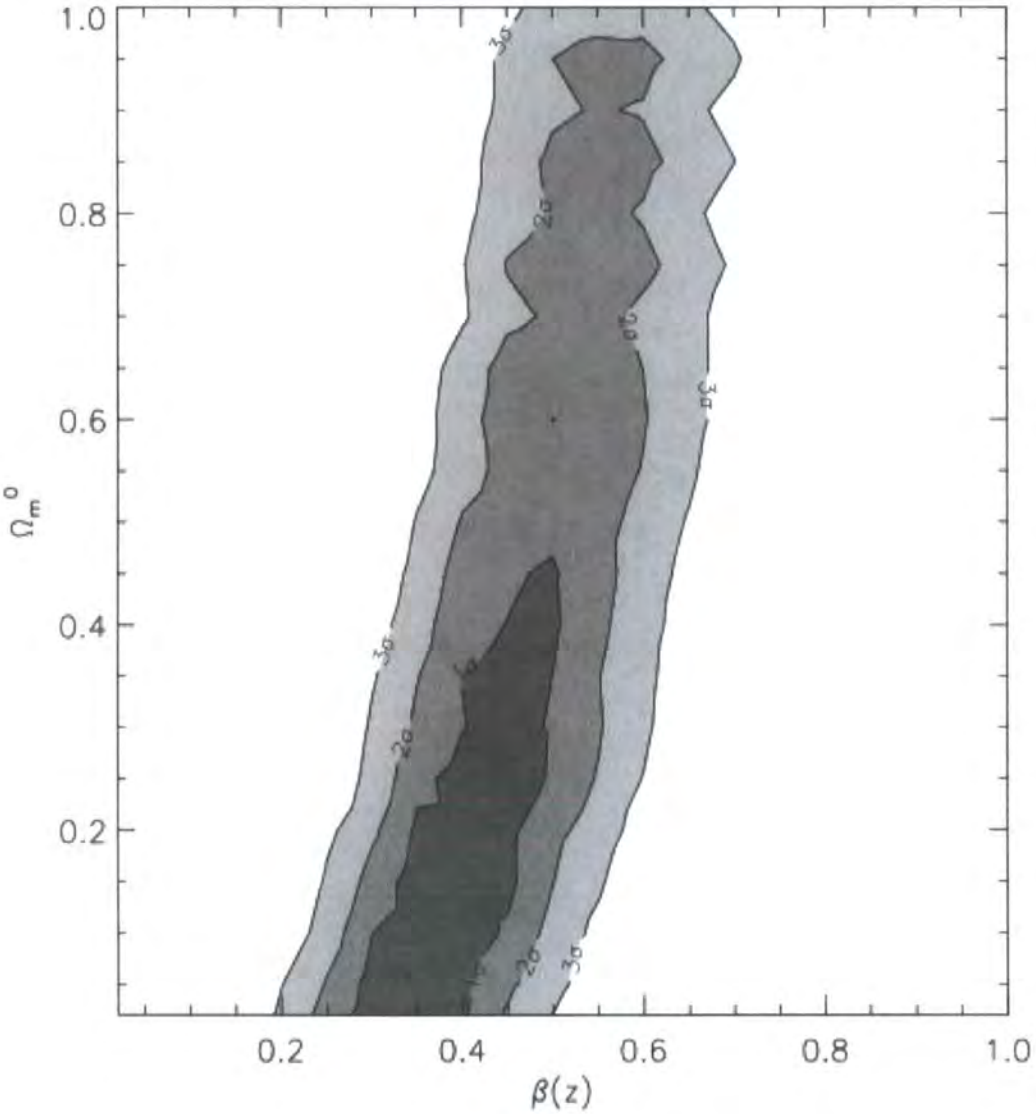

Figure 4.3: Likelihood contours of $\Omega_{\rm m}^0$-$\beta(z = 0.55)$ using the geometric method of Alcock-Paczynski test and modelling the redshift-space distortions. The best-fit values are $\Omega_{\rm m} = 0.10^{+0.35}_{-0.10}$ and $\beta(z = 0.55) = 0.40 \pm 0.05$ with a velocity dispersion of $\langle w_z^2 \rangle^{1/2} = 330 {\rm kms}^{-1}$. Note how a value of $\Omega_{\rm m} \sim 0.3$ is not ruled out but also the large degeneracy along the $\Omega_{\rm m}$ direction. A Λ cosmology is assumed, along with a model where $\gamma = 1.72$ and a (starting) value of $r_0 = 7.45\ h^{-1}$ Mpc.

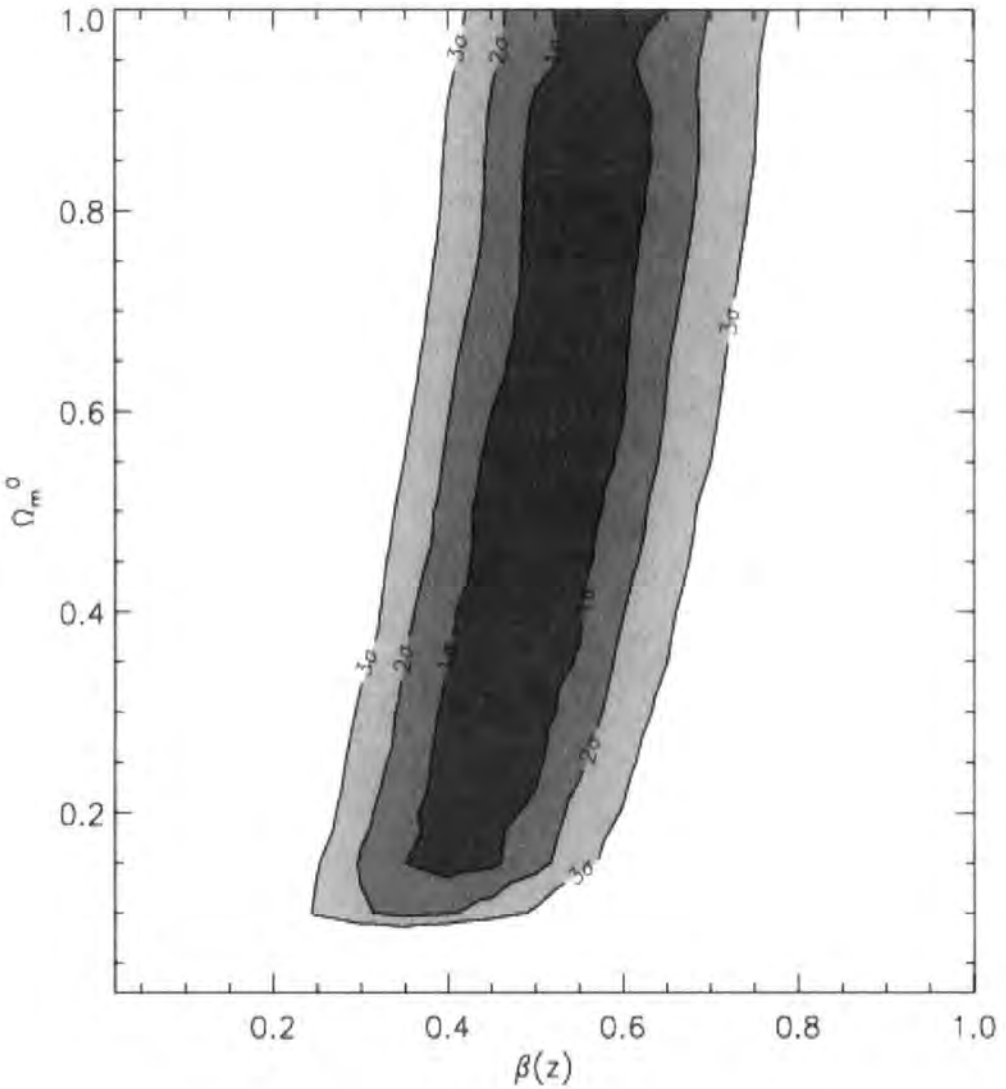

Figure 4.4: Likelihood contours of $\Omega_{\rm m}^0$-$\beta(z = 0.55)$ using the geometric method of Alcock-Paczynski test and modelling the redshift-space distortions, assuming an EdS cosmology. The best-fit values are $\Omega_{\rm m} = 0.40^{+0.60}_{-0.25}$ and $\beta = 0.45^{+0.20}_{-0.10}$ using a model with $\gamma = 1.67$ and a (starting) correlation length of $r_0 = 5.65\ \ h^{-1}$ Mpc. A value of $\Omega_{\rm m} \sim 1.0$ lies within our 1σ contour but again there is a large degeneracy along the $\Omega_{\rm m}$ direction.

2003, Fig. 6) in the numerator.

Then, the equivalent averaged correlation function in real-space can be determined by

$$\bar{\xi}^r(z=0) = \frac{\bar{\xi}^s(z=0)}{1+\frac{2}{3}\beta(z=0)+\frac{1}{5}\beta(z=0)^2} \tag{4.16}$$

where $\bar{\xi}^s$ comes from equation 4.15 and we take the value of β for the 2dFGRS as $\beta(z=0) = 0.49 \pm 0.09$ (Hawkins et al., 2003). Now the real-space mass correlation is obtained with

$$\bar{\xi}^r_{\rm mass}(z=0) = \frac{\bar{\xi}^r(z=0)}{b(z=0)^2}, \tag{4.17}$$

where $b(z=0)$ is given for each test cosmology by

$$b(z=0) = \frac{\Omega_{\rm m}^{0.6}(z=0)}{\beta(z=0)^2}. \tag{4.18}$$

Once we have determined the real-space correlation function of the mass at $z=0$, its value at $z=0.55$ is obtained using linear perturbation theory. Hence, at $z=0.55$, the real-space correlation function of the mass will be:

$$\bar{\xi}^r_{\rm mass}(z=0.55) = \frac{\bar{\xi}^r_{\rm mass}(z=0)}{G(z=0.55)^2}, \tag{4.19}$$

Here, $\bar{\xi}^r_{\rm mass}$ is the volume-averaged correlation function (with $1 < r < 20\ \ h^{-1}$ Mpc) and $G(z)$ is the growth factor of perturbations, given by linear theory and depends on cosmology, in this case the test cosmology (Carroll et al., 1992; Peebles, 1984).

Once the value of $\bar{\xi}^r_{\rm mass}(z=0.55)$ is obtained for a given test cosmology, the process to find $\beta(z=0.55)$ is similar to the one used to find $\bar{\xi}^r_{\rm mass}(z=0)$, but now the steps are performed in reverse: $\bar{\xi}^s(z=0.55)$ can be measured in a similar way as $\bar{\xi}^s(z=0)$. The bias factor at $z \approx 0.55$ is given by:

$$b^2(z=0.55) = \frac{\bar{\xi}^r(z=0.55)}{\bar{\xi}^r_{\rm mass}(z=0.55)}, \tag{4.20}$$

where $\bar{\xi}^r_{\rm mass}$ is given by equation 4.19 and $\bar{\xi}^r(z=0.55)$ is obtained by:

$$\bar{\xi}^r(z=0.55) = \frac{\bar{\xi}^s(z=0.55)}{1+\frac{2}{3}\beta(z=0.55)+\frac{1}{5}\beta(z=0.55)^2} \tag{4.21}$$

The value of $\beta(z=0.55)$ can then be determined by:

$$\beta(z=0.55) = \frac{\Omega_{\rm m}(z=0.55)^{0.6}}{b(z=0.55)}, \tag{4.22}$$

where $b(z=0.55)$ is given by equation 4.20 and $\Omega_{\rm m}(z=0.55)$ is the value of the matter density at $z=0.55$, given by equation 4.8 for a flat universe. In the end, for a given value of $\Omega^0_{\rm m}$ in the test cosmology, $\beta(z)$ will be obtained by solving a second order polynomial equation (see Hoyle et al., 2002). The confidence levels on the computed values of $\beta(z=0.55)$ can be obtained by considering the errors on this calculation. These errors are estimated by identifying the factors that contribute to the error, and adding the components in quadrature. Here, the components contributing to the error on $\beta(z=0.55)$ are $\beta(z=0)$, $\bar{\xi}^s(z=0)$ and $\bar{\xi}^s(z=0.55)$.

Using this evolution of clustering method produces constraints on the $\Omega_{\rm m}$-β plane that break the degeneracies found when modelling the redshift-space distortions alone. We can now work out the joint-2 parameter best fitting regions. This is shown in Figure 4.5, where the 1, 2 and 3 sigma error bars are plotted (dashed lines). When we consider the 1-sigma error on each quantity separately we find, $\Omega_{\rm m} = 0.25^{+0.10}_{-0.15}$, $\beta = 0.45 \pm 0.05$ with a $\langle w_z^2 \rangle^{1/2}$ of 330kms^{-1}. A model $\xi(r)$ is assumed with $\gamma = 1.72$ and $r_0 = 7.45\ \ h^{-1}$ Mpc, as is a Λ cosmology.

The case of the combined constraint for the EdS assumed cosmology is shown in Figure 4.6. The $\xi(r)$ model with $\gamma = 1.67$ and $r_0 = 5.65\ \ h^{-1}$ Mpc is assumed and we find $\Omega_{\rm m} = 0.35 \pm 0.15$ and $\beta = 0.45 \pm 0.05$. Although the 3-sigma contours still reject the EdS model, the rejection is less than in the Λ assumed case. Overall we conclude that the combined constraints on β are the strongest with $\beta = 0.45 \pm 0.05$ consistently produced whatever the assumed cosmology or

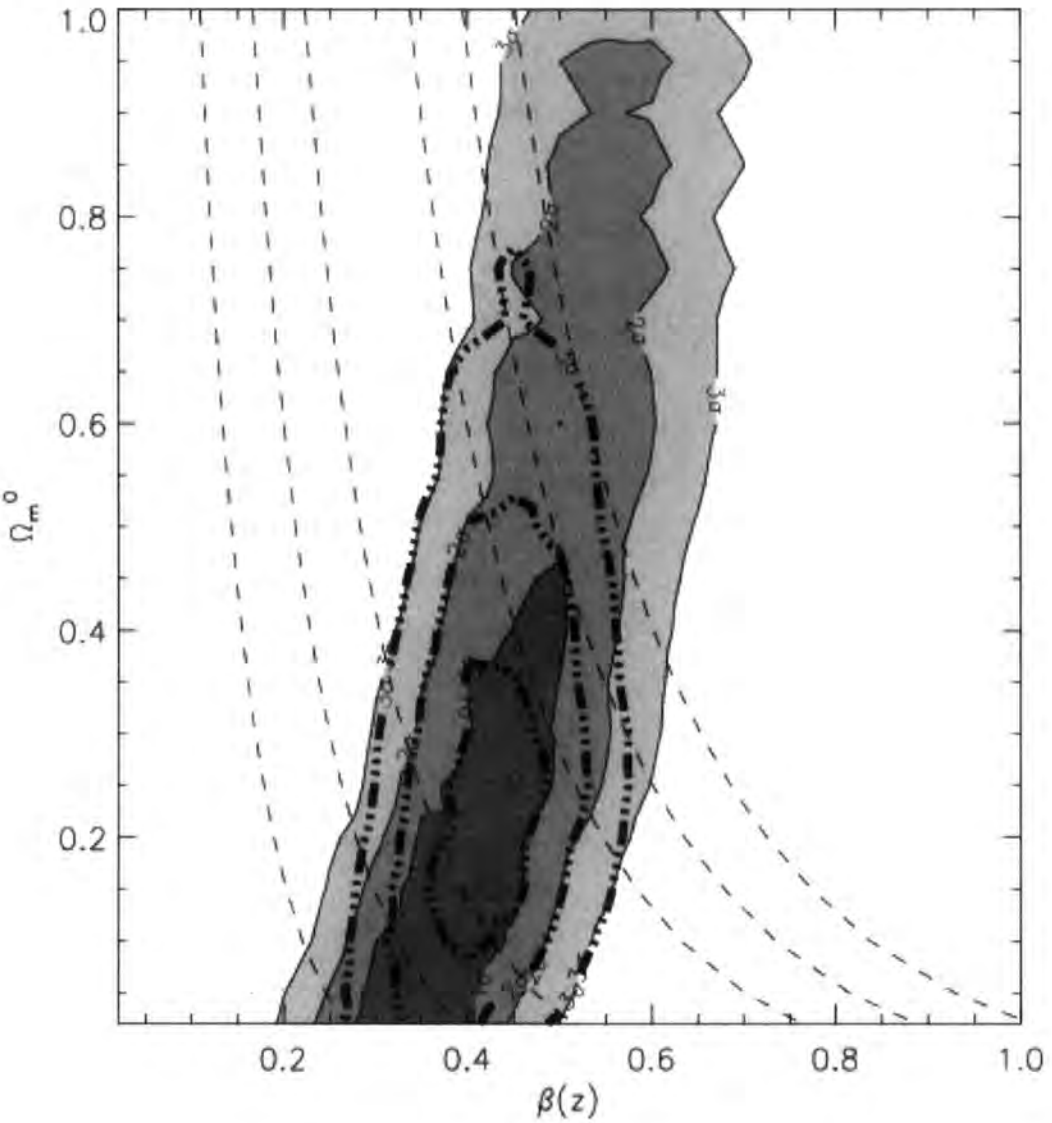

Figure 4.5: Joint likelihood contours of Ω_m^0-$\beta(z = 0.55)$ using the geometric method of Alcock-Paczynski test, modelling the redshift-space distortions and including the evolution of clustering constraints, assuming the Λ cosmology. The solid regions are the likelihood contours as given in Figure 4.3, while the thin dashed lines are the likelihood contours from the evolution of clustering constraints. The joint-constraint best-fit values are given by the thick dot-dashed lines and are $\Omega_m = 0.25^{+0.10}_{-0.15}$, $\beta = 0.45 \pm 0.05$ (marked with the cross) with a $\langle w_z^2 \rangle^{1/2}$ of $330 \mathrm{kms}^{-1}$.

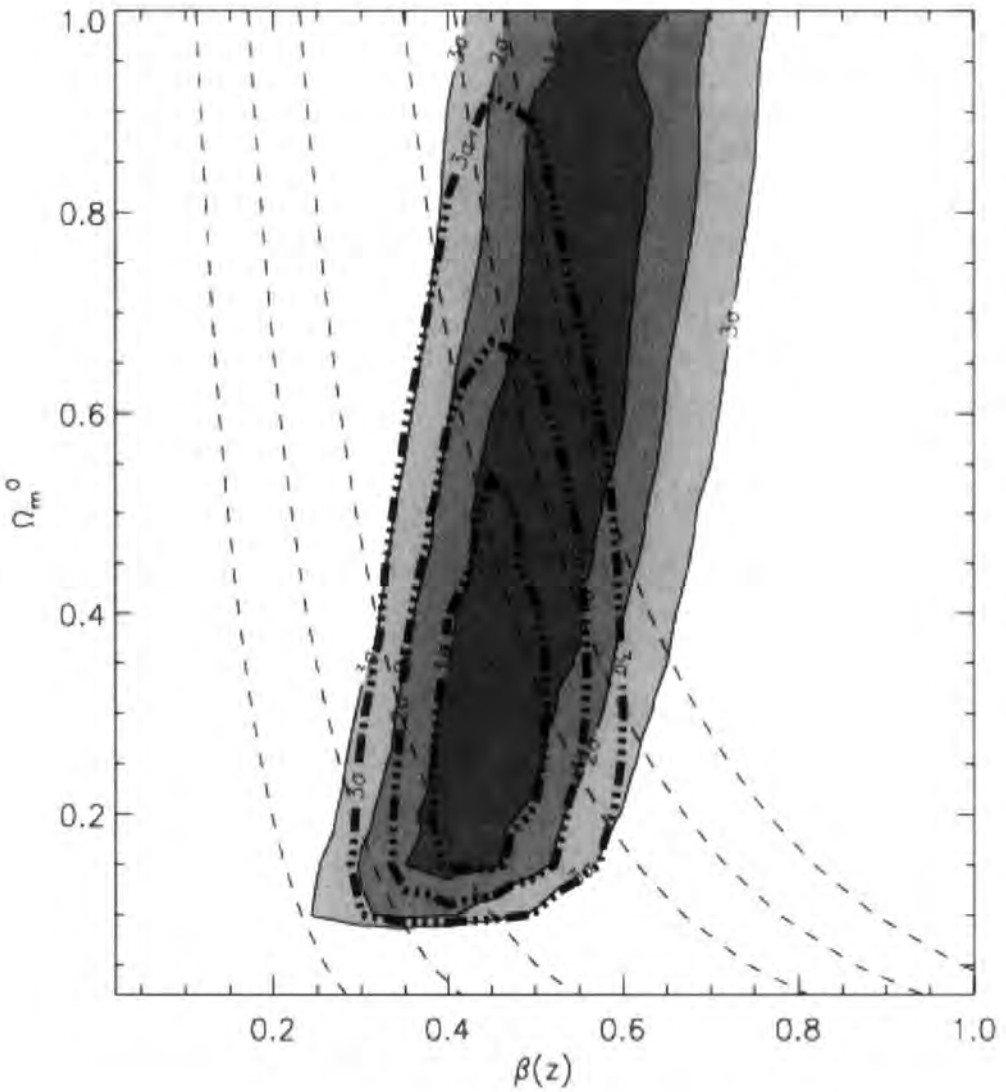

Figure 4.6: Joint likelihood contours for $\Omega_{\rm m}^0$-$\beta(z = 0.55)$ using the geometric method of Alcock-Paczynski test, modelling the redshift-space distortions and including the evolution of clustering constraints, assuming an EdS cosmology. The joint best-fit has $\Omega_{\rm m} = 0.35 \pm 0.15$, $\beta = 0.45 \pm 0.05$ (marked with the cross) and a $\langle w_z^2 \rangle^{1/2}$ of 330kms^{-1}. When the joint constraints are considered, a value of $\Omega_{\rm m} = 1.0$ can be ruled out at the 3σ level.

$\xi(r)$ model. Though the combined constraints on $\Omega_{\rm m}$ are less strong and give $\Omega_{\rm m} \approx 0.3 \pm 0.15$, they still appear consistent with the standard Λ model.

As another check, we can use the ratio $\xi(s)/\xi(r)$ to determine β from equation 4.3 (see Figure 4.7). We assume that β is scale-independent, the z-space distortions are only affected by the large-scale infall and are not contaminated by random peculiar motions. Fitting over the scales, $5 < s < 70\ \ h^{-1}$ Mpc, we find $\beta = 0.47 \pm 0.14$, which is consistent with our determination using the distortions. The 1-σ error comes from a standard χ^2 analysis using the $\xi(s)/\xi(r)$ ratios and their errors; these are derived from adding the jackknife errors on $\xi(s)$ and $\xi(r)$ in quadrature. We note that this procedure does not take into account the non-independence of the correlation function points, suggesting that the relatively large error quoted above on β may still be a lower limit.

The low values of $\Omega_{\rm m} \approx 0.30$ and the value of $\beta = 0.45$ we find from the 2SLAQ LRG survey are in line with what is generally expected in the current standard cosmological model. Although the constraint on β is tight, the constraint on $\Omega_{\rm m}$ is less so and in particular the EdS value is not rejected at 3σ when clustering distortions only are considered. However, when the combined evolution and redshift distortions are considered, the EdS value is rejected at the 3σ level.

Using equation 4.22, $\Omega_{\rm m}(z = 0) = 0.30 \pm 0.15$ and $\beta(z = 0.55) = 0.45 \pm 0.05$, we find that $b(z = 0.55) = \Omega_{\rm m}(z = 0.55)^{0.6}/\beta(z = 0.55) = 1.66 \pm 0.35$, showing that the 2SLAQ LRGs are highly biased objects. This can be compared with the value inferred for SDSS LRGs at redshift $z = 0.55$ which are found to have a value of $b = 1.81 \pm 0.04$ (Padmanabhan et al. 2006, Fig. 13). The 2SLAQ LRG value is consistent with this SDSS LRG value; of course a slightly lower bias may have been expected for 2SLAQ LRGs due to the higher space density and bluer/lower

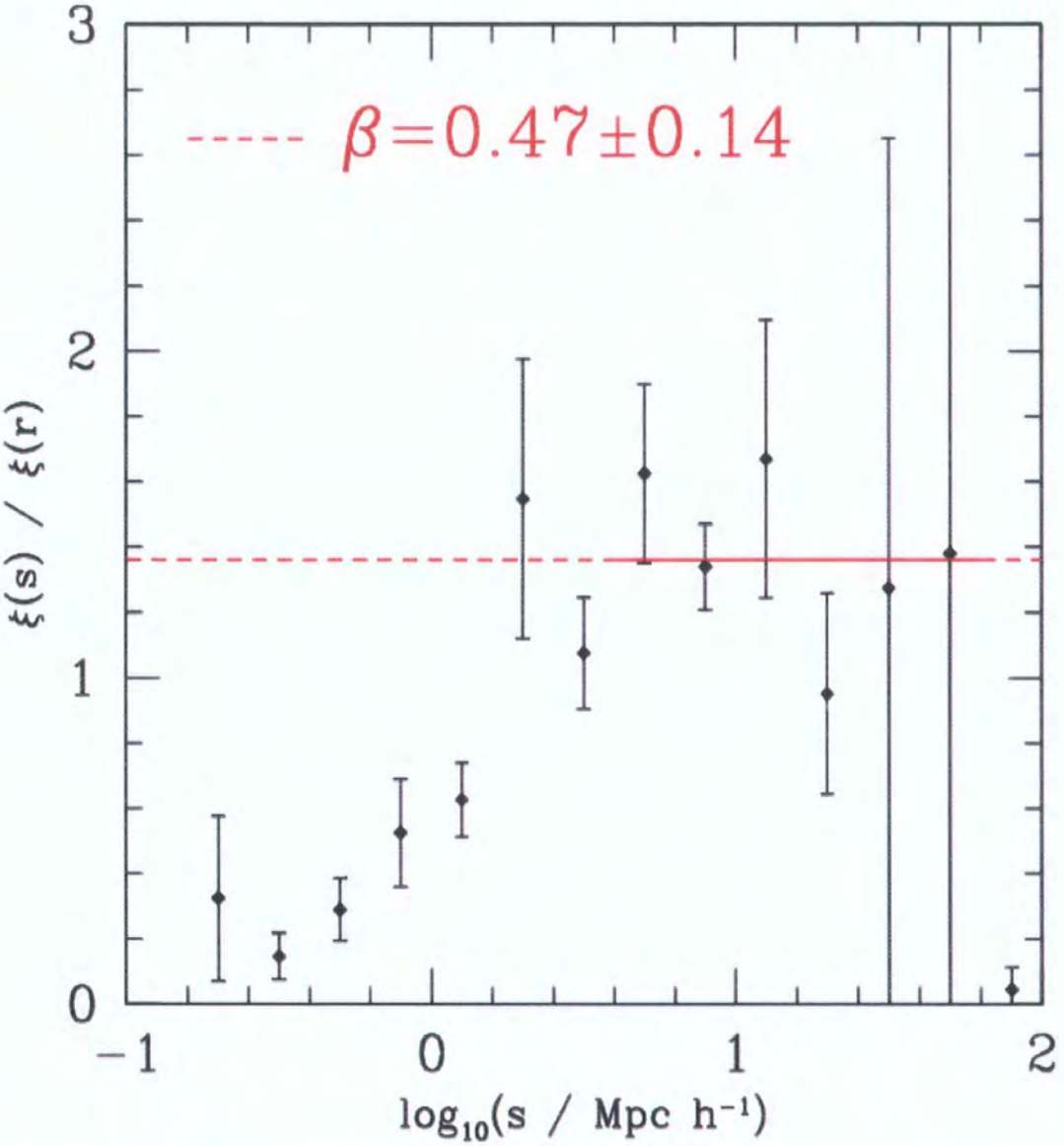

Figure 4.7: The ratio of the redshift-space correlation function to the real-space correlation function, measured from the 2SLAQ LRG survey. We assume a Λ cosmology for these measurements and fitting over the scales of 5 - 70 h^{-1} Mpc find that $\beta = 0.47 \pm 0.14$, in very good agreement with our redshift-space distortion/evolution of clustering technique measurements.

luminosity selection cut. If we assume the value found in recent studies of $\Omega_{\rm m}(z=0)=0.25$ (Cole et al., 2005; Eisenstein et al., 2005; Tegmark et al., 2006; Percival et al., 2006a,b), then our estimate of b becomes $b=1.56\pm0.33$.

Although we leave discussion about the bias estimate and the accuracy of the β-model to future investiagtion, we do compare the non-linear mass correlation function as numerically calculated for the standard cosmology (Colín et al., 1999) to the 2SLAQ LRG $\xi(r)$, in Figure 3.10. The errors in $\xi(\sigma,\pi)$ are smaller at separations 5 to 20 h^{-1} Mpc, than at 1 h^{-1} Mpc, so our estimates of bias from $\xi(\sigma,\pi)$ are weighted towards these larger scales. Even so, there appears to be evidence for potential scale-dependent bias with the relative amplitudes of $\xi_{\rm mass}$ and $\xi(r)$ in Fig. 3.10. Once again, we leave more detailed investigations into this issue to a future project.

Finally, taking the value of $b(z=0.55)=1.66\pm0.35$, we can relate $b(z=0)$ to $b(0.55)$ using the bias evolution model (Fry, 1996)

$$b(z)=1+[b(0)-1]G(\Omega_{\rm m}(0),\Omega_\Lambda(0),z), \tag{4.23}$$

where $G(\Omega_{\rm m}(0),\Omega_\Lambda(0),z)$ is the linear growth rate of the density perturbations (Peebles, 1980, 1984; Carroll et al., 1992). There are many other bias models, but here we are making the simple assumptions that galaxies formed at early times and their subsequent clustering is governed purely by their discrete motion within the gravitational potential produced by the matter density perturbations. This model would be appropriate, for example, in a "high-peaks" biasing scenario where early-type galaxies formed at a single redshift and their co-moving space density then remained constant to the present day. There may be evidence for such a simple evolutionary history in the observed early-type stellar mass/luminosity functions (e.g. Metcalfe et al., 2001; Brown et al., 2006; Wake et al., 2006). From equation 4.23, and taking $b(0.55)=1.66$, implies a value today of $b(0)=1.52$ at $z\sim0.1$. This leads to a predicted

correlation length today of $r_0(z = 0) = 8.5 \pm 1.6 \ \ h^{-1}$ Mpc (assuming ΛCDM) which is consistent with the value of $r_0 = 8.0 \pm 1.0 \ \ h^{-1}$ Mpc found earlier from the luminosity matched luminous early-type sample from the 2dFGRS.

Therefore, these correlation function evolution results suggest that there seems to be no inconsistency with the idea that the LRGs have a constant co-moving space density, as may be suggested by the luminosity function results. But, we note that the LF results of Wake et al. (2006) apply to a colour-cut sample, (where 2SLAQ LRGs are carefully matched to SDSS LRGs) whereas our clustering results are only approximately matched to the 2dFGRS. It will be interesting to see if this results holds when the clustering of the exactly matched high and low redshift LRGs are compared (see Wake et al., 2007, in prep.).

4.2 CONCLUSIONS

In this chapter, we have performed a detailed analysis of the redshift-space distortions apparent in the clustering signal of the 2SLAQ LRGs. Our main conclusions for this chapter are as follows.

1. From redshift distortion models and the geometric Alcock-Paczynski test we find $\Omega_{\rm m} = 0.10^{+0.35}_{-0.10}$ and $\beta(z = 0.55) = 0.40 \pm 0.05$ with a velocity dispersion of $\langle w_z^2 \rangle^{1/2} = 330 {\rm kms}^{-1}$, assuming a Λ cosmology. With EdS as the assumed cosmology, $\Omega_{\rm m} = 0.40^{+0.60}_{-0.25}$ and $\beta = 0.45^{+0.20}_{-0.10}$ with the best-fitting velocity dispersion remaining at $\langle w_z^2 \rangle^{1/2} = 330 {\rm kms}^{-1}$. However, in both cases, we also find a degeneracy along the $\Omega_{\rm mass,0}$-β plane.

2. By considering the evolution of clustering from $z \sim 0$ to $z_{\rm LRG} = 0.55$ we can break this degeneracy and find that $\Omega_{\rm m} = 0.25^{+0.10}_{-0.15}$ and $\beta = 0.45 \pm 0.05$ (with a $\langle w_z^2 \rangle^{1/2}$ of $330 {\rm kms}^{-1}$) assuming a Λ cosmology. When the EdS cosmology is assumed, we find $\Omega_{\rm m} = 0.35 \pm 0.15$ and $\beta = 0.45 \pm 0.05$ (again $\langle w_z^2 \rangle^{1/2} = 330 {\rm kms}^{-1}$). When the joint constraints are considered, a value of $\Omega_{\rm m} = 1.0$ can be ruled out at the 3σ level. We believe these estimates of $\beta(z = 0.55)$ are reasonably robust but the values of $\Omega_{\rm m}$ are more degenerate, although the above estimate (from averaging the 2 cosmologies) of $\Omega_{\rm m} = 0.30 \pm 0.15$ is in agreement with concordance values.

3. If we assume a Λ cosmology with $\Omega_{\rm m}(z = 0) = 0.3$ and $\beta(z = 0.55) = 0.45$ then the value for the 2SLAQ LRG bias at $\bar{z} = 0.55$ is $b = 1.66 \pm 0.35$, in line with other recent measurements of LRG bias (Padmanabhan et al. 2006).

4. Assuming this $b(z = 0.55) = 1.66$ value, and adopting a simple "high-peaks" bias prescription which assumes LRGs have a constant co-moving space density, we predict

$r_0 = 8.5 \pm 1.6\ h^{-1}$ Mpc for LRGs at $z \approx 0.1$. This is not inconsistent with the observed result for luminosity matched 2dFGRS early-type galaxies at this redshift.

The clustering and redshift-space distortion results complement the other results from the 2SLAQ Survey e.g. Wake et al. (2006), Wake et al. (2007, in prep.) and da Angela et al. (2006, in prep). Luminous Red Galaxies may be considered to be "red and dead" but they have recently been realised to be very powerful tools for both constraining galaxy formation and evolution theories as well as cosmological probes. Future projects utilising LRGs (e.g. to measure the baryon acoustic oscillations or to study LRGs at higher redshift/fainter magnitudes) will give us more insights into today's greatest astrophysical problems, including the epoch of massive galaxy formation and the acceleration of the cosmological expansion and this is now where we turn our attention.

CHAPTER 5

THE AAOMEGA-VST *ATLAS* SURVEY

"Mallory, education is the silver bullet. Education is everything. We don't need little changes. We need gigantic, monumental changes. Schools should be palaces. The competition for the best teachers should be fierce. They should be making six figure salaries. Schools should be incredibly expensive for government and absolutely free of charge to its citizens, just like national defense. That's my position. I just haven't figured out how to do it yet."

- Sam Seaborn, *The West Wing*.

This chapter is concerned with Luminous Red Galaxies at redshifts of $z \sim 0.7$. In particular, the motivation and selection techniques that would be used to perform a large, spectroscopic redshift survey over a range of redshifts from $z \sim 0.5$ to 1. The aim of such a survey would be in order to measure the baryon acoustic oscillations at these redshifts, and hence potentially place a constraint on the equation of state parameter, w, and its evolution with redshift.

5.1 MOTIVATION

Large-scale structure (LSS) studies are one road into investigating "Dark Energy" (DE) and its potential evolution (e.g. Blake & Glazebrook, 2003; Seo & Eisenstein, 2003, 2005, 2007; Angulo

et al., 2007). This has been powerfully demonstrated by recent results from the Luminous Red Galaxy (LRG) Sloan Digital Sky Survey (SDSS), (e.g. Eisenstein et al., 2005; Tegmark et al., 2006; Percival et al., 2006a,b) and indeed the 2dFGRS (Cole et al., 2005). Luminous Red Galaxies (LRGs) are predominantly massive early-type galaxies and are intrinsically luminous ($\gtrsim 3L^*$) (Eisenstein et al., 2003; Loh & Strauss, 2006; Wake et al., 2006). They are strongly biased objects, having values of $b \sim 2$, (e.g. the previous chapter; Padmanabhan et al., 2006) where b is the linear bias and relates, in the linear regime, the underlying mass density distribution to that of the luminous tracers via $\delta_g = b\,\delta_m$. As such and coupled to their very clean and efficient selection, LRGs are excellent tracers of large-scale structure and can be used as cosmological probes. Eisenstein et al. (2005), Tegmark et al. (2006), Percival et al. (2006a) and Percival et al. (2006b) use positions and spectroscopic redshifts from the SDSS LRG Survey in order to accurately measure the correlation function and the power spectrum. Specifically, a detection of the baryon acoustic oscillations (BAOs) in the galaxy distribution is made. BAOs in the galaxy distribution are caused by sound waves propagating through the baryon-photon plasma in the early ($z > 1100$) Universe. At recombination, these sound waves are "frozen" into the distribution of matter at a preferred scale (see e.g. Eisenstein & Hu, 1998; Meiksin et al., 1999; Yamamoto et al., 2006; Eisenstein et al., 2006, for further BAO details). Thus, just as there are preferred angular scales in the Cosmic Microwave Background (CMB) radiation temperature anisotropy, there are low amplitude, preferred scales in the galaxy distribution. With measurements of the BAOs now starting to appear feasible, there is a push to carry out large galaxy surveys at higher redshift, with the primary goal of tracking the evolution of dark energy and the related equation of state parameter, $w_{\rm DE}(z)$, over cosmic time. As such, several new galaxy redshift surveys have proposed.

Field Name	R.A. (J2000)	Dec (J2000)	No. of exposures	Average seeing(″)					Average airmass				
COSMOS	10h 00m 28.6s	02d 12m 21.0s	0+7+0+6+0	–	2.0	–	3.0	–	–	1.39	–	1.27	–
COMBO-17 S11	11h 42m 58.0s	−01d 42m 50.0s	2+6+4+0+9	2.0	1.8	1.7	–	1.9	1.15	1.19	1.21	–	1.19
2SLAQ d05	13h 21m 36.0s	−00d 12m 35.0s	8+0+0+5+0	1.9	–	–	1.6	–	1.22	–	–	1.19	–

Table 5.1: The 3 AAOmega LRG Pilot fields. The fourth column gives the number of 1200 second exposures on the 5 consecutive nights of the pilot run, 03 March 2006 through 07 March 2006. Note that the 9 exposures taken in the S11 field on the night of 07 March 2006 targeted objects which had a z-band magnitude selection of $19.5 < z < 20.2$.

One of these surveys is the VST-AAΩ *ATLAS* (Shanks, 2007) which will utilise photometry from the SDSS, as well as new imaging from the 2.6m VLT Survey Telescope (VST), in order to provide high-redshift LRG targets for the AAOmega fibre-fed spectrograph on the Anglo-Australian Telescope (AAT). AAOmega retains the fibre-fed multi-object capability from the old 2dF instrument but the top-end spectrographs have been replaced with a new single bench mounted spectrograph, with a red and a blue arm. Sharp et al. (2006) gives complete instrument details.

In this chapter we present the results from a "Proof of Concept" Pilot study for VST-AAΩ *ATLAS* . Although the primary driver for the Pilot study is to investigate the nature of dark energy at high redshift via the BAOs, there are also several other areas of interest. By comparing clustering results at $1 < r < 10 \ \ h^{-1}$ Mpc scales from low, $z < 0.4$, intermediate, $z = 0.55$, and high, $z \sim 0.7$ redshift LRG studies (Zehavi et al. (2005a), Chapter 2 and Chapter 6 respectively), we can begin to learn about the formation and evolution of the most massive galaxies (and hence, potentially the most massive dark matter haloes) from high redshift.

5.2 SDSS LRG SELECTION

At its heart the AAOmega LRG Pilot relies on single-epoch photometric data from the SDSS (York et al., 2000; Gunn et al., 2006) to provide targets for the recently commissioned AAOmega instrument on the 3.9m Anglo-Australian Telescope (AAT).

The target selection was designed to select high-redshift LRGs out to $z \simeq 1$ with a mean redshift of $z \simeq 0.7$. Using the SDSS Data Release 4 (DR4), we extracted photometric data for objects classified as galaxies. Three different selections were then applied to the downloaded data, with the selections being designed to recover a target sky density of ~ 90 objects per square degree.

We repeated the *gri*-band based selection that was used in the 2SLAQ LRG Survey. We will not repeat the full selection criteria here (the reader is referred to Chapter 2 or Cannon et al. (2006) for further details) but note that LRGs are selected in the $(g-r)$-$(r-i)$ colour-colour plane with $17.5 < i_{\rm deV} < 19.8$, where $i_{\rm deV}$ is the i-band de Vaucouleurs magnitude.

Now with the aim of measuring significantly higher redshifts than the 2SLAQ LRG Survey ($\bar{z}_{\rm 2SLAQ} = 0.55$), two further selections were carried out, this time in the $(r-i)$-$(i-z)$ colour-colour plane. The second selection takes objects in the magnitude range $19.8 < i_{\rm deV} < 20.5$, while the third selection had objects in the magnitude range $19.5 < z < 20.2$, where z is the SDSS "Model" magnitude (Fukugita et al., 1996; Stoughton et al., 2002). These magnitude ranges were based on experience gained from the 2SLAQ LRG Survey as well as the expected performance of the new AAOmega instrument, such that LRGs with a significantly higher redshift than the previous survey could be selected and observed in a relatively short exposure ($\sim$ 1.5 hours). Within these two higher redshift *riz*-band selections, objects were assigned different observational priorities. The line "$e_{\parallel}$" was defined, akin to $c_{\parallel}$ in Eisenstein et al. (2001)

and $d_{\parallel}$ in Cannon et al. (2006), as

$$e_{\parallel} = (i - z) + \frac{9}{7}(r - i) \geq 2.0. \tag{5.1}$$

and is used to define a boundary in the *riz*-plane. (All colours reported here, such as those given in Equation 5.1, are again based on "Model" magnitudes). A higher priority *riz*-plane cut was imposed with

$$0.5 \leq (r - i) \leq 1.8, \tag{5.2}$$

$$0.6 \leq (i - z) \leq 1.5, \tag{5.3}$$

$$e_{\parallel} \geq 2.0. \tag{5.4}$$

The lower priority cut has

$$0.2 \leq (i - z) \leq 0.6, \tag{5.5}$$

$$x \leq (r - i) \leq 1.8, \tag{5.6}$$

where x was the smaller of $e_{\parallel}$ and 1.2 at the given $(i - z)$. These cuts can be seen in Figure 5.1 where the two priorities are shown by the regions marked A and B. The two evolutionary tracks in Figure 5.1 the stellar population synthesis code based on Bruzual & Charlot (2003). The solid line being a "single burst" model, where star formation occurs in a single instantaneous burst at high redshift and then has the stellar population evolving passively. The dashed line on the other hand is based on a model with continuous star formation, with the timescale of star formation given as $\tau = 1$ Gyr, where τ is a decay constant in that the star formation rate (SFR) is $\propto \exp^{-t/\tau}$. Both models assume a Salpeter IMF (Salpeter, 1955) with solar metallicity and a galaxy formation redshift of $z_{\rm form} = 10$ and are identical to those presented in Chapter 2. The evolutionary tracks start near $(r - i) = (i - z) = 0.4$ for zero redshift, turn upwards near

	Spectra Obtained	Qop ≥ 3	LRGs	gri	$i < 20.5$	$z < 20.2$
COSMOS	321	200	156	67	89	0
COMBO-17 S11	604	367	254	55	119	80
2SLAQ d05	345	237	177	50	127	0
total	**1270**	**804**	**587**	**172**	**335**	**80**

Table 5.2: Redshift Statistics for the AAOmega LRG Pilot Run. Note these numbers use data that was subject to initial, relatively poor, instrument performance due to e.g. fringed fibres. This will have since been corrected. The difference in numbers between the last two columns is accounted for by foreground M-stars.

$(r - i) = 1.3$ corresponding to redshift $z = 0.7$ and then turn down again near $(i - z) \sim 1.1$ corresponding to redshift $z = 1.0$. These turning points correspond to the Ca H+K 4000Å break moving into the i- and z-bands respectively. The solid circles show the colour evolution at redshift $z = 0.0, 0.5, 1.0$ and 1.5.

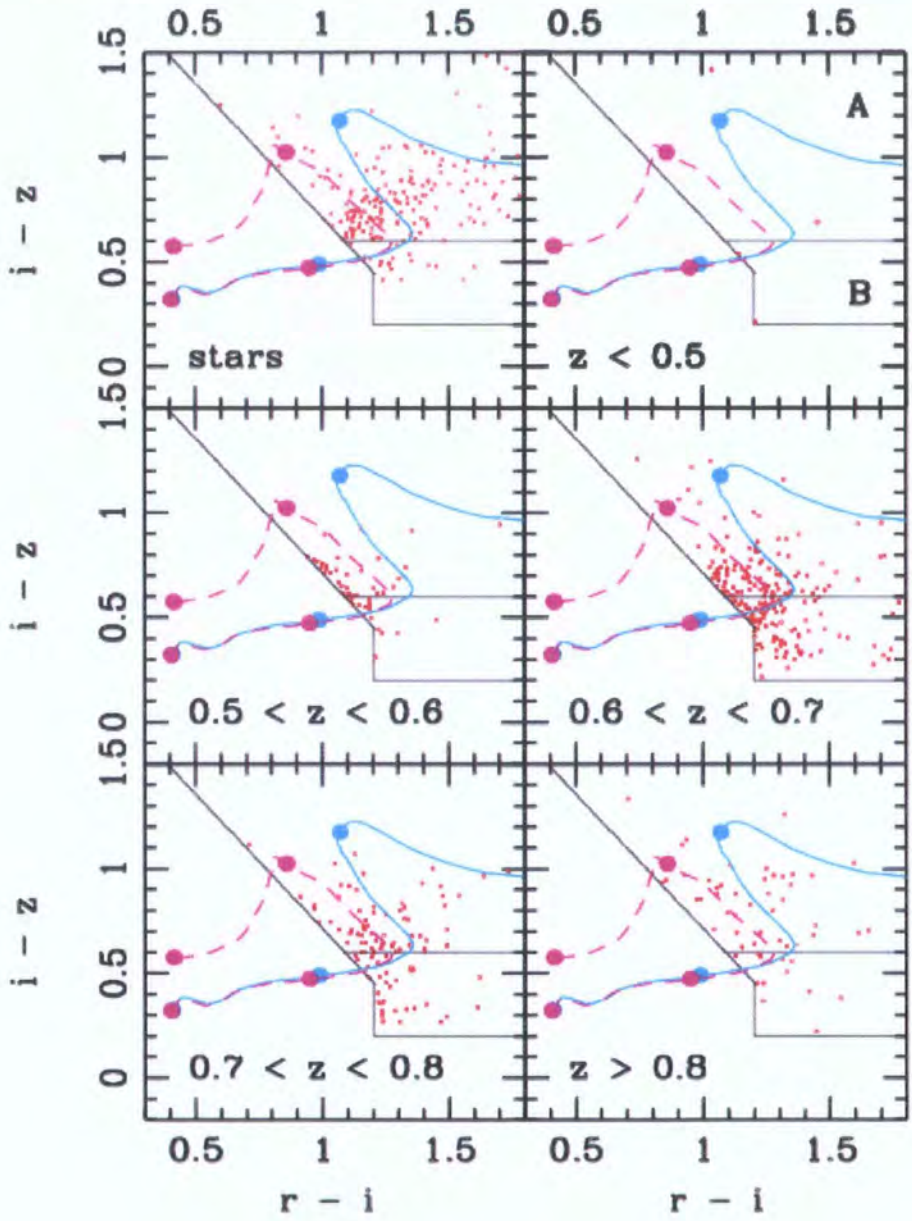

Figure 5.1: The selection of $z \sim 0.7$ LRGs using the SDSS riz-bands. The (red) dots are objects with confirmed spectroscopic redshifts for both the $19.8 < i_{\rm deV} < 20.5$ and $19.5 < z < 20.2$ magnitude selections. The tracks are Bruzual & Charlot models, details given in the text with the solid (cyan) line being a "single burst" model and the dashed (magenta) line having being a τ=1 Gyr model. The diagonal lines are $e_{\parallel} = 2.0$. The area labelled "A" in the top right redshift $z < 0.5$ panel gives the colour-colour space for the higher priority sample, while area "B" is for the lower priority sample.

LRG Sample/ Field (Seeing)	d05 (1.″6)	S11 (1.″8)	COSMOS (2.″1)
gri $i < 19.8$ (2SLAQ)	88 ± 19	70 ± 22	64 ± 24
riz $19.8 < i < 20.5$	84 ± 13	60 ± 11	50 ± 9

Table 5.3: LRG percentage redshift completeness rates (Quality=3-5) as estimated for $\simeq$ 80 unfringed fibres between fibres 200-299 in a 1.5hr exposure (stars excluded). Better observing conditions (d05) yield completenesses consistent with 2SLAQ. Poorer observing conditions (S11 and COSMOS) yield lower completeness. The COSMOS data had average airmass 1.4 plus some cloud, as well as poorer seeing.

5.3 AAOmega Spectroscopy

5.3.1 Observational Details

Observations were made on the nights of 03 March 2006 to 07 March 2006 inclusive; the first three nights were Dark nights, the last two were Grey nights. Of these nights, a total of $\simeq$ 2 were lost to cloud and seeing was frequently poor on the others (see Table 5.1). We observed in 3 fields including the COSMOS field (Scoville et al., 2006a), the COMBO-17 S11 field (Wolf et al., 2001) and a previously observed 2SLAQ Survey field, d05 (Cannon et al., 2006), the coordinates of which are also given in Table 5.1. All data were taken with the same spectrograph set-up. The 5700Å dichroic was used. For the red arm spectrograph the 385R grating was centred at 7625Å; for the blue arm spectrograph the 580V grating was centred at 4800Å. However, no blue arm data was used in our analysis as the S/N was low, as expected for red galaxies.

Data reduction was performed using the 2dF data reduction pipeline software, `2dfdr` (Bailey et al., 2005) and the redshifts were derived using Zcode developed by Will Sutherland and

others for the 2dFGRS Survey (Colless et al., 2001, and references therein). The modifications to ZCODE originally made for the higher redshift $z \sim 0.5$ galaxies in the 2SLAQ LRG Survey (Cannon et al., 2006) were retained. The final catalogue from the AAOmega LRG Pilot contains 1270 unique galaxy spectra with 804 objects having reliable "Qop ≥ 3" redshifts (where "Qop" is the same quantitiy as discussed previously) see Table 5.2. Of these, 217 objects had M-type stellar spectra leaving 587 high-redshift LRGs. The COSMOS field contributed 156 LRGs out of 321 obtained spectra, the 2SLAQ d05 field 177/345 and the S11 field 254/604. The greater number of spectra obtained in S11 was due to the fact that objects in the field were targeted not only with the $19.8 < i < 20.5$ selection but also with the $19.5 < z < 20.2$ z-band selection.

The full AAOmega LRG Pilot Survey catalogue will be published on-line with the publication of the accompanying paper. In the next Section we report in more detail on the properties of the high-redshift LRGs.

5.3.2 Redshift Completeness

The LRG redshift completeness statistics for each field are given in Table 5.3. Our overall completeness was relatively low, say compared to the 2SLAQ LRG Survey (Cannon et al., 2006), but one of the main reasons for this was due to the several technical issues associated with the new AAOmega instrument, which have since been corrected. When checks were made on the d05 field, we found that the redshift completeness rates for our riz, $19.8 < i_{\rm deV} < 20.5$ targets as estimated from ≈ 80 "unfringed" fibres were $90 \pm 9\%$ in 3 hour exposures, $84 \pm 13\%$ in 1.5 hour exposures and $46 \pm 9\%$ in a 1 hour exposure in $1.''6$ seeing. Thus, using the full number of sub-exposures we found no significant increase in redshift completeness compared to a 1.5 hour exposure, although this may still be due to conditions varying within the 3 hour

exposure time. But our general conclusion is that with reasonable seeing and transparency, we should be able to achieve 85-90% redshift completeness in a 1.5 hour exposure.

We also confirmed that the exposure time needed to obtain reliable redshifts of LRGs selected in the same manner as the 2SLAQ survey (using a *gri*-band, $i < 19.8$ selection) was cut by a factor of ~ 4 from the old 2dF instrument, and that the completenesses of the 1.5 hour LRG samples are consistent with the high completenesses achieved for 2SLAQ LRGs.

The improved AAOmega throughput and sky subtraction enables us to work further into the near-infrared, allowing us to probe higher redshifts.

5.3.3 Redshift Distribution

The *raison d'être* of the VST-AAΩ *ATLAS* Pilot run was to test if we could readily select $z \sim 0.7$ LRGs using single-epoch SDSS *riz*-photometry. As can be seen in Figure 5.2, this proved feasible. The mean redshift of our $19.8 < i_{\rm deV} < 20.5$ magnitude sample was $z = 0.681 \pm 0.005$, with a strong tail out to redshift $z = 0.8$ and indeed some objects at $z = 0.9$. We found that there was no major difference between the samples with different priorities (areas "A" and "B" in Figure 5.1). Also shown in Figure 5.1 are the *riz*-band colours for the objects with spectroscopically confirmed redshifts. When the magnitude limits applied were changed from $19.8 < i_{\rm deV} < 20.5$ to $19.5 < z < 20.2$, the mean redshift increased to $z = 0.698 \pm 0.015$. However, for the remainder of this analysis we only consider objects with $19.8 < i_{\rm deV} < 20.5$. The mean redshift for our *gri*-band, $17.7 < i_{\rm deV} < 19.8$ selection was very comparable to the 2SLAQ LRG Survey at $z = 0.578 \pm 0.006$.

As can be seen from Table 5.2, a significant fraction (27%) of our obtained $Q{\rm op} \geq 3$ objects were M-type stars. However, as shown in Figure 5.3, *a posteriori* checking shows that we can

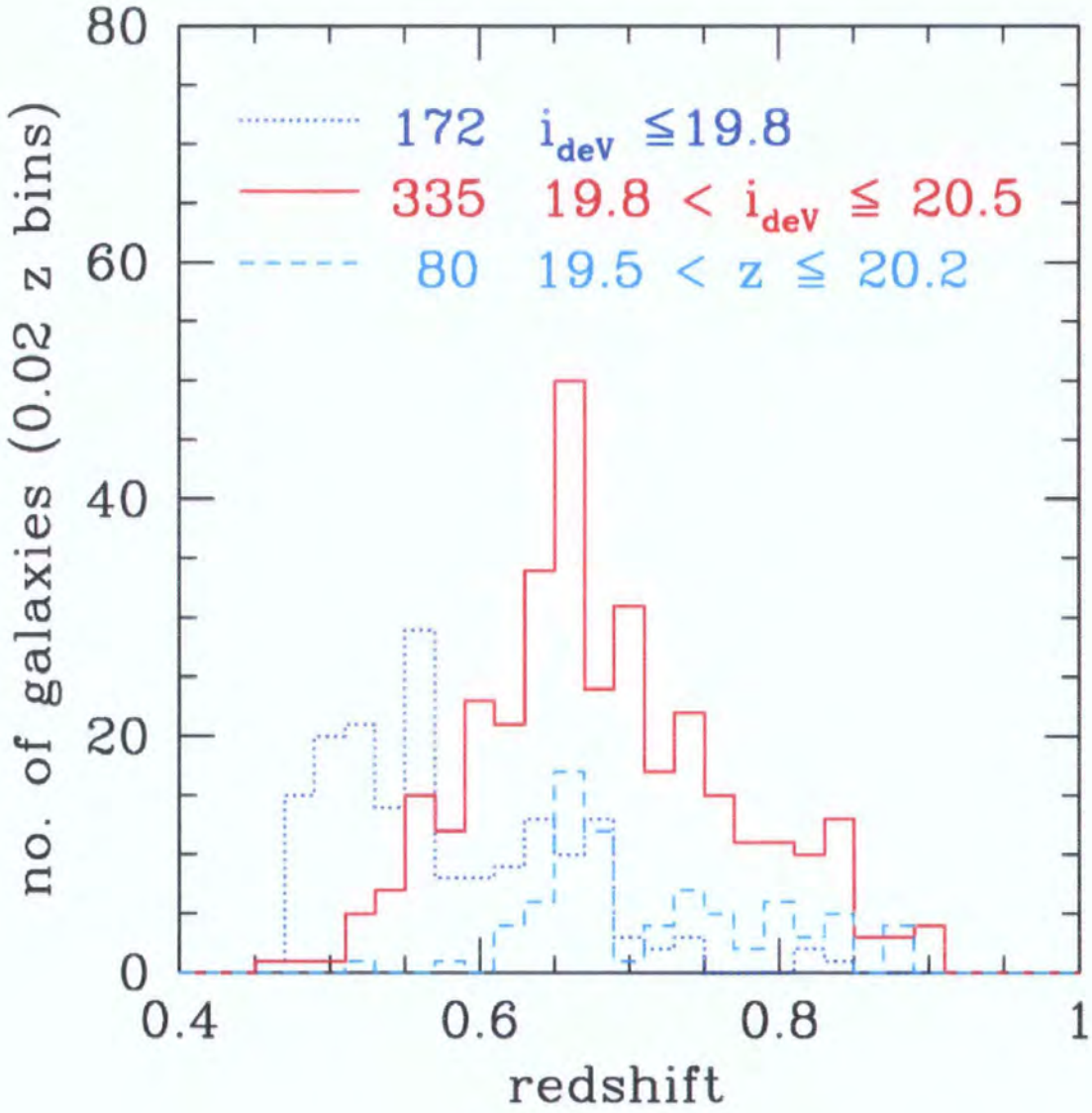

Figure 5.2: The $N(z)$ of the AAOmega LRG Pilot Run showing that $z \leq 0.9$ can be readily selected using SDSS *riz*-photometry. The dotted (blue) line shows the distribution for the *gri*-selection, while the solid (red) line and the dashed (cyan) line the *riz*-selections with magnitude cuts in the i and z-bands respectively.

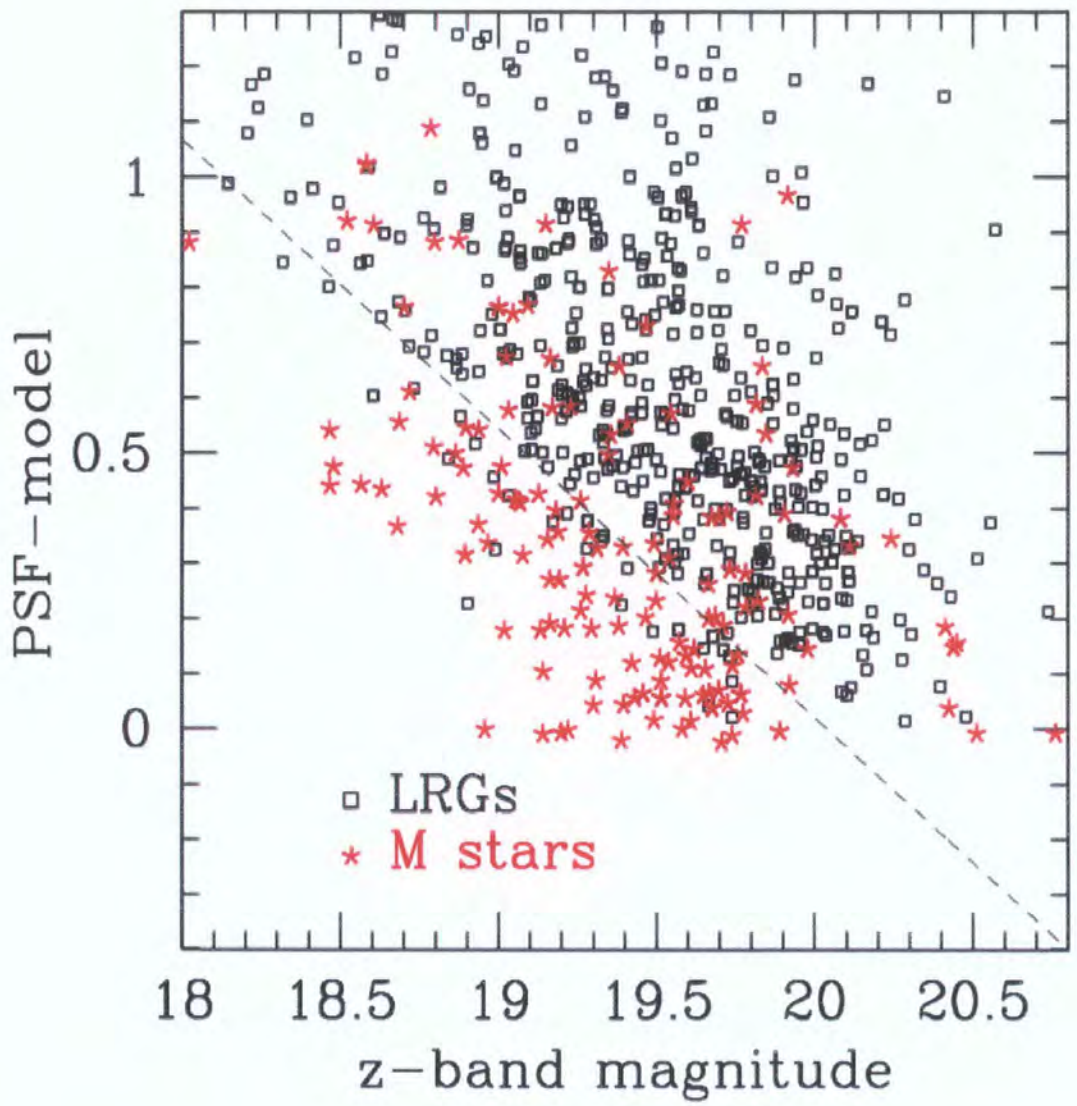

Figure 5.3: Star-galaxy separation using SDSS z-band magnitudes. All objects with $Qop \geq 3$ and $19.8 < i_{\rm deV} < 20.5$ are shown, with objects having stellar spectra plotted as (red) stars and objects having high-redshift LRG spectra plotted as (black) open squares. The ordinate gives the difference between the "PSF" and "Model" z-band magnitudes as given from the SDSS DR4 imaging.

reject these stars using a star-galaxy separation in the z-band, rather than the standard SDSS separation performed in the r-band. The stellar contamination drops to 16%, with very few high-redshift galaxies being lost. Employing near-IR imaging data, specifically a $J - K > 1.3$ cut, would dramatically reduce the stellar contamination further, to the level of a few percent.

Our observations therefore suggest a VST-AAΩ *ATLAS* spectroscopic redshift survey strategy to pursue BAOs with AAOmega LRGs might consist of 1.5 hour exposures with

- $\simeq$ 100 fibres placed on *gri*-selected $i < 19.8$ LRGs with $z \simeq 0.55$ and
- $\simeq$ 260 fibres placed on *riz*-selected $19.8 < i < 20.5$ LRGs with $z \simeq 0.7$

in order to obtain 360 000 LRGs over 3000deg^2 which will give an $\sim 4\times$ bigger effective volume than the original SDSS LRG Survey of 45,000 LRGs (Eisenstein et al., 2005). We shall compare this strategy with other strategies in Section 6.2.3 below.

5.3.4 2SLAQ, COMBO-17 and AAOmega Comparison

In Figure 5.4 we show a comparison between the spectroscopic redshifts we recorded from our AAOmega observations and those measured photometrically by the Classifying Objects by Medium-Band Observations (COMBO-17) survey (e.g. Wolf et al., 2001; Bell et al., 2004a; Phleps et al., 2006). As can be seen, the 43 common photometric and spectroscopic redshifts match extremely well for the objects for which we have secure redshifts (Qop ≥ 3). There seems to be a slight trend for the photometric redshifts to underestimate the spectroscopic redshift. Why this is the case is not well understood. Excluding 5 "catastrophic failures", where $|\Delta z| \geq 0.2$, the average offset between the COMBO-17 photometric and AAOmega spectroscopic redshifts is $\overline{\Delta z} = 0.026 \pm 0.005$, in the sense that COMBO-17 redshifts are too small. There are 3 spectroscopically confirmed stars that COMBO-17 classified as galaxies.

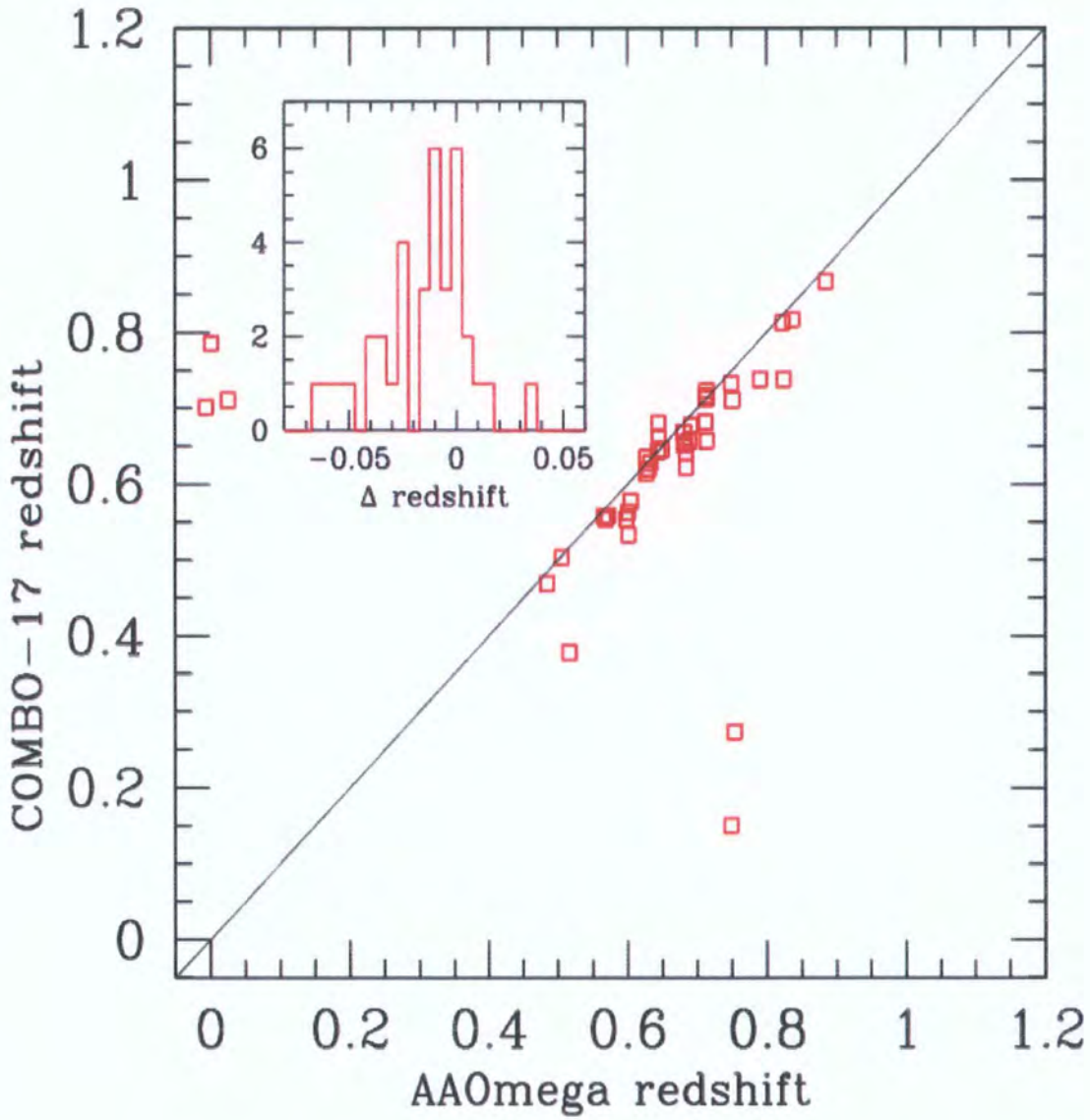

Figure 5.4: COMBO-17 photometric redshifts vs. AAOmega spectroscopic redshifts. The solid line is the 1:1 relation. The insert shows the histogram of $\Delta z = z_{\rm spec} - z_{\rm phot}$ for AAOmega and COMBO-17 redshifts respectively.

We also compare the spectroscopic redshifts measured by AAOmega with those obtained in the 2SLAQ LRG Survey. We find, for the Qop $\geq$ 3 LRGs common in both, the mean $\Delta z = 8.4 \times 10^{-4}$ with the spread on the difference in redshifts being 1.24×10^{-3} i.e. 370 km s^{-1}. If the error is split evenly between the two surveys, then the error on AAOmega LRG redshifts is $\pm 370/\sqrt{2} = 260$ km s^{-1}.

In the next Chapter we report in more detail on the properties of the high-redshift LRGs.

CHAPTER 6

THE CLUSTERING PROPERTIES OF $z \sim 0.7$ LRGS

The telex machine is kept so clean As it types to a waiting world.

And mother feels so shocked, Father's world is rocked,

And their thoughts turn to Their own little girl.

Sweet 16 ain't so peachy keen, No, it ain't so neat to admit defeat.

They can see no reasons, 'Cause there are no reasons What reason do you need to be shown?

- The Boomtown Rats, *I Don't Like Mondays*.

Chapter 6 of this thesis reports on the clustering properties of $z \sim 0.7$ LRGs using data from the AAOmega LRG Pilot Run. These results are put in context as to the next generation of redshift surveys, with a detailed comparison made with BAO Surveys using Emission Line Galaxies (ELGs).

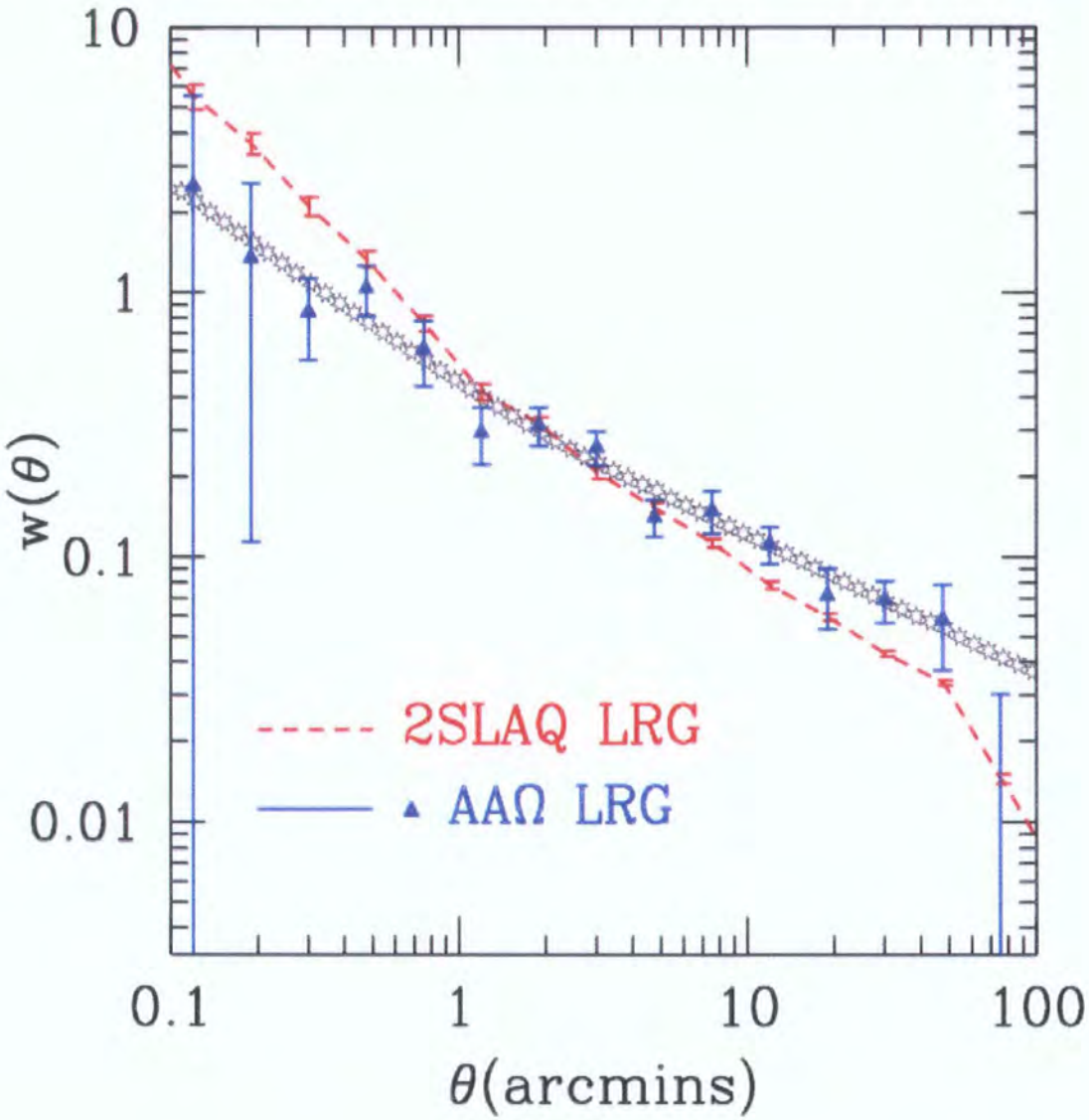

Figure 6.1: The AAOmega LRG Pilot angular correlation function, $w(\theta)$, is given by the solid (blue) triangles. The (black) open stars are an estimation for an assumed 2-point correlation function of $w(\theta)$, given our redshift distribution and projecting using Limber's Formula. From these fits, we find $r_{0,ss} = 6.50 \pm 0.32 \ \ h^{-1}$ Mpc and $\gamma = 1.80 \pm 0.16$ for $r < 1 \ \ h^{-1}$ Mpc and $r_{0,ls} = 8.5 \pm 1.0 \ \ h^{-1}$ Mpc and $\gamma = 1.52 \pm 0.08$ for $r > 1 \ \ h^{-1}$ Mpc. The dashed (red) line is the $w(\theta)$ measurement from the 2SLAQ LRG Survey.

6.1 LRG Clustering Results

6.1.1 AAOmega LRG Projected Correlation Function, $w(\theta)$

Using the procedure described in Chapter 3, the projected angular correlation function, $w(\theta)$ for the AAOmega LRG Pilot Survey is presented in Figure 6.1. The solid (blue) triangles are the measurement made utilising the "Input Catalogue" from which objects were selected as potential high-redshift LRG candidates. Approximately 2 300 objects were used in this measurement from 6 fields and all these objects were potential targets having passed the *riz*-cuts discussed above. It should also be noted that the star-galaxy separation discussed above was applied to this input sample. The error bars associated with the AAOmega LRG $w(\theta)$ measurement are *field-to-field* errors (see Chapter 3). We will not take into account the fact that the clustering measurements are correlated and as such, the errors should only be taken as indicative.

Although a single power-law has traditionally been fitted to the angular correlation function for galaxies, in Chapter 3 we found that a 2 power-law model was required to fit the 2SLAQ LRG $w(\theta)$. Following that work, we use Limber's Formula (see Phillipps et al., 1978) to relate the 3-D correlation function, ξ, to the measured $w(\theta)$. A double power-law of the form

$$\xi(r) = \begin{cases} (r/r_{0,\mathrm{ss}})^{-\gamma_{\mathrm{ss}}} & r < r_{\mathrm{b}} \quad \text{and} \\ (r/r_{0,\mathrm{ls}})^{-\gamma_{\mathrm{ls}}} & r > r_{\mathrm{b}} \end{cases} \tag{6.1}$$

where 'ss' and 'ls' stand for small scales and large scales respectively, is assumed and calculated from Limber's formula. We find that values of $r_{0,ss} = 6.50 \pm 0.32\ h^{-1}$ Mpc and $\gamma = 1.80 \pm 0.16$ for $r_{\mathrm{b}} < 1.5\ h^{-1}$ Mpc, and $r_{0,ls} = 8.5 \pm 1.0\ h^{-1}$ Mpc and $\gamma = 1.52 \pm 0.08$ for $r_{\mathrm{b}} > 1.5\ h^{-1}$ Mpc are consistent with our observational data. Here we can see that the $w(\theta)$ measurement for the AAOmega high-redshift data is comparable to the $z = 0.55$ data from the 2SLAQ LRG survey

given by the dashed (red) line (Chapter 3). At both small and large-scales, the AAOmega $w(\theta)$ slope is shallower than the 2SLAQ LRG measurement, with $\gamma = 1.80$ for AAOmega compared to $\gamma = 2.17$ for 2SLAQ LRGs at angles $\theta \lesssim 2$ arcminute and $\gamma = 1.52$ for AAOmega compared to $\gamma = 1.67$ for 2SLAQ LRGs at angles $\theta \gtrsim 2$ arcminute (Chapter 3). However, given the associated errors, the two measurements are in reasonable agreement. We leave further analysis of the angular correlation function as reported here to Sawangwit et al. (2007, in prep.) who shall investigate the evidence for a double power-law feature in a much larger LRG sample.

Given the AAOmega LRG Pilot $N(z)$ (Figure 5.2) and using Limber's Formula the AAOmega $w(\theta)$ amplitude is expected to be 13% lower than the 2SLAQ LRG amplitude if there is no clustering evolution in comoving coordinates. Thus in terms of the overall amplitude, this reinforces the impression given in Figure 6.1 that AAOmega LRG have a higher large-scale amplitude than 2SLAQ LRGs.

6.1.2 De-projected Correlation Function, $w_p(\sigma)$

We have used the minimum variance estimator suggested by Landy & Szalay (1993) to calculate the 3-D correlation function, $\xi(\sigma, \pi)$, where σ is the separation across the line-of-sight, while π is the separation along the line-of-sight,

$$\xi(\sigma,\pi) \;=\; 1 + \left(\frac{N_{rd}}{N}\right)^2 \frac{DD(\sigma,\pi)}{RR(\sigma,\pi)} - 2\left(\frac{N_{rd}}{N}\right)\frac{DR(\sigma,\pi)}{RR(\sigma,\pi)}. \tag{6.2}$$

We use bin widths of $\delta \log(\sigma/\ h^{-1}\ \mathrm{Mpc}) = \delta \log(\pi/\ h^{-1}\ \mathrm{Mpc}) = 0.2$ and the number density of random points was 20× that of the LRGs. Using the Landy & Szalay estimator and the same method as in Chapter 3, we then calculated the de-projected correlation function, $w_p(\sigma)$, by summing along the line-of-sight direction

$$w_p(\sigma) \;= 2\int_0^\infty \xi(\sigma,\pi)\, d\pi. \tag{6.3}$$

In practice we set the upper limit on the integral to be $\pi_{\rm max} \simeq 40\ \ h^{-1}$ Mpc. However, the results did seem to be quite sensitive to this choice, especially at large, $\sigma \gtrsim 40\ \ h^{-1}$ Mpc scales.

The random catalogue was constructed taking into account the angular incompleteness and the radial distribution of the objects in this Pilot. For each 2dF field we generated a "quadrant bullseye" angular mask which consisted of 5 concentric rings divided into 4 quadrants was constructed. Using both the input catalogue and the 2dF instrument configuration positions, a completeness map was made in each of the 20 sectors. These completenesses then went into mimicking the angular selection function with the random catalogue. Corrections for fibre collisions on small, $\lesssim 30$ arcseconds, scales were made by taking the ratio of the input catalogue $w(\theta)$ to the observed redshift catalogue $w(\theta)$, as described in Chapter 3. The radial distribution was described by a high-order polynomial fit to the AAOmega $N(z)$ for the 335 $19.8 < i < 20.5$ selected LRGs given in Figure 5.2.

The $w_p(\sigma)$ for the AAOmega LRG Pilot Survey is shown in Figure 6.2. Again, the error bars are given by 'field-to-field' estimates, where N is now 3, since we are using data only from the COSMOS, S11 and d05 fields. Also shown is the $w_p(\sigma)$ from the 2SLAQ LRG Survey, given by the (red) dashed line (Chapter 3), and the SDSS LRG Sample with $-23.2 < M_g < -21.2$, shown by the (black) stars (Zehavi et al., 2005a).

We now describe the real-space correlation function, $\xi(r)$ as a simple single power-law model of the form

$$\xi(r) = \left(\frac{r}{r_0}\right)^{-\gamma}. \tag{6.4}$$

We fit $w_p(\sigma)$ for r_0 and γ and invoke the inversion method described by e.g. Saunders et al. (1992), Hawkins et al. (2003), da Ângela et al. (2006) and in Chapter 3. We fit in the range $1.0 < \sigma < 40.0\ \ h^{-1}$ Mpc, because Figure 6.2 shows that there is little data on scales $\sigma <$

1 h^{-1} Mpc and which is why we choose only to fit a single power-law here. Performing a $\Delta\chi^2$-fit following the prescription given by Press et al. (1992, Chap. 15) and we find values of $r_0 = 9.03 \pm 0.93$ and $\gamma = 1.73 \pm 0.08$ for our AAOmega LRG *riz*-selected, $19.8 < i_{\rm deV} < 20.5$ sample. It can be seen from Table 6.1 that the above result is consistent with the large-scale slope and the amplitude found at $r > 1$ h^{-1} Mpc from $w(\theta)$.

6.1.3 Redshift-space Correlation Function, $\xi(s)$

Figure 6.3 shows our estimate of the 3-D redshift-space correlation function, $\xi(s)$. Our error estimates are based on "field-to-field" errors. For $\xi(s)$, we return to a double power-law model of the form given in equation 6.1, with the motivation for this now coming from the effect that galaxy peculiar velocities are known to have when measuring the correlation function in redshift-space. On small scales, there is the "Fingers-of-God" effect due to intrinsic velocity dispersions and on large-scales, the parameter β characterises the "boost" in the redshift-space correlation function due to coherent infall into clusters. Thus, we adopt the same procedure as previously for the 2SLAQ LRG Survey and perform a χ^2-fit using a simple double power-law model. We find that, $s_{0,\rm ss} = 16.5^{+4.0}_{-3.0}$ with $\gamma_{\rm ss} = 1.09 \pm 0.12$ on scales $s < 4.5$ h^{-1} Mpc and $s_{0,\rm ls} = 9.9 \pm 0.3$ with $\gamma_{\rm ls} = 1.83 \pm 0.27$ on scales $s > 4.5$ h^{-1} Mpc. The clustering strength for the $19.8 < i < 20.5$, *riz*-selected AAOmega LRGs is again comparable to the 2SLAQ LRG Survey, where $s_{\rm ss} = 17.3^{+2.5}_{-2.0}$ and $\gamma_{\rm ss} = 1.03 \pm 0.07$ on scales $s < 4.5$ h^{-1} Mpc and $s_{\rm ls} = 9.40 \pm 0.19$ and $\gamma_{\rm ls} = 2.02 \pm 0.07$ on scales $s > 4.5$ h^{-1} Mpc.

Using the model of Kaiser (1987), we can find the parameter β via

$$\xi(s) = \xi(r)\left(1 + \frac{2}{3}\beta + \frac{1}{5}\beta^2\right). \tag{6.5}$$

We use our power-law fit to $\xi(r)$ and our large-scale power-law fit to $\xi(s)$ and find that the

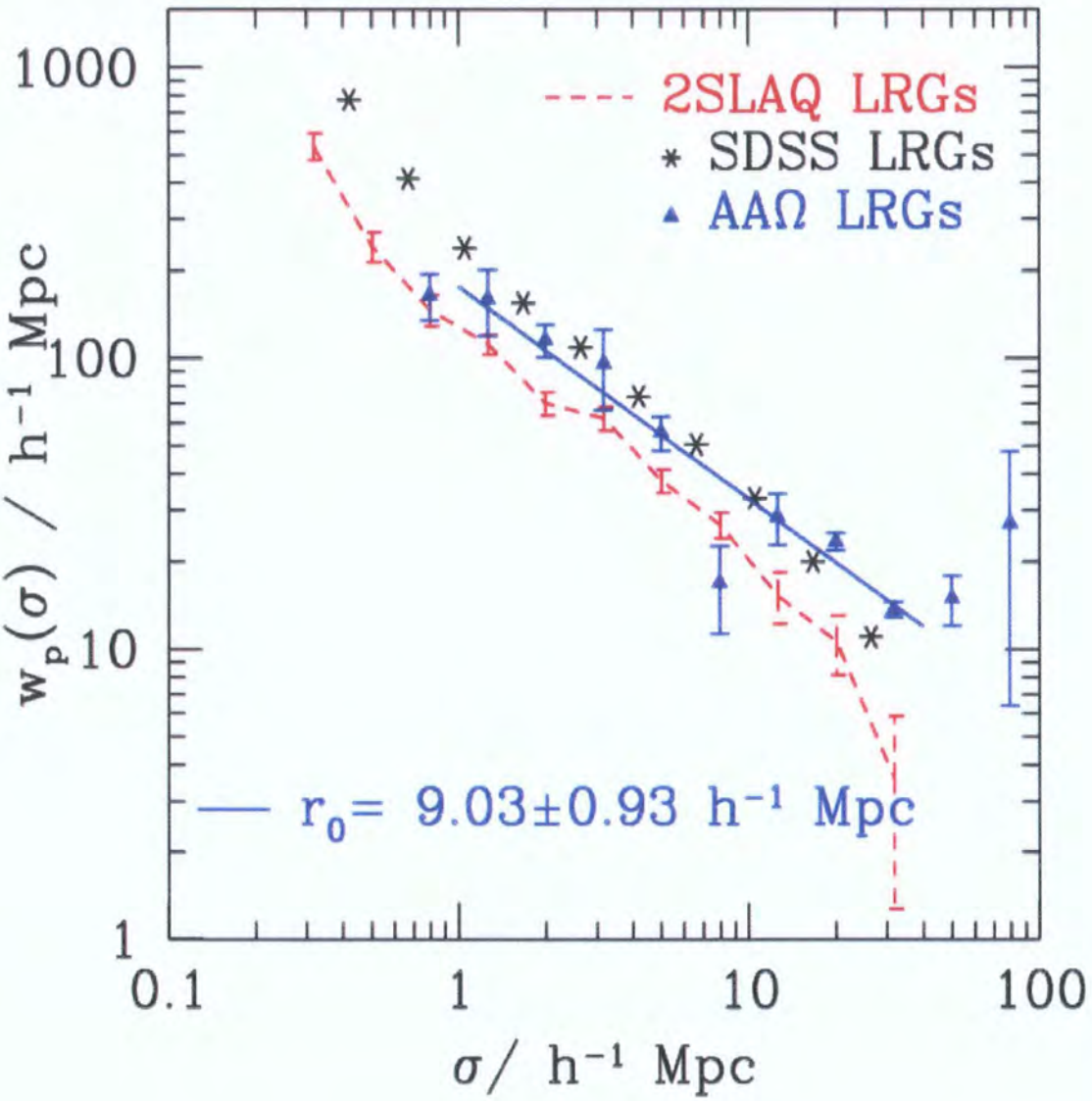

Figure 6.2: The AAOmega LRG Pilot projected Correlation Function, $w_p(\sigma)$. The (blue) triangles are the measurements from the 3 observed fields with the associated "Field-to-Field" errors quoted. The dotted (blue) line is the best-fit single-power law model to the AAOmega data. The 2SLAQ LRG $w_p(\sigma)$ is given by the (red) dashed line, while the (black) stars are points from the SDSS LRG Sample (Zehavi et al., 2005a), with $-23.2 < M_g < -21.2$.

Survey	h^{-1} Mpc	γ	Reference
VST-AAΩ *ATLAS* LRG	$r_0 = 8.5 \pm 1.0$	1.52 ± 0.08	from $w(\theta)$
VST-AAΩ *ATLAS* LRG	$r_0 = 9.03 \pm 0.93$	1.73 ± 0.08	from $w_p(\sigma)$
VST-AAΩ *ATLAS* LRG	$s_0 = 9.9 \pm 0.3$	1.83 ± 0.27	from $\xi(s)$
SDSS LRG	$s_0 = 11.85 \pm 0.23$	1.91 ± 0.07	Zehavi et al. (2005a)
SDSS LRG	$r_0 = 9.80 \pm 0.20$	1.94 ± 0.02	Zehavi et al. (2005a)
2SLAQ LRG	$s_0 = 9.40 \pm 0.19$	1.98 ± 0.07	Chapter 3
2SLAQ LRG	$r_0 = 7.45 \pm 0.35$	1.72 ± 0.06	Chapter 3

Table 6.1: Values of s_0 and r_0 from the VST-AAΩ *ATLAS* LRG Pilot using the $w(\theta)$ measurement, the fit to $w_p(\sigma)$ and the $\xi(s)$ calculation with $s > 4.5$ h^{-1} Mpc. Values from the SDSS LRG Survey (Zehavi et al., 2005a, the $-23.2 < M_g < -21.2$ sample) and the 2SLAQ LRG Survey are also given. Note that due to redshift-space distortions and other non-linear effects, r_0 will usually be smaller than s_0.

ratio $\xi(s)/\xi(r) = 1.3 \pm 0.3$ corresponding to a value of $\beta \simeq 0.4$ on a scale of 8 h^{-1} Mpc. This is not inconsistent with the value $\beta = 0.45 \pm 0.05$ found for the 2SLAQ LRGs. Nevertheless, for a reasonable value of β, our values of $s_0 = 9.9 \pm 0.3$ h^{-1} Mpc and $r_0 = 9.0 \pm 0.9$ h^{-1} Mpc appear consistent. These high clustering amplitudes clearly suggest that at redshifts of $z \simeq 0.7$, LRGs remain very strongly clustered.

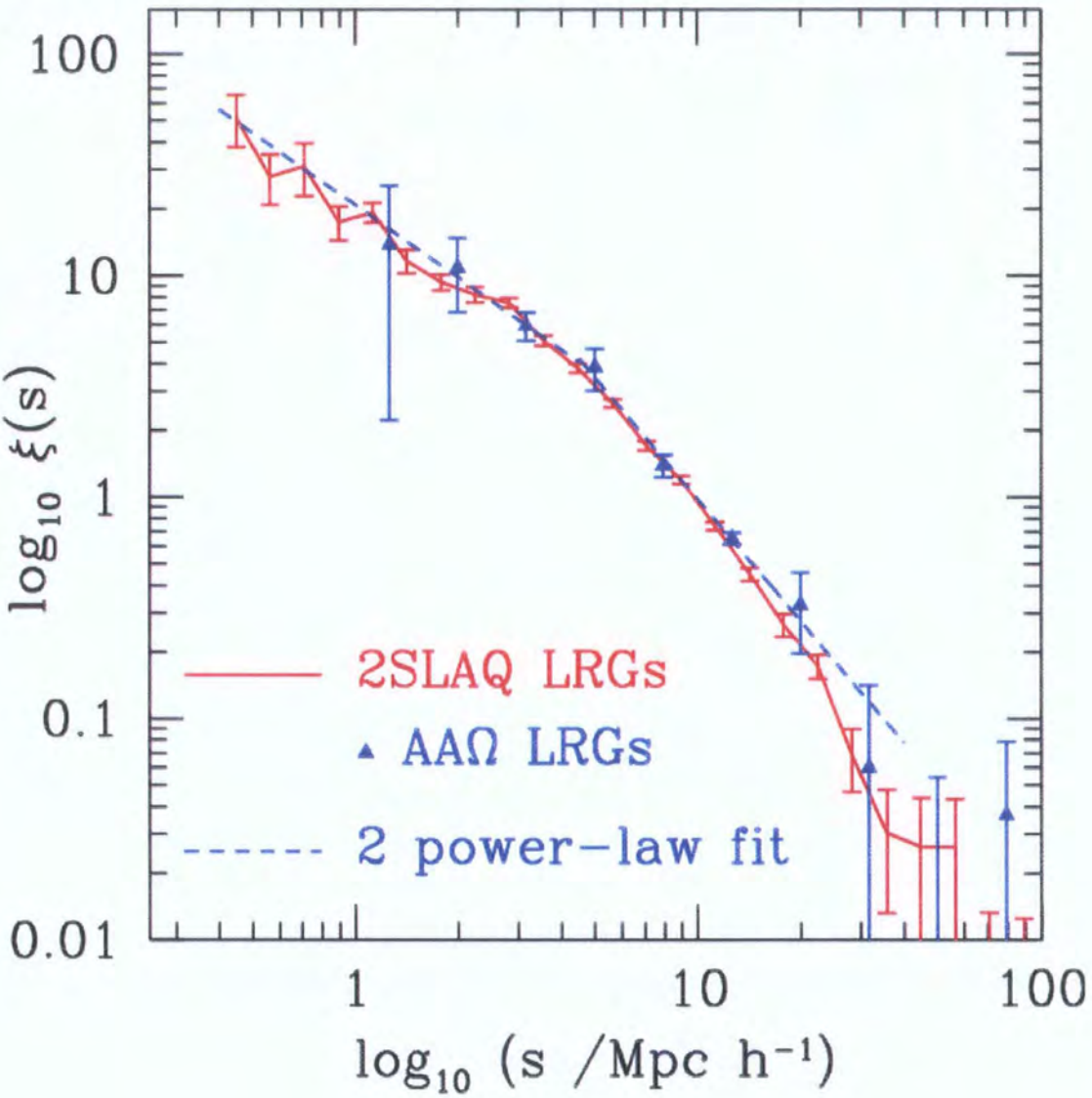

Figure 6.3: The AAOmega LRG Pilot redshift-space correlation function, $\xi(s)$. The (blue) triangles are the measurements from the *riz*-selected $19.8 < i_{\rm deV} < 20.5$ sample, with "Field-to-Field" errors. The dashed (red) line is the redshift-space correlation function from the 2SLAQ LRG Survey.

6.2 DISCUSSION

6.2.1 Bias of LRGs at $z \simeq 0.7$

We have found that a 2-power law fit is consistent with AAOmega $w(\theta)$ data. The slopes of the AAOmega power-law are both less than those for the 2SLAQ LRG Survey. This could be due to evolution with redshift but the errors on the AAOmega $w(\theta)$ are too large for this difference to be significant. Certainly the large scale results from $\xi(s)$ are perfectly consistent with the two surveys having the same large-scale slope and amplitude (see Fig. 6.3).

To see what sort of consistency with 2SLAQ might be expected, we can predict the value of the linear bias, b, at redshift $z = 0.7$ by utilising the values measured by 2SLAQ at lower redshift, $b(z = 0.55) = 1.66 \pm 0.35$, and the bias evolution model given by Fry (1996), Croom & Shanks (1996) and used previously in Chapter 4. Thus, assuming a growth rate of $G(0.3, 0.7, z)$, to relate $\xi_{\rm mm}(z = 0.55)$ to $\xi_{\rm mm}(z = 0.7)$, we therefore expect $\xi_{\rm gg}(z = 0.7) = 0.98\,\xi_{\rm gg}(z = 0.55)$ from this model.

From Table 6.1, the r_0 values between 2SLAQ and AAOmega LRGs are consistent, although the errors on the AAOmega r_0 measurement are big. But the errors on $\xi(s)$ are smaller, and even here, the s_0 values are agree to within the errors (see also Figure 6.3). The consistency of the clustering results is expected, since the 0.7 magnitudes deeper $19.8 < i_{deV} < 20.5$ selection was based on experience from the 2SLAQ LRG Survey and primarily designed to select similarly highly-biased red galaxies at redshift $z \simeq 0.7$. We conclude that the LRG correlation function amplitudes are similar at redshifts $z = 0.55$ and $z \simeq 0.7$ and that there is still no inconsistency with the simple bias model where the comoving density of LRGs are assumed to be constant with redshift.

6.2.2 Predictions of halo occupation models

An alternative approach to interpreting our measured level of clustering is to use the halo occupation model, in which the galaxy field is taken to be a superposition of contributions from dark-matter haloes, weighted by the number of galaxies per halo, $N(M)$. This methodology was used recently by Phleps et al. (2006) to model the projected correlations in the COMBO-17 survey, and we apply exactly the same method as described in that paper to model our AAOmega data. We adopt a standard matter power spectrum, with $\Omega_m = 0.3$, $\Omega_b = 0.045$, $h = 0.73$, $\sigma_8 = 0.85$, and a scalar spectral index of 0.97. The occupation model is the simplest possible: $N(M) = (M/M_{\rm min})^{\alpha}$ for $M > M_{\rm min}$. These two free parameters are reduced to one if the model is also required to match the number density of LRGs, which is approximately $0.0002\,h^3\,{\rm Mpc}^{-3}$.

Realistic occupation models will be more complicated than this simple power-law form, but Phleps et al. argue that the results can be expressed quite robustly in terms of an effective halo mass – i.e. the average halo mass weighted by the number of galaxies. For our current data, the occupation parameters that best match the clustering measurements are $\alpha \simeq 0.7$ and $M_{\rm min} \simeq 2 \times 10^{13} h^{-1} M_{\odot}$. These imply an average halo mass for the AAOmega LRGs at $z \simeq 0.7$ of $M_{\rm eff} \simeq 7 \times 10^{13} h^{-1} M_{\odot}$. Reasonably enough for particularly rare and luminous galaxies such as those studied here, this mass is somewhat larger than the figure found by Phleps et al. for the COMBO-17 red-sequence galaxies at $z \simeq 0.6$, which was $M_{\rm eff} \simeq 1.6 \times 10^{13} h^{-1} M_{\odot}$, using the same methodology. Our AAOmega figure for $M_{\rm eff}$ is in fact almost identical to the average mass deduced for $z = 0$ red-sequence galaxies in SDSS. Of course, this coincidence does not imply any direct correspondence between these populations: the haloes that host our $z \simeq 0.7$ LRGs will have become much more massive by the present.

The other conclusion that can be drawn from the halo modelling is that the AAOmega $w_p(\sigma)$ results seem surprisingly high at $\sigma > 30h^{-1}$Mpc. The error bars are of course already quite large there, but this is probably telling us that the field-to-field scatter is not yielding an adequate estimate of the error.

6.2.3 LRGs versus ELGs

One of the key questions that the AAOmega LRG Pilot Survey was designed to address, was whether a "blue" or a "red" galaxy survey be the more advantageous when pursuing BAOs at high redshift. In the previous sections, we have presented the $N(z)$ and clustering amplitudes for $\bar{z} = 0.68$ Luminous Red Galaxies.

Scale	**ELG**		**LRG**		$V_{\rm eff}$ **LRG / ELG**	
$k/h\,{\rm Mpc}^{-1}$	$P/h^{-3}\,{\rm Mpc}^3$	$V_{\rm eff}/h^{-3}{\rm Gpc}^3$	$P/h^{-3}\,{\rm Mpc}^3$	$V_{\rm eff}/h^{-3}{\rm Gpc}^3$	167/123 nts.	Equal no. nts.
0.02	4.6×10^4	0.97	1×10^5	2.1	2.2	1.6
0.05	1.8×10^4	0.70	4×10^4	1.6	2.3	1.7
0.15	4.6×10^4	0.32	1×10^4	0.73	2.3	1.7

Table 6.2: A comparison between the effective volumes probed by two AAOmega-based BAO Surveys, one using Luminous Red Galaxies (LRGs) and one using Emission Line Galaxies (ELGs). We assume a factor of 2.1 between the clustering amplitudes of LRGs and ELGs. The second last column is an effective volume ratio for 360 000 LRGs over 3000 deg^2 with 70-90% completeness (1.5hr exposures per field) versus 400 000 ELGs over 1000 deg^2 (1hr exposure) with 80% completeness both assuming 9hr nights. This gives a total observing requirement of 167 nights for LRGs and 123 nights for ELGs, implying the effective volume ratios given in the sixth column. The last column is the effective volume ratio assuming the same number of nights for both projects.

Glazebrook et al. (2007) select "blue" emission line galaxies (ELGs) using SDSS and *GALEX* Far ultra-violet (FUV) and Near ultra-violet (NUV) imaging (Martin et al., 2005), for the *WiggleZ* BAO Dark Energy Survey. By using the reported $N(z)$ in Glazebrook et al. (2007, Figure 2) which has an average redshift of $z \simeq 0.6 \pm 0.2$ as well as their estimate of the clustering amplitude, we can make a comparison with our data. The clustering amplitude reported initially in Glazebrook et al. (2007) is $s_0 = 3.81 \pm 0.20\ h^{-1}$ Mpc (their Figure 3). However, it has recently been suggested that an improved *GALEX* ELG Selection for *WiggleZ* may give a higher ELG clustering amplitude of $\sim 6\ h^{-1}$ Mpc (C. Blake priv. comm.). We use this higher value, along with the appropriate redshift distributions for ELGs (truncated at redshift $z < 0.5$) and LRGs (from our Fig. 5.2) and assuming that bias is scale independent, we can calculate the effective volume surveyed using (e.g. Tegmark et al., 2006):

$$V_{\rm eff} = \int \left[\frac{n(\mathbf{r})\, P_g(k)}{1 + n(\mathbf{r})\, P_g(k)} \right]^2 dV. \tag{6.6}$$

where $n(\mathbf{r})$ is the comoving number density of the sample, (in units of h^3 Mpc^{-3}) and $P_g(k)$ is the value of the galaxy Power Spectrum at wavenumber k (with units of h Mpc^{-1}). For the LRG Survey we assume ≈360 000 redshifts are required with 100 fibres targeted on $i < 19.8$, redshift $z \simeq 0.55$ 2SLAQ LRGs with 90% completeness, to account for 5% redshift incompleteness and 5% stellar contamination, and 260 fibres on $19.8 < i < 20.5$ $z \simeq 0.7$ AAOmega LRGs with 70% completeness (15% redshift incompleteness and 15% stellar contamination). For the ELG Survey, we assume 360 fibres targeted on ELGs, as described above, with 80% redshift completeness. Therefore, we see that *(i)* a 167 night LRG survey would have greater than twice the effective volume of a 123 night ELG survey as envisaged by Glazebrook et al. and *(ii)* for equal telescope time, an LRG survey will sample 1.7 times the effective volume of an ELG Survey (see Table 6.2).

The above results are approximately in line with those of Parkinson et al. (2007) who present "Figures of Merit" (FoM) calculations to judge the optimality of different survey designs for future galaxy redshift-based BAO experiments. Their Fig. 6 and Table 10 in Sect 6.3 suggests that, generally speaking, for surveys with one low redshift bin, "red" galaxies are the optimal tracers to use for a BAO Survey using an AAOmega-style instrument.

Furthermore, recent work by Angulo et al. (2007), who used N-body simulations coupled with a flavour of the semi-analytical model GALFORM (Baugh et al., 2005), predict the accuracies obtained by future galaxy redshift surveys on measuring w and Δw where $w(z)$ is the Dark Energy Equation of State parameter. Taking values from Angulo et al. (2007, their Table 2) for their red sample C and their blue sample E which most closely represent the clustering amplitudes for the proposed LRG Survey and the *WiggleZ*, and scaling to their respective volumes, we can make an estimate for the accuracy of Δw for these surveys. Using these `BASICC` simulation results, we predict a value of $\Delta w = 8.4\%$ for our proposed VST-AAΩ *ATLAS* Survey versus a $\Delta w = 11.5\%$ for the *WiggleZ* Survey. Thus again on the basis of these simulations, the *WiggleZ* survey will take approximately twice the number of nights to achieve the same error on w as the proposed VST-AAΩ *ATLAS* LRG survey.

6.3 CONCLUSIONS

We have reported on the AAOmega-AAT LRG Pilot observing run to establish the feasibility of a large spectroscopic survey ("The VST-AAΩ *ATLAS* ") and present some of the first results from the new AAOmega instrument. We have confirmed that AAOmega represents at least a factor of four improvement in throughput in its red (> 5700Å) arm as compared to the old 2dF spectrographs. Utilising this new sensitivity, we observed Luminous Red Galaxies (LRGs) selected using single epoch SDSS *riz*-photometry in 3 fields including the COSMOS field, the COMBO-17 S11 field and the previously observed 2SLAQ Survey field, d05. Our main conclusions are:

- We detect 1270 objects in three fields, of which 587 are confirmed high-redshift LRGs. The mean redshift for each selection was $\bar{z} = 0.578 \pm 0.006$ from the *gri*-band selection with $17.5 < i_{\rm deV} < 20.5$, $\bar{z} = 0.681 \pm 0.005$ from the *riz*-band selection with $19.8 < i_{\rm deV} < 20.5$ and $\bar{z} = 0.698 \pm 0.015$ from the *riz*-band selection with $19.5 < z < 20.2$. At $i < 20.5$, 84% redshift completeness for LRGs was achieved in 1.5hr exposures in average conditions.

- We have compared our AAOmega spectroscopic redshifts to spectroscopic and photometric redshifts obtained by the 2SLAQ LRG Survey and COMBO-17 respectively. We find excellent agreement with the 2SLAQ spectroscopic redshifts, but a suggestion that there is a systematic tendency of the photometric redshifts to underestimate the spectroscopic redshifts.

- We find that a simple power-law model gives a best fit value of $r_0 = 9.03 \pm 0.93$ for our $\bar{z} = 0.681$ LRG sample, compared to $r_0 = 9.80 \pm 0.20$ for the $-21.2 < M_r < 23.2$ SDSS LRG sample and $r_0 = 7.30 \pm 0.34$ for the $\bar{z} = 0.55$ 2SLAQ LRG sample. This confirms that

high-redshift luminous red galaxies are very good large-scale structure tracers, similar to their lower redshift counterparts (Zehavi et al., 2005a; Eisenstein et al., 2005, and the 2SLAQ LRGs).

- Finally, this Pilot project shows that a large-scale AAOmega spectroscopic survey of highly biased $z \sim 0.7$ 360 000 LRGs over 3000deg^2, would be a very promising and competitive route in order to determine the baryon acoustic oscillations. In order to achieve the same S/N on BAO using AAOmega, an ELG redshift survey will require 1.7 times as many nights.

Having now seen there is strong evidence that LRGs evolutionary bias can be described by a simple "high-peaks" bias model, we now turn our attention to the evolution of the luminous matter in these galaxies. Previously the comment has been made that luminous red galaxies are suspected to be predominantly passively evolving, early-type galaxies. Having targeted galaxies in the COSMOS field, we now use proceed to use archival data to investigate this claim, and that is the basis for the following chapter.

CHAPTER 7

THE INFRARED AND MORPHOLOGICAL PROPERTIES OF $z \sim 0.7$ LRGS

Dear kindly social worker, They say go earn a buck. Like be a soda jerker, Which means like be a schmuck. It's not I'm anti-social, I'm only anti-work. Gloryosky! That's why I'm a jerk!

- ACTION, *Gee, Officer Krupke!* - West Side Story.

The final part of this thesis is concerned with *i*) using data from the *Spitzer* Space Telescope to study the Near Infrared (NIR) and Mid Infrared (MIR) properties of $z \sim 0.7$ Luminous Red Galaxies and *ii*) using data from the *Hubble* Space Telescope to study the morphological properties of redshift $z \sim 0.7$ Luminous Red Galaxies.

7.1 SCIENTIFIC MOTIVATION

With the ever-growing databases of massive galaxies from the SDSS MAIN and LRG galaxy surveys, we now can observe the properties of low, $z < 0.5$, LRGs to unprecedented accuracy (e.g. Hogg et al., 2002; Eisenstein et al., 2003).

Theoretically however, the existence of massive, passively–evolved ellipticals has been a major challenge for some models of galaxy evolution. For example, in the favoured hierarchical Cold Dark Matter (CDM) model of structure formation, such massive galaxies are expected to be formed at late times ($z \ll 2$) from the build-up of numerous, smaller galaxies. Also, to match e.g. the bright end of the luminosity function, recent theoretical models have to invoke prescriptions such as feedback from Active Galactic Nuclei (AGN) in order to stop star-formation in massive galaxies at low-z to better reproduce the observations discussed above (e.g. Kawata & Gibson, 2005; Scannapieco et al., 2005; Bower et al., 2006; Croton et al., 2006). Furthermore, the presence of high redshift, $z \gtrsim 2$, heavily obscured galaxies with extreme amounts (> 100 $M_{\odot}$/yr) of star formation, are now firmly detected using sub-millimetre observations (e.g. Smail et al., 1997). Meanwhile, the connection between star formation and luminous AGN (i.e. QSO) activity, due to the fuelling of the central supermassive black hole (SMBH) that seem ubiquitous in massive galaxies, and that of galaxy assembly at high redshift, remains tantalisingly elusive.

Thus, the connection between galaxies at high redshift, undergoing large amounts of star-formation and the most massive galaxies seen today with generally older, passive stellar populations, comes by studying $z \sim 0.5 - 1$ luminous red galaxies. The near ($\sim 1 - 5\mu$m) and mid ($\sim 5 - 30\mu$m) infrared wavelengths are vital for this study since by studying this population at these wavelengths, we can look for galaxies that might have obscured star formation activity. Furthermore, morphological information tells us about the dynamics of individual systems and combining these observations may give insights into the transformation of star-forming galaxies into passively evolving systems.

With the launch of the new suite of space satellites, such as *Spitzer*, *XMM-Newton* and *Chandra*, we have begun to survey the star-formation levels of $z > 1$ galaxies at unprecedented

levels, as well as make a census of dusty, optically obscured AGN at these redshifts. This, coupled with the spectacular performance of the Advanced Camera for Surveys (ACS) on the *Hubble Space Telescope* (HST), permits us to make connections regarding the links between central supermassive black holes, QSO activity, star-formation and morphologies in intermediate redshift LRGs.

The layout of this chapter is as follows. In Section 7.2 we give a very general overview of the *Spitzer* Space Telescope and the IRAC instrument. In Section 7.3 we note how we obtained the near infrared (NIR) and mid-infrared (MIR) *Spitzer* data in the COSMOS field and in Section 7.4 we report on the infrared colours of our AAOmega LRG Sample. In Section 7.5 we investigate the morphological properties of our redshift $z \leq 0.9$ sample and make some qualitative comparisons to recent theoretical work. We present the chapter's conclusions and look towards further work in Section 7.6.

7.2 THE *Spitzer* SPACE TELESCOPE

The *Spitzer* Space Telescope was launched on 25 August 2003. During its mission, *Spitzer* has obtained images and spectra by detecting the infrared emission radiated by objects between wavelengths of 3 and 180μm. Consisting of a 0.85-metre telescope and three cryogenically-cooled science instruments - the IRAC, IRS and MIPS - *Spitzer* is the largest space infrared telescope ever launched. The telescope is cooled to $\sim$ 5K (Werner, 2006) so that it can observe infrared signals without interference from the telescope's own heat. Also, the telescope must be protected from the heat of the Sun and the infrared radiation emitted by the Earth. To do this, *Spitzer* carries a solar shield and is in an Earth-trailing solar orbit. This orbit places Spitzer far enough away from the Earth to allow the telescope to cool without having to carry large amounts of cryogen.

A list of acronyms and abbreviations that will be used in the remainder of this chapter is given in Table 7.1 and further details regarding *Spitzer* can be found in Werner et al. (2004) and Werner (2006).

7.2.1 THE INFRARED ARRAY CAMERA

The Infrared Array Camera (IRAC) is a four-channel* camera carried by *Spitzer* that provides simultaneous 5.2 $\times$ 5.2 arcminutes images at 3.6, 4.5, 5.8, and 8.0μm. Two adjacent fields of view are imaged in pairs (3.6 and 5.8μm; 4.5 and 8.0μm) using dichroic beamsplitters. All four detector arrays in the camera are 256 $\times$ 256 pixels in size, resulting in a pixel size of $\sim$1.2 $\times$1.2 arcsec. The two short wavelength channels use indium antimonide (InSb) detector arrays and the two longer wavelength channels use arsenic-doped silicon (Si:As) detectors,

*The terms "channel" and bands are used interchangeably to describe the four IRAC wavelength windows.

AOR:	Astronomical Observation Request	A completed observation
BCD:	Basic Calibrated Data	Data image (FITS format)
BUNC:	Name of the error image associated with the BCD	FITS format
GAIA:	Graphical Astronomy and Image Analysis	Image analysis software
IRAC:	The Infrared Array Camera	*Spitzer* instrument
IRS:	The Infrared Spectrograph	"
MIPS:	The Multiband Imaging Photometer	"
MOPEX:	Mosaicking and Point Source Extraction	*Spitzer* software
SSC:	*Spitzer* Science Center	Pasadena, California.

Table 7.1: A list of *Spitzer* names, acronyms and abbreviations. A brief description is given in the right hand column.

Wavelength/μm	Array Type	Field of View	Pixel Size (arcsec)
3.6	InSb	$5.21' \times 5.21'$	1.221
4.5	InSb	$5.18' \times 5.18'$	1.213
5.8	Si:As	$5.21' \times 5.21'$	1.222
8.0	Si:As	$5.21' \times 5.21'$	1.220

Table 7.2: Details for the Infrared Array Camera (IRAC) onboard *Spitzer* .

these details are summarised in Table 7.2. The IRAC instrument is well suited to our needs because of its high sensitivity, relatively large field of view and simultaneous four-colour imaging. Further details about IRAC can be found in Fazio et al. (2004), the *Spitzer Observer's Manual* and the *IRAC Data Handbook*, the latter two sources can be found on the SSC website `http://ssc.spitzer.caltech.edu`.

7.3 *Spitzer*, IRAC DATA AND THE COSMOS FIELD

Having specifically targeted and obtained spectra using AAOmega for intermediate, $z \approx 0.7$ LRGs in the COSMOS field, we now present technical details on how *Spitzer* IRAC data was obtained and analysed.

7.3.1 LEOPARD

From the SSC website, the *Leopard* archive software, Version 6.1, was downloaded and run. Using Leopard and through the *Query* and *By Campaign/Observer* menu, the Program Title "S-COSMOS: The Spitzer Deep Survey of the HST COSMOS 2-degree ACS field" (ID number 20070) was selected and data taken by IRAC in all four IRAC bands was obtained. A choice of three epochs was possible and on inspection, Epoch 1 was seen to be the most complete. Consequently sixteen regions, named COSMOS_1 through COSMOS_16, were downloaded and unzipped, with a total of 1 660 BCD frames being stored. For some, still unknown reason, a significant region of COSMOS_16 was found to be incomplete due to genuine lack of data, rather than download issues. However, since only one object detected by AAOmega had a secure ($Q_{\rm op} \geq 3$) redshift in this incomplete area, we proceed without making any major adjustments. Details of the downloaded data are given in Table 7.3.

7.3.2 DATA REDUCTION AND MOPEX

The individual BCDs for all four channels were then reduced and mosaiced using the MOPEX software, version 030106 (with additional help provided by J. Geach). There are essentially two ways to compensate for image artifacts in the fames and mosaic: 1) The fully interactive mosaicking method run with the mosaic.pl script and a "namelist" file provided in the MOPEX

Field Designation	RA	DEC	AOR Key
COSMOS_1	10h 02m 58.0s	+02d 52m 30.0s	15543296
COSMOS_2	10h 01m 18.0s	+02d 52m 30.0s	15543040
COSMOS_3	09h 59m 38.0s	+02d 52m 30.0s	15542784
COSMOS_4	09h 57m 58.0s	+02d 52m 30.0s	15542272
COSMOS_5	10h 02m 58.0s	+02d 27m 30.0s	15541248
COSMOS_6	10h 01m 18.0s	+02d 27m 30.0s	15540736
COSMOS_7	09h 59m 38.0s	+02d 27m 30.0s	15540224
COSMOS_8	09h 57m 58.0s	+02d 27m 30.0s	15539968
COSMOS_9	10h 02m 58.0s	+02d 02m 30.0s	15539712
COSMOS_10	10h 01m 18.0s	+02d 02m 30.0s	15546368
COSMOS_11	09h 59m 38.0s	+02d 02m 30.0s	15546112
COSMOS_12	09h 57m 58.0s	+02d 02m 30.0s	15545856
COSMOS_13	10h 02m 58.0s	+01d 37m 30.0s	15545344
COSMOS_14	10h 01m 18.0s	+01d 37m 30.0s	15544832
COSMOS_15	09h 59m 38.0s	+01d 37m 30.0s	15544576
COSMOS_16	09h 57m 58.0s	+01d 37m 30.0s	15543808

Table 7.3: The *Spitzer* COSMOS IRAC fields, from Leopard (Version 6.1) for all four channels. AOR Key is an identifier used in Leopard.

software or 2) using the easymosaic.pl script which essentially has a namelist file hardwired in. The namelist file is a configuration file which contains several module blocks of various input parameters and settings used in the mosaicking process. Each module block can be toggled on or off, and if toggled on, a set of input parameters must be specified. The difference between running in the fully interactive mode and using the easymosaic script, is that seeing as the namelist file is 'hardwired-in', no freedom of module or parameter choice is left for the user when using easymosaic.

Due to lack of experience with the *Spitzer* pipeline and also time constraints, the easymosaic.pl route was preferred with the difference compared to a full-blown analysis negligible for our purposes (J. Geach; priv. comm.). The easymosaic procedure produces four mosaic .fits images; 1) the un-reduced mosaic.fits; 2) the coverage map mosaic_cov.fits, 3) the uncertainty mosaic based on the data scatter mosaic_std.fits and 4) median_mosaic.fits. The median_mosaic.fits image is the primary science frame which should have been successfully reduced and cleaned (e.g. cosmic-rays rejected).

We show the results of this process in Figure 7.1 which gives the entire 1.4×1.4 deg^2 COSMOS field in the 3.6μm channel, while Figure 7.2 is a zoom-in showing the large-scale structure reported at redshift $z \approx 0.73$ by Guzzo et al. (2007). In the latter figure the redshifts of our AAOmega targeted objects are also given but care has to be taken as not all redshifts are $Q_{\rm op} \geq 3$.

After mosiacking the 8.0μm data, we saw that the background was upto $\times 70$ higher and much more variable across the field than for the 3.6 and 4.5μm cases. Since we do not know the reason for this, we have only attempted to deal with this problem by using a local background in the aperture photometry. This effectively assumes the problem is in the bias subtraction

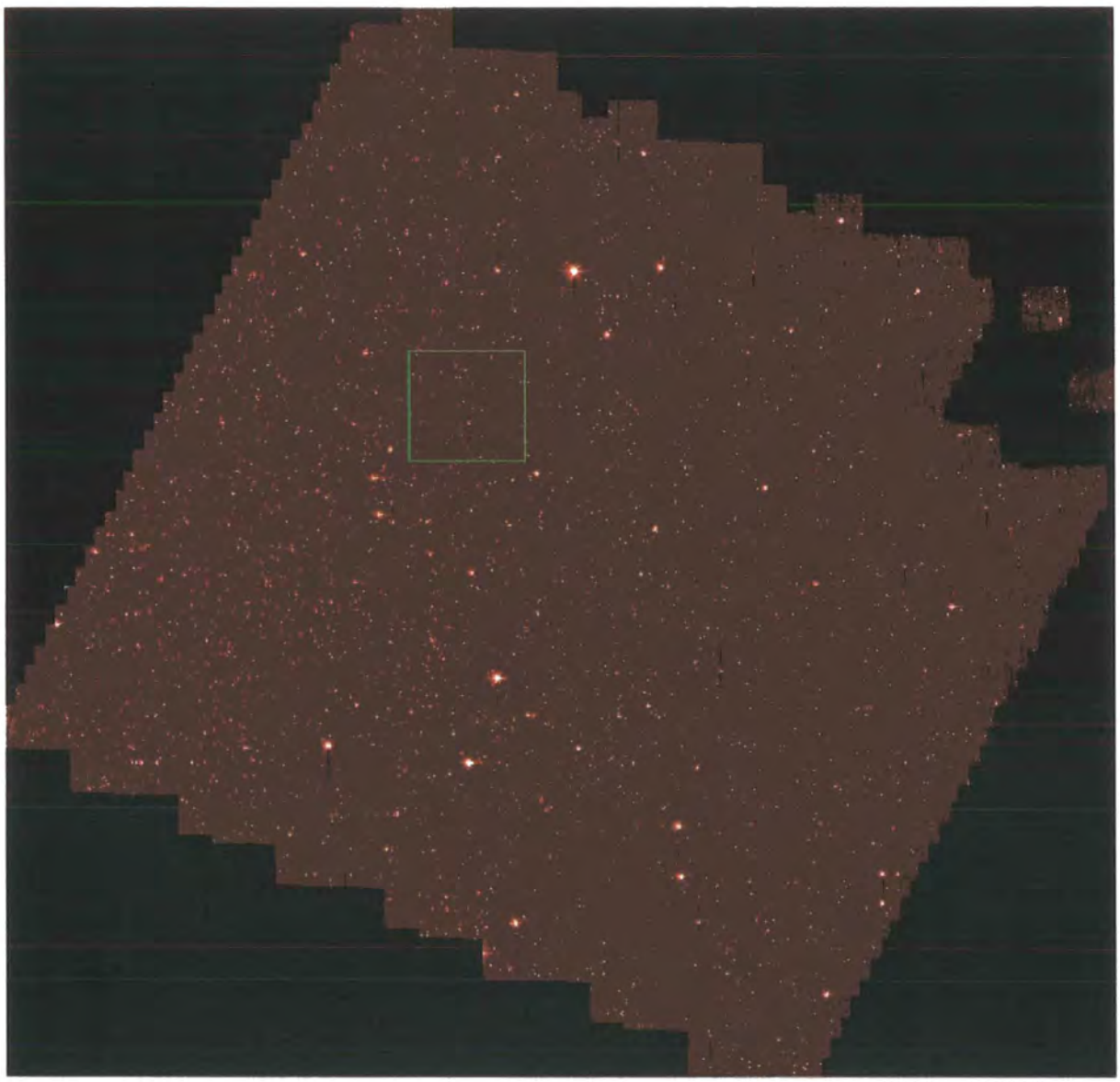

Figure 7.1: The COSMOS field at 3.6μm. Note the missing data in COSMOS_16. Also note that the white dots are not cosmic rays but actual detections of bright sources. The green box gives an indication of the region zoomed in for Figure 7.2. The cardinal directions run parallel/perpendicular to the sides of the imaged area with North increasing towards the top left-hand corner and East increasing downwards towards the bottom left-hand corner.

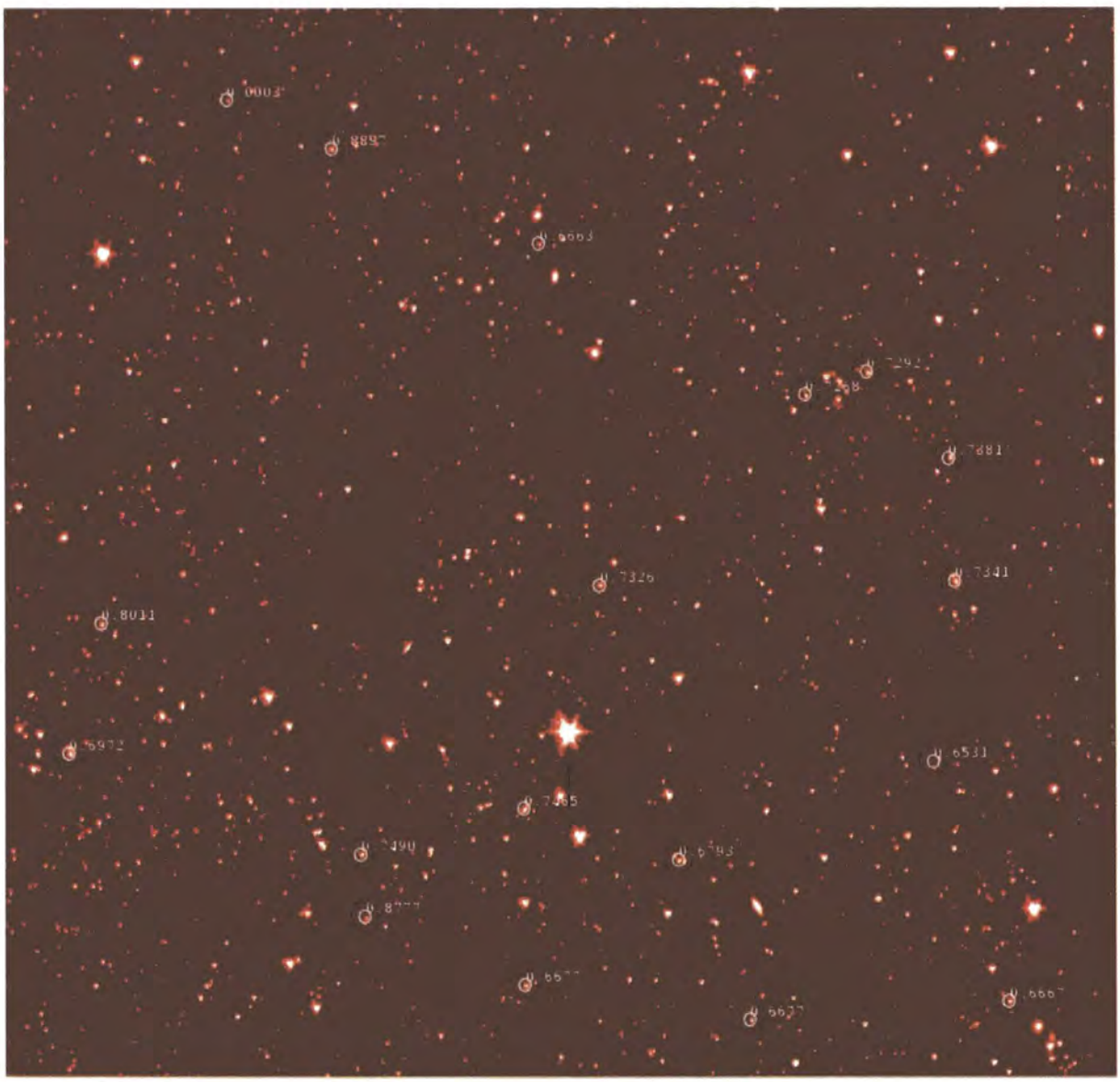

Figure 7.2: A zoom in on the COSMOS field, showing the large structure at redshift $z \sim 0.73$ as reported in Guzzo et al. (2007) in the 3.6μm band. Redshifts from AAOmega are given but not all redshifts are $Q_{\rm op} \geq 3$.

rather than the gain of the detector.

7.3.3 APERTURE PHOTOMETRY

Details of the procedures used for performing aperture photometry on the COSMOS field at 3.6μm, 4.5μm and 8.0μm are now given.[†]

PHOTOM is a *Starlink* package (Eaton et al., 2002) for measuring the sky corrected magnitudes and fluxes of astronomical objects, within circular and elliptical apertures, using either the aperture or optimal extraction algorithms. We use PHOTOM (version 1.9-0) running in AUTOPHOTOM mode, for aperture extraction on our 3.6, 4.5 and 8.0 μm COSMOS data with the steps below:

1. Open the *Spitzer* median_mosaic.fits with GAIA.

2. In GAIA, use the *Image Analysis* menu, choosing *Positions* and *Import Plain text file.*

3. Open your input file, which will have a list of objects and their positions in Right Ascension and Declination. For our purposes, this was a file of 5 columns, Object ID, RA, Dec, redshift and $Q_{\rm op}$. Name your output file and then select UPDATE, which will convert the RAs and Decs into image x and y-positions (X_POS and Y_POS).

4. Convert the .fits file into .sdf format, e.g. using the *Starlink* `fits2ndf` tool within the CONVERT package.

5. Start the *photom* package:

   > `photom`

[†]Much thanks is due to P. Draper and N. Metcalfe for their help here as well as the information on the SSC website.

6. Run the *autophotom* package:

   > `autophotom image_name INFILE OUTFILE.`

   Details are given in the text below for a description of the format of the INPUT/OUTPUT files. Our command line was:

   `> autophotom COSMOS_1thru16_3pnt6 AUTOPHOTOM_INFILE_temp4`

   `AUTOPHOTOM_OUTFILE_temp4_v2 SKYEST=2 SKYMAG=20.09`

   and we give further details below on the choice of the AUTOPHOTOM options used here.

7. Study the `outfile`. Note the MAG, MAGERR and SKY values.

8. If the aperture extraction has been successful, then the 4th and 5th columns in the output file are the objects' magnitude and magnitude error respectively.

For Aperture Extraction, the input/output file must contain one line per object that has the following information: INDEX XPOS YPOS MAG MAGERR SKY SIGNAL CODE MAJOR ECCEN ANGLE POSITIONS SHAPE, where the fields have the meanings given in Table 7.4. Values that are unknown initially (MAG, MAGERR, SKY, and SIGNAL) are set to 0.0 and the derived values are used to replace these fields on exit. The CODE field is set to "OK" initially. The POSITIONS field has either the value "annulus" or "regions", to indicate how the sky regions are determined. The SHAPE field should be set to "circle" or "ellipse" to indicate the aperture shape. In our case, "annulus" is chosen of the POSITIONS and "circle" for SHAPE. Other lines in the Input file may be comments or definitions of the sky regions. Comment lines start with the "#" character, sky regions either with "#ANN" or "#SKY". The format for these lines are:

#ANN INDEX INNER_SCALE/SIZE OUTER_SCALE/SIZE

INDEX	=	unique integer identifying this object.
XPOS	=	X coordinate of object.
YPOS	=	Y coordinate of object.
MAG	=	current magnitude of object.
MAGERR	=	current error in magnitude of object.
SKY	=	current estimate of sky value for object.
SIGNAL	=	current estimate of the total count in object.
CODE	=	current object status.
MAJOR	=	length of semi-major axis of aperture.
ECCEN	=	eccentricity of object aperture.
ANGLE	=	position angle of object aperture.
POSITIONS	=	how the sky regions are determined.
SHAPE	=	shape of the aperture.

Table 7.4: The *AUTOPHOTOM* IP/OP file format.

Channel	Flux density/Jy	Zero Points	m(AB) = m(Vega) +
1	280.9 ± 4.1	17.30	2.79
2	179.7 ± 2.6	16.81	3.26
3	115.0 ± 1.7	16.33	3.73
4	64.13 ± 0.9	15.69	4.40

Table 7.5: IRAC zero magnitude flux densities in Janskys and the zero-points are in AB magnitudes. Table expanded from Reach et al. (2005), `http://ssc.spitzer.caltech.edu/irac/calib/` and `http://ssc.spitzer.caltech.edu/tools/magtojy`.

The # is used so that other programs can skip over this information. If the POSITIONS field of an object is set to "annulus", then at least one "#ANN" line must be present for this object, this defines the scales or sizes for the inner and outer loci of the sky region. We choose the inner radius to be 5.0 and the outer radius to be 25.0. Checks showed that the magnitudes obtained were relatively insensitive to these values once you were away from the central galaxy light and the outer value wasn't too large ($\lesssim 50$).

SKYEST selects the estimator to be used to evaluate the background level in the sky aperture. By setting SKYEST=2, this toggles on the "Mean with 2 sigma rejection" mode, i.e. all pixels with data values within 2 standard deviations of the mean are averaged.

IRAC images have units of MegaJanskys per steradian (MJy/sr). To convert these into flux densities per pixel units, one has to convert steradians into arcseconds squared and then multiply by the area of the pixel. As given by Table 7.2, for a BCD frame the pixel area is

approximately 1.22 arcseconds squared, whereas in the pipeline mosaic the pixel size by default is 1.2 arcseconds squared exactly. So for the pipeline mosaic a pixel value needs to be multiplied by

$$\frac{1 \times 10^{12}\,\mu\text{Jy}}{4.2545 \times 10^{10}\,\text{arcsec}^2} \times 1.2\,\text{arcsec} \times 1.2\,\text{arcsec} = 33.8464\,\mu\text{Jy per pixel} \tag{7.1}$$

to obtain flux densities in units of μJy per pixel.

Once the flux density of your source in the given aperture is measured, you can convert from Jy into magnitudes using the relation

$$m_{\text{obj}} = m_{\text{zero}} - 2.5 \times \log_{10}(S) \tag{7.2}$$

where m_{obj} and m_{zero} are the object and zero-point magnitudes respectively and S is signal. Thus, using the zero-magnitude flux densities in Table 7.5, a zero-magnitude object in the 3.6μm band should have $S = 280.9\,\text{Jy}/33.84638 \times 10^{-6}\,\text{Jy} = 8.30 \times 10^6$ counts. Therefore, equation 7.2 becomes

$$\begin{aligned} 0 \quad &= m_{\text{zero}} - 2.5 \times \log_{10}(8.30 \times 10^6) \\ \Longrightarrow \quad & m_{\text{zero}} = 17.30 \end{aligned} \tag{7.3}$$

with the other magnitude zero-points given in Table 7.5. Further details about the IRAC magnitude system, absolute calibration and magnitude zero-points are given in Reach et al. (2005).

Finally, for use with SDSS bands, a conversion is needed from the IRAC bands which have a Vega magnitude system to those of the SDSS which use the AB magnitude system. This conversion is 2.79 in Channel 1, giving the value for SKYMAG as 17.30 + 2.79 = 20.09 (as used by *autophotom*).

7.4 NEAR INFRARED COLOURS OF $z \leq 0.9$ LRGS

Having downloaded and performed aperture photometry on the COSMOS field using 3.6, 4.5 and 8.0 μm data as described above, we now endeavour to look for trends of near infrared colours with redshift, using the spectroscopic redshifts we obtained from the AAOmega LRG Pilot observations.

Figure 7.3 shows the [i-3.6μm] colour, where i is the SDSS model magnitude and our "τ = 1 Gyr" and "Single Burst" Bruzual and Charlot model tracks are also plotted plotted. By qualitatively studying Fig. 7.3 we can see that both the models fit the data well and to within the errors associated with the measured infrared magnitude and subsequent colour determination.

In Figure 7.4 we show the near infrared colour of [3.6μm - 4.5μm] versus redshift. We again plot our "τ = 1 Gyr" and "Single Burst" models. What can be seen immediately from these near IR bands is that the size of the magnitude error bars, which are derived from the 3.6μm measurements only, dominate the signal. We can also see that there seems to be no obvious [3.6μm - 4.5μm] colour cut that separates stellar and extra-galactic objects. Although both models have very similar colour trends that fit the data well, we note that the majority of the points (for both stars and galaxies) seem to have [3.6μm - 4.5μm] colours redder than those predicted by the model tracks. One initial explanation of this could be connected with the size and shape of the aperture used to do the photometry. It is conceivable that a slight change to these parameters could produce the $\approx 0.05 - 0.1$ magnitude colour shift that would allow the models to fit the data more successfully.

In Figure 7.5 we show the near infrared colour of [3.6μm - 8.0μm] versus redshift. Again we see the substantial magnitude errors dominating the measured signal. Even taking this into account, it seems as if there are a host of points at redshifts of $z \approx 0.65$ and [3.6μm -

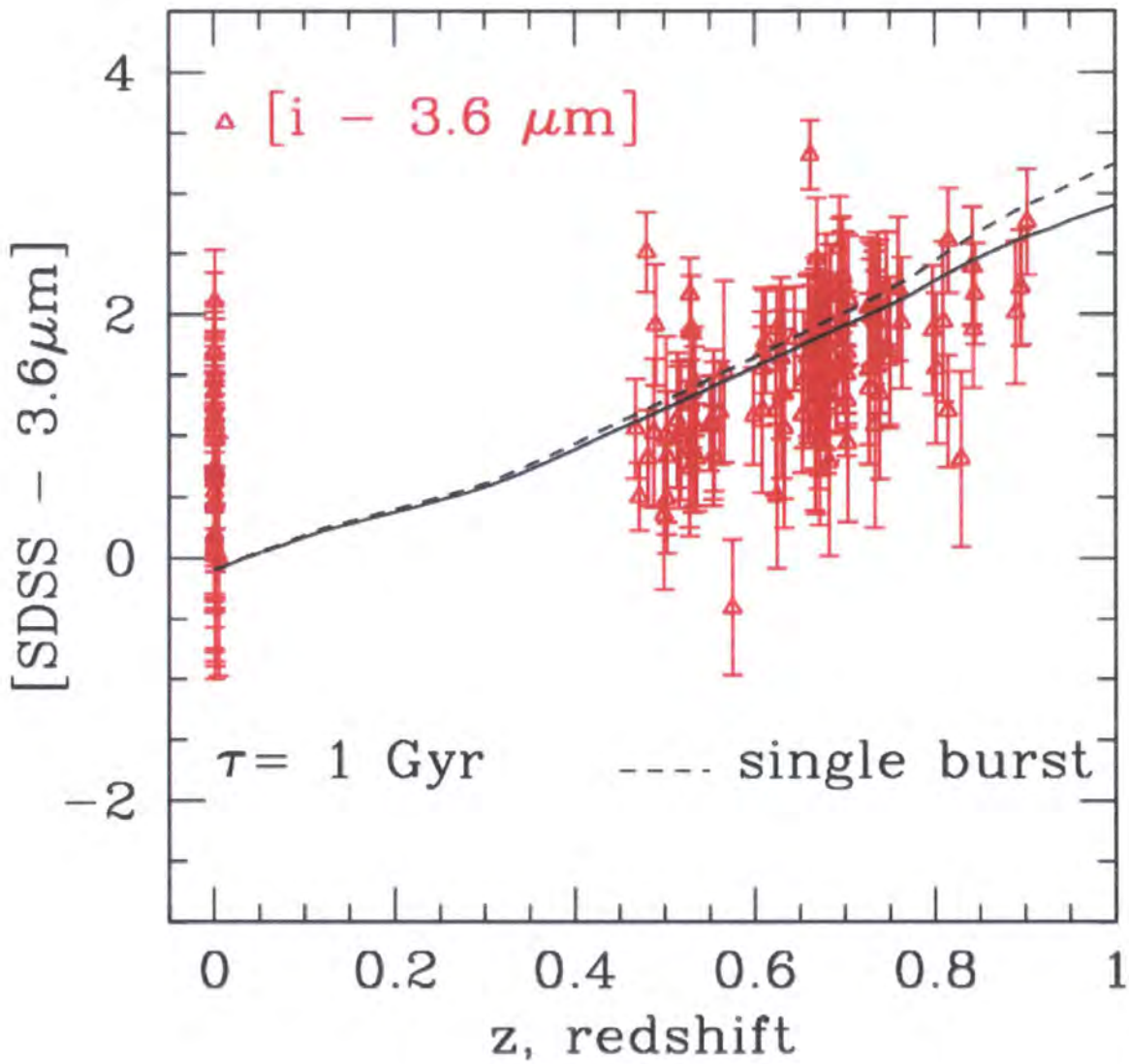

Figure 7.3: SDSS i-band - 3.6μm colours for AAOmega COSMOS LRGs as a function of redshift. The solid line is for the "$\tau = 1$ Gyr" model, while the dashed line is the "Single Burst" model (details in Chapter 2).

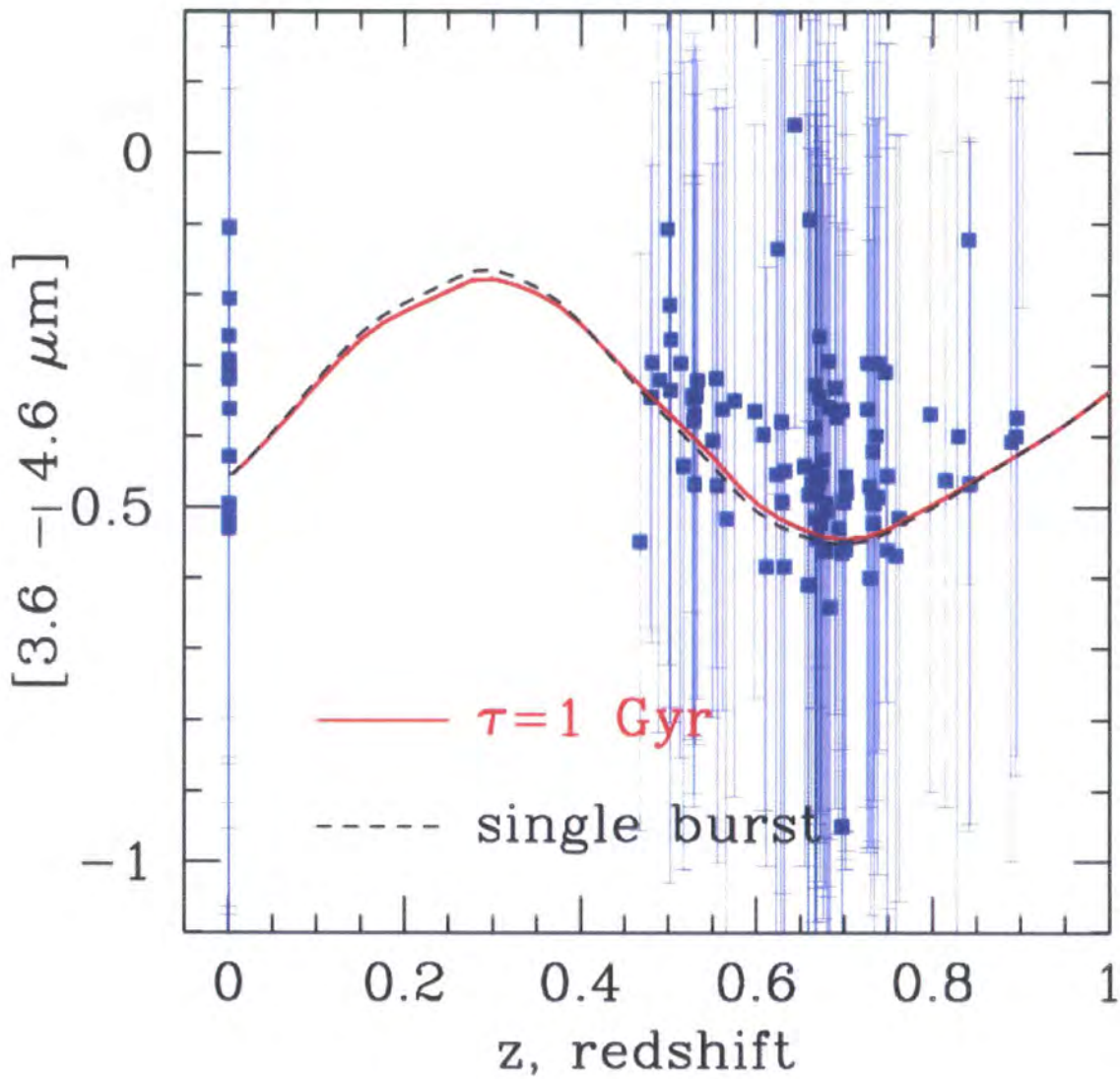

Figure 7.4: 3.6μm - 4.5 μm Near Infrared colours for AAOmega COSMOS LRGs as a function of redshift. The solid, red line is for the "$\tau = 1$ Gyr" model, while the dashed, black line is the "Single Burst" model (details in Chapter 2).

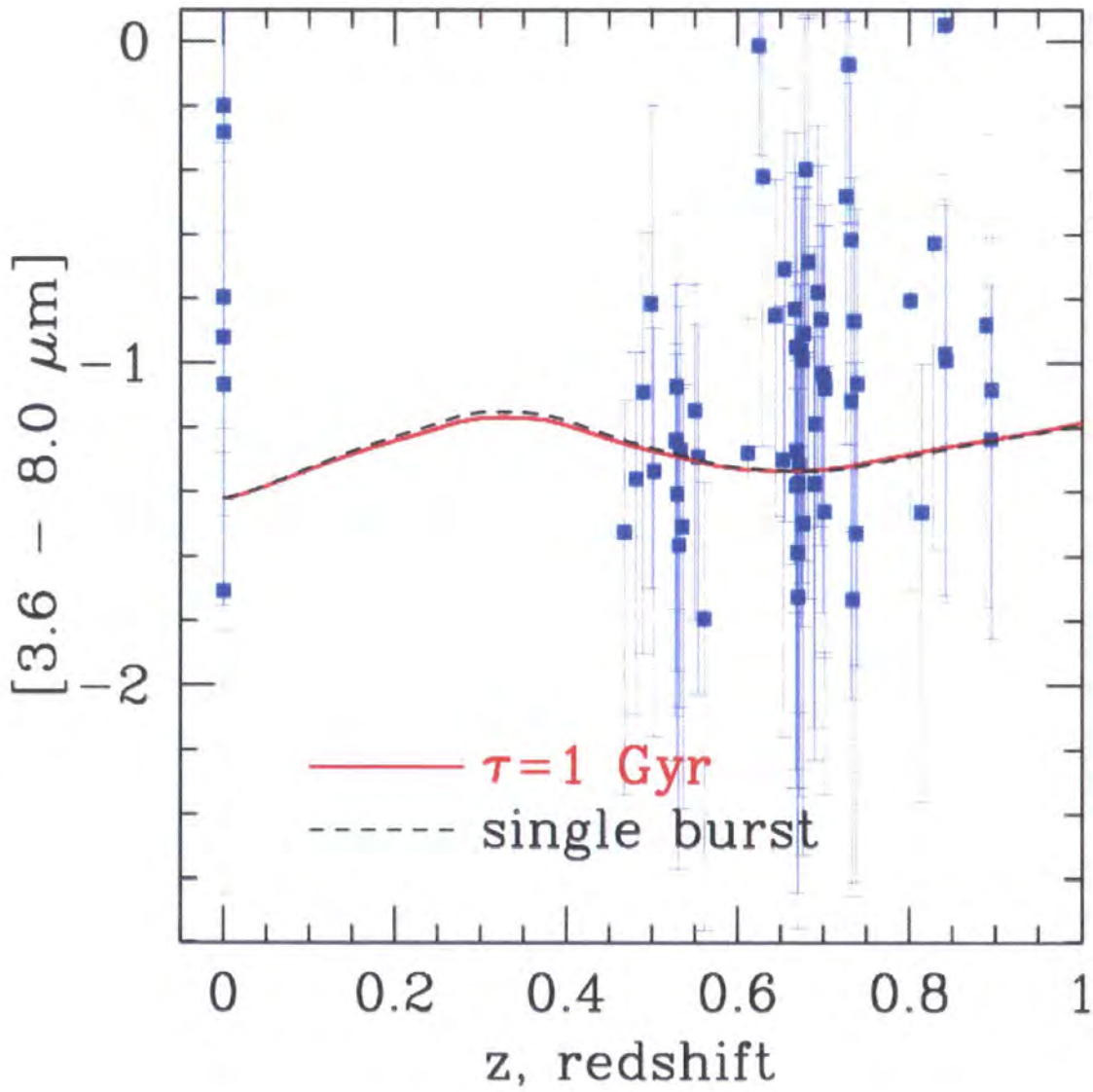

Figure 7.5: 3.6μm - 8.0 μm Near Infrared colours for AAOmega COSMOS LRGs as a function of redshift. The solid, red line is for the "$\tau = 1$ Gyr" model, while the dashed, black line is the "Single Burst" model (details in Chapter 2).

8.0μm]= -0.8 to -1.0 that are not consistent with either set of model tracks. Exactly why this is the case remains currently unexplained and requires further investigation. There is also a discrepancy in the number of points plotted between Figures 7.4 and 7.5. We believe this is due to the 8.0μm sources simply being too faint to be detected. For reasons still unknown, when downloading the 8.0μm data, instead of receiving one set of BCD frames with an exposure time of 100 seconds (as was the case for Channels 1, 2 and 3), two sets of BCD frames were recovered, each of 50s. After several unsuccessful attempts, we were then able only to combine the frames for one 50s set, rather than double up. This might have contributed to the fact that $\sim$ 25% of the objects detected in 3.6 and 4.5μm are no detected at 8.0μ.

Figure 7.6 shows the $(r-z)-(z-3.6\mu\text{m})$ colour-colour plane for the COSMOS objects. This time, in the two-colour plane, the stellar locus for faint M-stars appears to be located away from the main extra-galactic sample. A visual inspection suggests that the "$\tau = 1$ Gyr" model might predict the colour-colour redshift evolution of the LRGs more accurately but most of the information differentiating the models is coming from the $(r-z)$ colour. There are a few "outliers" in the $r-z-3.6\mu$m-plane but again this is more from the $(r-z)$ colour. The morphologies of these outliers can be examined to see if they are typical "early-type" galaxies. This gives us the motivation for the next section.

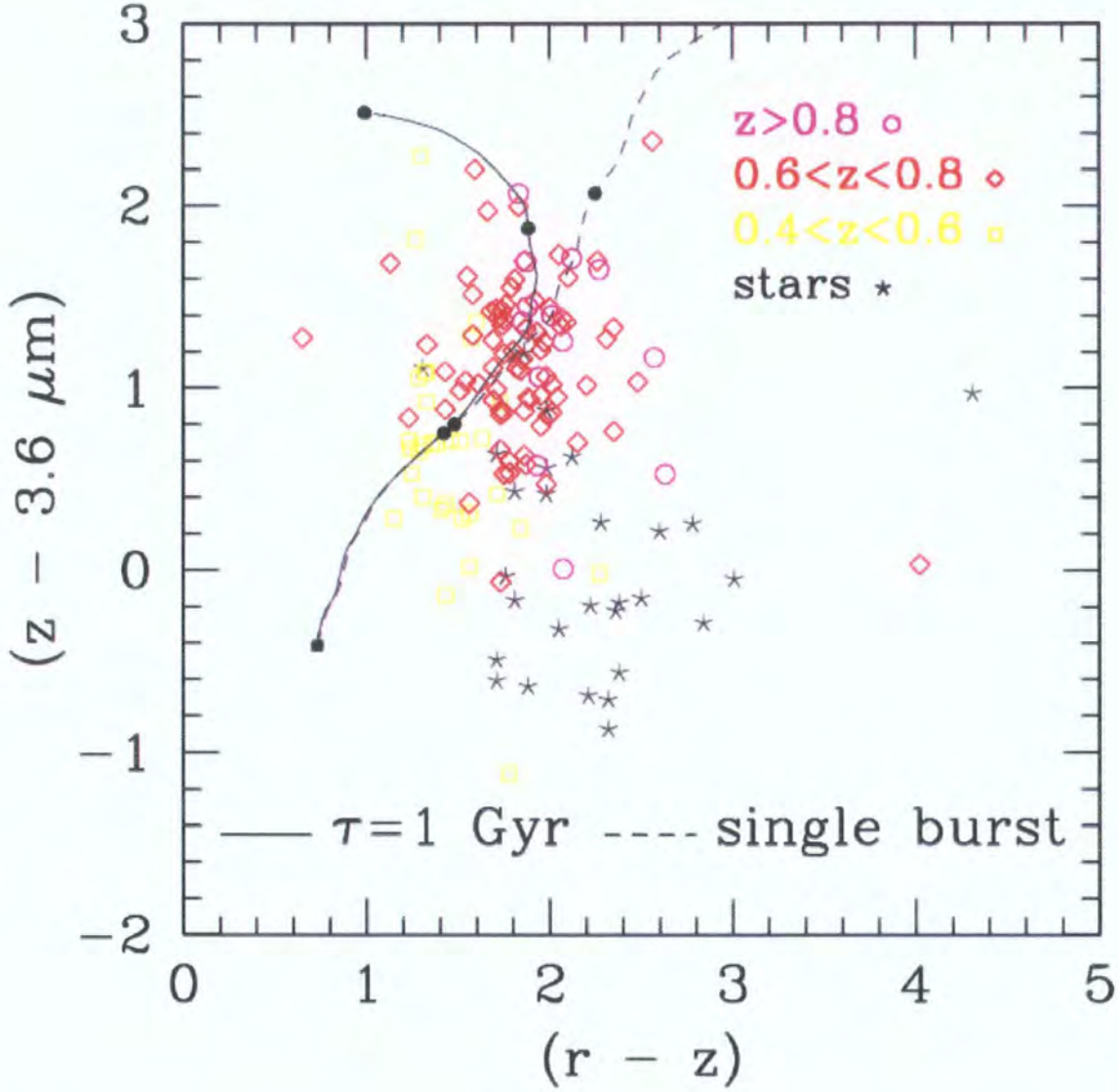

Figure 7.6: $r - z - 3.6\mu$m colour-colour plane for AAOmega COSMOS LRGs. Galaxies with confirmed redshifts $0.4 < z < 0.6$ are given as open, yellow, squares; Galaxies with confirmed redshifts $0.6 < z < 0.8$ are given as open, red, diamonds; Galaxies with confirmed redshifts $z > 0.8$ are given as open, magenta, circles; The black stars are objects with confirmed stellar spectra. The solid line is for the "$\tau = 1$Gyr" model, while the dashed line is the "Single Burst" model. The corresponding redshift $z = 0$ point for the models is located towards the bottom left corner (solid square). The solid circles on the model tracks then give the redshift $z = 0.5, 1.0$ and 1.5 points.

7.5 MORPHOLOGIES

The COSMOS field has been imaged using the Advanced Camera for Surveys (ACS) instrument onboard the *Hubble Space Telescope* (see Scoville et al. (2006b) for further details regarding the *HST* - COSMOS imaging campaign).

Using data courtesy of the NASA/ IPAC Infrared Science Archive[‡] we obtained ACS images for 80 out of 156 LRGs that we had confirmed spectroscopic redshifts. Several LRGs that lie in the 2 degree field of 2dF/AAOmega were lost since the COSMOS field is 2 square degrees and thus $\simeq 1.4$ degrees on a side. Some LRGs were also lost due to the IPAC Infrared Science Archive simply not having ACS coverage. All 80 galaxies were visually inspected and given a simple morphological classification. We classified our galaxies into 4 classes, based on the standard Hubble types - an *Elliptical* class where a galaxy showed strong signs of a spheroidal morphology; an *S0* class where there were indications of a lenticular nature and a *Spiral* class where spiral arms were clearly seen. The *Other* class was used when a galaxy could not be placed easily into the previous three classes. Within each class, a second designator was used, d, for disturbed, to note when a galaxy might have a clear underlying classification, but also showed signs of a recent disturbance. The results from this simple classification are given in Figure 7.7.

From there we clearly see that the majority, 65%, of the total sample are relaxed, well evolved, elliptical systems. Furthermore, when we split the sample into high ($z > 0.55$) and low ($z < 0.55$) samples, we see that this fraction does not significantly change (66% vs. 63% respectively). We compare and contrast our results - where we have one dominant population

[‡]which is operated by the Jet Propulsion Laboratory, California Institute of Technology, under contract with the National Aeronautics and Space Administration

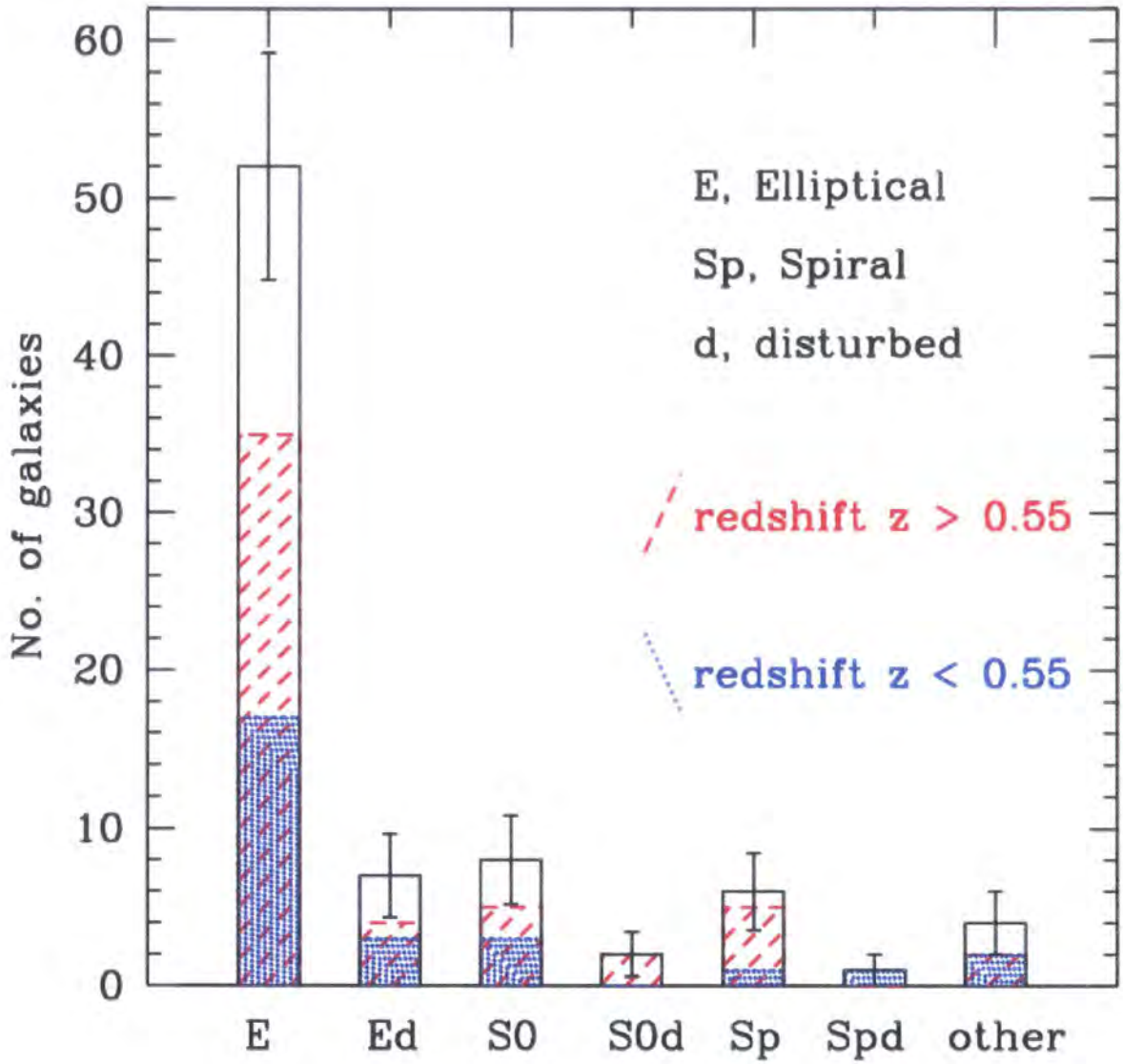

Figure 7.7: Morphologies of the AAOmega COSMOS LRGs. The blue, dotted histograms are for objects with confirmed spectroscopic redshifts of $z < 0.55$. The red, hatched histograms are for objects with redshifts of $z > 0.55$. The morphologies are classified according to a standard Hubble-type. E standing for elliptical, S0 for lenticular, and Sp for Spiral. A "d" after one of these classes means that the galaxy had a regular underlying morphology but looked recently disturbed. The "other" class is for objects that can not obviously be placed in any of the other three categories.

- with those of the K20 galaxy redshift survey Cimatti et al. (2002) who found that EROs at $z \approx 1$ are split roughly equally into 2 populations, one passively evolving and the other dusty and star-forming (see also Metcalfe et al., 2006).

This observed low ($z < 0.55$) redshift fraction of 63% for elliptical galaxies is broadly in-line with Almeida et al. (2007, in prep.) who use two flavours of semi-analytical models to predict LRG properties. These authors claim that 59% and 58% of LRGs are early-types at $z = 0.5$ using the Baugh et al. (2005) and Bower et al. (2006) models, respectively. A direct comparison is difficult since Almeida et al. use the "bulge-to-total stellar mass" ratio, B/T, to define morphology (where an object with B/T ≥ 0.6 is classed as early-type). The difference between their working redshift of $z = 0.5$ versus our low-z observed sample with $\bar{z} \sim 0.52$, should be negligible for our purposes.

A discrepancy seems to come when we consider the other morphological classes. Almeida et al. suggest a Spiral (B/T < 0.4) ratio of 37% (21%) for the Baugh et al. (2005) (Bower et al., 2006) models, compared to our measured fraction of $< 10\%$. These authors suggest the explanation to their significant fraction of late-type, disk-dominated systems is due to their model LRGs exhibiting significant dust extinction. (Almeida et al. also suggest the difference between the late-type fractions of the two models is due to differences in the mass resolution of the halo merger trees used by the two models.) We would like to put a 'simpler' explanation forward to explain the differences between our observations and the models and that is there could well be severe selection effects in play. Our sample should not be thought of as statistically complete and that the morphological signature could well be affected by e.g. fibre magnitude cuts which could preferentially select *against* objects with an exponential luminosity profile. That said, we know LRGs at low redshift are predominantly early-types (Eisenstein et al.,

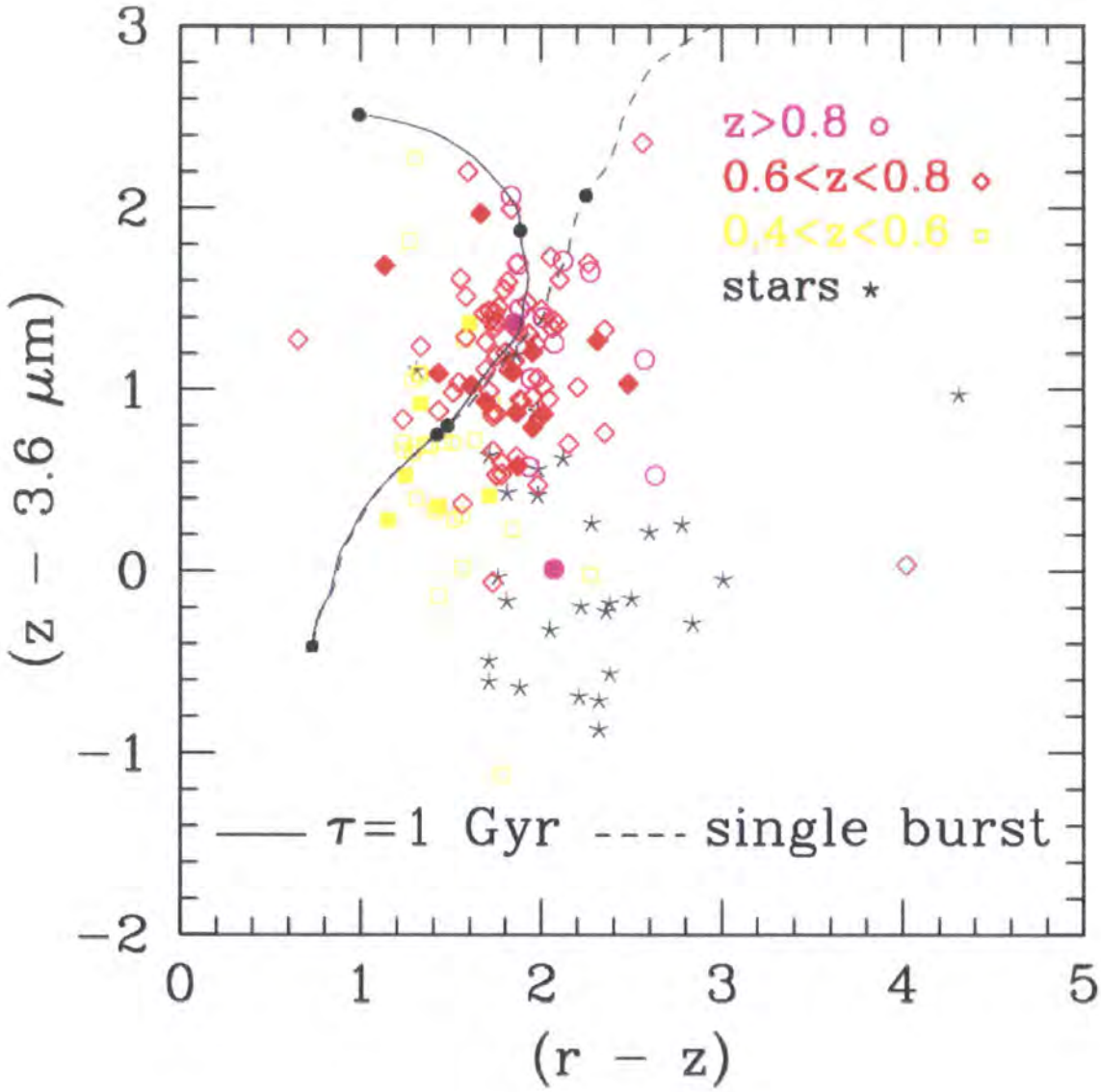

Figure 7.8: $r - z - 3.6\mu$m colour-colour plot for AAOmega COSMOS LRGs with the same colour scheme as in Figure 7.6 but this time objects with non-Elliptical (i.e. S0, Spiral or Other) morphologies are given by filled yellow, red or magenta points; elliptical objects are given as similarly coloured open symbols.

2003) and there is good evidence that suggests the morphological Hubble Tuning Fork sequence is well in place by $z \sim 1$ (e.g. Schade et al., 1999; Conselice et al., 2004).

The original motivation for this morphological classification was to see if the $r - z - 3.6$ "outlier" objects showed regular morphologies. As such, we show Figure 7.8 where the filled points now indicate which galaxies have been classed as having S0, Spiral or Other morphologies. Although it appears that 2 of the points in the top-left hand region of the $r - z - 3.6$ plane have non-Elliptical morphologies, there is no strong differential in the $r - z - 3.6$ plane between galaxies classed as having Elliptical and non-Elliptical morphologies. Note though how the bluest $z > 0.8$ point is some distance from the model tracks and has a non-Elliptical morphology.

Figure 7.9 shows the near-IR [3.6μm- 8.0 μm] colours for galaxies with Elliptical (open red squares), non-Elliptical (blue stars) and Spiral (green circles) morphologies. We can see that the 5 galaxies that are classified as spirals from ACS imaging data, have 3.6μm and 8.0 μm detections that are *redder* than both the general population and the non-Elliptical population. A possible explanation would be to suggest that these galaxies classed as having Spiral morphologies might be undergoing a period of star formation and hence, the reddening that we observe, could be coming from dust emission due to obscured star formation. Since we originally selected our sample in the optical to be a passively evolving, early-type population, it would be little surprise if the predominant morphological type in the near IR was also early-type. Thus any deviation from a regular, elliptical morphology that does arise potentially needs to be explained, with one idea being that we are seeing galaxies with Spiral morphologies transform, via S0s, into the Ellipticals we see today. However, it should be stressed that this is currently a tentative explanation which would need further investigations to confirm.

Figure 7.10 show the $r - i - z$ plane where the galaxies are also split into Ellipticals (shown

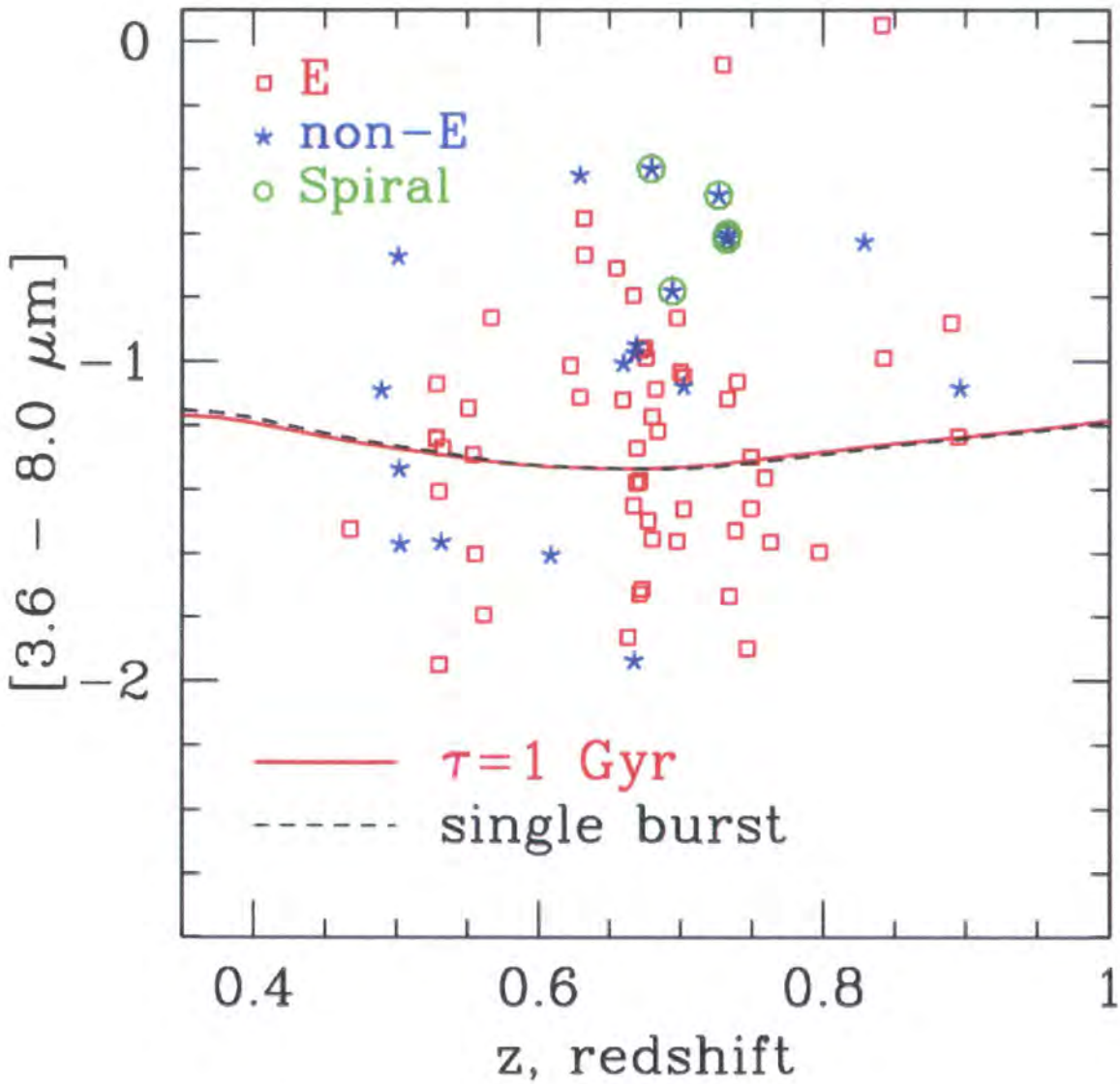

Figure 7.9: 3.6μm - 8.0 μm near Infrared colours as a function of redshift with morphologies. The open red squares give galaxies classed as Elliptical, the blue stars give galaxies that were not classed as Elliptical and the green circles show galaxies classed as having a Spiral morphology. The solid, red line is for the "τ = 1 Gyr" model, while the dashed, black line is the "Single Burst" model.

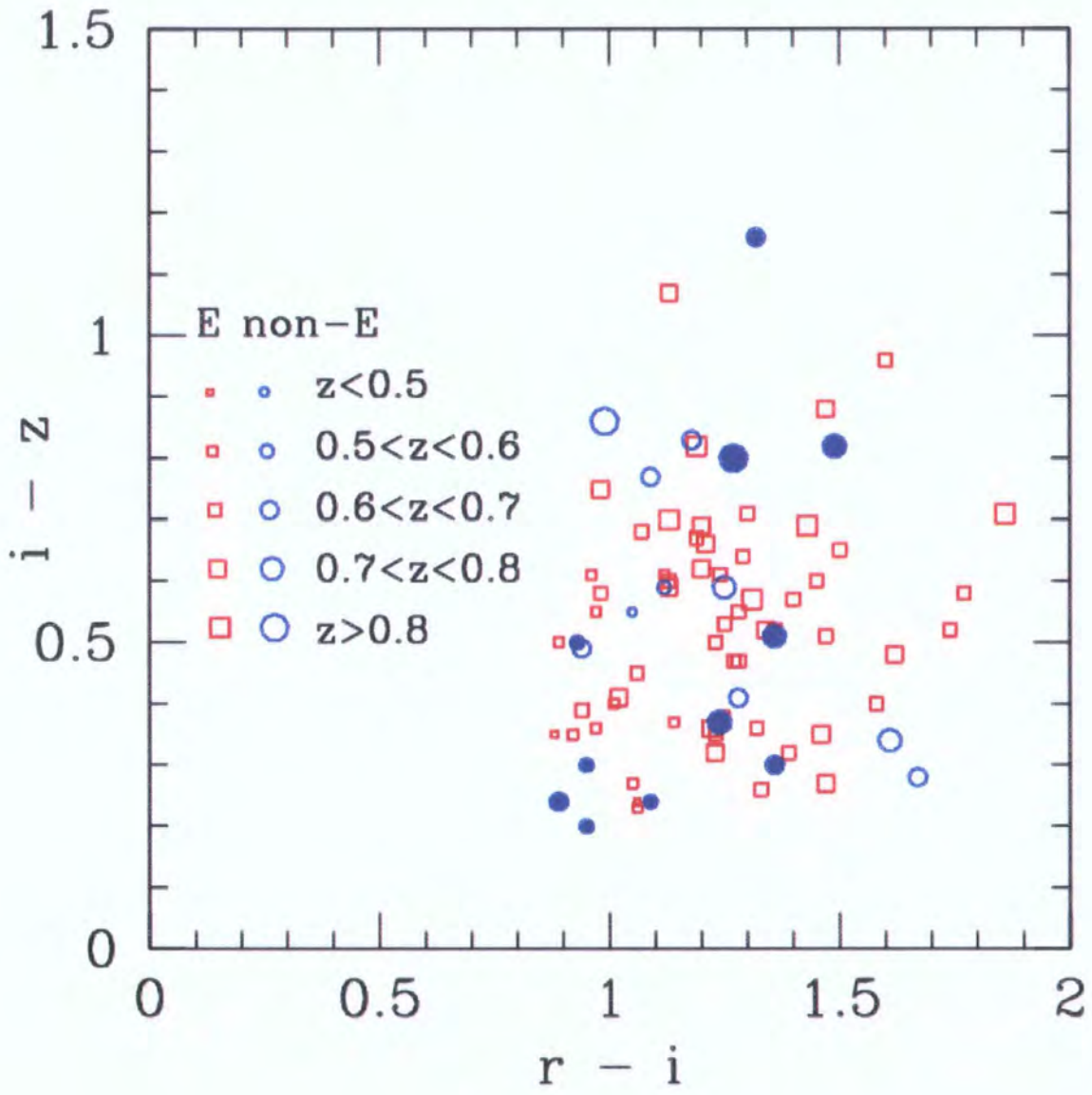

Figure 7.10: $r-i-z$ plot with a selection of AAOmega COSMOS LRGs and their morphologies with redshifts. Filled symbols are those galaxies with a Spiral morphology. The size of the points allude to the galaxy's redshift.

by red squares) and non-Ellipticals (shown by blue circles). Filled symbols are those galaxies with a Spiral morphology. Again, we see no trend in this colour-colour plane that might be connected to morphology. As such, we do not think that the excess reddening seen in the [3.6μm-8.0 μm] colour for the Spirals is due to dust extinction, as this would show up in a $r - i - z$ plot.

In Figure 7.11 we show a set of 9 postage stamp ACS images to represent our AAOmega LRG sample of elliptically classed galaxies across our full redshift range. Finally, in Figure 7.12 we show a collection of interesting objects including an early-type galaxy at redshift $z = 0.49$ with a dust lane akin to the local Sombrero galaxy, three examples of "Grand Design" spirals and strong evidence for an on-going merger with two double-cores.

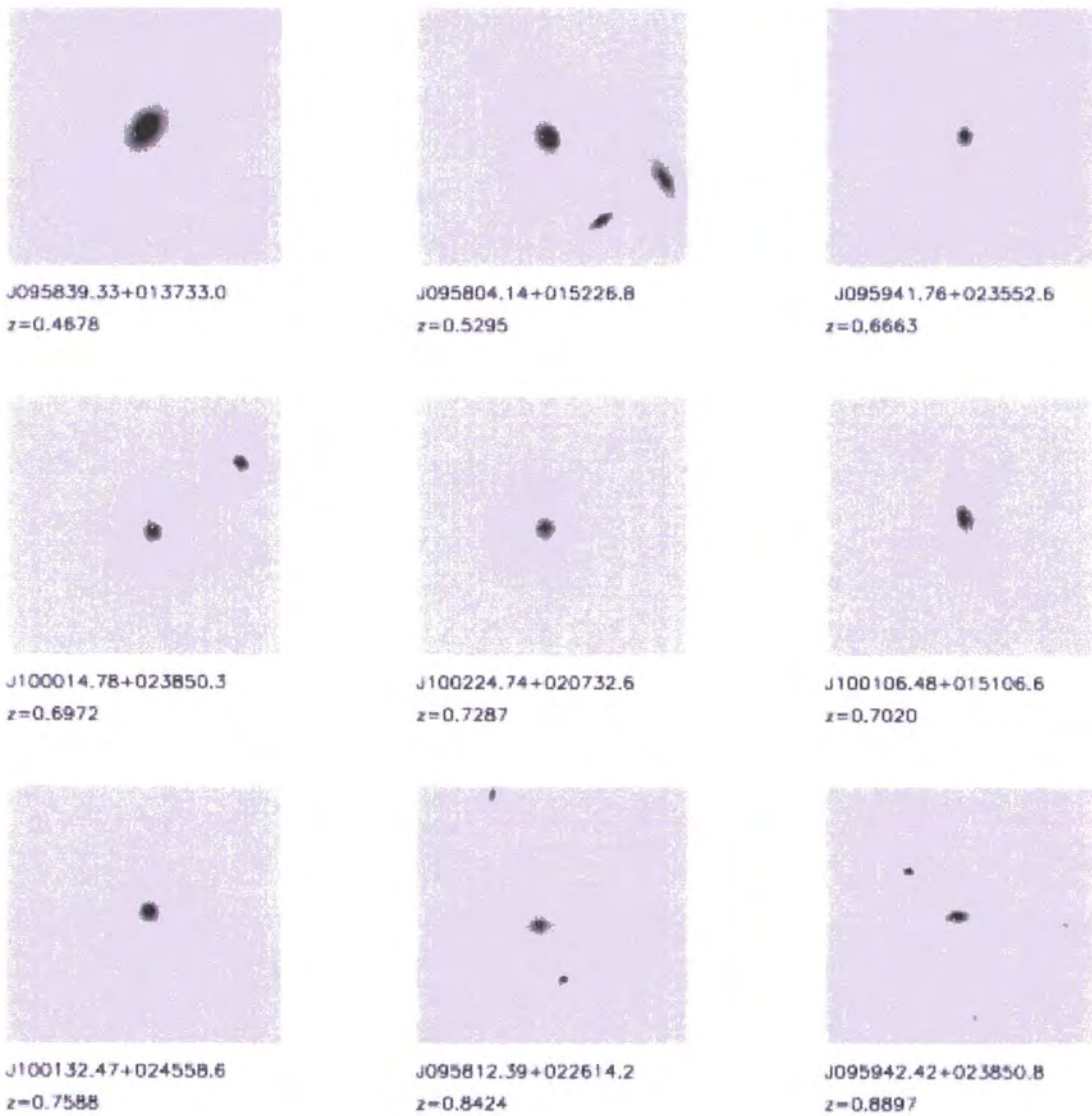

Figure 7.11: A selection of AAOmega COSMOS LRGs with regular, elliptical morphologies with varying redshifts

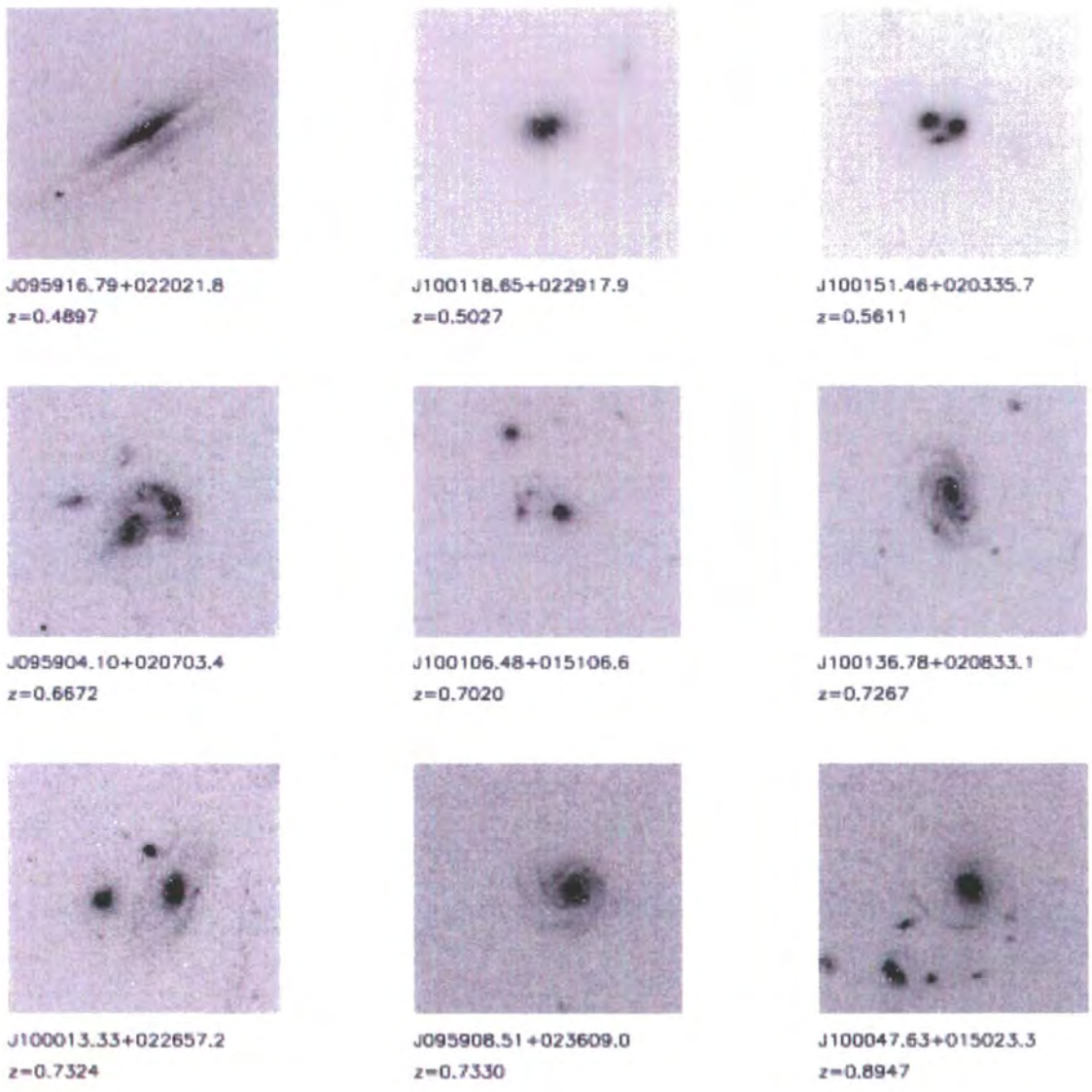

Figure 7.12: A selection of AAOmega COSMOS LRGs with interesting morphologies or features. Note the dust lane in J095916.79+022021.8 (top left), the "Grand Design" spirals (middle right, bottom left and bottom centre) and the on-going merger with two double-cores (middle left).

7.6 CONCLUSIONS AND FUTURE WORK

Using data from the IRAC instrument onboard the *Spitzer* Space satellite, as well as data from the ACS instrument on the *Hubble Space Telescope* we have studied the properties of redshift $z \sim 0.7$ LRGs in the COSMOS field. Our main conclusions are:

- The data available via the IPAC and *Spitzer* Science Center is a very valuable astronomical resource.
- The Bruzual and Charlot stellar synthesis models seem to reproduce the observed near-infrared colours reasonably well, but the errors on the recovered magnitudes will have to be better understood in order to make any quantitative claims.
- Our sample of LRGs have predominantly early-type morphology, with $\sim$ 65% being visually classified as Elliptical from ACS data. This fraction does not significantly change when the sample is split into high ($z > 0.55$) and low ($z < 0.55$) redshift ranges.
- This fraction of classified Ellipticals is in good agreement with recent semi-analytical model work by Almeida et al. However, there is a discrepancy with the fraction of spirals seen in the models. We suggest that this should currently be treated with caution since our observational sample is not statistically complete and could be open to several selection effects.
- For galaxies that don't have regular, early-type morphologies, we do not see a trend in either the optical or optical-NIR colour-colour plane to suggest a galaxy morphology-colour link. However, we suggest a tentative interpretation for the reddening seen the [3.6-8.0μm] spiral population, suggesting that it could be caused by dust emission due to obscured star formation.

With the extensive, high-sensitivity multi-wavelength coverage of the COSMOS field, the scientific potential for this area of sky is huge. As this thesis was being prepared (in early 2007) a number of COSMOS Survey papers were posted to the astro-ph Arxiv pre-print server in anticipation for the special ApJS COSMOS issue. The main papers related to this work are Sanders et al. (2007), Scoville et al. (2006a) and Guzzo et al. (2007). Sanders et al. (2007) describes in detail the *Spitzer*-COSMOS survey parameters, mapping strategy, data reduction procedures and also preliminary number counts. Scoville et al. (2006a) gives the outline of the entire COSMOS observing campaign and Guzzo et al. (2007) reports on tha large-scale structure at redshift $z \sim 0.73$ in the COSMOS field.

Future work would be targeted at gaining MIPS (24μm -160 μm) and X-ray data in order to investigate the issues raised here such as the redshift versus NIR colour comparison to stellar synthesis models and whether one can detect a trend of colour with varying morphological type.

More ambitious projects could involve studying the clustering properties of *Spitzer* COSMOS galaxies in order to probe high-redshift massive galaxies and the connection between nuclear and star-forming activity and the growth the ubiquitous central super-massive black hole.

CHAPTER 8

CONCLUSIONS AND FUTURE PROSPECTS

"For my part I know nothing with any certainty, but the sight of the stars makes me dream."

- Vincent Van Gogh

8.1 SUMMARY OF RESULTS AND CONCLUSIONS

In Chapter One of this thesis, we reviewed the current Cosmological Model and discussed how recent measurements of the CMB and LSS have provided new constraints on the values of $\Omega_{\rm M}$ and Ω_Λ. In Chapter Two, we briefly reviewed the technical aspects of the Sloan Digital Sky Survey and mentioned some of the more relevant results from the SDSS LRG Survey. We then introduced the 2dF-SDSS LRG And QSO Survey giving object selection, observational and data reduction details. In Chapter Three we presented clustering measurements of 2SLAQ LRGs using the 2-point correlation function. In Chapter 4, we analysed the redshift-space distortions apparent in the clustering signal of the 2SLAQ LRGs in order to provide constraints on cosmological parameters, $\Omega_{\rm M}$ and β. From there we measured the linear bias parameter b. In Chapter 5 we suggested a route into utilising SDSS *riz*-band photometry that could be used in readily selecting LRGs with redshifts $z \sim 0.7$ and showed that such a selection could

be used for a future galaxy redshift survey. In Chapter 6 we presented, using data from the AAOmega LRG Pilot run, the clustering properties of $z \sim 0.7$ LRGs. Finally in Chapter 7, we used archive *Spitzer* and *HST* data to study the near-infrared and morphological properties of a sample of our $z \sim 0.7$ LRGs in the COSMOS field.

As such, the main conclusions of this thesis are as follows.

- We have found that for the real-space correlation function, $\xi(r)$, for redshift $\bar{z} = 0.55$ 2SLAQ LRGs, which have a magnitude selection limit of $i < 19.8$, to be well described by a single power-law model with a slope of $\gamma = 1.72 \pm 0.06$ and correlation length of $r_0 = 7.45 \pm 0.35\ \ h^{-1}$ Mpc, assuming a ΛCDM Cosmology.

- Dynamical analysis of the redshift-space distortions present in the clustering signal of the 2SLAQ LRGs imply a value of $\Omega_{\rm m} = 0.10^{+0.35}_{-0.10}$ and $\beta = 0.40 \pm 0.05$. The best-fit velocity dispersion is 330 km s^{-1}. When this information is combined with analysis using the properties of galaxy clustering seen at low redshift and the subsequent mass evolution, we find $\Omega_{\rm m} = 0.30 \pm 0.15$ and $\beta = 0.45 \pm 0.05$.

- Using our derived values for $\Omega_{\rm M}$ and β, we calculate a linear bias term of $b(z = 0.55) = 1.66 \pm 0.35$. We then find this is consistent with measurements of the clustering lengths of low-redshift luminous, early-type galaxies, assuming a "high-peaks" bias model.

- We prove that using the new AAOmega instrument on the AAT would be a competitive route into performing a large redshift survey in order to measure the BAOs at high, $z \sim 0.7$ redshift, in order to place constraints on w, the equation of state parameter.

- We measure the cluster properties of the $z \sim 0.7$ AAOmega LRGs and find that they are highly biased objects with a redshift-space correlation length of $s_0 = 9.9 \pm 0.5$.

- We find again that this clustering amplitude is consistent with a "high-peaks" bias mode and that a typical $z \sim 0.7$ LRG inhabits a halo of $M_{\rm eff} \simeq 7 \times 10^{13} h^{-1} M_{\odot}$. Our AAOmega figure for $M_{\rm eff}$ is in fact almost identical to the average mass deduced for $z = 0$ Red Sequence galaxies in the SDSS but this coincidence does not imply any direct correspondence between these populations as the haloes that host $z \simeq 0.7$ LRGs will have become much more massive by the present day.

- Finally, using data from the *Spitzer* and *Hubble Space Telescope* , we present information regarding NIR colours and morphology. We see that a large, 65%, fraction of our sample shows signs of regular elliptical morphology in-line with current semi-analytic model predictions. However, we find no trend for galaxy morphology with colour in either the optical-optical nor the optical-NIR colour-colour plane, although we speculate that the reddening seen in the [3.6-8.0μm] spiral population could be caused by dust emission due to obscured star formation.

8.1.1 Results in a Wider Context

We now, very briefly, place our results in a wider context. First, the results presented in this thesis sit very well with the ever-growing amount of evidence suggesting that the most massive galaxies formed at high redshifts, e.g. early work by Eggen et al. (1962) and Larson (1975), and then passively evolved to the present day with very little major merger activity e.g. recent papers by Masjedi et al. (2006) and Wake et al. (2006). However, the details of the mechanisms behind how the most massive galaxies form and evolve and their connection to the build-up of the Red Sequence (e.g. Bell et al., 2004b; Conselice, 2006; Brown et al., 2006; White et al., 2007) are *still* currently not fully understood.

Second, the Alcock-Paczynski test will provide a very elegant method for checking the geometry of the universe in the future as the uncertainties surrounding this measurement will only decrease as the size of galaxy samples continue to increase. Other recent work using QSOs as large-scale structure probes (da Ângela et al., 2006) suggest that these objects could be used as cosmological probes but if Dark Energy does become prevalent at late times, massive galaxies at $z = 0.5 - 1.5$ will remain the best AP tracers since their high space density and clustering strength of the LRGs will reduce statistical errors (da Ângela, 2006).

Finally, it will be imperative to fully understand redshift-space distortions for the next generation of BAO surveys. If astronomers are determined to make 1% percent measurements of the Hubble Parameter and the Angular Diameter distance, then all the effects of non-linear gravitational collapse, galaxy clustering bias and redshift-space distortions will have to be taken into account when measuring the baryon acoustic oscillation signal. Otherwise, no matter how much observational capital is spent, the full potential of the BAO route to determining $w(z)$ and the properties of Dark Energy will not be realised.

8.2 Future Prospects

During the research for and writing of this thesis, several future avenues of investigation were suggested. In a specific sense, a selection of future projects coming directly out of the work presented in this thesis would include:

- A more detailed investigation into the form and evolution of $w(\theta)$. For many years, the belief that the angular correlation function was a single power-law at all scales was strongly held. However, with the recent leap in data quantity and quality due to galaxy surveys, we no longer believe this to be the whole story. Sawangwit et al. (2007, in prep.) are

bringing the vast galaxy database of the SDSS to bear on this issue and will investigate in more detail not only the form, but also the evolutionary properties and if there is any evidence for the BAO signal in $w(\theta)$.

- More investigation into the evolution of galaxy clustering with HOD Models. This thesis has mainly been concerned with observations of massive galaxies. However, to fully explore galaxy formation and evolution, observations have to be confronted with theoretical predictions. The Halo Occupation Distribution model is a relatively recent venture that attempts to explain the observed clustering properties of galaxies. A natural theoretical extension of the work presented here would be to use the methods and models of Zehavi et al. (2005b), Phleps et al. (2006) and White et al. (2007) in greater detail to pursue a better physical understanding of massive galaxy clustering.

- The re-visiting of the COSMOS field with AAOmega to increase our sample of $r-i-z$ selected objects and continuing our investigations into the morphological properties of redshift $z \sim 0.7$ LRGs. However, this may well be superceded by current work by the COSMOS collaboration who already have obtained and used large amounts of telescope time for their zCOSMOS project (Lilly et al., 2007, in prep.). However, with the data potentially becoming public on release of the relevant papers, independent cross-checks should be possible.

In a more general capacity, there are several future projects that are connected to the work within this thesis. These include:

- The AAOmega-UKIDSS-SDSS (AUS) Survey, which is a currently ongoing survey of QSOs and LRGs, the latter having redshifts of $z \sim 1$. The AUS in some way can be thought of

as the successor to the 2SLAQ Survey, although currently its main science driver is the pursuit of the optically faint QSO population at high, $2.8 < z < 5.5$ redshift. The AUS survey is utilising the large area infrared imaging from the UKIRT Infrared Deep Sky Surveys (UKIDSS) in order to accurately select the most massive red galaxies at redshifts $0.7 < z < 1.0$. A total sample of $\approx$ 2 500 is the goal and studying the luminosity function and of course the correlation function of this population would be a natural extension to the work reported in this thesis.

- The *WiggleZ* Dark Energy Survey is also is also a recently started project to measure the redshifts of 400 000 emission line galaxies (ELGs) over 1 000 degrees^2 of sky over a redshift range of $0.5 < z < 1.0$, with the aim of detecting the BAO signature to high enough precision in the galaxy power spectrum to make a measurement of the equation of state parameter w and see if it is a function of redshift. On a personal note, can I just state here for the record, that although the evidence in Chapter 6 suggests that LRGs would potentially be a more promising route to the detection of BAOs, I have very few doubts that the *WiggleZ* Survey will deliver on its claims and am very excited to see the results from this project, hopefully in 2009.

- Discussions are currently underway regarding the use of the 2.5m Apache Point telescope, after SDSS-II is completed in June 2008. Of these "AS2" projects, the Baryon Oscillation Spectroscopic Survey (BOSS, `http://cosmology.lbl.gov/BOSS/`) is directly relevant to the work presented in Chapters 5 and 6. The BOSS proposal suggested in the AS2 White Paper is for a large spectroscopic survey of 1.5 million LRGs out to redshifts $z \approx 0.7$ selected from 10,000 square degrees of AS2 and SDSS imaging. This, coupled with the observations of Lyman-α absorption in the spectra of 100 000 high-redshift QSOs

($2.3 < z < 2.8$) (see McDonald & Eisenstein (2006) for further details on this high-redshift BAO aspect) could be an exceptionally powerful experiment. However, as mentioned above, a much fuller and deeper understanding of the BAO systematics caused by e.g. redshift-space distortions will be needed in order to fully appreciate these "2nd generation" BAO Surveys.

Bibliography

Alcock, C. & Paczynski, B. 1979, Nature, 281, 358

Angulo, R., Baugh, C. M., Frenk, C. S., & Lacey, C. G. 2007, ArXiv Astrophysics e-prints, astro-ph/0702543

Bailey, J. A., Heald, R., & Croom, S, M. 2005, The 2DFDR Data Reduction System Users Manual., AAO, `http://www.aao.gov.au/AAO/2dF/manual.html`

Ballinger, W. E., Heavens, A. F., & Taylor, A. N. 1995, MNRAS, 276, L59

Ballinger, W. E., Peacock, J. A., & Heavens, A. F. 1996, MNRAS, 282, 877

Baugh, C. M., Lacey, C. G., Frenk, C. S., Granato, G. L., Silva, L., Bressan, A., Benson, A. J., & Cole, S. 2005, MNRAS, 356, 1191

Bell, E. F., McIntosh, D. H., Barden, M., Wolf, C., Caldwell, J. A. R., Rix, H.-W., Beckwith, S. V. W., Borch, A., Häussler, B., Jahnke, K., Jogee, S., Meisenheimer, K., Peng, C., Sanchez, S. F., Somerville, R. S., & Wisotzki, L. 2004a, ApJ Lett., 600, L11

Bell, E. F., Wolf, C., Meisenheimer, K., Rix, H.-W., Borch, A., Dye, S., Kleinheinrich, M., Wisotzki, L., & McIntosh, D. H. 2004b, ApJ, 608, 752

Bennett, C. L., Halpern, M., Hinshaw, G., Jarosik, N., Kogut, A., Limon, M., Meyer, S. S., Page, L., Spergel, D. N., Tucker, G. S., Wollack, E., Wright, E. L., Barnes, C., Greason, M. R., Hill, R. S., Komatsu, E., Nolta, M. R., Odegard, N., Peiris, H. V., Verde, L., & Weiland, J. L. 2003, ApJS, 148, 1

Blake, C., Collister, A., Bridle, S., & Lahav, O. 2007, MNRAS, 374, 1527

Blake, C. & Glazebrook, K. 2003, ApJ, 594, 665

Blanton, M. R., Lin, H., Lupton, R. H., Maley, F. M., Young, N., Zehavi, I., & Loveday, J. 2003, AJ, 125, 2276

Boesgaard, A. M. & Steigman, G. 1985, ARA&A, 23, 319

Bower, R. G., Benson, A. J., Malbon, R., Helly, J. C., Frenk, C. S., Baugh, C. M., Cole, S., & Lacey, C. G. 2006, MNRAS, 370, 645

Brown, M. J. I., Dey, A., Jannuzi, B. T., Brand, K., Benson, A. J., Brodwin, M., Croton, D. J., & Eisenhardt, P. R. 2006, ArXiv Astrophysics e-prints, astro-ph/0609584

Bruzual, G. & Charlot, S. 2003, MNRAS, 344, 1000

Burles, S., Nollett, K. M., Truran, J. W., & Turner, M. S. 1999, Physical Review Letters, 82, 4176

Cannon, R., Drinkwater, M., Edge, A., Eisenstein, D., Nichol, R., Outram, P., Pimbblet, K., de Propris, R., Roseboom, I., Wake, D., Allen, P., Bland-Hawthorn, J., Bridges, T., Carson, D., Chiu, K., Colless, M., Couch, W., Croom, S., Driver, S., Fine, S., Hewett, P., Loveday, J., Ross, N., Sadler, E. M., Shanks, T., Sharp, R., Smith, J. A., Stoughton, C., Weilbacher, P., Brunner, R. J., Meiksin, A., & Schneider, D. P. 2006, MNRAS, 372, 425

Carroll, S. M., Press, W. H., & Turner, E. L. 1992, ARA&A, 30, 499

Cimatti, A., Daddi, E., Mignoli, M., Pozzetti, L., Renzini, A., Zamorani, G., Broadhurst, T., Fontana, A., Saracco, P., Poli, F., Cristiani, S., D'Odorico, S., Giallongo, E., Gilmozzi, R., & Menci, N. 2002, Astron. & Astrophys., 381, L68

Coil, A. L., Davis, M., Madgwick, D. S., Newman, J. A., Conselice, C. J., Cooper, M., Ellis, R. S., Faber, S. M., Finkbeiner, D. P., Guhathakurta, P., Kaiser, N., Koo, D. C., Phillips, A. C., Steidel, C. C., Weiner, B. J., Willmer, C. N. A., & Yan, R. 2004, ApJ, 609, 525

Cole, S., Fisher, K. B., & Weinberg, D. H. 1994, MNRAS, 267, 785

Cole, S., Norberg, P., Baugh, C. M., Frenk, C. S., Bland-Hawthorn, J., Bridges, T., Cannon, R., Colless, M., Collins, C., Couch, W., Cross, N., Dalton, G., De Propris, R., Driver, S. P., Efstathiou, G., Ellis, R. S., Glazebrook, K., Jackson, C., Lahav, O., Lewis, I., Lumsden, S., Maddox, S., Madgwick, D., Peacock, J. A., Peterson, B. A., Sutherland, W., & Taylor, K. 2001, MNRAS, 326, 255

Cole, S., Percival, W. J., Peacock, J. A., Norberg, P., Baugh, C. M., Frenk, C. S., Baldry, I., Bland-Hawthorn, J., Bridges, T., Cannon, R., Colless, M., Collins, C., Couch, W., Cross, N. J. G., Dalton, G., Eke, V. R., De Propris, R., Driver, S. P., Efstathiou, G., Ellis, R. S., Glazebrook, K., Jackson, C., Jenkins, A., Lahav, O., Lewis, I., Lumsden, S., Maddox, S., Madgwick, D., Peterson, B. A., Sutherland, W., & Taylor, K. 2005, MNRAS, 362, 505

Colín, P., Klypin, A. A., Kravtsov, A. V., & Khokhlov, A. M. 1999, ApJ, 523, 32

Colless, M., Dalton, G., Maddox, S., Sutherland, W., Norberg, P., Cole, S., Bland-Hawthorn, J., Bridges, T., Cannon, R., Collins, C., Couch, W., Cross, N., Deeley, K., De Propris, R.,

Driver, S. P., Efstathiou, G., Ellis, R. S., Frenk, C. S., Glazebrook, K., Jackson, C., Lahav, O., Lewis, I., Lumsden, S., Madgwick, D., Peacock, J. A., Peterson, B. A., Price, I., Seaborne, M., & Taylor, K. 2001, MNRAS, 328, 1039

Colless, M., Peterson, B. A., Jackson, C., Peacock, J. A., Cole, S., Norberg, P., Baldry, I. K., Baugh, C. M., Bland-Hawthorn, J., Bridges, T., Cannon, R., Collins, C., Couch, W., Cross, N., Dalton, G., De Propris, R., Driver, S. P., Efstathiou, G., Ellis, R. S., Frenk, C. S., Glazebrook, K., Lahav, O., Lewis, I., Lumsden, S., Maddox, S., Madgwick, D., Sutherland, W., & Taylor, K. 2003, ArXiv Astrophysics e-prints, astro-ph/0306581

Collister, A., Lahav, O., Blake, C., Cannon, R., Croom, S., Drinkwater, M., Edge, A., Eisenstein, D., Loveday, J., Nichol, R., Pimbblet, K., de Propris, R., Roseboom, I., Ross, N., Schneider, D. P., Shanks, T., & Wake, D. 2007, MNRAS, 375, 68

Conselice, C. 2006, in American Astronomical Society Meeting Abstracts, Vol. 209, 181.02

Conselice, C. J., Grogin, N. A., Jogee, S., Lucas, R. A., Dahlen, T., de Mello, D., Gardner, J. P., Mobasher, B., & Ravindranath, S. 2004, ApJ Lett., 600, L139

Croom, S. M., Boyle, B. J., Shanks, T., Smith, R. J., Miller, L., Outram, P. J., Loaring, N. S., Hoyle, F., & da Ângela, J. 2005, MNRAS, 356, 415

Croom, S. M. & Shanks, T. 1996, MNRAS, 281, 893

Croom, S. M., Smith, R. J., Boyle, B. J., Shanks, T., Miller, L., Outram, P. J., & Loaring, N. S. 2004, MNRAS, 349, 1397

Croton, D. J., Springel, V., White, S. D. M., De Lucia, G., Frenk, C. S., Gao, L., Jenkins, A., Kauffmann, G., Navarro, J. F., & Yoshida, N. 2006, MNRAS, 365, 11

Curtis, H. D. 1920, JRASC, 14, 317

da Ângela, J. 2006, PhD Thesis

da Ângela, J., Outram, P. J., Shanks, T., Boyle, B. J., Croom, S. M., Loaring, N. S., Miller, L., & Smith, R. J. 2005, MNRAS, 360, 1040

da Ângela, J., Shanks, T., Croom, S. M., Weilbacher, P., Brunner, R. J., Couch, W. J., Miller, L., Myers, A. D., Nichol, R. C., Pimbblet, K. A., de Propris, R., Richards, G. T., Ross, N. P., Schneider, D. P., & Wake, D. A. 2006, ArXiv Astrophysics e-prints, astro-ph/0612401

Davis, M. & Peebles, P. J. E. 1983, ApJ, 267, 465

de Bernardis, P., Ade, P. A. R., Bock, J. J., Bond, J. R., Borrill, J., Boscaleri, A., Coble, K., Crill, B. P., De Gasperis, G., Farese, P. C., Ferreira, P. G., Ganga, K., Giacometti, M., Hivon, E., Hristov, V. V., Iacoangeli, A., Jaffe, A. H., Lange, A. E., Martinis, L., Masi, S., Mason, P. V., Mauskopf, P. D., Melchiorri, A., Miglio, L., Montroy, T., Netterfield, C. B., Pascale, E., Piacentini, F., Pogosyan, D., Prunet, S., Rao, S., Romeo, G., Ruhl, J. E., Scaramuzzi, F., Sforna, D., & Vittorio, N. 2000, Nature, 404, 955

Dicke, R. H., Peebles, P. J. E., Roll, P. G., & Wilkinson, D. T. 1965, ApJ, 142, 414

Eaton, N., Draper, P. W., & Allan, A. 2002, *PHOTOM — A Photometry Package: Starlink User Note 45*, `http://star-www.rl.ac.uk/`

Eggen, O. J., Lynden-Bell, D., & Sandage, A. R. 1962, ApJ, 136, 748

Einstein, A. 1916, Annalen der Physik, 354, 769

Eisenstein, D. J., Annis, J., Gunn, J. E., Szalay, A. S., Connolly, A. J., Nichol, R. C., Bahcall, N. A., Bernardi, M., Burles, S., Castander, F. J., Fukugita, M., Hogg, D. W., Ivezić, Ž.,

Knapp, G. R., Lupton, R. H., Narayanan, V., Postman, M., Reichart, D. E., Richmond, M., Schneider, D. P., Schlegel, D. J., Strauss, M. A., SubbaRao, M., Tucker, D. L., Vanden Berk, D., Vogeley, M. S., Weinberg, D. H., & Yanny, B. 2001, AJ, 122, 2267

Eisenstein, D. J., Hogg, D. W., Fukugita, M., Nakamura, O., Bernardi, M., Finkbeiner, D. P., Schlegel, D. J., Brinkmann, J., Connolly, A. J., Csabai, I., Gunn, J. E., Ivezić, Ž., Lamb, D. Q., Loveday, J., Munn, J. A., Nichol, R. C., Schneider, D. P., Strauss, M. A., Szalay, A., & York, D. G. 2003, ApJ, 585, 694

Eisenstein, D. J. & Hu, W. 1998, ApJ, 496, 605

Eisenstein, D. J., Seo, H.-j., & White, M. 2006, ArXiv Astrophysics e-prints

Eisenstein, D. J., Zehavi, I., Hogg, D. W., Scoccimarro, R., Blanton, M. R., Nichol, R. C., Scranton, R., Seo, H.-J., Tegmark, M., Zheng, Z., Anderson, S. F., Annis, J., Bahcall, N., Brinkmann, J., Burles, S., Castander, F. J., Connolly, A., Csabai, I., Doi, M., Fukugita, M., Frieman, J. A., Glazebrook, K., Gunn, J. E., Hendry, J. S., Hennessy, G., Ivezić, Z., Kent, S., Knapp, G. R., Lin, H., Loh, Y.-S., Lupton, R. H., Margon, B., McKay, T. A., Meiksin, A., Munn, J. A., Pope, A., Richmond, M. W., Schlegel, D., Schneider, D. P., Shimasaku, K., Stoughton, C., Strauss, M. A., SubbaRao, M., Szalay, A. S., Szapudi, I., Tucker, D. L., Yanny, B., & York, D. G. 2005, ApJ, 633, 560

Eke, V. R., Baugh, C. M., Cole, S., Frenk, C. S., Norberg, P., Peacock, J. A., Baldry, I. K., Bland-Hawthorn, J., Bridges, T., Cannon, R., Colless, M., Collins, C., Couch, W., Dalton, G., de Propris, R., Driver, S. P., Efstathiou, G., Ellis, R. S., Glazebrook, K., Jackson, C., Lahav, O., Lewis, I., Lumsden, S., Maddox, S., Madgwick, D., Peterson, B. A., Sutherland, W., & Taylor, K. 2004, MNRAS, 348, 866

Elgarøy, Ø., Lahav, O., Percival, W. J., Peacock, J. A., Madgwick, D. S., Bridle, S. L., Baugh, C. M., Baldry, I. K., Bland-Hawthorn, J., Bridges, T., Cannon, R., Cole, S., Colless, M., Collins, C., Couch, W., Dalton, G., de Propris, R., Driver, S. P., Efstathiou, G. P., Ellis, R. S., Frenk, C. S., Glazebrook, K., Jackson, C., Lewis, I., Lumsden, S., Maddox, S., Norberg, P., Peterson, B. A., Sutherland, W., & Taylor, K. 2002, Physical Review Letters, 89, 061301

Fazio, G. G., Hora, J. L., Allen, L. E., Ashby, M. L. N., Barmby, P., Deutsch, L. K., Huang, J.-S., Kleiner, S., Marengo, M., Megeath, S. T., Melnick, G. J., Pahre, M. A., Patten, B. M., Polizotti, J., Smith, H. A., Taylor, R. S., Wang, Z., Willner, S. P., Hoffmann, W. F., Pipher, J. L., Forrest, W. J., McMurty, C. W., McCreight, C. R., McKelvey, M. E., McMurray, R. E., Koch, D. G., Moseley, S. H., Arendt, R. G., Mentzell, J. E., Marx, C. T., Losch, P., Mayman, P., Eichhorn, W., Krebs, D., Jhabvala, M., Gezari, D. Y., Fixsen, D. J., Flores, J., Shakoorzadeh, K., Jungo, R., Hakun, C., Workman, L., Karpati, G., Kichak, R., Whitley, R., Mann, S., Tollestrup, E. V., Eisenhardt, P., Stern, D., Gorjian, V., Bhattacharya, B., Carey, S., Nelson, B. O., Glaccum, W. J., Lacy, M., Lowrance, P. J., Laine, S., Reach, W. T., Stauffer, J. A., Surace, J. A., Wilson, G., Wright, E. L., Hoffman, A., Domingo, G., & Cohen, M. 2004, ApJS, 154, 10

Feldman, H. A., Kaiser, N., & Peacock, J. A. 1994, ApJ, 426, 23

Fry, J. N. 1996, ApJ Lett., 461, L65

Fukugita, M., Ichikawa, T., Gunn, J. E., Doi, M., Shimasaku, K., & Schneider, D. P. 1996, AJ, 111, 1748

Glazebrook, K., Blake, C., Couch, W., Forbes, D., Drinkwater, M., Jurek, R., Pimbblet, K., Madore, B., Martin, C., Small, T., Forster, K., Colless, M., Sharp, R., Croom, S., Woods,

D., Pracy, M., Gilbank, D., Yee, H., & Gladders, M. 2007, ArXiv Astrophysics e-prints, astro-ph/0701876

Gunn, J. E., Carr, M., Rockosi, C., Sekiguchi, M., Berry, K., Elms, B., de Haas, E., Ivezić, Ž., Knapp, G., Lupton, R., Pauls, G., Simcoe, R., Hirsch, R., Sanford, D., Wang, S., York, D., Harris, F., Annis, J., Bartozek, L., Boroski, W., Bakken, J., Haldeman, M., Kent, S., Holm, S., Holmgren, D., Petravick, D., Prosapio, A., Rechenmacher, R., Doi, M., Fukugita, M., Shimasaku, K., Okada, N., Hull, C., Siegmund, W., Mannery, E., Blouke, M., Heidtman, D., Schneider, D., Lucinio, R., & Brinkman, J. 1998, AJ, 116, 3040

Gunn, J. E., Siegmund, W. A., Mannery, E. J., Owen, R. E., Hull, C. L., Leger, R. F., Carey, L. N., Knapp, G. R., York, D. G., Boroski, W. N., Kent, S. M., Lupton, R. H., Rockosi, C. M., Evans, M. L., Waddell, P., Anderson, J. E., Annis, J., Barentine, J. C., Bartoszek, L. M., Bastian, S., Bracker, S. B., Brewington, H. J., Briegel, C. I., Brinkmann, J., Brown, Y. J., Carr, M. A., Czarapata, P. C., Drennan, C. C., Dombeck, T., Federwitz, G. R., Gillespie, B. A., Gonzales, C., Hansen, S. U., Harvanek, M., Hayes, J., Jordan, W., Kinney, E., Klaene, M., Kleinman, S. J., Kron, R. G., Kresinski, J., Lee, G., Limmongkol, S., Lindenmeyer, C. W., Long, D. C., Loomis, C. L., McGehee, P. M., Mantsch, P. M., Neilsen, Jr., E. H., Neswold, R. M., Newman, P. R., Nitta, A., Peoples, J. J., Pier, J. R., Prieto, P. S., Prosapio, A., Rivetta, C., Schneider, D. P., Snedden, S., & Wang, S.-i. 2006, AJ, 131, 2332

Guzzo, L., Cassata, P., Finoguenov, A., Massey, R., Scoville, N. Z., Capak, P., Ellis, R. S., Mobasher, B., Taniguchi, Y., Thompson, D., Ajiki, M., Aussel, H., Boehringer, H., Brusa, M., Calzetti, D., Comastri, A., Franceschini, A., Hasinger, G., Kasliwal, M. M., Kitzbichler, M. G., Kneib, J. ., Koekemoer, A., Leauthaud, A., McCracken, H. J., Murayama, T., Nagao,

T., Rhodes, J., Sanders, D. B., Sasaki, S., Shioya, Y., Tasca, L., & Taylor, J. E. 2007, ArXiv Astrophysics e-prints, astro-ph/0701482

Hamilton, A. J. S. 1992, ApJ Lett., 385, L5

—. 1993, ApJ, 417, 19

Hatton, S. & Cole, S. 1998, MNRAS, 296, 10

Hawkins, E., Maddox, S., Cole, S., Lahav, O., Madgwick, D. S., Norberg, P., Peacock, J. A., Baldry, I. K., Baugh, C. M., Bland-Hawthorn, J., Bridges, T., Cannon, R., Colless, M., Collins, C., Couch, W., Dalton, G., De Propris, R., Driver, S. P., Efstathiou, G., Ellis, R. S., Frenk, C. S., Glazebrook, K., Jackson, C., Jones, B., Lewis, I., Lumsden, S., Percival, W., Peterson, B. A., Sutherland, W., & Taylor, K. 2003, MNRAS, 346, 78

Heavens, A. F. & Taylor, A. N. 1995, MNRAS, 275, 483

Hinshaw, G., Nolta, M. R., Bennett, C. L., Bean, R., Doré, O., Greason, M. R., Halpern, M., Hill, R. S., Jarosik, N., Kogut, A., Komatsu, E., Limon, M., Odegard, N., Meyer, S. S., Page, L., Peiris, H. V., Spergel, D. N., Tucker, G. S., Verde, L., Weiland, J. L., Wollack, E., & Wright, E. L. 2006, ArXiv Astrophysics e-prints, astro-ph/0603451

Hogg, D. W., Blanton, M., Strateva, I., Bahcall, N. A., Brinkmann, J., Csabai, I., Doi, M., Fukugita, M., Hennessy, G., Ivezić, Ž., Knapp, G. R., Lamb, D. Q., Lupton, R., Munn, J. A., Nichol, R., Schlegel, D. J., Schneider, D. P., & York, D. G. 2002, AJ, 124, 646

Hoyle, F., Outram, P. J., Shanks, T., Boyle, B. J., Croom, S. M., & Smith, R. J. 2002, MNRAS, 332, 311

Hubble, E. 1929, Proceedings of the National Academy of Science, 15, 168

Hütsi, G. 2006a, Astron. & Astrophys., 449, 891

—. 2006b, Astron. & Astrophys., 459, 375

Jannuzi, B. T. & Dey, A. 1999, in ASP Conf. Ser. 191: Photometric Redshifts and the Detection of High Redshift Galaxies, ed. R. Weymann, L. Storrie-Lombardi, M. Sawicki, & R. Brunner, 111

Jarosik, N., Barnes, C., Greason, M. R., Hill, R. S., Nolta, M. R., Odegard, N., Weiland, J. L., Bean, R., Bennett, C. L., Doré, O., Halpern, M., Hinshaw, G., Kogut, A., Komatsu, E., Limon, M., Meyer, S. S., Page, L., Spergel, D. N., Tucker, G. S., Wollack, E., & Wright, E. L. 2006, ArXiv Astrophysics e-prints, astro-ph/0603452

Kaiser, N. 1987, MNRAS, 227, 1

Kawata, D. & Gibson, B. K. 2005, MNRAS, 358, L16

Lahav, O., Lilje, P. B., Primack, J. R., & Rees, M. J. 1991, MNRAS, 251, 128

Landy, S. D. & Szalay, A. S. 1993, ApJ, 412, 64

—. 2002, ApJ, 579, 76

Larson, R. B. 1975, MNRAS, 173, 671

Le Fèvre, O., Guzzo, L., Meneux, B., Pollo, A., Cappi, A., Colombi, S., Iovino, A., Marinoni, C., McCracken, H. J., Scaramella, R., Bottini, D., Garilli, B., Le Brun, V., Maccagni, D., Picat, J. P., Scodeggio, M., Tresse, L., Vettolani, G., Zanichelli, A., Adami, C., Arnaboldi, M., Arnouts, S., Bardelli, S., Blaizot, J., Bolzonella, M., Charlot, S., Ciliegi, P., Contini, T., Foucaud, S., Franzetti, P., Gavignaud, I., Ilbert, O., Marano, B., Mathez, G., Mazure,

A., Merighi, R., Paltani, S., Pellò, R., Pozzetti, L., Radovich, M., Zamorani, G., Zucca, E., Bondi, M., Bongiorno, A., Busarello, G., Lamareille, F., Mellier, Y., Merluzzi, P., Ripepi, V., & Rizzo, D. 2005, Astron. & Astrophys., 439, 877

Lewis, I. J., Cannon, R. D., Taylor, K., Glazebrook, K., Bailey, J. A., Baldry, I. K., Barton, J. R., Bridges, T. J., Dalton, G. B., Farrell, T. J., Gray, P. M., Lankshear, A., McCowage, C., Parry, I. R., Sharples, R. M., Shortridge, K., Smith, G. A., Stevenson, J., Straede, J. O., Waller, L. G., Whittard, J. D., Wilcox, J. K., & Willis, K. C. 2002, MNRAS, 333, 279

Li, C., Kauffmann, G., Jing, Y. P., White, S. D. M., Börner, G., & Cheng, F. Z. 2006, MNRAS, 368, 21

Loh, Y.-S. & Strauss, M. A. 2006, MNRAS, 366, 373

Loveday, J., Peterson, B. A., Maddox, S. J., & Efstathiou, G. 1996, ApJS, 107, 201

Madgwick, D. S., Hawkins, E., Lahav, O., Maddox, S., Norberg, P., Peacock, J. A., Baldry, I. K., Baugh, C. M., Bland-Hawthorn, J., Bridges, T., Cannon, R., Cole, S., Colless, M., Collins, C., Couch, W., Dalton, G., De Propris, R., Driver, S. P., Efstathiou, G., Ellis, R. S., Frenk, C. S., Glazebrook, K., Jackson, C., Lewis, I., Lumsden, S., Peterson, B. A., Sutherland, W., & Taylor, K. 2003, MNRAS, 344, 847

Martin, D. C., Fanson, J., Schiminovich, D., Morrissey, P., Friedman, P. G., Barlow, T. A., Conrow, T., Grange, R., Jelinsky, P. N., Milliard, B., Siegmund, O. H. W., Bianchi, L., Byun, Y.-I., Donas, J., Forster, K., Heckman, T. M., Lee, Y.-W., Madore, B. F., Malina, R. F., Neff, S. G., Rich, R. M., Small, T., Surber, F., Szalay, A. S., Welsh, B., & Wyder, T. K. 2005, ApJ Lett., 619, L1

Martínez, V. J. & Saar, E. 2002, *Statistics of the Galaxy Distribution*, published by Chapman & Hall/CRC, Boca Raton, ISBN: 1584880848

Masjedi, M., Hogg, D. W., Cool, R. J., Eisenstein, D. J., Blanton, M. R., Zehavi, I., Berlind, A. A., Bell, E. F., Schneider, D. P., Warren, M. S., & Brinkmann, J. 2006, ApJ, 644, 54

Mather, J. C., Cheng, E. S., Eplee, Jr., R. E., Isaacman, R. B., Meyer, S. S., Shafer, R. A., Weiss, R., Wright, E. L., Bennett, C. L., Boggess, N. W., Dwek, E., Gulkis, S., Hauser, M. G., Janssen, M., Kelsall, T., Lubin, P. M., Moseley, Jr., S. H., Murdock, T. L., Silverberg, R. F., Smoot, G. F., & Wilkinson, D. T. 1990, ApJ Lett., 354, L37

Matsubara, T. & Suto, Y. 1996, ApJ Lett., 470, L1

Matsubara, T. & Szalay, A. S. 2001, ApJ Lett., 556, L67

McDonald, P. & Eisenstein, D. 2006, ArXiv Astrophysics e-prints, astro-ph/0607122

Meiksin, A., White, M., & Peacock, J. A. 1999, MNRAS, 304, 851

Metcalfe, N., Shanks, T., Campos, A., McCracken, H. J., & Fong, R. 2001, MNRAS, 323, 795

Metcalfe, N., Shanks, T., Weilbacher, P. M., McCracken, H. J., Fong, R., & Thompson, D. 2006, MNRAS, 370, 1257

Minchin, R., Davies, J., Disney, M., Boyce, P., Garcia, D., Jordan, C., Kilborn, V., Lang, R., Roberts, S., Sabatini, S., & van Driel, W. 2005, ApJ Lett., 622, L21

Myers, A. D., Outram, P. J., Shanks, T., Boyle, B. J., Croom, S. M., Loaring, N. S., Miller, L., & Smith, R. J. 2003, MNRAS, 342, 467

Netterfield, C. B., Ade, P. A. R., Bock, J. J., Bond, J. R., Borrill, J., Boscaleri, A., Coble, K., Contaldi, C. R., Crill, B. P., de Bernardis, P., Farese, P., Ganga, K., Giacometti, M., Hivon, E., Hristov, V. V., Iacoangeli, A., Jaffe, A. H., Jones, W. C., Lange, A. E., Martinis, L., Masi, S., Mason, P., Mauskopf, P. D., Melchiorri, A., Montroy, T., Pascale, E., Piacentini, F., Pogosyan, D., Pongetti, F., Prunet, S., Romeo, G., Ruhl, J. E., & Scaramuzzi, F. 2002, ApJ, 571, 604

Norberg, P., Baugh, C. M., Hawkins, E., Maddox, S., Madgwick, D., Lahav, O., Cole, S., Frenk, C. S., Baldry, I., Bland-Hawthorn, J., Bridges, T., Cannon, R., Colless, M., Collins, C., Couch, W., Dalton, G., De Propris, R., Driver, S. P., Efstathiou, G., Ellis, R. S., Glazebrook, K., Jackson, C., Lewis, I., Lumsden, S., Peacock, J. A., Peterson, B. A., Sutherland, W., & Taylor, K. 2002a, MNRAS, 332, 827

Norberg, P., Cole, S., Baugh, C. M., Frenk, C. S., Baldry, I., Bland-Hawthorn, J., Bridges, T., Cannon, R., Colless, M., Collins, C., Couch, W., Cross, N. J. G., Dalton, G., De Propris, R., Driver, S. P., Efstathiou, G., Ellis, R. S., Glazebrook, K., Jackson, C., Lahav, O., Lewis, I., Lumsden, S., Maddox, S., Madgwick, D., Peacock, J. A., Peterson, B. A., Sutherland, W., & Taylor, K. 2002b, MNRAS, 336, 907

Padmanabhan, N., Budavári, T., Schlegel, D. J., Bridges, T., Brinkmann, J., Cannon, R., Connolly, A. J., Croom, S. M., Csabai, I., Drinkwater, M., Eisenstein, D. J., Hewett, P. C., Loveday, J., Nichol, R. C., Pimbblet, K. A., De Propris, R., Schneider, D. P., Scranton, R., Seljak, U., Shanks, T., Szapudi, I., Szalay, A. S., & Wake, D. 2005, MNRAS, 359, 237

Padmanabhan, N., Schlegel, D. J., Seljak, U., Makarov, A., Bahcall, N. A., Blanton, M. R., Brinkmann, J., Eisenstein, D. J., Finkbeiner, D. P., Gunn, J. E., Hogg, D. W., Ivezic, Z.,

Knapp, G. R., Loveday, J., Lupton, R. H., Nichol, R. C., Schneider, D. P., Strauss, M. A., Tegmark, M., & York, D. G. 2006, ArXiv Astrophysics e-prints, astro-ph/0605302

Page, L., Hinshaw, G., Komatsu, E., Nolta, M. R., Spergel, D. N., Bennett, C. L., Barnes, C., Bean, R., Doré, O., Dunkley, J., Halpern, M., Hill, R. S., Jarosik, N., Kogut, A., Limon, M., Meyer, S. S., Odegard, N., Peiris, H. V., Tucker, G. S., Verde, L., Weiland, J. L., Wollack, E., & Wright, E. L. 2006, ArXiv Astrophysics e-prints, astro-ph/0603450

Parkinson, D., Blake, C., Kunz, M., Bassett, B. A., Nichol, R. C., & Glazebrook, K. 2007, ArXiv Astrophysics e-prints, astro-ph/0702040

Peacock, J. A. 1999, *Cosmological Physics*, pp. 704. Cambridge, UK: Cambridge University Press ISBN 0521422701

Peacock, J. A., Cole, S., Norberg, P., Baugh, C. M., Bland-Hawthorn, J., Bridges, T., Cannon, R. D., Colless, M., Collins, C., Couch, W., Dalton, G., Deeley, K., De Propris, R., Driver, S. P., Efstathiou, G., Ellis, R. S., Frenk, C. S., Glazebrook, K., Jackson, C., Lahav, O., Lewis, I., Lumsden, S., Maddox, S., Percival, W. J., Peterson, B. A., Price, I., Sutherland, W., & Taylor, K. 2001, Nature, 410, 169

Peebles, P. J. E. 1980, *The Large-Scale Structure of the Universe*, Princeton University Press

—. 1984, ApJ, 284, 439

—. 1993, *Principles of Physical Cosmology*, Princeton Series in Physics, Princeton, NJ: Princeton University Press (Princeton Series in Physics, Princeton, NJ: Princeton University Press, —c1993)

Peebles, P. J. E. & Yu, J. T. 1970, ApJ, 162, 815

Penzias, A. A. & Wilson, R. W. 1965, ApJ, 142, 419

Percival, W. J., Baugh, C. M., Bland-Hawthorn, J., Bridges, T., Cannon, R., Cole, S., Colless, M., Collins, C., Couch, W., Dalton, G., De Propris, R., Driver, S. P., Efstathiou, G., Ellis, R. S., Frenk, C. S., Glazebrook, K., Jackson, C., Lahav, O., Lewis, I., Lumsden, S., Maddox, S., Moody, S., Norberg, P., Peacock, J. A., Peterson, B. A., Sutherland, W., & Taylor, K. 2001, MNRAS, 327, 1297

Percival, W. J., Nichol, R. C., Eisenstein, D. J., Frieman, J. A., Fukugita, M., Loveday, J., Pope, A. C., Schneider, D. P., Szalay, A. S., Tegmark, M., Vogeley, M. S., Weinberg, D. H., Zehavi, I., Bahcall, N. A., Brinkmann, J., Connolly, A. J., & Meiksin, A. 2006a, ArXiv Astrophysics e-prints, astro-ph/0608636

Percival, W. J., Nichol, R. C., Eisenstein, D. J., Weinberg, D. H., Fukugita, M., Pope, A. C., Schneider, D. P., Szalay, A. S., Vogeley, M. S., Zehavi, I., Bahcall, N. A., Brinkmann, J., Connolly, A. J., Loveday, J., & Meiksin, A. 2006b, ArXiv Astrophysics e-prints, astro-ph/0608635

Percival, W. J., Sutherland, W., Peacock, J. A., Baugh, C. M., Bland-Hawthorn, J., Bridges, T., Cannon, R., Cole, S., Colless, M., Collins, C., Couch, W., Dalton, G., De Propris, R., Driver, S. P., Efstathiou, G., Ellis, R. S., Frenk, C. S., Glazebrook, K., Jackson, C., Lahav, O., Lewis, I., Lumsden, S., Maddox, S., Moody, S., Norberg, P., Peterson, B. A., & Taylor, K. 2002, MNRAS, 337, 1068

Perlmutter, S., Aldering, G., Goldhaber, G., Knop, R. A., Nugent, P., Castro, P. G., Deustua, S., Fabbro, S., Goobar, A., Groom, D. E., Hook, I. M., Kim, A. G., Kim, M. Y., Lee, J. C., Nunes, N. J., Pain, R., Pennypacker, C. R., Quimby, R., Lidman, C., Ellis, R. S., Irwin,

M., McMahon, R. G., Ruiz-Lapuente, P., Walton, N., Schaefer, B., Boyle, B. J., Filippenko, A. V., Matheson, T., Fruchter, A. S., Panagia, N., Newberg, H. J. M., Couch, W. J., & The Supernova Cosmology Project. 1999, ApJ, 517, 565

Phillipps, S., Fong, R., Fall, R. S. E. S. M., & MacGillivray, H. T. 1978, MNRAS, 182, 673

Phleps, S., Peacock, J. A., Meisenheimer, K., & Wolf, C. 2006, Astron. & Astrophys., 457, 145

Press, W. H., Teukolsky, S. A., Vetterling, W. T., & Flannery, B. P. 1992, *Numerical Recipes in FORTRAN: The Art of Scientific Computing*, Cambridge University Press

Ratcliffe, A., Shanks, T., Parker, Q. A., & Fong, R. 1998, MNRAS, 296, 191

Reach, W. T., Megeath, S. T., Cohen, M., Hora, J., Carey, S., Surace, J., Willner, S. P., Barmby, P., Wilson, G., Glaccum, W., Lowrance, P., Marengo, M., & Fazio, G. G. 2005, PASP, 117, 978

Richards, G. T., Croom, S. M., Anderson, S. F., Bland-Hawthorn, J., Boyle, B. J., De Propris, R., Drinkwater, M. J., Fan, X., Gunn, J. E., Ivezić, Ž., Jester, S., Loveday, J., Meiksin, A., Miller, L., Myers, A., Nichol, R. C., Outram, P. J., Pimbblet, K. A., Roseboom, I. G., Ross, N., Schneider, D. P., Shanks, T., Sharp, R. G., Stoughton, C., Strauss, M. A., Szalay, A. S., Vanden Berk, D. E., & York, D. G. 2005, MNRAS, 360, 839

Riess, A. G., Filippenko, A. V., Challis, P., Clocchiatti, A., Diercks, A., Garnavich, P. M., Gilliland, R. L., Hogan, C. J., Jha, S., Kirshner, R. P., Leibundgut, B., Phillips, M. M., Reiss, D., Schmidt, B. P., Schommer, R. A., Smith, R. C., Spyromilio, J., Stubbs, C., Suntzeff, N. B., & Tonry, J. 1998, AJ, 116, 1009

Riess, A. G., Strolger, L.-G., Casertano, S., Ferguson, H. C., Mobasher, B., Gold, B., Challis, P. J., Filippenko, A. V., Jha, S., Li, W., Tonry, J., Foley, R., Kirshner, R. P., Dickinson, M., MacDonald, E., Eisenstein, D., Livio, M., Younger, J., Xu, C., Dahlen, T., & Stern, D. 2006, ArXiv Astrophysics e-prints, astro-ph/0611572

Riess, A. G., Strolger, L.-G., Tonry, J., Casertano, S., Ferguson, H. C., Mobasher, B., Challis, P., Filippenko, A. V., Jha, S., Li, W., Chornock, R., Kirshner, R. P., Leibundgut, B., Dickinson, M., Livio, M., Giavalisco, M., Steidel, C. C., Benítez, T., & Tsvetanov, Z. 2004, ApJ, 607, 665

Roseboom, I. G., Pimbblet, K. A., Drinkwater, M. J., Cannon, R. D., de Propris, R., Edge, A. C., Eisenstein, D. J., Nichol, R. C., Smail, I., Wake, D. A., Bland-Hawthorn, J., Bridges, T. J., Carson, D., Colless, M., Couch, W. J., Croom, S. M., Driver, S. P., Hewett, P. C., Loveday, J., Ross, N., Schneider, D. P., Shanks, T., Sharp, R. G., & Weilbacher, P. 2006, MNRAS, 373, 349

Sadler, E. M., Cannon, R. D., Mauch, T., Hancock, P. J., Wake, D. A., Ross, N., Croom, S. M., Drinkwater, M. J., Edge, A. C., Eisenstein, D., Hopkins, A. M., Johnston, H., Nichol, R., Pimbblet, K. A., De Propris, R., Roseboom, I. G., Schneider, D. P., & Shanks, T. 2006, ArXiv Astrophysics e-prints, astro-ph/0612019

Salpeter, E. E. 1955, ApJ, 121, 161

Sánchez, A. G., Baugh, C. M., Percival, W. J., Peacock, J. A., Padilla, N. D., Cole, S., Frenk, C. S., & Norberg, P. 2006, MNRAS, 366, 189

Sanders, D. B., Salvato, M., Aussel, H., Ilbert, O., Scoville, N., Surace, J. A., Frayer, D. T., Sheth, K., Helou, G., Brooke, T., Bhattacharya, B., Yan, L., Kartaltepe, J., Barnes, J. E.,

Blain, A. W., Calzetti, D., Capak, P., Carilli, C., Carollo, C. M., Comastri, A., Daddi, E., Ellis, R. S., Elvis, M., Fall, M., Franceschini, A., Giavalisco, M., Hasinger, G., Impey, C., Koekemoer, A., Le Fevre, O., Lilly, S., Liu, M. C., McCracken, H. J., Mobasher, B., Renzini, A., Rich, M., Schinnerer, E., Shopbell, P. L., Taniguchi, Y., Thompson, D. J., Urry, C. M., & Williams, J. P. 2007, ArXiv Astrophysics e-prints, astro-ph/0701318

Saunders, W., Rowan-Robinson, M., & Lawrence, A. 1992, MNRAS, 258, 134

Scannapieco, E., Silk, J., & Bouwens, R. 2005, ApJ Lett., 635, L13

Schade, D., Lilly, S. J., Crampton, D., Ellis, R. S., Le Fèvre, O., Hammer, F., Brinchmann, J., Abraham, R., Colless, M., Glazebrook, K., Tresse, L., & Broadhurst, T. 1999, ApJ, 525, 31

Scoville, N., Aussel, H., Brusa, M., Capak, P., Carollo, C. M., Elvis, M., Giavalisco, M., Guzzo, L., Hasinger, G., Impey, C., Kneib, J. ., LeFevre, O., Lilly, S. J., Mobasher, B., Renzini, A., Rich, R. M., Sanders, D. B., Schinnerer, E., Schminovich, D., Shopbell, P., Taniguchi, Y., & Tyson, N. D. 2006a, ArXiv Astrophysics e-prints, astro-ph/0612305

Scoville, N., Benson, A., Blain, A. W., Calzetti, D., Comastri, A., Capak, P., Carilli, C., Carlstrom, J. E., Carollo, C. M., Colbert, J., Daddi, E., Ellis, R. S., Elvis, M., Ewald, S. P., Fall, M., Franceschini, A., Giavalisco, M., Green, W., Griffiths, R. E., Guzzo, L., Hasinger, G., Impey, C., Kneib, J., Koda, J., Koekemoer, A., Lefevre, O., Lilly, S., Liu, C. T., McCracken, H. J., Massey, R., Mellier, Y., Miyazaki, S., Mobasher, B., Mould, J., Norman, C., Refregier, A., Renzini, A., Rhodes, J., Rich, M., Sanders, D. B., Schiminovich, D., Schinnerer, E., Scodeggio, M., Sheth, K., Shopbell, P. L., Taniguchi, Y., Tyson, N., Urry, C. M., Van Waerbeke, L., Vettolani, P., White, S. D. M., Yan, L., & Zamorani, G. 2006b, ArXiv Astrophysics e-prints, astro-ph/0612306

Scranton, R., Johnston, D., Dodelson, S., Frieman, J. A., Connolly, A., Eisenstein, D. J., Gunn, J. E., Hui, L., Jain, B., Kent, S., Loveday, J., Narayanan, V., Nichol, R. C., O'Connell, L., Scoccimarro, R., Sheth, R. K., Stebbins, A., Strauss, M. A., Szalay, A. S., Szapudi, I., Tegmark, M., Vogeley, M., Zehavi, I., Annis, J., Bahcall, N. A., Brinkman, J., Csabai, I., Hindsley, R., Ivezic, Z., Kim, R. S. J., Knapp, G. R., Lamb, D. Q., Lee, B. C., Lupton, R. H., McKay, T., Munn, J., Peoples, J., Pier, J., Richards, G. T., Rockosi, C., Schlegel, D., Schneider, D. P., Stoughton, C., Tucker, D. L., Yanny, B., & York, D. G. 2002, ApJ, 579, 48

Seo, H.-J. & Eisenstein, D. J. 2003, ApJ, 598, 720

—. 2005, ApJ, 633, 575

—. 2007, ArXiv Astrophysics e-prints, astro-ph/0701079

Shanks, T. 2007, in prep.

Shanks, T., Bean, A. J., Ellis, R. S., Fong, R., Efstathiou, G., & Peterson, B. A. 1983, ApJ, 274, 529

Shanks, T., Sutton, D. H., Fong, R., & Metcalfe, N. 1989, MNRAS, 237, 589

Sharp, R., Saunder, W., Smith, G., Churilov, V., Correll, D., Dawson, J., Farrel, T., Frost, G., Haynes, R., Heald, R., Lankshear, A., Mayfield, D., Waller, L., & Whittard, D. 2006, ArXiv Astrophysics e-prints, astro-ph/0606137

Smail, I., Ivison, R. J., & Blain, A. W. 1997, ApJ Lett., 490, L5

Smith, R. E., Scoccimarro, R., & Sheth, R. K. 2007, Phys. Rev. D, 75, 063512

Smoot, G. F., Bennett, C. L., Kogut, A., Wright, E. L., Aymon, J., Boggess, N. W., Cheng, E. S., de Amici, G., Gulkis, S., Hauser, M. G., Hinshaw, G., Jackson, P. D., Janssen, M.,

Kaita, E., Kelsall, T., Keegstra, P., Lineweaver, C., Loewenstein, K., Lubin, P., Mather, J., Meyer, S. S., Moseley, S. H., Murdock, T., Rokke, L., Silverberg, R. F., Tenorio, L., Weiss, R., & Wilkinson, D. T. 1992, ApJ Lett., 396, L1

Spergel, D. N., Bean, R., Dore', O., Nolta, M. R., Bennett, C. L., Hinshaw, G., Jarosik, N., Komatsu, E., Page, L., Peiris, H. V., Verde, L., Barnes, C., Halpern, M., Hill, R. S., Kogut, A., Limon, M., Meyer, S. S., Odegard, N., Tucker, G. S., Weiland, J. L., Wollack, E., & Wright, E. L. 2006, ArXiv Astrophysics e-prints, :astro-ph/0603449

Spergel, D. N., Verde, L., Peiris, H. V., Komatsu, E., Nolta, M. R., Bennett, C. L., Halpern, M., Hinshaw, G., Jarosik, N., Kogut, A., Limon, M., Meyer, S. S., Page, L., Tucker, G. S., Weiland, J. L., Wollack, E., & Wright, E. L. 2003, ApJS, 148, 175

Stoughton, C., Lupton, R. H., Bernardi, M., Blanton, M. R., Burles, S., Castander, F. J., Connolly, A. J., Eisenstein, D. J., Frieman, J. A., Hennessy, G. S., Hindsley, R. B., Ivezić, Ž., Kent, S., Kunszt, P. Z., Lee, B. C., Meiksin, A., Munn, J. A., Newberg, H. J., Nichol, R. C., Nicinski, T., Pier, J. R., Richards, G. T., Richmond, M. W., Schlegel, D. J., Smith, J. A., Strauss, M. A., SubbaRao, M., Szalay, A. S., Thakar, A. R., Tucker, D. L., Vanden Berk, D. E., Yanny, B., Adelman, J. K., Anderson, Jr., J. E., Anderson, S. F., Annis, J., Bahcall, N. A., Bakken, J. A., Bartelmann, M., Bastian, S., Bauer, A., Berman, E., Böhringer, H., Boroski, W. N., Bracker, S., Briegel, C., Briggs, J. W., Brinkmann, J., Brunner, R., Carey, L., Carr, M. A., Chen, B., Christian, D., Colestock, P. L., Crocker, J. H., Csabai, I., Czarapata, P. C., Dalcanton, J., Davidsen, A. F., Davis, J. E., Dehnen, W., Dodelson, S., Doi, M., Dombeck, T., Donahue, M., Ellman, N., Elms, B. R., Evans, M. L., Eyer, L., Fan, X., Federwitz, G. R., Friedman, S., Fukugita, M., Gal, R., Gillespie, B., Glazebrook, K.,

Gray, J., Grebel, E. K., Greenawalt, B., Greene, G., Gunn, J. E., de Haas, E., Haiman, Z., Haldeman, M., Hall, P. B., Hamabe, M., Hansen, B., Harris, F. H., Harris, H., Harvanek, M., Hawley, S. L., Hayes, J. J. E., Heckman, T. M., Helmi, A., Henden, A., Hogan, C. J., Hogg, D. W., Holmgren, D. J., Holtzman, J., Huang, C.-H., Hull, C., Ichikawa, S.-I., Ichikawa, T., Johnston, D. E., Kauffmann, G., Kim, R. S. J., Kimball, T., Kinney, E., Klaene, M., Kleinman, S. J., Klypin, A., Knapp, G. R., Korienek, J., Krolik, J., Kron, R. G., Krzesiński, J., Lamb, D. Q., Leger, R. F., Limmongkol, S., Lindenmeyer, C., Long, D. C., Loomis, C., Loveday, J., MacKinnon, B., Mannery, E. J., Mantsch, P. M., Margon, B., McGehee, P., McKay, T. A., McLean, B., Menou, K., Merelli, A., Mo, H. J., Monet, D. G., Nakamura, O., Narayanan, V. K., Nash, T., Neilsen, Jr., E. H., Newman, P. R., Nitta, A., Odenkirchen, M., Okada, N., Okamura, S., Ostriker, J. P., Owen, R., Pauls, A. G., Peoples, J., Peterson, R. S., Petravick, D., Pope, A., Pordes, R., Postman, M., Prosapio, A., Quinn, T. R., Rechenmacher, R., Rivetta, C. H., Rix, H.-W., Rockosi, C. M., Rosner, R., Ruthmansdorfer, K., Sandford, D., Schneider, D. P., Scranton, R., Sekiguchi, M., Sergey, G., Sheth, R., Shimasaku, K., Smee, S., Snedden, S. A., Stebbins, A., Stubbs, C., Szapudi, I., Szkody, P., Szokoly, G. P., Tabachnik, S., Tsvetanov, Z., Uomoto, A., Vogeley, M. S., Voges, W., Waddell, P., Walterbos, R., Wang, S.-i., Watanabe, M., Weinberg, D. H., White, R. L., White, S. D. M., Wilhite, B., Wolfe, D., Yasuda, N., York, D. G., Zehavi, I., & Zheng, W. 2002, AJ, 123, 485

Strauss, M. A., Weinberg, D. H., Lupton, R. H., Narayanan, V. K., Annis, J., Bernardi, M., Blanton, M., Burles, S., Connolly, A. J., Dalcanton, J., Doi, M., Eisenstein, D., Frieman, J. A., Fukugita, M., Gunn, J. E., Ivezić, Ž., Kent, S., Kim, R. S. J., Knapp, G. R., Kron, R. G., Munn, J. A., Newberg, H. J., Nichol, R. C., Okamura, S., Quinn, T. R., Richmond, M. W., Schlegel, D. J., Shimasaku, K., SubbaRao, M., Szalay, A. S., Vanden Berk, D.,

Vogeley, M. S., Yanny, B., Yasuda, N., York, D. G., & Zehavi, I. 2002, AJ, 124, 1810

Sunyaev, R. A. & Zeldovich, Y. B. 1970, Ap&SS, 7, 3

Taylor, E. N. & Webster, R. L. 2005, ApJ, 634, 1067

Tegmark, M. 1997, Physical Review Letters, 79, 3806

Tegmark, M., Eisenstein, D. J., Strauss, M. A., Weinberg, D. H., Blanton, M. R., Frieman, J. A., Fukugita, M., Gunn, J. E., Hamilton, A. J. S., Knapp, G. R., Nichol, R. C., Ostriker, J. P., Padmanabhan, N., Percival, W. J., Schlegel, D. J., Schneider, D. P., Scoccimarro, R., Seljak, U., Seo, H.-J., Swanson, M., Szalay, A. S., Vogeley, M. S., Yoo, J., Zehavi, I., Abazajian, K., Anderson, S. F., Annis, J., Bahcall, N. A., Bassett, B., Berlind, A., Brinkmann, J., Budavari, T., Castander, F., Connolly, A., Csabai, I., Doi, M., Finkbeiner, D. P., Gillespie, B., Glazebrook, K., Hennessy, G. S., Hogg, D. W., Ivezić, Ž., Jain, B., Johnston, D., Kent, S., Lamb, D. Q., Lee, B. C., Lin, H., Loveday, J., Lupton, R. H., Munn, J. A., Pan, K., Park, C., Peoples, J., Pier, J. R., Pope, A., Richmond, M., Rockosi, C., Scranton, R., Sheth, R. K., Stebbins, A., Stoughton, C., Szapudi, I., Tucker, D. L., Berk, D. E. V., Yanny, B., & York, D. G. 2006, Phys. Rev. D, 74, 123507

Uomoto, A., Smee, S., Rockosi, C., Burles, S., Pope, A., Friedman, S., Brinkmann, J., Gunn, J., Nichol, R., & SDSS Collaboration. 1999, in Bulletin of the American Astronomical Society, Vol. 31, Bulletin of the American Astronomical Society, 1501

Verde, L., Heavens, A. F., Percival, W. J., Matarrese, S., Baugh, C. M., Bland-Hawthorn, J., Bridges, T., Cannon, R., Cole, S., Colless, M., Collins, C., Couch, W., Dalton, G., De Propris, R., Driver, S. P., Efstathiou, G., Ellis, R. S., Frenk, C. S., Glazebrook, K., Jackson,

C., Lahav, O., Lewis, I., Lumsden, S., Maddox, S., Madgwick, D., Norberg, P., Peacock, J. A., Peterson, B. A., Sutherland, W., & Taylor, K. 2002, MNRAS, 335, 432

Wake, D. A., Nichol, R. C., Eisenstein, D. J., Loveday, J., Edge, A. C., Cannon, R., Smail, I., Schneider, D. P., Scranton, R., Carson, D., Ross, N. P., Brunner, R. J., Colless, M., Couch, W. J., Croom, S. M., Driver, S. P., da Ângela, J., Jester, S., de Propris, R., Drinkwater, M. J., Bland-Hawthorn, J., Pimbblet, K. A., Roseboom, I. G., Shanks, T., Sharp, R. G., & Brinkmann, J. 2006, MNRAS, 372, 537

Werner, M. 2006, Astronomy and Geophysics, 47, 11

Werner, M. W., Roellig, T. L., Low, F. J., Rieke, G. H., Rieke, M., Hoffmann, W. F., Young, E., Houck, J. R., Brandl, B., Fazio, G. G., Hora, J. L., Gehrz, R. D., Helou, G., Soifer, B. T., Stauffer, J., Keene, J., Eisenhardt, P., Gallagher, D., Gautier, T. N., Irace, W., Lawrence, C. R., Simmons, L., Van Cleve, J. E., Jura, M., Wright, E. L., & Cruikshank, D. P. 2004, ApJS, 154, 1

White, M., Zheng, Z., Brown, M. J. I., Dey, A., & Jannuzi, B. T. 2007, ApJ Lett., 655, L69

Wild, V., Peacock, J. A., Lahav, O., Conway, E., Maddox, S., Baldry, I. K., Baugh, C. M., Bland-Hawthorn, J., Bridges, T., Cannon, R., Cole, S., Colless, M., Collins, C., Couch, W., Dalton, G., De Propris, R., Driver, S. P., Efstathiou, G., Ellis, R. S., Frenk, C. S., Glazebrook, K., Jackson, C., Lewis, I., Lumsden, S., Madgwick, D., Norberg, P., Peterson, B. A., Sutherland, W., & Taylor, K. 2005, MNRAS, 356, 247

Wolf, C., Dye, S., Kleinheinrich, M., Meisenheimer, K., Rix, H.-W., & Wisotzki, L. 2001, Astron. & Astrophys., 377, 442

Yamamoto, K., Bassett, B. A., Nichol, R. C., Suto, Y., & Yahata, K. 2006, Phys. Rev. D, 74, 063525

York, D. G., Adelman, J., Anderson, Jr., J. E., Anderson, S. F., Annis, J., Bahcall, N. A., Bakken, J. A., Barkhouser, R., Bastian, S., Berman, E., Boroski, W. N., Bracker, S., Briegel, C., Briggs, J. W., Brinkmann, J., Brunner, R., Burles, S., Carey, L., Carr, M. A., Castander, F. J., Chen, B., Colestock, P. L., Connolly, A. J., Crocker, J. H., Csabai, I., Czarapata, P. C., Davis, J. E., Doi, M., Dombeck, T., Eisenstein, D., Ellman, N., Elms, B. R., Evans, M. L., Fan, X., Federwitz, G. R., Fiscelli, L., Friedman, S., Frieman, J. A., Fukugita, M., Gillespie, B., Gunn, J. E., Gurbani, V. K., de Haas, E., Haldeman, M., Harris, F. H., Hayes, J., Heckman, T. M., Hennessy, G. S., Hindsley, R. B., Holm, S., Holmgren, D. J., Huang, C.-h., Hull, C., Husby, D., Ichikawa, S.-I., Ichikawa, T., Ivezić, Ž., Kent, S., Kim, R. S. J., Kinney, E., Klaene, M., Kleinman, A. N., Kleinman, S., Knapp, G. R., Korienek, J., Kron, R. G., Kunszt, P. Z., Lamb, D. Q., Lee, B., Leger, R. F., Limmongkol, S., Lindenmeyer, C., Long, D. C., Loomis, C., Loveday, J., Lucinio, R., Lupton, R. H., MacKinnon, B., Mannery, E. J., Mantsch, P. M., Margon, B., McGehee, P., McKay, T. A., Meiksin, A., Merelli, A., Monet, D. G., Munn, J. A., Narayanan, V. K., Nash, T., Neilsen, E., Neswold, R., Newberg, H. J., Nichol, R. C., Nicinski, T., Nonino, M., Okada, N., Okamura, S., Ostriker, J. P., Owen, R., Pauls, A. G., Peoples, J., Peterson, R. L., Petravick, D., Pier, J. R., Pope, A., Pordes, R., Prosapio, A., Rechenmacher, R., Quinn, T. R., Richards, G. T., Richmond, M. W., Rivetta, C. H., Rockosi, C. M., Ruthmansdorfer, K., Sandford, D., Schlegel, D. J., Schneider, D. P., Sekiguchi, M., Sergey, G., Shimasaku, K., Siegmund, W. A., Smee, S., Smith, J. A., Snedden, S., Stone, R., Stoughton, C., Strauss, M. A., Stubbs, C., SubbaRao, M., Szalay, A. S., Szapudi, I., Szokoly, G. P., Thakar, A. R., Tremonti, C., Tucker, D. L., Uomoto, A.,

Vanden Berk, D., Vogeley, M. S., Waddell, P., Wang, S.-i., Watanabe, M., Weinberg, D. H., Yanny, B., & Yasuda, N. 2000, AJ, 120, 1579

Zehavi, I., Blanton, M. R., Frieman, J. A., Weinberg, D. H., Waddell, P., Yanny, B., & York, D. G. 2002, ApJ, 571, 172

Zehavi, I., Eisenstein, D. J., Nichol, R. C., Blanton, M. R., Hogg, D. W., Brinkmann, J., Loveday, J., Meiksin, A., Schneider, D. P., & Tegmark, M. 2005a, ApJ, 621, 22

Zehavi, I., Weinberg, D. H., Zheng, Z., Berlind, A. A., Frieman, J. A., Scoccimarro, R., Sheth, R. K., Blanton, M. R., Tegmark, M., Mo, H. J., Bahcall, N. A., Brinkmann, J., Burles, S., Csabai, I., Fukugita, M., Gunn, J. E., Lamb, D. Q., Loveday, J., Lupton, R. H., Meiksin, A., Munn, J. A., Nichol, R. C., Schlegel, D., Schneider, D. P., SubbaRao, M., Szalay, A. S., Uomoto, A., & York, D. G. 2004, ApJ, 608, 16

Zehavi, I., Zheng, Z., Weinberg, D. H., Frieman, J. A., Berlind, A. A., Blanton, M. R., Scoccimarro, R., Sheth, R. K., Strauss, M. A., Kayo, I., Suto, Y., Fukugita, M., Nakamura, O., Bahcall, N. A., Brinkmann, J., Gunn, J. E., Hennessy, G. S., Ivezić, Ž., Knapp, G. R., Loveday, J., Meiksin, A., Schlegel, D. J., Schneider, D. P., Szapudi, I., Tegmark, M., Vogeley, M. S., & York, D. G. 2005b, ApJ, 630, 1

ACKNOWLEDGEMENTS

If you've just read the previous 200 or so pages, well done. However, if you've skipped all that just to read this, I don't totally blame you. So, I must start with a HUGE big thank you to Tom who has basically put up with me and my ramblings, excuses, late mornings, trips away, football banter and in general for the last 3 and a half years or so. So many funny tales, the potential highlight of which being the Frontier's Dinner and our trip to Oz. I don't think I'll ever forget when "Smack my Bitch Up" came on at 4am in the AAT control room.

Phil, whose guidance for the first two years of me PhD was so vital. Also, cheers for all the stimulating discussions that were started and kudos to Bill, who was always able give as good as he got. Rich and Utane have been absolutely cracking office mates. Cheers lads - the "work hard, play hard" office attitude was always much appreciated and I think the Empire is in very good hands.

Other members of the clan that have to be mentioned are José, George, as well as Marc, and my pre-decessor, Adam.

"Basically" I have to thank everyone in the XGal group but special shouts out go tae: David Wake, Alastair Edge, John Lucey (who got me to Durham in the first place some 7+ years ago!!), Shaun Cole (whose help during my UG years proved vital), Carlton Baugh, Mark Swinbank and Nigel Metcalfe. Chris Simpson and Nick Schurch were loud.

And then there is The Lads:

Craig "The DevilFish" B., Rob "Let us Pause" C., Hugh "Pain is weakness leaving the body" D., Jim "Take my Breath Away" G., Mark "Nozbo" N., Jim "Verge, The Ladies just don't get me" M., David "I still know what you did last summer" RS., and Jon "I know what I want,

and I ain't happy till I get it" S. Cheers boys, I'm gonna miss you and our weekly Gambrinus gatherings. Cheers also to the Ustinov AFC a.k.a. Jim and Tony.

They know this already but Derek and Tim were superb housemates. Tim - I'd have moved in with you sooner if I'd known about your curry making skills, Dez - I really don't know how you did it for 3 plus years ;-)

Zoë gets a whole line to herself because she is an absolute babe. xxxx xxxx xxxx

And Finally, the family. MPMR, Mum and Dad, who are very simply my Sunshine on Leith.